Coherence Phenomenon in Mesoscopic Systems

Thesis submitted for the degree of
Doctor of Philosophy (Science)

in

Physics (Theoretical)

by

Urbashi Satpathi

Department of Physics
University of Calcutta
August 2015

To my Family

Acknowledgments

This thesis will be incomplete without expressing my gratitude to peers, friends, faculties and family.

Back in 2010, my thesis started under the supervision of Prof. Prosenjit Singha Deo, in Satyendra Nath Bose National Centre for Basic Sciences (SNBNCBS). I am thankful to him for guiding me and giving me the opportunity to work in the mesmerizing world of mesoscopic physics. He has been a proactive, humble, friendly mentor. Apart from his pedagogy, even his hobby: 'Bird-watching' has arisen a similar interest and perspective in me towards the "Mother Nature". I have learnt a lot from him.

I am highly obliged to Prof. Priya Mahadevan for being pragmatic and supportive both during class and off-class, in SNBNCBS. I will cherish the moments we shared together; specially during DAE-SSPS 2014 conference in Vellore, where she was very helpful. I am also grateful to Prof. A. K. Raychaudhuri for supporting me. He has acknowledged my work in various symposiums and conferences. I would like to extend these words of thanks to Prof. S. S. Manna, Prof. Ranjan Chaudhuri, Prof. Manu Mathur, Prof. Bimalendu Bhattacharjee, Prof. P. K. Mukhopadhyay and Prof. T. S. Dasgupta, for there constant support in building my career. I would also like to thank the non teaching staff members of SNBNCBS, the sysadmin, the library staff and the security staff, who have always ensured a congenial, safe and knowledge environment in the campus. Well, I also thank all the gardeners in our institute, who have nurtured the mango trees (juicy mangoes) in our campus, which enthuse us in SNBNCBS campus.

I acknowledge Prof. Indrani Bose of Bose Institute, Kolkata and Prof. Bikas K. Chakrabarti of SINP, Kolkata, for reviewing my work in yearly evaluation during my Ph.D.

I would like to acknowledge INSPIRE-DST and SNBNCBS for financially supporting this research.

I am grateful to all my teachers in Lady Brabourne College and Presidency University, specially I would like to thank Dr. Muktish Acharrya who is among my favourite teachers from Presidency University. He has been a bolster in different walks of life, be it professional or personal. I also thank Dr. B. B. Bhattacharjee for helping me during my post-graduation and introducing me to the world of research.

Life within the campus would not have been easy without my friends around me. I am grateful to Hemant da, Sumit, Shinde, Kaloni, Sujit, Jasashree and my best friends Injamam and Rabeya. Their social discussions, knowledge share and friendship have inspired me every single day and will enthuse me forever. Specially Rabeya being industrious, has always encouraged me to challenge my limits and to push myself harder. She has rather been a sister than a friend and has always supported me.

It is very difficult to gratify parents in words though. This thesis is dedicated to my father Mr. Bhakta Ranjan Satpathi, who has been my mentor and teacher, and will be throughout my life. His selfless love, motivation and care always ensured that I am on the right path towards my goals. In fact, dedicating my thesis might be a small gift for him. I would like to thank my mother Mrs. Swapna Satpathi, who has been my inspiration throughout. I have learnt to become a resolver, be it any field, from her. Her methods of resolutions are remarkable and helped me during rough days in the institute. I also thank my sister Mowsumi for encouraging me to take Physics as a subject and to pursue research. In addition I thank my in-laws Mr. Swapan Kumar Panda and Mrs. Lakhmi Panda

for all their love and support during this journey. Last but nevertheless, I thank my husband Mr. Suman Kumar Panda for constantly and patiently supporting me day and night. His love, support, encouragement, pragmatism has made the end phase of this journey quite smoother.

I would further like to thank all the organizers/organizations for their support during my visit to below mentioned conferences/schools :

1. Anniversary Workshop on Transport in Nanostructures (10th Capri Spring School), Capri, Italy, April 28th- May 03rd, 2014.
2. International Conference on Nano Science and Technology (ICONSAT-2014), Punjab University, Mohali, India, March 2-5, 2014.
3. International Conference on Nanomaterials and Electronics Engineering- ICNEE 2012, Kuala Lumpur, Malaysia, July 24-26, 2012.
4. International Conference on Nano Science and Technology (ICONSAT-2012), Hyderabad, India, 20-23 January, 2012.
5. International Nonequilibrium Winter School, IISER, Kolkata, India, December 27, 2011 - January 11, 2012.
6. Workshop on Low Dimensional Quantum Systems, HRI, Allahabad, India, October 10-13, 2011.
7. International School on Topology in Quantum Matter, IISc, Bangalore, India, June 29- July 13, 2011.
8. International Conference on Mesoscopic physics and spectroscopy, SNBNCBS, Kolkata, India, November 22-24, 2010.

Urbashi Satpathi
Kolkata, India
August, 2015

List of Publications

1. **Urbashi Satpathi** and P. Singha Deo
   Injectance and a paradox
   Int. Journ. of Mod. Phy. B, 26, 1250028 (2012).

2. **Urbashi Satpathi**
   Current Delivered by an STM Tip in Landauer-Büttiker Formalism
   Applied Mechanics and Materials, Vol. 229-231 (Nov 2012) pp 1630-1634.

3. **Urbashi Satpathi** and P. Singha Deo
   Spontaneous symmetry breaking in quasi one dimension
   AIP Conf. Proc., 1665, 090019 (2015).

4. **Urbashi Satpathi**, Sumit Ghosh, Ashim Kumar Ray and P. Singha Deo
   Localization of electrons in internal frame
   Communicated.

5. **Urbashi Satpathi** and P. Singha Deo
   Negative partial density of states in mesoscopic systems
   Submitted.

Contents

List of Figures

Chapter 1

Introduction: Mesoscopic systems and fabrication of devices

Traditionally all systems accessible in nature, are divided into two distinct categories, macroscopic and microscopic [1], depending on the dimension of the system. In a layman language, if the dimension of the system is large enough so that it is visible with bare eyes, then the system is macroscopic; but if we can't see the system directly, then it is a microscopic system. The governing principles of phenomena occurring in two domains, i.e. macroscopic and microscopic, are quite distinct. The former category follows deterministic classical mechanics and the later category follows indeterministic quantum mechanics.

The statics and kinetics in macroscopic systems has been completely described by classical or Newtonian mechanics. For example, given an initial position of a particle with a velocity at a certain time, any succeeding states at later times can be readily computed along a distinguishable particle trajectory. This picture, however, turned out to be an inadequate eye to examine properties and behaviours of individual and aggregates of constituents at the atomic and subatomic levels. To perceive correct understanding of phenomena in such environment is beyond the range of classical physics, requiring alternative thinking to replace deterministic reduction of systems.

A tremendous insight has been gained in early twentieth century by brilliant scientists who successfully and beautifully established theoretical framework of quantum physics. Quantum physics

describes statics and kinetics in microscopic world by introducing the description of wave function as a solution to Schrödinger equation [2] to incorporate the intrinsic particle-like and wave-like nature of quantum entities. Furthermore, quantum world exhibits substantial characteristics: duality of wave and particle [3], indistinguishability [4], quantization [5], Heisenberg uncertainty principle [5, 6], finite zero-point energy [5, 7], and quantum entanglement [8]. The duality features coherence in the dynamics of quantum particles in quantum world, linking to correlation effects in systems. Quantum particles in the coherent state have a well defined energy and a well-defined phase configuration.

In Greek terminology, 'meso' means intermediate, the term 'mesoscopic' [9–15] was coined in the early 1980s. Mesoscopic systems have dimensions intermediate between macroscopic world of bulk materials and microscopic world of atoms and molecules. Mesoscopic physics is a wide branch of condensed matter physics, which bridge the gap between macroscopic systems and microscopic systems. Condensed matter physics is a significant branch of physics which deals mostly with phenomena occurring in solids, for example, optical, thermal, mechanical, magnetic, etc. properties. The systems mostly considered in condensed matter physics, consists of many building blocks or unit cells, or atoms. These unit cells arrange themselves in perfect order to form a perfect lattice or arrange themselves in random order to form an imperfect lattice. In both these cases, only bulk property of the system is known. Both macroscopic and mesoscopic systems comprises of large number of atoms, then the question arises is, how to distinguish them? The first difference is, for macroscopic systems, the average of the constituent particles is significant, in the contrary, for mesoscopic systems the fluctuations around the average becomes significant. Another difference is, macroscopic systems most vividly obeys laws of classical mechanics, whereas mesoscopic systems obeys laws of quantum mechanics.

Now the question is there is wide dimensional gap between the macroscopic and microscopic systems, then as the definition implies, is there no limitation to the dimensions of mesoscopic systems? Yes there is. The limit where quantum effects become important has been given the name of mesoscopic physics. Carrier transport in this limit exhibits both particle and wave characteristics. The dimensions whether macroscopic or microscopic depends on certain length scales [16,17]. These scales are :

1. The de-Broglie wavelength (λ) : This is the length of the electron wave related to momentum of the electrons.

2. Mean free path (L_m) : The length after which initial momentum is changed or distance between two collisions.

3. Phase Coherence length (L_ϕ) : The length scale over which the wave moves coherently.

A detailed description of these length scales will be covered later on, in this chapter. The systems whose dimensions are less than these length scales are characterised under microscopic systems, while the others with dimensions greater than these length scales are characterised under macroscopic systems. Before going into details of these length scales, we would like to introduce the heterostructure two dimensional electron gas (2-DEG), a device widely used in mesoscopic and semiconductor industries.

Since the 1980s, the semiconductor technology has reached a level of sophistication that allows for the fabrication of heterostructure with length scales in the mesoscopic regime, meaning that the length scales of the structure are below the characteristic scattering lengths of the carriers such that coherent quantum transport effects are observed. Since these length scales generally depend very strongly on the material, the temperature, and the applied electric or magnetic fields the structural dimensions may vary between a few nanometres and a micrometer. One way of reaching the mesoscopic regime without the use of nano-fabrication techniques is to reduce the scattering rates and thus enhance the characteristic length scales up to the micrometer range. Therefore, one of the key structures that first enabled quantum transport experiments is the 2-DEG that forms at the interface of an undoped (or intrinsic) *GaAs* substrate and a doped (or extrinsic) *AlGaAs* barrier.

1.1 Two dimensional electron gas

A two dimensional electron gas (2-DEG) [16–18] can be artificially created by strong confinement in one direction (conventionally called the transverse direction or the z-direction) of an ordinary electron gas found in a semiconductor. Say for example two semiconductor layers, or semiconductor-insulator layers are brought in contact to each other. Then due to energy gap, there is charge transfer between

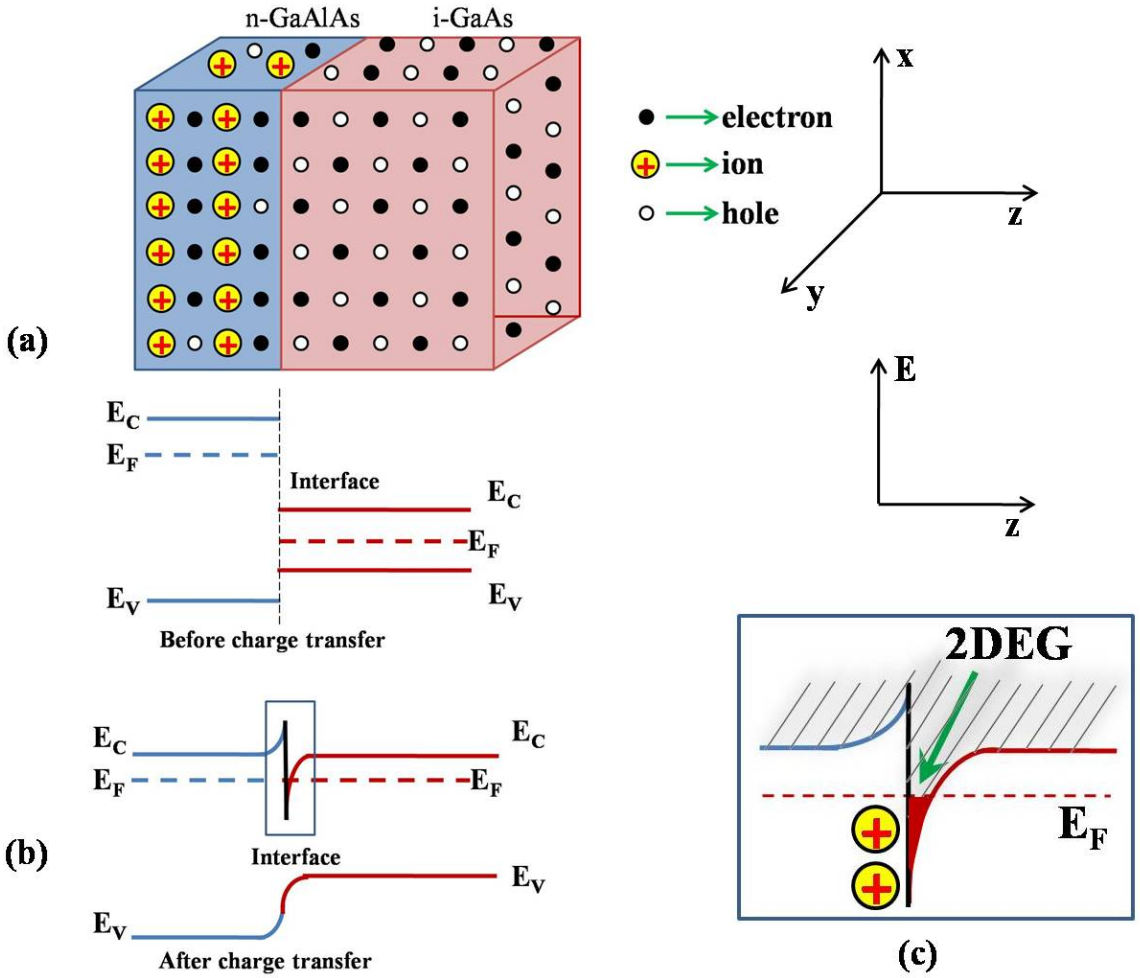

Figure 1.1 Formation of 2-DEG. a) Upper: *GaAlAs* and *GaAs* heterojunction, blue region for *GaAlAs* and red region for *GaAs*. *GaAlAs* is doped with positively charged ions (yellow coloured big dots), and hence electrons (shown by block dots) are large in number and holes (shown by white dots) are very few in number, while *GaAs* is undoped hence the number of electrons and holes are equal. The axes define the three spatial directions. Lower: Band structure of *GaAlAs* and *GaAs*, before charge transfer. (b) Band structure after they have been brought into contact, i.e after charge transfer. (c) The magnified view of the well formed at the interface (in the *GaAs* side) shown by the red region, where the Fermi level is within the conduction band. This well is 2-DEG, which is formed at the *GaAs* side.

the two layers, which gives rise to a electrostatic potential that causes the bands to bend at the interface and a formation of narrow well at the interface. Due to confinement in the transverse direction in the well, transverse modes are formed, which participate in electron conduction. When the energy band separation is much larger than the thermal energy k_BT, only the lowest energy band will be relevant for conduction, and the electron gas in the well effectively behaves like a two-dimensional conductor.

In most of the experiments on mesoscopic systems, heterojunctions of III-V semiconductors such as $GaAs/GaAlAs$[1] are used, where 2-DEG is formed at the interface of intrinsic semiconductor $i-GaAs$ and extrinsic semiconductor $n-GaAlAs$. The reason behind using these semiconductors, is their similar lattice constants and the coefficient of expansion. This reduces boundary scattering and leads to a dramatic increase in the mobility of the 2-DEG. To understand properly how this 2-DEG is formed at the interface of *GaAs* and *GaAlAs*, let us consider the band diagram of the two semiconductors. The formation of 2-DEG is illustrated in Fig. 1.1. In n-type extrinsic semiconductor, the semiconductor is doped with positively charged ions (commonly called donors), hence electrons are majority carriers and holes are minority carriers, and in intrinsic semiconductors the number of electrons and holes are equal. The band diagram[2] before charge transfer is exemplified in Fig. 1.1(a). For *GaAlAs*, the Fermi energy E_F lies closer to the conduction band E_C, and for *GaAs* the Fermi energy is intermediate between conduction band E_C and valence band E_V, the conduction band is higher for *GaAlAs* than *GaAs*. When the two semiconductors are brought in contact to each other, the electrons move from higher density region (i.e. *GaAlAs*) to lower density region (i.e. *GaAs*), leaving behind positive dopant ions which causes electrostatic energy to build up at the interface. Eventually, the electrostatic energy is so large, that electrons can no longer cross over to the other side, and the system reaches equilibrium. This new charge distribution or charge transfer results in bending of bands at the interface (Fig. 1.1(b)). Which further results in a single Fermi level throughout the band. The conduction band now develops a narrow well at the interface (shown in Fig. 1.1(c) by

[1] *GaAlAs* is an alloy of *GaAs* and *AlAs* and has a zincblende crystal structure. The actual formula is $Ga_{1-x}Al_xAs$, where x is integer between 0 and 1.

[2] When atoms organise into the periodic structures found in crystalline solid [19, 20], the atomic energy levels merge into bands where closely spaced energy levels are associated with different momenta. The number of energy levels in each band is proportional to the number of atoms in the lattice.

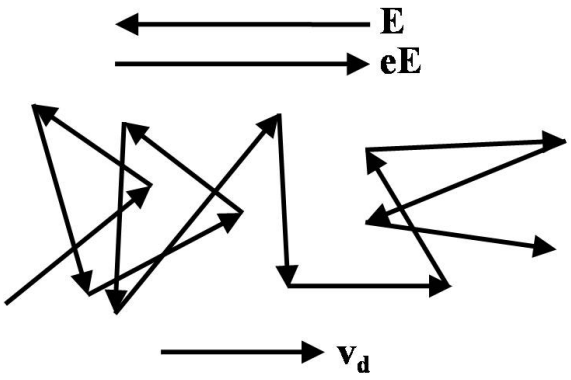

Figure 1.2 In the presence of an electric field, the electrons acquire a drift velocity superposed on their random motion.

the red region), where the Fermi energy is inside the well. Within this narrow well the electrons are confined in a direction normal to the interface (z direction), but free to move along the interface (x, y directions), and hence this well serves as a 2-DEG.

The carrier concentration in a 2-DEG typically ranges from $2 \times 10^{11}/cm^2$ to $2 \times 10^{12}/cm^2$. 2-DEG is widely used as a FET (Field effect transistor), MODFET (Modulation doped FET), HEMT (High electron mobility transistor). The quantum mechanical motion of electrons in 2-DEG allows the investigation of various coherent quantum phenomena, like quantum Hall effect [21], Coulomb blockage [22] and conductance quantization [23, 24].

1.1.1 Mobility

As stated in the previous section of 2-DEG, what makes it special in miniaturization industry is its extremely low mobility. Then let us briefly explain the meaning of mobility [16]. In equilibrium, the conduction electrons move here and there randomly in all directions, with an effective zero current. If an electric field E is applied, then the electrons are drifted in the direction opposite to the field with drift velocity v_d, as shown in Fig. 1.2. At steady state, the rate at which they lose momentum p due to scattering forces is equal to the rate at which the electrons receive momentum from the external field, i.e.,

$$\left[\frac{dp}{dt}\right]_{scattering} = \left[\frac{dp}{dt}\right]_{field}$$

Hence,

$$\begin{aligned} \frac{m_e v_d}{\tau_m} &= eE \\ v_d &= \frac{e\tau_m}{m_e}E \end{aligned} \tag{1.1}$$

where, m_e is effective mass[3] of electron and τ_m is momentum relaxation time. The mobility is defined as the ratio of the drift velocity to the electric field,

$$\mu = \frac{v_d}{E} = \frac{e\tau_m}{m_e} \tag{1.2}$$

In 2-DEG, the carrier concentrations of $10^{12}/cm^2$ have been obtained in a layer of thickness 100Å with mobilities of $10^6 cm^2/Vs$. The reason is the spatial separation between the donor atoms in *GaAlAs* layer and the conduction electrons in the *GaAs* layer. This reduces the scattering cross section due to the impurities which leads to weaker scattering.

1.2 Important length scales

In mesoscopic systems, a number of different length scales come into play. These different length scales are associated with different processes, and determine the types of interference that can be observed in quantum transport measurements.

1.2.1 de Broglie wavelength

The length between two maxima or minima of the interference pattern gives the measure of wavelength. An example is shown in Fig. 1.3(a). de Broglie wavelength λ is the shortest length scale and is related to momentum p by,

$$\lambda = \frac{h}{p} \tag{1.3}$$

[3]Effective mass m_e is given by $\frac{\hbar^2}{\frac{d^2E}{dk^2}}$, where $E(k)$ is the energy of electron. m_e is generally different from the real mass $m_0 = 9.11 \times 10^{-31} kg$. It can be both positive and negative depending on the sign of $\frac{d^2E}{dk^2}$. For electrons m_e is positive and for holes it is negative.

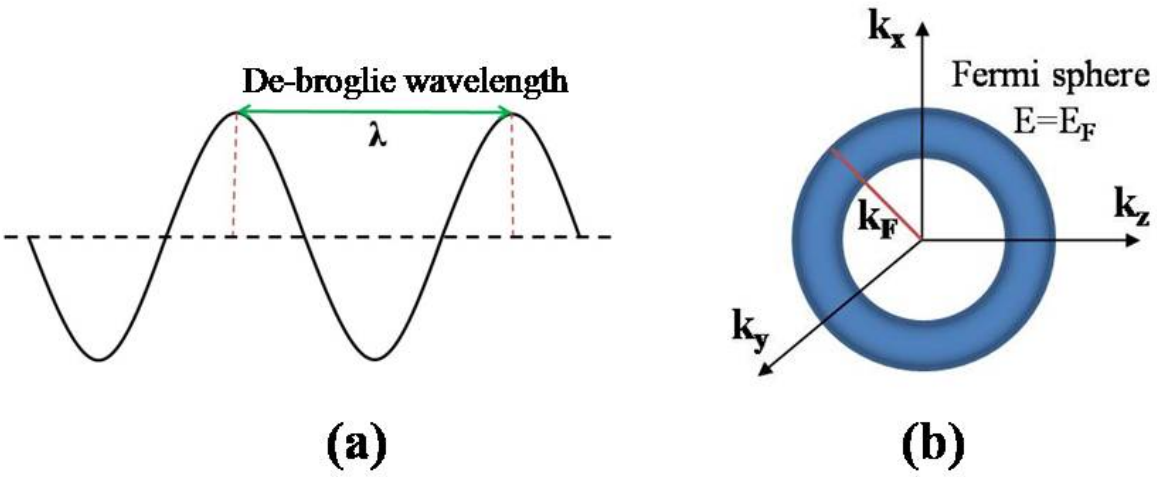

Figure 1.3 Few length scales shown in reference to section 1.2. (a) de Broglie wave length. (b) Fermi sphere of radius k_F, the electrons within the shaded region participate in conduction.

where, $h = 6.63 \times 10^{-34} Js$ is the Planck's constant. Another form of the de Broglie equation is the connection between momentum p and wave vector k,

$$p = \hbar k \tag{1.4}$$

where $\hbar = \frac{h}{2\pi}$ is reduced Planck's constant. The origin of this length scale is the hypothesis of Louis de Broglie [3] in the year 1924 in his thesis, where it was proposed that as light has both wave and particle property, electron which is a particle is also associated with a wave called matter wave having wavelength λ. The existence of matter waves for electrons was first experimentally observed by Davisson and Germer [25] in 1927. The relationship is now known to hold for all types of matter: all matter exhibits properties of both particles and waves. de Broglie's extension of the concept of wave-particle duality for light (photons) to matter (electrons), further helped in interpreting the electrons as standing wave in Bohr model [26].

1.2.2 Fermi wavelength

Electrons are not particles only having charge but also spin one-half. Thus they are subject to Pauli-exclusion principle [5], following which no two electrons can be placed in the same energy level. Consequently, electrons are places in different states, the first one in the lowest energy state, the next

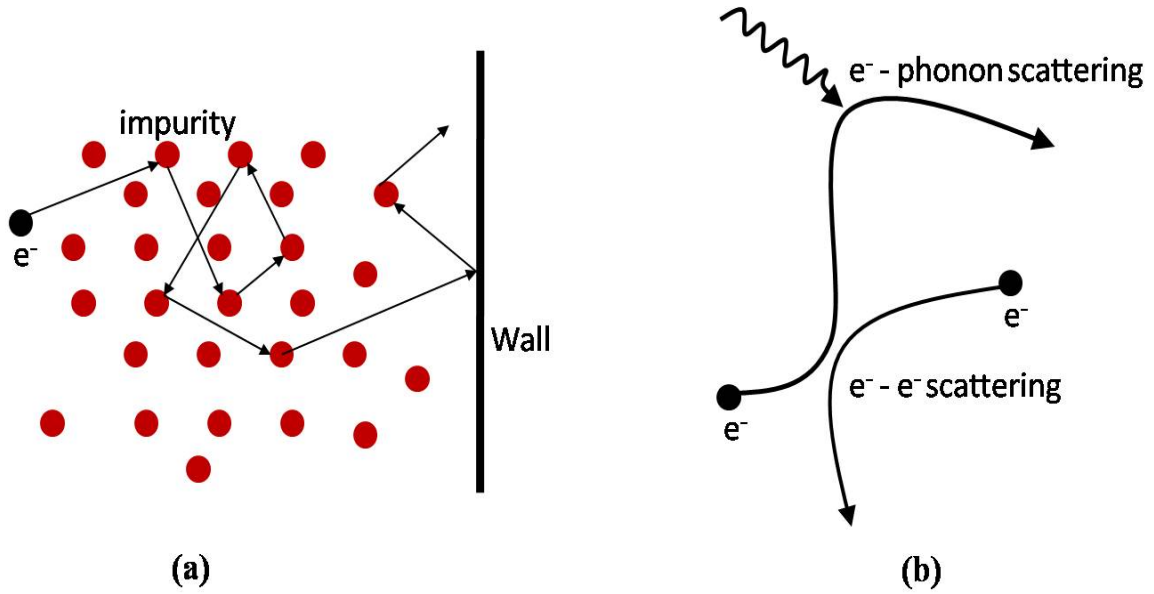

Figure 1.4 Scattering of electrons. (a) Elastic scattering occurring at localised, time independent scattering centres, like impurities and walls. (b) Inelastic scattering processes via time dependent mechanisms such as lattice vibrations or phonons and electron-electron interactions.

in the next higher energy state, and so on. With all the electrons placed in different states, the last electron is placed at the highest energy state of the system, which is called Fermi energy E_F. In this energy state, the electrons have de-Broglie wavelength λ_F,

$$\lambda_F = \frac{h}{p_F} = \frac{2\pi}{k_F} \tag{1.5}$$

where, p_F and k_F are Fermi momentum and Fermi wave vector. For electron conduction, only electrons in the vicinity of Fermi state with energy E_F, will participate. In Fig. 1.3(b) the Fermi sphere is shown where the region of electrons participating in conduction is shown by the shaded region. Electrons away from the Fermi level, have much longer wavelengths. λ_F is the smallest length scale in mesoscopic systems. It varies from few Å (1 Å $= 10^{-10}m$) in metals to a few hundred Å ($10nm$) in 2-DEG hetero-junctions.

1.2.3 Mean free path

In mesoscopic systems or conductor, there are free electrons which moves freely here and there, as if they are in vacuum. Any hindrance such as lattice vibrations (phonons), impurities, grain boundaries

leads to collisions with electrons. Due to collision electrons gets scattered from one state to another, thereby changing their momentum. Depending on whether the scattering is elastic or inelastic the energy and momentum of the electrons changes. The elastic and inelastic scattering [27] of electrons is represented in Fig. 1.4. Elastic scattering changes momentum but does not change energy, while inelastic scattering changes both momentum and energy of incident particles. Elastic scattering is characterised by, $E_{initial} = E_{final}$ and $|k_{initial}| = |k_{final}|$, however, the direction of propagation of the electrons (i.e. wave vector) before and after scattering need not be the same, $\vec{k}_{initial} \neq \vec{k}_{final}$. Mean free path L_m is the average distance travelled by the electron between successive elastic scattering events, and is given by,

$$L_m = v_F \tau_m \tag{1.6}$$

where, τ_m is the average time between successive scattering events and is known as elastic scattering time or momentum relaxation time. τ_m is related to the collision time τ_c by a relation,

$$\frac{1}{\tau_m} \longrightarrow \frac{1}{\tau_c}\alpha_m \tag{1.7}$$

where α_m is the 'effectiveness' factor of an individual collision in destroying initial momentum. The value of α_m lies between 0 and 1, depending on the strength or angle of scattering. L_m will become shorter and shorter, with an increase of the density of scatterers. This is termed as momentum relaxation length in many literatures. In the same way inelastic scattering is characterised by, $E_{initial} \neq E_{final}$ and $\vec{k}_{initial} \neq \vec{k}_{final}$. The average distance travelled by the electron between successive inelastic scattering events, is called inelastic mean free path L_i. In disordered metals (metals having impurities), L_m is about 100Å, whereas for 2-DEG L_m is of the order of 10μm.

1.2.4 Phase coherence length

Now let us relate the scattering phenomena to the phase of the travelling electron wave. Let us consider an electron which is allowed to follow the same path twice. In case of elastic scattering, the electron retracing the path for the second time, will experience exactly same environment as the first time, and so will scatter in the same way as during its first travel. So, we conclude that elastic scattering does not randomise the phase of the electron wave. This has to be contrasted to the case

of inelastic scatterings. If the electron starts to follow the path for the second time, the scattering will be different as it depends on mechanisms that act statistically in time and space. Because of the random nature of these scattering interactions, the phase is changed. Elastic mechanisms only modify the wave patterns of electrons contained in the system of interest which may lead to an increased complexity of the pattern, whereas inelastic effects modify the wave patterns and can even completely suppress these. Phase coherence length L_ϕ [27] represents the distance an electron wave can travel before its phase becomes randomised, and is given by,

$$L_\phi = v_F \tau_\phi \tag{1.8}$$

where, τ_ϕ is phase relaxation time and is related to τ_c (in a similar way as in the case of τ_m),

$$\frac{1}{\tau_\phi} \longrightarrow \frac{1}{\tau_c}\alpha_\phi \tag{1.9}$$

where, α_ϕ is the effectiveness factor of an individual collision in destroying initial phase. The systems whose dimensions are less than phase coherence length L_ϕ belongs to mesoscopic systems. The phase coherence length L_ϕ is the characteristic length for interferences of electronic wave functions. L_ϕ increases with decreasing temperature and can be much greater than the mean free path L_m. In disordered metals, L_ϕ is of the order of few μm and for 2-DEG it is more than 20 μm.

1.2.5 Thermal length

The thermal length L_T is the typical length scale over which different components of a wave-packet associated with an electron acquires a phase difference of the order of unity.

$$L_T = v_F \tau_T = \frac{\hbar v_F}{k_B T} \tag{1.10}$$

where, $\tau_T = \frac{\hbar}{k_B T}$ is the thermal time, k_B is Boltzmann constant and T is the temperature. At non-zero temperatures, electrons wave-packet have energy width equal to thermal energy $k_B T$, and L_T is the characteristic length.

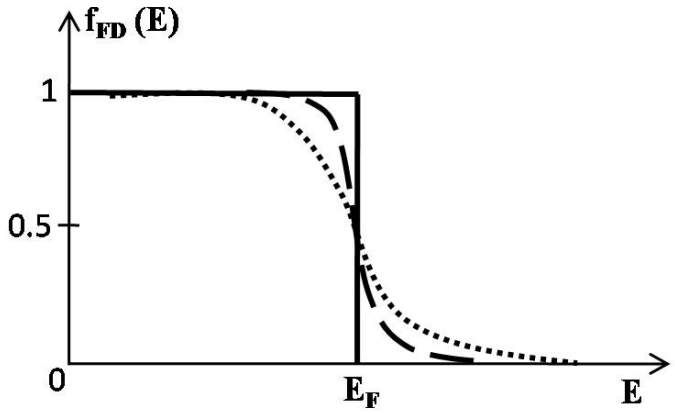

Figure 1.5 The Fermi-Dirac distribution for T=0 E_F (solid), T$\sim 0.1E_F$ (dash) and T$\sim 0.3E_F$ (dot).

1.3 Important energy scales

In this section we will discuss few energy scales which are important in mesoscopic systems. In particular, the thermal energy, the Fermi energy and Thouless energy will be discussed, in this section.

1.3.1 Thermal energy

At finite temperature the electrons have energy called thermal energy k_BT. According to equipartition theorem, thermal energy is equally distributed between all degrees of freedom. For each degree of freedom, the thermal energy is $\frac{k_BT}{2}$. So in a f dimensional system, electron has a thermal energy of

$$E_T = f\frac{k_BT}{2} \tag{1.11}$$

where, f is number of degrees of freedom. These degrees of freedom may include pure translational motion, rotational motion, vibrational motion and associated potential energies. In general, due to quantum mechanical reasons, the availability of any such degrees of freedom is a function of the energy in the system, and therefore depends on the temperature.

1.3.2 Fermi energy

As discussed earlier no two electrons can be placed in the same quantum state due to Pauli exclusion principle. The electrons are filled in different energy states following Fermi-Dirac distribution [28],

$$f_{FD}(E,T) = \frac{1}{1+e^{\frac{E-E_F}{k_BT}}} \tag{1.12}$$

where, E_F is the Fermi energy, i.e., the maximum energy upto which electrons are filled at zero temperature. The Fermi-Dirac distribution for zero temperature and higher temperatures are shown in Fig. 1.5. For $E < E_F$, the occupation of electrons is unity and for $E > E_F$, the occupation is zero. At zero temperature, an abrupt transition from unity to zero occupation is seen. For increasing temperature, the transition becomes smeared over an energy interval of a few times the thermal energy k_BT. This implies that at large temperatures, there are empty states below E_F and some filled states above E_F. Fermi energy also depends on dimensions of the system containing electrons. A further description of different dimensional systems and there Fermi energy, density of states, which are generally studied in mesoscopic physics is given in Appendix A.

1.3.3 Thouless energy

We finalise this section by introducing an energy scale called 'Thouless energy' [29] named after its founder David J. Thouless. The Thouless energy E_{Th} provides a measure of the relation between the energy of a state and phase evolution in a restricted area of space of size L (say). Assume an ideal scattering free crystal. An electron wave of wave vector $\vec{k}$ and energy E, travelling over a distance L acquires a phase $\phi = kL$. If the wave vector of the state is changed from $\vec{k}$ to $\vec{k}+\Delta\vec{k}$, then the phase will change by

$$\Delta\phi = \Delta kL \tag{1.13}$$

Again energy and wave vector are related by,

$$E = \frac{\hbar^2 k^2}{2m_e} \tag{1.14}$$

Therefore,

$$\frac{dE}{dk} = \frac{\hbar^2 k}{m_e} = \hbar v \tag{1.15}$$

where, $v = \frac{\hbar k}{m_e}$ is velocity of the wave. Thus for the change in energy due to change in wave vector by $\triangle k$, one finds

$$\Delta E = \frac{dE}{dk}\Delta k = \hbar v \frac{\Delta\phi}{L} = \frac{\hbar\Delta\phi}{\tau_L} \tag{1.16}$$

where, τ_L is the time taken by the wave to traverse distance L. If we take, $\Delta\phi = 1$, then we get Thouless energy E_{Th} given by

$$E_{Th} = \frac{\hbar}{\tau_L} \tag{1.17}$$

Thus the Thouless energy for a system of size L is related to the time it takes for an electron wave to cover this distance (L).

1.4 Electronic transport regime

The length scales discussed in section 1.2 provide different transport regimes in mesoscopic systems under different restrictions. These conditions are enabled on the dimension L of the system under consideration. To define the different regimes [27] we first have to discriminate between the quantum case and the classical case. Evidently in the classical case we are not interested in any effect arising due to wave nature of the electrons, and so the Fermi wavelength λ_F should be small compared to all other length scales in the problem. In contrast, for the quantum case the wave nature is a crucial ingredient, as this allows typical quantum effects like interference to occur. This also implies that the phase of the electron wave should be preserved sufficiently over the system, otherwise no phase relationship is possible. Another way of discriminating different regimes is the scattering phenomena. If the electrons are scattering very often during their traversal of the system then they are said to behave 'diffusively', their paths are similar to random walk well known in Brownian motion. If on the other hand, the electron can traverse the system without any scattering i.e., following a straight line, its motion is said to 'ballistic'. Based on these arguments, we can set up the conclusion on different regimes as,

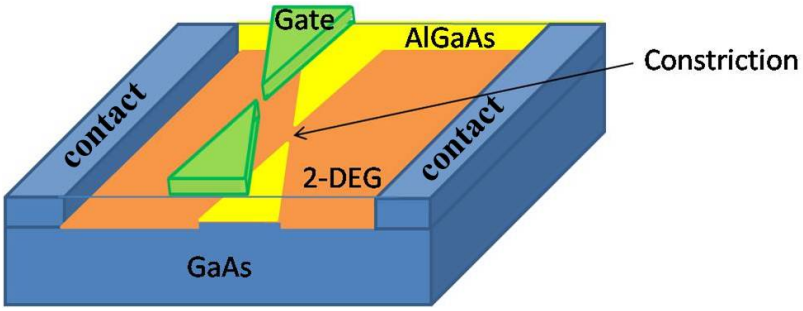

Figure 1.6 Schematic cross-sectional view of a quantum point contact (QPC), defined in a high-mobility 2-DEG at the interface of a *GaAsGaAlAs* heterojunction. The QPC is formed when a negative voltage is applied to the gate electrodes on top of the *GaAlAs* layer. The orange area represents the 2-DEG and the yellow area is the depleted region. Transport measurements are made by employing contacts to the 2-DEG at either side of the constriction. This figure is adapted from ref. [35].

1. Diffusive transport regime : $\lambda_F, L_m, L_T << L, L_\phi (or, L_i)$.

2. Ballistic transport regime : $L < \lambda_F, L_m, L_T, L_\phi (or, L_i)$.

The definitions of phase coherence length L_ϕ in Eq. (1.8) and thermal length L_T in Eq. (1.10) are trivial in ballistic regime, but not in the diffusive regime. In diffusive regime, phase coherence length is given by,

$$L_\phi = \sqrt{D\tau_\phi} \tag{1.18}$$

and thermal length is given by,

$$L_T = \sqrt{D\tau_T} \tag{1.19}$$

where, D is diffusion coefficient and is given by,

$$D = \frac{v_f^2 \tau_m}{2} \tag{1.20}$$

1.5 Quantum point contact (QPC)

The study of ballistic transport through point contacts in metals has a long history [30–33]. Point contacts in metals act like small conducting slit in a thin insulating layer, separating bulk metallic

conductors (with mean free path L_m much larger than the size of the slit). Actual point contacts usually are fabricated by pressing a metal needle on a metallic single crystal, followed by spot-welding. Ballistic transport has been studied in this way in a variety of metals. Point contacts in bulk doped semiconductors have been fabricated by passing two wedge-shaped specimens close together. One limitation of these techniques is that of a point contact is not continuously variable.

Quantum point contacts (QPC) in 2-DEG discussed in section 1.1 cannot be fabricated by the same method, since the electron gas is confined at the $GaAs-GaAlAs$ interface in the sample interior. By means of a split gate [34–36] on top of the heterostructure, one can define short and narrow constrictions [35] in the 2-DEG of variable width comparable to the Fermi wavelength λ_F. The split gate is fabricated using a combination of electron beam and optical lithography [37]. The gate pattern require two point contacts positioned next to each other on the 2-DEG boundary. The cross sectional view of a 2-DEG is shown in Fig. 1.6. Note that the actual 2-DEG boundary between the two point contacts is a depletion potential wall below the gate (which extends laterally beyond the gate pattern). The effect of a negative gate voltage is to deplete gradually the electron gas under the gate structure. Beyond the depletion region, no mobile carriers are present under the gate, and two conducting constrictions are formed, of width about $50nm$. Such a constriction is called a quantum point contact (QPC) (see Fig. 1.6). Two high mobility 2-DEG regions thus are isolated electrically from the rest of the 2-DEG, apart from the narrow constriction or QPC, under the openings of the gate. A further increase of the negative voltage forces the constriction to become progressively narrower, until they are fully pinched off. By this technique, it is possible to define QPCs of variable width W (say).

The 2-DEG in a $GaAsGaAlAs$ heterojunction has a Fermi wave length which is a hundred times larger than in a metal. This makes it possible to study a constriction with an opening comparable to the wave length.

Chapter 2

Coherence and Scattering phase shift

Wave propagation in a random medium is a phenomenon common to many areas of physics. There has been a recent resurgence of interest following the discovery, both in optics and quantum mechanics, of surprising coherent effects in a regime in which disorder was thought to be sufficiently strong to eliminate a priori all interference effects.

2.1 Coherence vs Decoherence

Let us start with an introduction to '*coherence*', as this is the phenomena broadly studied in this thesis. In a quantum mechanical (or at least semi-classical) description, electrons carry not only momentum, energy and spin but also a phase. Coherence [38, 39] is related to the definite phase relationship at different points of space and time. For a source to be coherent it must emit electrons of single frequency or the frequency spread must be very small. Also the electron wavefront must have a shape which remains constant in time. Coherence is thus sub-categorised as temporal coherence and spatial coherence. Temporal coherence is measure of phase and amplitude of electrons at a spacial point, at different moments in time. An example where temporal coherence is observed is Michelson Morley experiment, where the incident wave traverses different arms of the interferometer, the lengths of the arms being different introduces a temporal shift to the fringes. Spatial coherence is measure of phase and amplitude of electrons at same time but at different points in space. An experiment where spacial coherence is observed is Young's double slit experiment, where the waves passes through

two spatially separated slits and meet at the screen equally spaced from the slits. Due to the spatial separation the visibility of fringes changes from maxima to minima.

An ideal monochromatic wave represented by a harmonic function, extends from $-\infty$ to ∞ in time at any fixed point. So, the amplitude is constant and the phase varies linearly in time. So, the prediction of phase and amplitude is possible over an entire scale of time. Such a wave is truly temporally coherent. But practically, a source emits electrons in short pulses called wavepulse, during a time scale of $\Delta t = 10^{-8}s$. As the source emits electrons in a random fashion, there will be no phase relationship between the pulses coming from different electrons. However at a given space point, the prediction of phase and amplitude is possible at two different instants of time provided that the same wavepulse is still passing through the point. Thus Δt is the longest time interval over which such prediction is possible. The electron is said to be coherent for the time Δt. This time $\Delta t = \tau_\phi$ is called phase coherence time. The length of the wavepulse is, $L_\phi = v_F \tau_\phi$ is called phase coherence length. Thus it is the length upto which the phase relationship between the interfering electrons remain constant. If the path difference between the interfering waves becomes greater than L_ϕ, then the interfering waves does not have a definite phase relationship.

In order to better understand the nature of this coherence length, it is useful to review some notions related to quantum coherence. Consider an ensemble of quantum particles contained in a cubic box of side length L in D dimensions. The possible quantum states are coherent superposition of wave-functions such that the quantum state of the system is coherent over the whole volume LD. There are many examples in which quantum coherence extends up to the macroscopic scale : superconductivity, super-fluidity, free electron gas at zero temperature, coherent states of the photon field, etc.

Quantum 'decoherence' is a dynamical process whereby a system's phase relations become de-localized due to interaction and subsequent entanglement with its environment. This delocalization[1] forces the quantum system into a state that is apparently classical (or apparently an eigenstate) by prodigiously suppressing features that typically give rise to so-called quantum behaviour. The suppression of quantum coherence results from phenomena linked to the existence of incoherent and irreversible processes due to the coupling of electrons to their environment. This environment con-

[1]The terms decoherence and delocalization are loosely used in this thesis, as both are more or less the same phenomena.

sists of degrees of freedom with which the electrons interact : thermal excitations of the atomic lattice (phonon), impurities having internal degrees of freedom, interaction with other electrons, etc. This irreversibility is a source of decoherence for the electrons and its description is a difficult problem. The phase coherence length L_ϕ generically describes the loss of phase coherence due to irreversible processes. In metals, the phase coherence length is a decreasing function of temperature. In practice, L_ϕ is of the order of a few microns for temperatures less than one kelvin.

To understand the origin of these coherent effects, it may be useful to recall some general facts about interferences. Although quite spectacular in quantum mechanics, their description is more intuitive in the context of physical optics. For this reason, we begin with a discussion of interference effects in optics. When two or more waves (disturbances) meet at a point simultaneously, then they result in a resultant wave due to principle of superposition. The intensity of resultant wave is maximum or minimum depending on whether the waves are in same phase or in opposite phase. This phenomenon is known as *interference*. This phenomenon was experimentally observed in Young's double slit experiment, discussed below.

2.2 Double slit interference

The set up of the famous Young's double slit experiment is shown in Fig. 2.1. Suppose there is a narrow slit S, which act as source for monochromatic wave of wavelength λ. There are two slits S_1 and S_2 equidistant from the source. The monochromatic waves spread out from slit S and reaches the slits S_1 and S_2 in the same time. The slits are spatially separated from each other by a distance d. The waves starting from S_1 and S_2 spreads and diverge towards the screen kept at a distance D from the centre of the slits C'. Since these wave packets originate from the same source, and reaches the slits spatially separated at the same point of time, hence these wave packets are spatially coherent in nature. The waves splitting from these slits (or coherent sources) interfere to give interference pattern on the screen. At the center of the screen C, the waves from the two sources travel equal distances and are in phase. As we move away from the center, the path travelled by the waves from one source is larger than that travelled by the waves from the other source. When the difference in path is equal to half a wavelength, destructive interference occurs. When the difference in path length is equal to a

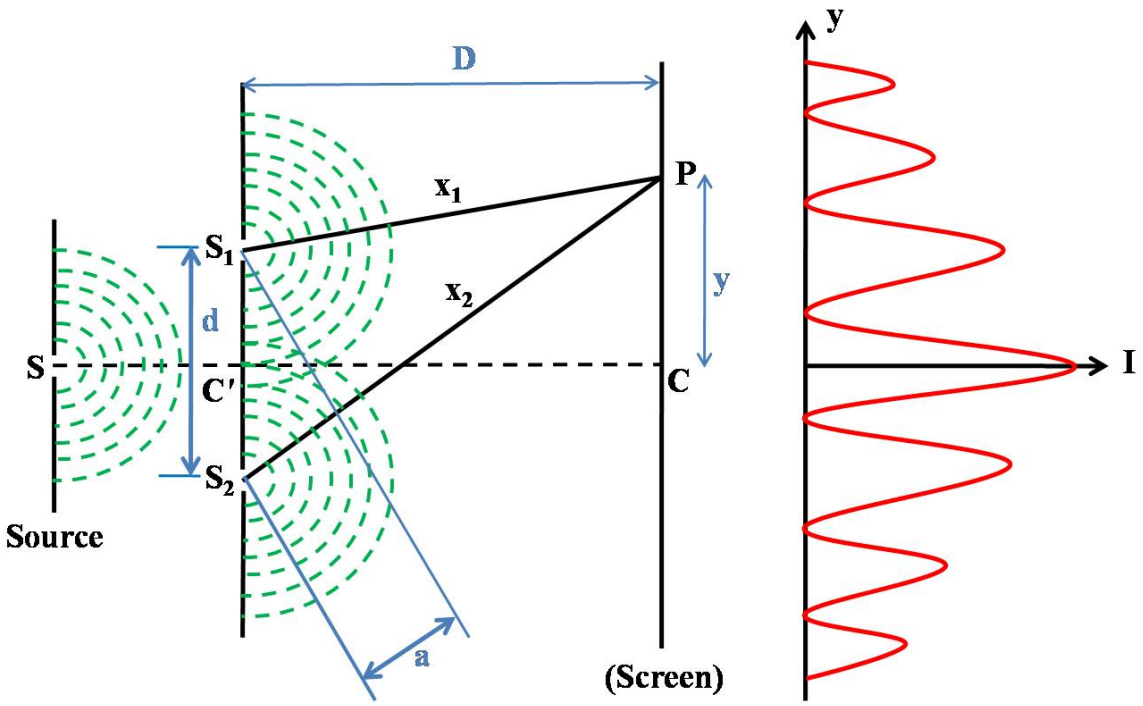

Figure 2.1 Schematic diagram of Young's double slit experiment.

wavelength, constructive interference occurs. Let P be any arbitrary point (movable detector) on the screen at a distance y from centre C of the screen. The distance travelled from S_1 to P is x_1, and S_2 to P is x_2, both are different. The intensity I of the interference is measured at P and shown as a function of y in Fig. 2.1. I is maximum at the centre (C) of the screen, when $y = 0$ and decreases equally on both sides in the direction of increasing y. A wave is characterised by wave function, which is further represented by amplitude and phase. Let us consider the wave functions along paths S_1P and S_2P be $\psi_1 = a_1 e^{i\phi_1}$ and $\psi_2 = a_2 e^{i\phi_2}$, respectively. Then intensity I is given by,

$$\begin{aligned} I &= |\,\psi_1 + \psi_2\,|^2 \\ &= |\,a_1\,|^2 + |\,a_2\,|^2 + |\,a_1\,||\,a_2\,|\,cos[\phi_1 - \phi_2] \end{aligned} \tag{2.1}$$

Therefore the phase difference $\delta = \phi_1 - \phi_2$ controls the intensity and hence determines their interference pattern. From Fig. 2.2, we can calculate the path difference, where,

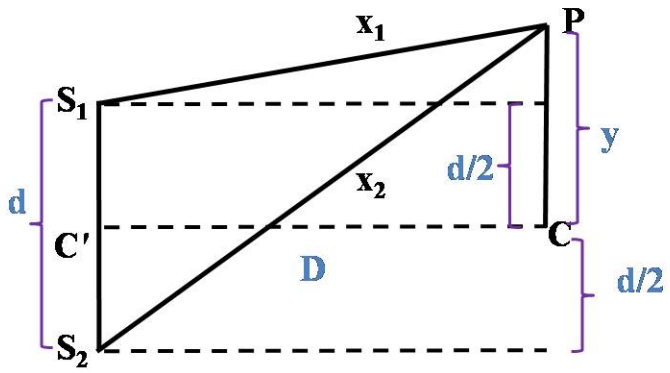

Figure 2.2 Simplification of the paths followed by the waves till they meet at point P on the screen, shown in Fig. 2.1.

$$S_2P = x_2 = \sqrt{\left[D^2 + \left(y + \frac{d}{2}\right)^2\right]}$$
$$= D\sqrt{\left[1 + \left(\frac{y+\frac{d}{2}}{D}\right)^2\right]}$$

Since, $D >> d$,

$$x_2 = D\left[1 + \frac{1}{2}\left(\frac{y+\frac{d}{2}}{D}\right)^2\right]$$

and

$$S_1P = x_1 = D\left[1 + \frac{1}{2}\left(\frac{y-\frac{d}{2}}{D}\right)^2\right]$$

then

$$(x_2 - x_1) = \frac{y}{D}d \tag{2.2}$$

The phase difference between the interfering waves is related to the path difference and is given by

$$\delta = \frac{2\pi}{\lambda}(x_2 - x_1) \tag{2.3}$$

Using Eq. (2.2)

$$\delta = \frac{y}{D}\frac{2\pi d}{\lambda} \tag{2.4}$$

This two slit interference can be interpreted both in terms of classical and quantum interference. In both the cases the wave divides in two parts, the two parts goes through two different slits and finally meet at the detector, where we get the interference pattern. Than what is the big deal about quantum interference? There is a big difference in the two stories. The difference is local and non-local phenomenon. Classically, there is local information regarding the two slits, which control the interference pattern. But in quantum mechanics, it is the phase difference (given by Eq. (2.4)), which controls the interference pattern. Quantum interference is non-local phenomenon [40]. How? A very simple and clear description can be found in ref. [40]. Let us consider a function $f(p)$, which is function of momentum p, then in classical mechanics,

$$\frac{f(p)}{dt} = \frac{\partial f}{\partial p}\frac{dp}{dt} = -\frac{\partial f}{\partial p}\frac{dV(x)}{dx}$$

This implies in classical mechanics for a variable (say momentum) to change, require the information of potential at that point. In quantum mechanics, it is the modulo variable (say modulo momentum $e^{\frac{ipL}{\hbar}}$), which is to be considered, then

$$\begin{aligned}\frac{d}{dt}e^{\frac{ipL}{\hbar}} &= \frac{iL}{\hbar}e^{\frac{ipL}{\hbar}}\frac{dp}{dt} = -\frac{iL}{\hbar}e^{\frac{ipL}{\hbar}}\frac{dV(x)}{dx} \\ &= -\frac{iL}{\hbar}e^{\frac{ipL}{\hbar}}\frac{V(x+L)-V(x)}{L} = \frac{i}{\hbar}e^{\frac{ipL}{\hbar}}[V(x+L)-V(x)]\end{aligned}$$

This implies, in quantum mechanics to study change in a variable, we need the information of the local potential as well as the potential at a distance L away from the point of measurement. Due to this, non-locality is introduced in quantum interference. Due to quantum interference, each particle not only goes through both the slits, but simultaneously traverse every possible trajectory to the target, not just theoretically but in experiment also. That is why, we get interference pattern, not just two patches of light illuminated from the slits, which is expected classically. Examples of quantum interference in devices are SQUID (Superconducting quantum interference device), quantum cryptography, quantum computation.

The interference results from superposition of the interfering wave amplitudes. The interference pattern will disappear as soon as unambiguous information about the path followed by the particle is known. Say for instance some detector, or magnetic field, or, scatterer is placed along one path, then due to non locality in quantum mechanics, the fringes will disappear. Which implies that the

two wave functions (or, quantum states) are not independent. If one path changes then the phase associated with the other path also changes, or vice-versa. A detailed discussion of this feature as well as details of different trajectories involved in interference is given in the next section. In the next section, we have shown the effect of introducing a magnetic field piercing the interferometer, on the interference pattern.

2.3 Aharanov-Bohm ring

The Young two-slit device surely provides the simplest example of an interference pattern in optics; understanding its analog in the case of electrons is necessary for the understanding of quantum interference effects [41]. This interference can be modified by Aharanov-Bohm effect. To get Aharanov-Bohm effect [42] in the original experiment [43, 44], an infinite solenoid is placed between the slits, such that the paths of the interfering electrons are along the region exterior to it. The magnetic field outside the solenoid is zero, so that classically it has no effect on the motion of the electrons which cannot enter the region inside the solenoid. In classical mechanics the motion of a charged particle is not affected by the presence of magnetic fields in regions from which the particle is excluded. In quantum mechanics for such a set up, a charged particle like an electron can undergo an observable phase shift and can change the interference fringes. The phase shift depends on the flux enclosed by the two alternative sets of paths. This is called *Aharanov-Bohm effect* [42]. The Aharanov-Bohm effect demonstrates that the electromagnetic potentials, rather than the electric and magnetic fields, are the fundamental quantities in quantum mechanics.

With the advent of sophisticated fabrication techniques that led to the development of mesoscopic physics, one can realise Aharanov-Bohm set up in solid state samples. Aharanov-Bohm effect is no longer of basic interest but can lead to a lot of device applications [45]. One can fabricate an Aharanov-Bohm set up made of semiconductor or metal and Aharanov-Bohm effects in such samples has been demonstrated in the laboratory [43, 44]. As discussed in Chapter 1, a 2-DEG can be formed at the interface of *GaAs* and *GaAlAs*, where the electrons are confined along the $z-$direction but free to move along x, y directions. With further fabrication, the electrons can be confined along both y, z directions, and the 2-DEG reduces to a quantum wire (see Appendix A), where the electrons are free to

move along $x-$direction. The typical dimension of the sample in the $y-$direction is comparable to the de-Broglie wavelength. Hence the $y-$component of the momentum gets quantized like that in a one dimensional quantum well. The energy gap between these quantized modes exceed thermal energy k_BT at the sub-kelvin temperatures in which these experiments are done. Hence these modes become independent and do not mix. At such sub-kelvin temperatures inelastic mean free path also exceeds a few microns. An interferometer of the type shown in Fig. 2.3 can be fabricated and connected to the reservoirs on either sides. S and D are reservoirs with electrochemical potential μ_1 and μ_2 respectively, where $\mu_1 > \mu_2$. Under this condition, the electrons move from S to D, i.e. from left to right. The ring is connected to the reservoirs via leads L, R. The leads are quantum wires of width W. Reservoir S acts as source of electrons and D act as sink (drain) of electrons. Magnetic flux Φ can be applied through the centre of the ring to get Aharanov-Bohm effect. Three of the transverse modes in the $y-$direction are depicted in Fig. 2.3 by dotted line, solid line and dashed line. Total length of the set up between the two reservoirs is less than the inelastic mean free path. In this regime the boundary condition in the direction is that of an open system. Hence these modes are propagating modes in the $x-$direction. They become perfect waveguides [46] and ideal candidates to exhibit Aharanov-Bohm effect. Aharanov-Bohm effect in such set ups of quantum wires has some complexities that do not crop up in the picture presented in the previous paragraph. In these set ups, the interference fringes have a rigidity and phase change of electron wave function may or may not be able to change the interference pattern.

Naively, one tends to think in analogy with the Young's double slit experiment that electrons (quantum mechanically are waves) originate from source, travels through lead L, split at junction J_1 and goes through two paths marked as II and III in Fig. 2.3. The electrons going through II and III again recombine at junction J_2 and are collected in sink D travelling through lead R. However, such pictures of motion in quantum mechanics is very vague. Electrons emitted from the source can be conceptualized as a wavepacket. Motion of this wavepacket is guided by time dependent Schrödinger equation. However, representing motion of an ensemble of electrons by the motion of a wavepacket includes many conceptual problems related to its dispersion and velocities. On the other hand one may completely discard the idea of representing the motion of electrons by a wavepacket and consider

a steady state current (in quantum mechanics referred as stationary beam of electrons) of electrons running from S to D along the leads and the two arms of the ring. In this picture there is no time dependence of the steady state current, hence no motion. One may think that the steady state current is due to many electrons moving together from S to D as it happens in classical steady state currents (like water current). But this concept has to be discarded in quantum mechanics because motion of individual electrons is undefined in quantum mechanics. Consider two identical particles in identical states (say, same value of k) incident on junction J_1. One of them can get reflected and the other can get transmitted. Only after a large number of such particles are incident at J_1 we can assign a well defined transmission probability and a reflection probability in quantum mechanics. This transmission and reflection probability can be calculated using time dependent wavepacket method or by the time independent stationary state method to obtain the same result. Any other quantity calculated from one picture should be meaningful in the other picture. Sometimes such meanings are easy to make out and sometimes problematic. This thesis will deal with many such problems.

Scattering of a stationary beam can be solved by partial wave analysis [41], which is the canonical method. The different transverse modes in Fig. 2.3 are the different partial waves. To formally get these partial modes, consider the Schrödinger equation in a quantum wire,

$$\left[-\frac{\hbar^2}{2m}\left(\frac{\partial^2}{\partial x^2}+\frac{\partial^2}{\partial y^2}\right)+V(x,y)\right]\psi(x,y)=E\psi(x,y) \tag{2.5}$$

In the leads, i.e., in regions I and IV, the electrons are confined along the y-direction by a hard wall confinement potential given by,

$$V(x,y)=V(y)=\begin{cases}0, & \text{for} -\frac{W}{2}\leq y\leq\frac{W}{2}\\ \infty & \text{for}|y|>\frac{W}{2}\end{cases}$$

The potential inside the ring, i.e. in regions II and III can depend on x as well as y. In regions I and IV, Eq. (2.5) reduces to,

$$\left[-\frac{\hbar^2}{2m}\left(\frac{\partial^2}{\partial x^2}+\frac{\partial^2}{\partial y^2}\right)+V(y)\right]\psi(x,y)=E\psi(x,y) \tag{2.6}$$

x and y are now separable. Let us consider,

$$\psi(x,y)=X(x)Y(y)$$

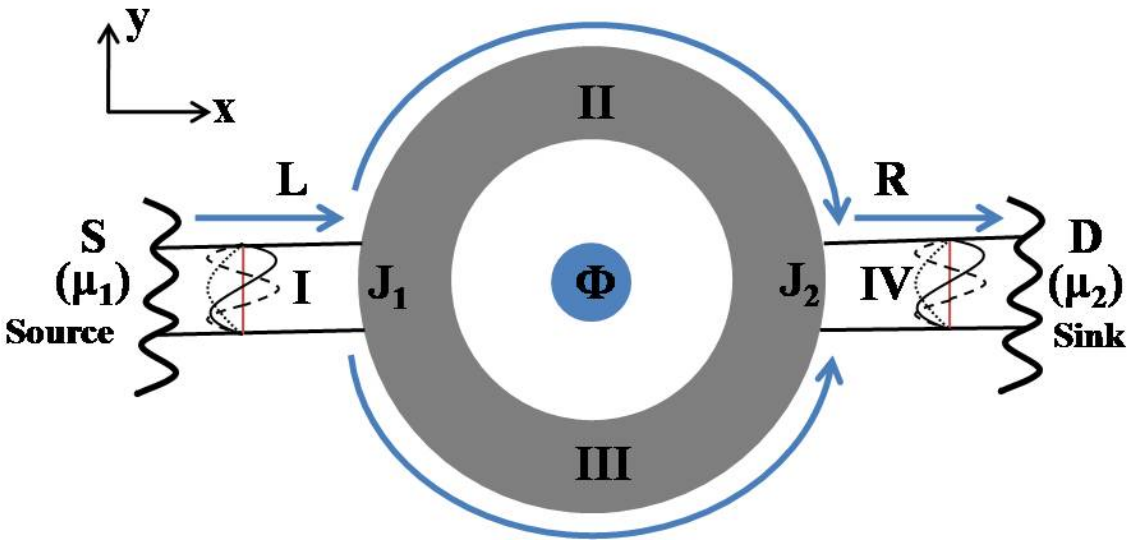

Figure 2.3 Schematic representation of a quasi one dimensional Aharanov-Bohm ring. S and D are reservoirs with electrochemical potential μ_1 and μ_2 respectively, where $\mu_1 > \mu_2$. Under this condition, the electrons move from S to D, i.e. from left to right. The reservoirs are connected to the ring via leads L,R. Different regions are marked as I,II,III and IV. The length of the two arms of the ring are l_1 and l_2, respectively. Three transverse modes are shown in the leads. The dotted line is for $n = 1$, the solid line is for $n = 2$ and the dashed line is for $n = 3$. The ring is embedded by a magnetic flux Φ, and the field is restricted within the shaded region in the centre.

Then after separating the variables, Eq. (2.6) can be decoupled as,

$$-\frac{\hbar^2}{2m}\frac{d^2X(x)}{dx^2} = E_1X(x) \tag{2.7}$$

$$-\frac{\hbar^2}{2m}\frac{d^2Y(y)}{dy^2} + V(y)Y(y) = E_2Y(y) \tag{2.8}$$

with solutions,

$$X_n(x) = A_ne^{ik_nx} + B_ne^{-ik_nx} \tag{2.9}$$

$$\text{and,} \qquad Y_n(y) = C_nsin\left[\frac{n\pi}{W}\left(y+\frac{W}{2}\right)\right] \tag{2.10}$$

$$\text{Therefore,} \qquad \psi_n(x,y) = \left(A'_ne^{ik_nx} + B'_ne^{-ik_nx}\right)sin\left[\frac{n\pi}{W}\left(y+\frac{W}{2}\right)\right] \tag{2.11}$$

Here $n = 1,2,....$, $A'_n = A_nC_n, B'_n = B_nC_n$ and $E = E_1 + E_2$, where,

$$E_1 = \frac{\hbar^2k_n^2}{2m} \qquad \text{and,} \qquad E_2 = \frac{n^2\pi^2\hbar^2}{2mW^2} \tag{2.12}$$

$$\text{or,} \qquad k_n = \sqrt{\frac{2mE}{\hbar^2} - \frac{n^2\pi^2}{W^2}} \tag{2.13}$$

Here E is the incident energy of the electron whose limits are determined by μ_1 and μ_2. However n can take any integer value. When $\frac{2mE}{\hbar^2} > \frac{n^2\pi^2}{W^2}$, then for such values of n, k_n is real and the mode ψ_n in Eq. (2.11) is a propagating mode. Whereas if $\frac{2mE}{\hbar^2} < \frac{n^2\pi^2}{W^2}$, then for such values of n, k_n is imaginary and the mode ψ_n in Eq. (2.11) is an evanescent mode. Consider that E is such that there are two propagating modes in region I and IV. These propagating modes are the two partial waves. So, the wave functions in region I and IV can be written as,

$$\psi_1^I = \left(\frac{e^{ik_1x}}{\sqrt{k_1}} + \frac{r_{11}e^{-ik_1x}}{\sqrt{k_1}}\right)sin\left[\frac{\pi}{W}\left(y+\frac{W}{2}\right)\right] \tag{2.14}$$

$$\psi_2^I = \left(\frac{r_{12}e^{-ik_2x}}{\sqrt{k_2}}\right)sin\left[\frac{2\pi}{W}\left(y+\frac{W}{2}\right)\right] \tag{2.15}$$

$$\psi_1^{IV} = \left(\frac{t_{11}e^{-ik_1x}}{\sqrt{k_1}}\right)sin\left[\frac{\pi}{W}\left(y+\frac{W}{2}\right)\right] \tag{2.16}$$

$$\psi_2^{IV} = \left(\frac{t_{12}e^{-ik_2x}}{\sqrt{k_2}}\right)sin\left[\frac{2\pi}{W}\left(y+\frac{W}{2}\right)\right] \tag{2.17}$$

These are obtained from ψ_n in Eq. (2.11) on applying open boundary conditions. These wave functions define the scattering problem. What they mean is the following. The beam of electrons incident

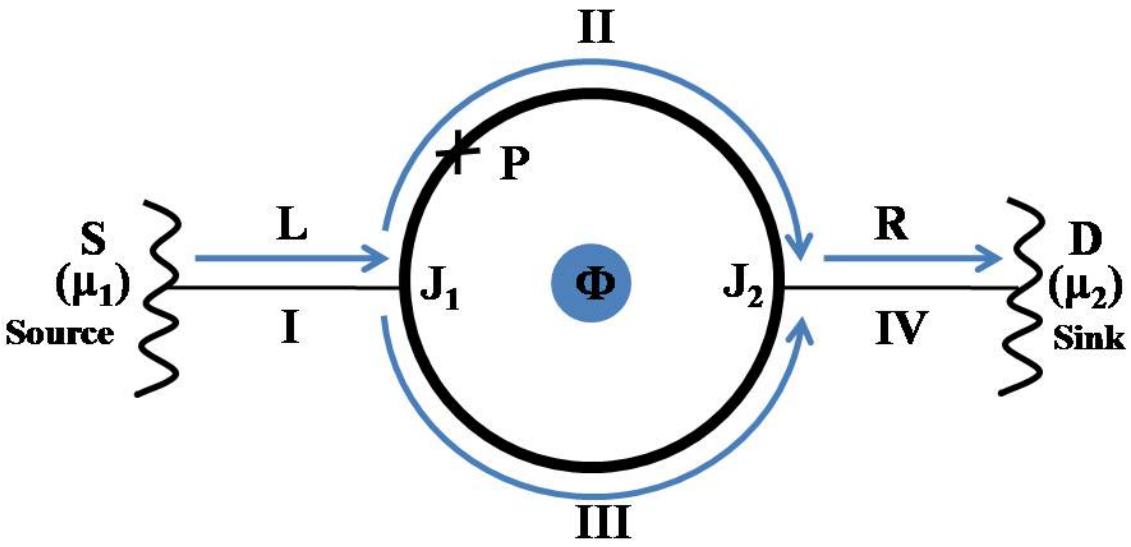

Figure 2.4 Schematic representation of Aharanov-Bohm ring. The ring is embedded by a magnetic flux Φ, and the field is restricted within the shaded region in the centre.

from the source along channel $n = 1$ is represented by $\frac{e^{ik_1 x}}{\sqrt{k_1}} sin\left[\frac{\pi}{W}\left(y+\frac{W}{2}\right)\right]$. The electrons reflected back to the source along channel $n = 1$ is represented by $\frac{r_{11}e^{-ik_1 x}}{\sqrt{k_1}} sin\left[\frac{\pi}{W}\left(y+\frac{W}{2}\right)\right]$. The electrons reflected back to the source along channel $n = 2$ is represented by $\frac{r_{12}e^{-ik_2 x}}{\sqrt{k_2}} sin\left[\frac{2\pi}{W}\left(y+\frac{W}{2}\right)\right]$. The electrons transmitted to the drain along channel $n = 1$ is represented by $\frac{t_{11}e^{-ik_1 x}}{\sqrt{k_1}} sin\left[\frac{\pi}{W}\left(y+\frac{W}{2}\right)\right]$. The electrons transmitted to the drain along channel $n = 2$ is represented by $\frac{t_{12}e^{-ik_2 x}}{\sqrt{k_2}}\left[\frac{2\pi}{W}\left(y+\frac{W}{2}\right)\right]$.

To demonstrate interference fringe rigidity in detail, now we consider a single mode Aharanov-Bohm ring and explicitly solve it. that basically means that only $n = 1$ is propagating. such a scattering set up is qualitatively and quantitatively similar to a one dimensional Aharanov-Bohm ring. The schematic representation of a one dimensional Aharanov-Bohm ring is shown in Fig. 2.4. The Schrödinger equation for this system (in the absence of magnetic field) is given by

$$\left[-\frac{\hbar^2}{2m}\frac{\partial^2}{\partial x^2}+V(x)\right]\psi(x) = E\,\psi(x) \tag{2.18}$$

The wave functions in different regions considering $V(x) = 0$ are given by,

$$\psi_I = e^{ikx} + re^{-ikx} \tag{2.19}$$

$$\psi_{II} = Ae^{ikx} + Be^{-ikx} \tag{2.20}$$

$$\psi_{III} = Ce^{ikx} + De^{-ikx} \tag{2.21}$$

$$\psi_{IV} = te^{ikx} \tag{2.22}$$

where r and t are reflection and transmission amplitudes respectively. k is the wave vector given by $k = \sqrt{\frac{2mE}{\hbar^2}}$ in the leads. These are the limiting cases that follow from Eqs. (2.14)−(2.17).

If we apply an Aharanov-Bohm flux in the centre of the ring, then the Schrödinger equation is given by

$$[\frac{1}{2m}(\hat{p} - \frac{e}{c}\vec{A})^2 + V(x)]\psi(x) = E\psi(x) \tag{2.23}$$

where, $\hat{p} = \frac{\hbar}{i}\frac{d}{dx}$ is the canonical momentum and $\vec{A}$ is the vector potential. Under gauge transformations,

$$\vec{A} \longrightarrow \vec{A} - \vec{\nabla}\chi \tag{2.24}$$

where χ is an arbitrary scalar function. We know magnetic field, $\vec{B} = \vec{\nabla} \times \vec{A}$. Since curl of a scalar function is zero, then magnetic field B is unchanged under this transformation,

$$\vec{B} = \vec{\nabla} \times \left(\vec{A} - \vec{\nabla}\chi\right) = \vec{\nabla} \times \vec{A}$$

We can substitute the gauge transformed vector potential in Eq. (2.23). However, that amounts to change the momentum and hence the wave vector in quantum mechanics. And so the substitution has to be accompanied with multiplying an appropriate phase factor in the wave function. Thus Eq. (2.23) is equivalent to,

$$[\frac{1}{2m}(\vec{p} - \frac{e}{c}(\vec{A} - \vec{\nabla}\chi))^2]\psi(x)e^{-\frac{ie}{\hbar c}\int \vec{\nabla}\chi.d\vec{x}} = [E - V(x)]\psi(x)e^{-\frac{ie}{\hbar c}\int \vec{\nabla}\chi.d\vec{x}} \tag{2.25}$$

Since χ is arbitrary, we can take,

$$\vec{A} = \vec{\nabla}\chi \tag{2.26}$$

Substituting Eq. (2.26) in Eq. (2.25), we get,

$$\frac{1}{2m}[\vec{p}]^2\psi(x)e^{-\frac{ie}{\hbar c}\int\vec{A}.d\vec{x}} = [E-V(x)]\psi(x)e^{-\frac{ie}{\hbar c}\int\vec{A}.d\vec{x}}$$

or,

$$\frac{1}{2m}[\vec{p}]^2\psi'(x) = [E-V(x)]\psi'(x) \tag{2.27}$$

where,

$$\psi'(x) = \psi(x)e^{-\frac{ie}{\hbar c}\int\vec{A}.d\vec{x}} \tag{2.28}$$

Eq. (2.27) is the gauge transformed Schrödinger equation. The phase factor multiplied to the wave function in Eq. (2.25) can be justified by showing Eq. (2.28) is identical to Eq. (2.23). To show this first we will evaluate L.H.S of the Eq. (2.27).

$$\begin{aligned}
\vec{p}^2\psi'(x) &= \vec{p}.\left[\vec{p}\psi'(x)\right] \\
\text{Now,}\quad \vec{p}\psi'(x) &= \vec{p}\left[\psi(x)e^{-\frac{ie}{\hbar c}\int\vec{A}.d\vec{x}}\right] \\
&= \vec{p}\left[\psi(x)\right]e^{-\frac{ie}{\hbar c}\int\vec{A}.d\vec{x}} + \psi(x)\vec{p}\left[e^{-\frac{ie}{\hbar c}\int\vec{A}.d\vec{x}}\right] \\
&= [\vec{p}\psi(x)]e^{-\frac{ie}{\hbar c}\int\vec{A}.d\vec{x}} - (\frac{e\vec{A}}{c})\psi(x)e^{-\frac{ie}{\hbar c}\int\vec{A}.d\vec{x}}
\end{aligned}$$

Therefore,

$$\begin{aligned}
\vec{p}^2\psi'(x) &= \vec{p}.\left[\{\vec{p}\psi(x)\}e^{-\frac{ie}{\hbar c}\int\vec{A}.d\vec{x}} - (\frac{e\vec{A}}{c})\psi(x)e^{-\frac{ie}{\hbar c}\int\vec{A}.d\vec{x}}\right] \\
&= \left\{\vec{p}^2\psi(x)\right\}e^{-\frac{ie}{\hbar c}\int\vec{A}.d\vec{x}} + \{\vec{p}\psi(x)\}\cdot\vec{p}[e^{-\frac{ie}{\hbar c}\int\vec{A}.d\vec{x}}] - \left[\vec{p}\cdot(\frac{e\vec{A}}{c})\right]\psi(x)e^{-\frac{ie}{\hbar c}\int\vec{A}.d\vec{x}} \\
&- (\frac{e\vec{A}}{c})\cdot[\vec{p}\psi(x)]e^{-\frac{ie}{\hbar c}\int\vec{A}.d\vec{x}} - (\frac{e\vec{A}}{c})\psi(x)\cdot\vec{p}[e^{\frac{-ie}{\hbar c}\int\vec{A}.d\vec{x}}] \\
&= \left\{\vec{p}^2\psi(x)\right\}e^{-\frac{ie}{\hbar c}\int\vec{A}.d\vec{x}} - \{\vec{p}\psi(x)\}.(\frac{e\vec{A}}{c})e^{-\frac{ie}{\hbar c}\int\vec{A}.d\vec{x}} - \left[\frac{e\vec{p}\cdot\vec{A}}{c}\right]\psi(x)e^{-\frac{ie}{\hbar c}\int\vec{A}.d\vec{x}} \\
&- (\frac{e\vec{A}}{c}).\vec{p}\psi(x)e^{-\frac{ie}{\hbar c}\int\vec{A}.d\vec{x}} - (\frac{e\vec{A}}{c})\psi(x).\left[(\frac{e\vec{A}}{c})e^{-\frac{ie}{\hbar c}\int\vec{A}.d\vec{x}}\right] \\
&= \left[\vec{p}^2\psi(x) - \vec{p}.(\frac{e\vec{A}\psi(x)}{c}) - (\frac{e\vec{A}}{c}).\{\vec{p}\psi(x)\} + \frac{e^2A^2}{c^2}\psi(x)\right]e^{-\frac{ie}{\hbar c}\int\vec{A}.d\vec{x}} \\
&= \left[\left(\vec{p}-\frac{e\vec{A}}{c}\right).\left(\vec{p}\psi(x) - \frac{e\vec{A}}{c}\psi(x)\right)\right]e^{-\frac{ie}{\hbar c}\int\vec{A}.d\vec{x}}
\end{aligned}$$

$$\text{or,} \qquad \vec{p}^2\psi'(x) = \left[\vec{p} - \frac{e\vec{A}}{c}\right]^2 \psi(x)e^{-\frac{ie}{\hbar c}\int \vec{A}.d\vec{x}} \tag{2.29}$$

Substituting Eq. (2.29) in Eq. (2.27), we get,

$$\frac{1}{2m}[\vec{p} - \frac{e\vec{A}}{c}]^2\psi(x)e^{-\frac{ie}{\hbar c}\int \vec{A}.d\vec{x}} = [E - V(x)]\psi(x)e^{-\frac{ie}{\hbar c}\int \vec{A}.d\vec{x}} \tag{2.30}$$

Cancelling $e^{-\frac{ie}{\hbar c}\int \vec{A}.d\vec{x}}$ from both sides we get

$$\frac{1}{2m}[\vec{p} - \frac{e\vec{A}}{c}]^2\psi(x) = [E - V(x)]\psi(x)$$

which is same as Eq. (2.23). So instead of solving Eq. (2.23) we can solve Eq. (2.27), i.e,

$$-\frac{\hbar^2}{2m}\frac{\partial^2\psi'(x)}{\partial x^2} = [E - V(x)]\psi'(x) \tag{2.31}$$

$$\text{or,} \qquad -\frac{\hbar^2}{2m}\frac{\partial^2\psi'(x)}{\partial x^2} = q^2\psi'(x) \tag{2.32}$$

where, $q^2 = E - V(x)$. Eq. (2.32) has solution of the form: $\psi'(x) \approx e^{\pm iqx}$. From, Eq. (2.28) we get,

$$\psi(x)e^{-\frac{ie}{\hbar c}\int \vec{A}.d\vec{x}} = \psi'(x)$$

Therefore

$$\psi(x)e^{-\frac{ie}{\hbar c}\int \vec{A}.d\vec{x}} = e^{\pm iqx}$$

or

$$\psi(x) = e^{i\int\left(\vec{q}+\frac{e\vec{A}}{\hbar c}\right).d\vec{x}} \tag{2.33}$$

So now as the magnetic flux is applied, the solutions given in Eqs. (2.19)−(2.22) will change. To understand the new wave functions it is more suitable to use the language of Feynmann path, which is an alternative method for the canonical method used to get Eqs. (2.19)−(2.22). The Feynmann path approach will also make it clear why to understand Aharanov-Bohm effect in solid state systems we have to discard the idea of beam splitting at J_1 and recombining at J_2. Consider the point P in Fig. 2.5 and let us try to find the wave function at P using Feynmann path approach. According to Feynmann path approach [16] the amplitude of the electron wave function at an arbitrary point P is the sum of amplitudes of the electron arriving at that point, along all possible classical paths with appropriate

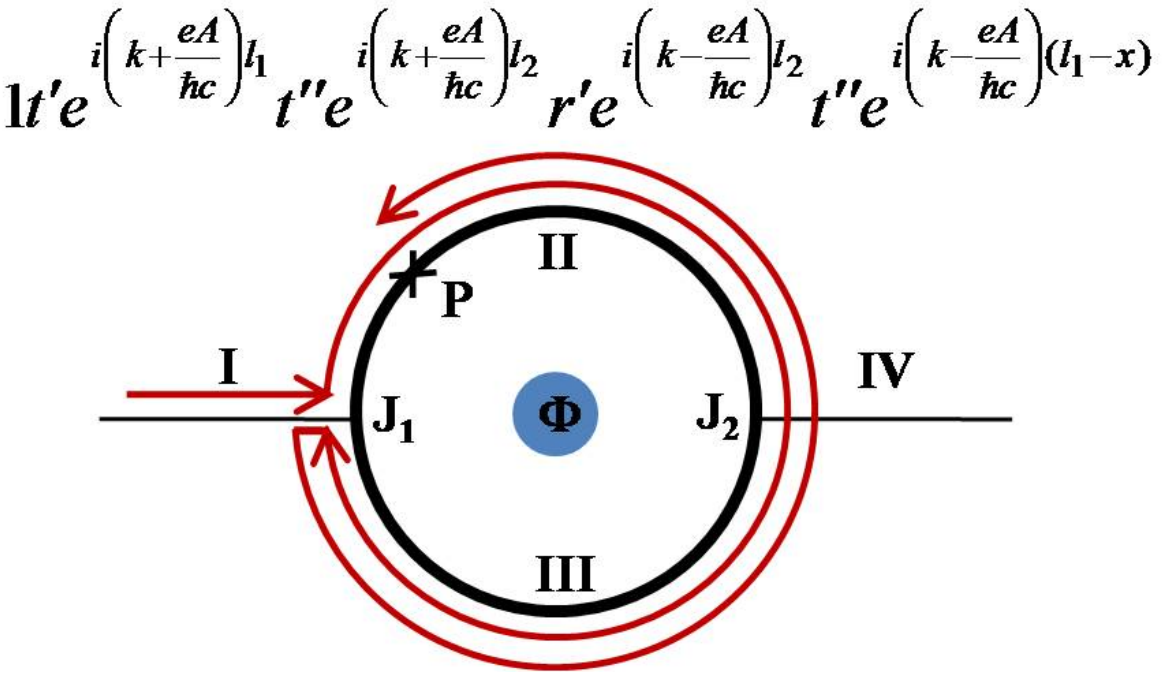

Figure 2.5 Feynmann path to describe a term $1t'e^{i\left(k+\frac{eA}{\hbar c}\right)l_1}t''e^{i\left(k+\frac{eA}{\hbar c}\right)l_2}r'e^{i\left(k-\frac{eA}{\hbar c}\right)l_2}t''e^{i\left(k-\frac{eA}{\hbar c}\right)(l_1-x)}$ in the series of Eq. (2.34). The path is shown by the red line.

weights. So it is not just a wave arriving at P after splitting at J_1 but all the infinite paths have to be considered. Using Feynmann path approach we get the wave function at P in region II (whose coordinate is x say),

$$\begin{aligned}\psi_{II}^{P} &= 1t'e^{i\left(k+\frac{eA}{\hbar c}\right)x}+1t'e^{i\left(k+\frac{eA}{\hbar c}\right)l_1}r''e^{i\left(k-\frac{eA}{\hbar c}\right)(l_1-x)}\\ &+ 1t'e^{i\left(k+\frac{eA}{\hbar c}\right)l_1}r''e^{i\left(k-\frac{eA}{\hbar c}\right)l_1}r'''e^{i\left(k+\frac{eA}{\hbar c}\right)x}+....\\ &+ 1t'e^{i\left(k+\frac{eA}{\hbar c}\right)l_1}t''e^{i\left(k+\frac{eA}{\hbar c}\right)l_2}r'e^{i\left(k-\frac{eA}{\hbar c}\right)l_2}t''e^{i\left(k-\frac{eA}{\hbar c}\right)(l_1-x)}+.... \qquad (2.34)\end{aligned}$$

Here t' is the transmission amplitude from region I to region II. t' is also the transmission amplitude from region I to region III. r'' is the reflection amplitude at junction J_2 for a particle in region II to be reflected back to region II. r''' is the reflection amplitude at junction J_1 for a particle in region II to be reflected back to region II. t'' is the transmission amplitude at junction J_2 for a particle in region II to be transmitted to region III and r' is the reflection amplitude at junction J_1 for a particle in region III to be reflected back to region III. l_1 and l_2 are the lengths of the two arms of the ring. The total length (or, circumference) of the ring is, $l = l_1 + l_2$. Each term in Eq. (2.34) is the contribution of

a distinct Feynmann path to the electron wave function. Let us consider one particular term, say the third term in Eq. (2.34), i.e., $1t'e^{i\left(k+\frac{eA}{\hbar c}\right)l_1}t''e^{i\left(k+\frac{eA}{\hbar c}\right)l_2}r'e^{i\left(k-\frac{eA}{\hbar c}\right)l_2}t''e^{i\left(k-\frac{eA}{\hbar c}\right)(l_1-x)}$. The corresponding path is shown in Fig. 2.5 by the red coloured line. The incident wave function in lead L is e^{ikx}, at junction J_1 ($x=0$) it is $e^{ik0}=1$. Now $1t'$ is transmitted from region I to region II across junction J_1. $1t'e^{i\int_0^{l_1}\left(\vec{k}+\frac{e\vec{A}}{\hbar c}\right).\vec{dx}}$ is transmitted from from J_1 to J_2 along upper arm. At J_2 it is transmitted to the lower arm i.e. region III with amplitude $1t'e^{i\left(k+\frac{eA}{\hbar c}\right)l_1}t''$. $1t'e^{i\left(k+\frac{eA}{\hbar c}\right)l_1}t''e^{i\int_0^{l_2}\left(\vec{k}+\frac{e\vec{A}}{\hbar c}\right).\vec{dx}}$ is transmitted from J_2 to J_1 along the lower arm. At junction J_1, this amplitude is reflected back to region III with amplitude $1t'e^{i\left(k+\frac{eA}{\hbar c}\right)l_1}t''e^{i\int_0^{l_2}\left(\vec{k}+\frac{e\vec{A}}{\hbar c}\right).\vec{dx}}r'$. This amplitude is transmitted from J_1 to J_2 along lower arm with amplitude,

$$1t'e^{i\left(k+\frac{eA}{\hbar c}\right)l_1}t''e^{i\int_0^{l_2}\left(\vec{k}+\frac{e\vec{A}}{\hbar c}\right).\vec{dx}}r'e^{i\int_{l_2}^{0}\left(\vec{k}+\frac{e\vec{A}}{\hbar c}\right).\vec{dx}} \tag{2.35}$$

Now,

$$\begin{aligned} e^{i\int_0^{l_2}\left(\vec{k}+\frac{e\vec{A}}{\hbar c}\right).\vec{dx}} &= e^{i\int_0^{l_2}\vec{k}.\vec{dx}}e^{i\int_0^{l_2}\frac{e\vec{A}}{\hbar c}.\vec{dx}} \\ &= e^{i\int_0^{l_2}kdx}e^{i\int_0^{l_2}\frac{eA}{\hbar c}dx} \\ &= e^{ikl_2}e^{i\frac{eA}{\hbar c}l_2} \\ \text{or,}\quad e^{i\int_0^{l_2}\left(\vec{k}+\frac{e\vec{A}}{\hbar c}\right).\vec{dx}} &= e^{i\left(k+\frac{eA}{\hbar c}\right)l_2} \end{aligned}$$

And,

$$\begin{aligned} e^{i\int_{l_2}^{0}\left(\vec{k}+\frac{e\vec{A}}{\hbar c}\right).\vec{dx}} &= e^{i\int_{l_2}^{0}\vec{k}.\vec{dx}}e^{i\int_{l_2}^{0}\frac{e\vec{A}}{\hbar c}.\vec{dx}} \\ &= e^{i\int_{l_2}^{0}-kdx}e^{i\int_{l_2}^{0}\frac{eA}{\hbar c}dx} \\ &= e^{i\int_0^{l_2}kdx}e^{-i\int_0^{l_2}\frac{eA}{\hbar c}dx} \\ &= e^{ikl_2}e^{-i\frac{eA}{\hbar c}l_2} \\ \text{or,}\quad e^{i\int_{l_2}^{0}\left(\vec{k}+\frac{e\vec{A}}{\hbar c}\right).\vec{dx}} &= e^{i\left(k-\frac{eA}{\hbar c}\right)l_2} \end{aligned}$$

Substituting these integrals in Eq. (2.35), we get,

$$1t'e^{i\left(k+\frac{eA}{\hbar c}\right)l_1}t''e^{i\left(k+\frac{eA}{\hbar c}\right)l_2}r'e^{i\left(k-\frac{eA}{\hbar c}\right)l_2} \tag{2.36}$$

It is the amplitude that has arrived at J_2 for the feynmann path. From junction J_2 this amplitude get transmitted to region II with amplitude $1t'e^{i\left(k+\frac{eA}{\hbar c}\right)l_1}t''e^{i\left(k+\frac{eA}{\hbar c}\right)l_2}r'e^{i\left(k-\frac{eA}{\hbar c}\right)l_2}t''$. This propagates from J_2

to point P resulting in an amplitude

$$1t' e^{i\left(k+\frac{eA}{\hbar c}\right)l_1} t'' e^{i\left(k+\frac{eA}{\hbar c}\right)l_2} r' e^{i\left(k-\frac{eA}{\hbar c}\right)l_2} t'' e^{i\int_{l_1}^{x}\left(\vec{k}+\frac{e\vec{A}}{\hbar c}\right).\vec{dx}} \tag{2.37}$$

Now,

$$\begin{aligned} e^{i\int_{l_1}^{x}\left(\vec{k}+\frac{e\vec{A}}{\hbar c}\right).\vec{dx}} &= e^{i\int_{l_1}^{x}\vec{k}.\vec{dx}} e^{i\int_{l_1}^{x}\frac{e\vec{A}}{\hbar c}.\vec{dx}} && (2.38)\\ &= e^{i\int_{l_1}^{x}-kdx} e^{i\int_{l_1}^{x}\frac{eA}{\hbar c}dx} && (2.39)\\ &= e^{i\int_{x}^{l_1}kdx} e^{-i\int_{x}^{l_1}\frac{eA}{\hbar c}dx} && (2.40)\\ e^{i\int_{l_1}^{x}\left(\vec{k}+\frac{e\vec{A}}{\hbar c}\right).\vec{dx}} &= e^{ik(l_1-x)} e^{-i\frac{eA}{\hbar c}(l_1-x)} && (2.41) \end{aligned}$$

Substituting this integral in Eq. (2.37) the amplitude at point P due to this trajectory shown by the red line in Fig. 2.5 reduces to,

$$1t' e^{i\left(k+\frac{eA}{\hbar c}\right)l_1} t'' e^{i\left(k+\frac{eA}{\hbar c}\right)l_2} r' e^{i\left(k-\frac{eA}{\hbar c}\right)l_2} t'' e^{ik(l_1-x)} e^{-i\frac{eA}{\hbar c}(l_1-x)} = 1t't''r't''e^{2ikl_1} e^{2ikl_2} e^{i\alpha} e^{-ikx} e^{-\frac{ieA}{\hbar c}(l_1-x)}$$

Here, $\alpha = \frac{e}{\hbar c} A l_1$. If l_2 changes, then the wave function at P in the upper arm changes. This is the the amplitude contributing to the wave function at point P for a particular feynmann path.

The wave function of region II at point P (Eq. (2.34)) due to all possible feynmann paths can be simplified as,

$$\begin{aligned} \psi_{II}^{P} &= e^{ikx} e^{\frac{ieA}{\hbar c}x} (1t' + 1t'r''r'''e^{2ikl_1} + ...)\\ &+ e^{-ikx} e^{-\frac{ieA}{\hbar c}(l_1-x)} (1t'r''e^{2ikl_1} e^{i\alpha} + 1t't''r't''e^{2ikl_1} e^{2ikl_2} e^{i\alpha} + ...) \end{aligned}$$

It can be further written as,

$$\psi_{II}^{P} = A e^{ikx} e^{\frac{ieA}{\hbar c}x} + B e^{-ikx} e^{-\frac{ieA}{\hbar c}(l_1-x)}$$

where

$$A = (1t' + 1t'r''r'''e^{2ikl_1} + ...)$$

and

$$B = (1t'r''e^{2ikl_1} e^{i\alpha} + 1t't''r't''e^{2ikl_1} e^{2ikl_2} e^{i\alpha} + ...).$$

Note that at constant magnetic field A and B are constants. Although B contains α, $|B|^2$ is independent of α. This is expected in one dimension. In quasi one dimension with multiple transverse modes, A and B will depend on α, which will be responsible for paramagnetic currents and the effect of centrifugal force. Similarly, the wave function in region III is,

$$\psi_{III} = Ce^{ikx}e^{\frac{ieA}{\hbar c}x} + De^{-ikx}e^{-\frac{ieA}{\hbar c}(l_2-x)} \tag{2.42}$$

Applying Griffiths boundary conditions, i.e.

1. The wave functions are continuous at the junctions.

   i.e., at a junction, $\psi_I = \psi_{II} = \psi_{III} = ...$

2. (Kirchoff's law) The total current (or first derivative of wave function) is conserved at a junction.

   i.e., at a junction $\sum_i \frac{d\psi_i}{dx} = 0$

Applying the first boundary condition at the junctions J_1 and J_2, we take,

$$\psi_I(0) = \psi_{II}(0) = \psi_{III}(l_2)$$

$$\psi_{II}(l_1) = \psi_{III}(0) = \psi_{IV}(0)$$

From this we get,

$$A + Be^{-i\alpha} = 1 + r \tag{2.43}$$

$$Ce^{ikl_2}e^{i\beta} + De^{-ikl_2} = 1 + r \tag{2.44}$$

$$Ae^{ikl_1}e^{i\alpha} + Be^{-ikl_1} = t \tag{2.45}$$

$$C + De^{-i\beta} = t \tag{2.46}$$

Here, $\beta = \frac{e}{\hbar c}Al_2$.

The other boundary condition i.e., Kirchoff's law, is not the same in the presence of magnetic field, let us see how. For getting the correct boundary condition we again start with the Schrödinger's equation in the presence of magnetic field, which is given by,

$$\left[\frac{1}{2m}\left(\frac{\hbar}{i}\frac{\partial}{\partial x} - \frac{e}{c}\vec{A}\right)^2 + V(x)\right]\psi(x) = E\psi(x)$$

or, in three dimensions (we replace x by r, and $\frac{\partial}{\partial x}$ by $\vec{\nabla}$) we can write the above equation in the form,

$$\begin{aligned}\left[\frac{1}{2m}\left(\frac{\hbar}{i}\vec{\nabla}-\frac{e}{c}\vec{A}\right)^2+V(r)\right]\psi(r) &= E\psi(r)\\ \Rightarrow -\frac{\hbar^2}{2m}\nabla^2\psi(r)+\frac{\hbar e}{2mic}\vec{\nabla}.\vec{A}+\frac{e^2A^2}{2mc^2}\psi(r)+V(r)\psi(r) &= E\psi(r)\end{aligned}$$

Integrating both sides over volume, we get,

$$\begin{aligned}\Rightarrow -\frac{\hbar^2}{2m}\int_{V'}\nabla^2\psi(r)dV'+\frac{\hbar e}{2mic}\int_{V'}\vec{\nabla}.\vec{A}dV'+\int_{V'}\frac{e^2A^2}{2mc^2}\psi(r)dV' &\\ +\int_{V'}V(r)\psi(x)dV' &= \int_{V'}E\psi(r)dV'\\ \Rightarrow -\frac{\hbar^2}{2m}\int_{V'}\vec{\nabla}.(\vec{\nabla}+\frac{e}{i\hbar c}\vec{A})\psi(r)dV'+\int_{V'}\frac{e^2A^2}{2mc^2}\psi(r)dV' &\\ +\int_{V'}V(r)\psi(r)dV' &= \int_{V'}E\psi(r)dV'\end{aligned}$$

Here V' is a small volume enclosed by a surface S' of the junction J_1 (say).

$$\begin{aligned}-\frac{\hbar^2}{2m}\lim_{V'\to 0}\int_{S'}(\vec{\nabla}-\frac{ie}{\hbar c}\vec{A})\psi(r).d\vec{S'}+\lim_{V'\to 0}\int_{V'}\frac{e^2A^2}{2mc^2}\psi(r)dV' &\\ +\lim_{V'\to 0}\int_{V'}V(r)\psi(r)dV'=\lim_{V'\to 0}\int_{V'}E\psi(r)dV' &\end{aligned}$$

Now

$$\begin{aligned}\lim_{V'\to 0}\int_{V'}\frac{e^2A^2}{2mc^2}\psi(x)dV'=0,\\ \lim_{V'\to 0}\int_{V'}V(x)\psi(x)dV'=0\end{aligned}$$

and

$$\lim_{V'\to 0}\int_{V'}E(x)\psi(x)dV'=0$$

as V' is shrinking to 0. Therefore it follows that

$$\int_{S'}(\vec{\nabla}-\frac{ie}{\hbar c}\vec{A})\psi(x).d\vec{S'}=0$$

For the partial waves the integration becomes a sum and we can write,

$$\sum(\vec{\nabla}-\frac{ie}{\hbar c}\vec{A})\psi(x)=0 \tag{2.47}$$

This is the Kirchoff's law in the presence of magnetic field. Hence in one dimension, Eq. (2.47) can be written as,

$$\sum_i\left\{\frac{d\psi_i}{dx_i}-\frac{ie}{\hbar c}A\right\}=0$$

Applying this boundary condition at the junctions J_1 and J_2, we get another set of equation given by,

$$\left(\frac{d\psi_I}{dx}\right)_0 = \left(\frac{d\psi_{II}}{dx} - \frac{ie}{\hbar c}A\psi_{II}\right)_0 + \left(\frac{d\psi_{III}}{dx} - \frac{ie}{\hbar c}A\psi_{III}\right)_{l_2}$$
$$\left(\frac{d\psi_{II}}{dx} - \frac{ie}{\hbar c}A\psi_{II}\right)_{l_1} + \left(\frac{d\psi_{III}}{dx} - \frac{ie}{\hbar c}A\psi_{III}\right)_0 = \left(\frac{d\psi_{IV}}{dx}\right)_0$$

From this we get,

$$ikA - ikBe^{-i\alpha} + ikCe^{ikl_2}e^{i\beta} - ikDe^{-ikl_2} = ik - ikr \tag{2.48}$$

$$ikAe^{ikl_1}e^{i\alpha} - ikBe^{-ikl_1} + ikC - ikDe^{-i\beta} = ikt \tag{2.49}$$

We will solve Eqs. (2.43), (2.44), (2.45), (2.46), (2.48) and (2.49) by matrix inversion to calculate A, B, C, D, r and t which are the amplitudes in the one dimensional ring described in Fig. 2.4. r and t are the reflection and transmission amplitudes. A, B, C, D, r and t become flux dependent through these boundary conditions. It is known that micro reversibility implies $|t(\phi)|^2 = |t(-\phi)|^2$. That is $|t(\phi)|^2$ is an even function of flux. From this section we can conclude that scattering phase shift of any arm cannot be independently measured due to presence of higher order feynmann paths, but in many experiments [47–49], people managed to measure scattering phase shift. A brief report on such experimental set up and measurements is given in the next section.

2.4 Measurement of scattering phase shift

A series of experiments [47–49] has recently confirmed that scattering phase shifts in quantum or mesoscopic systems can be measured. Non-locality in quantum mechanics does not allow us to determine a particular path in which the electron wave propagates. This is unlike classical waves. This problem was overcome by using additional probes and controlled decoherence.

Fig. 2.6 shows the experimental set up to measure scattering phase shift. The set up [47] is similar to double slit interferometer with one slit replaced by a quantum dot (QD). A QD is a small, confined puddle of electrons, with two tunnel barriers coupling it to two reservoirs. The electrons in the puddle occupy a discrete ladder of energy levels, with average level spacing Δ. E is the emitter which acts as source of electrons, C is the collector which acts as the sink of electrons, Φ is the magnetic flux

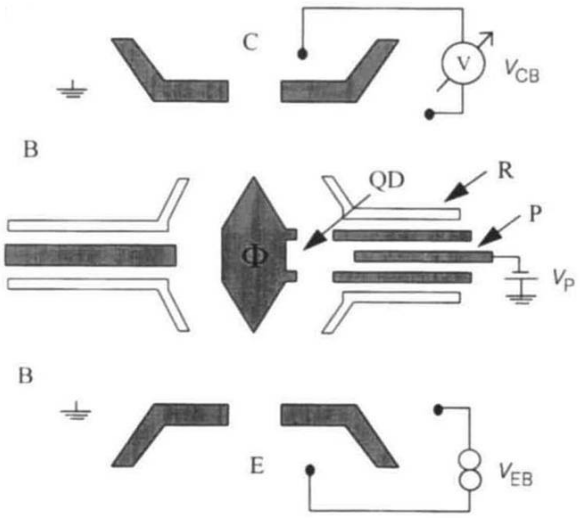

Figure 2.6 Schematic representation of the experimental set up used by Schuster et al. [47], which is similar to double slit interferometer with one slit replaced by a quantum dot. Electrons are transmitted from the emitter (E) to the collector (C) crossing an Aharanov-Bohm ring, with a quantum dot along one of the arm. Additional contacts to the base regions (B) allow the leakage of electrons travelling across the interferometer. V_P is the plunger gate voltage which controls the dot occupancy.

enclosed by the interferometer and V_P is the plunger gate voltage. A capacitively coupled metallic gate called plunger gate is used to tune the energy levels in the dot. Resonant tunnelling between the two reservoirs (through the tunnel barrier-puddle-tunnel barrier system) takes place and current flows when an energy is aligned with the Fermi energy level in the leads. When an electronic level drops below the Fermi level in the leads, it gets occupied and the number of electrons in the dot increases by one. Hence, changing V_P, the dot occupancy can be adjusted.

This set up is a four terminal configuration (shown in Fig. 2.6), which consists of emitter (E) and collector (C) QPC, and a base region (B) in between. The base contacts serve as draining reservoirs with zero chemical potential. The electron wave enters the interferometer from E, and being quantum mechanical in nature, goes through both the paths, one having a quantum dot and another without any quantum dot, simultaneously. To make sure that the electron travels through only these two classical paths i.e. to enable controlled decoherence, additional QPCs (the white gates (R) in Fig. 2.6) called reflectors are employed in the set up. They reflect the diverging electrons towards the slits and subsequently towards the collector, where the electrons interfere to give a interference pattern. In

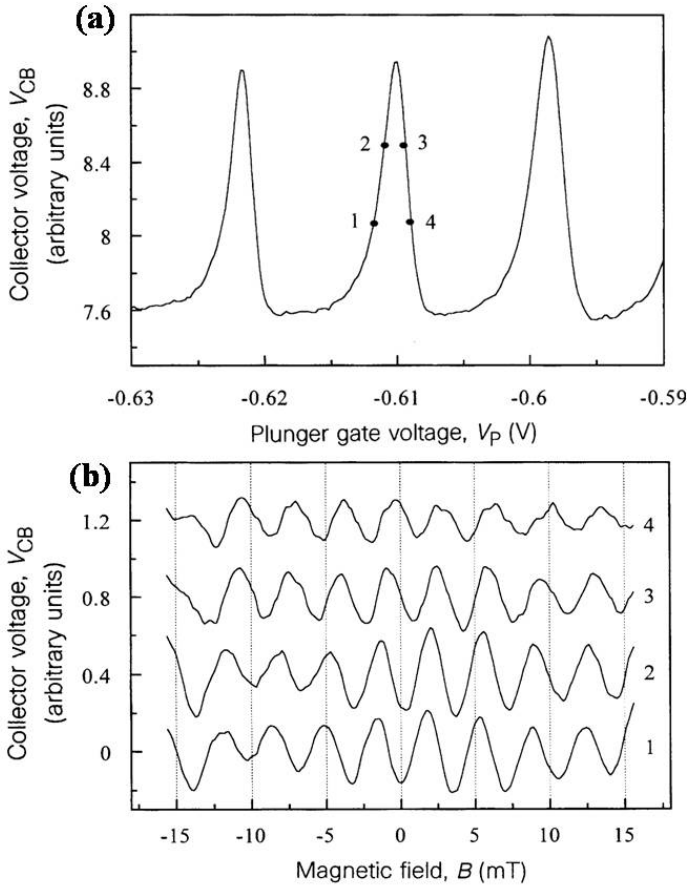

Figure 2.7 (a)The peaks in the collector-base voltage V_{CB} as a function of plunger gate voltage V_P at fixed magnetic field. (b) Aharanov-Bohm oscillations of V_{CB} as a function of magnetic field B, for fixed plunger gate voltage. The four curves correspond to four different values of V_P marked in Fig. 2.7(a). This figure is adapted from ref. [47].

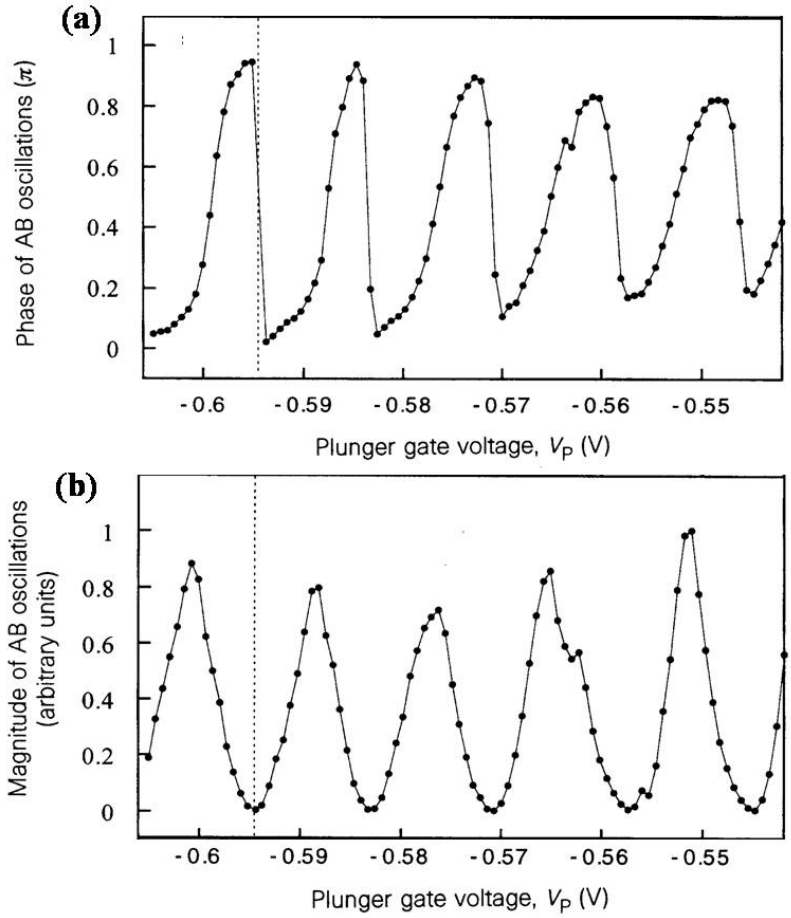

Figure 2.8 Evolution of the magnitude and phase of the transmission amplitude t_{QD} across a sequence of peaks. (a) Amplitude of Aharanov-Bohm oscillations as a function of V_P. Notice the minimum in each valley, separating consequent peaks. At the minimum, the amplitude is almost zero. (b) Phase of Aharanov-Bohm oscillations across the peaks of V_{CB}. The phase evolution is well described by Breit Wigner formula, but an unexpected phase drop of π is observed at the valley corresponding to minimum of the amplitude of Aharanov-Bohm oscillations. This figure is adapted from ref. [47].

the presence of magnetic flux through the interferometer, an Aharanov-Bohm phase is added to the phase shift, given by, $2\pi\frac{\Phi}{\phi_0}$, where $\phi_0 = \frac{h}{e}$ is the flux quantum. The oscillations of the interference pattern are controlled by both magnetic flux Φ and plunger gate voltage V_P. Fig. 2.7(a) shows the resonance peaks of collector-base voltage V_{CB} as a function of plunger gate voltage V_P for a fixed magnetic field. Few points are marked on one of the resonant peak, 1, 2, 3 and 4. Fixing V_P at respective marked points and changing the magnetic field, we get the interference pattern shown in Fig. 2.7(b). The pattern shows clear consistency with the Aharanov-Bohm effect. For various values of V_P, the oscillatory pattern was observed to shift, the shift being proportional to the phase of the transmission amplitude t_{QD} of the QD. The measurement of the shift of the oscillatory pattern allowed to extract the coefficient and phase of the QD across one resonance peak. The measured transmission is consistent with Briet Wigner resonance. The experimental data well fit the expression

$$t_{QD} = iC\frac{\Gamma/2}{\varepsilon + i\Gamma/2} \tag{2.50}$$

where, Γ is the broadening of the resonance, C is the complex amplitude independent of V_P and ε is its position measured from the Fermi level in the leads. For a complete picture they record the Aharanov-Bohm interference oscillations at many points along many the resonant peaks, and get to see the scattering phase shift, i.e., the phase shift of the quantum dot.

The experimentally observed scattering amplitude and phase shift are shown in Figs. 2.8(a) and 2.8(b). The phase has a periodic behaviour which is repeated at each resonance. At each resonance, the phase increases by π and between consequent resonances the phase behaviour shows a sharp drop of π. The increasing phase behaviour could be well understood and is consistent with the Breit-Wigner formula in Eq. (2.50). However, the phase drop in the valley separating consecutive peaks, raised a lot of questions on the correction of measured scattering phase. In order to confirm the measured phase shift is correct or not, the concept of Hilbert transform can be applied.

2.4.1 Hilbert transform

In the paper of Englman and Yahalom [50], they pointed out a relationship between transmission phase shifts and transmission amplitudes, which is model independent and depends on the analytical properties of transmission. Let us consider complex transmission amplitude (as a function of an

external parameter, the gate voltage V_P) be $t(V_P) = |t(V_P)|e^{i\theta_t(V_P)}$, then

$$ln|t(V_P)| = \frac{1}{\pi}P\int_{-\infty}^{\infty}\frac{\theta_t(V_P^{'})}{V_P^{'}-V_P}dV_P^{'} \quad (2.51)$$

$$\theta_t(V_P) = -\frac{1}{\pi}P\int_{-\infty}^{\infty}\frac{ln|t(V_P^{'})|}{V_P^{'}-V_P}dV_P^{'} \quad (2.52)$$

These are Hilbert transforms. These are similar to widely known Kramers-Kronig equations [51]. Scientists have applied this concept to the measured transmission (scattering) cross section, and found transmission (scattering) phase shift to be correctly measured. Even then measured scattering phase shift has many unexplained features which were not understood theoretically. For instance, the phase drop observed between the resonances in experiments was a matter of intense research in the past. Now it is known to be due to an effect known as Fano resonance.

2.4.2 Fano resonance

A Fano resonance [52] is a type of resonant scattering phenomenon that gives rise to an asymmetric line-shape. The Fano resonance line-shape is due to interference between two scattering amplitudes, one due to scattering within a continuum of states (the background process) and the second due to an excitation of a discrete state (the resonant process). The energy of the resonant state must lie in the energy range of the continuum (background) states for the effect to occur. Near the resonant energy, the background scattering amplitude typically varies slowly with energy while the resonant scattering amplitude changes both in magnitude and phase quickly. It is this variation that creates the asymmetric line profile. In the experiment of Schuster et al., Fano resonance is confirmed due to interference between discrete states, i.e, contribution of electrons passing through the reference path with a quantum dot, and the continuum state, i.e., the contribution of electrons passing through the arm without any quantum dot. The phase shows a sharp drop or line shape between the resonances due to this Fano resonance. At Fano resonance, we have also observed other puzzling and unexpected features which will be discussed later, in this thesis.

Now the next question arises, is what information is associated with the measurement of scattering phase shift? The answer is density of states (DOS). DOS play an important role in a number of different physical contexts. For example, thermodynamic properties, tunnelling phenomena, elec-

trical conduction phenomena, charging effects, etc. In mesoscopic systems, there is a hierarchy of partial DOS [53], which is not there in macroscopic systems. In the next chapter, we will discuss the relationship between scattering phase shifts and DOS in the next chapter.

Chapter 3

Scattering phase shift and Density of states

In Chapter 2, we have shown that scattering phase shift can be directly measured. Scattering phase shift is related to density of states of a scattering system or sample, which will be seen in this chapter. Before going into details on density of states, we would like to start with a general transport problem, since scattering is closely related to transport through the conductor.

In scattering theory, one distinguishes between sections of the system: The contacts (also called reservoirs), the leads and the scattering region (or the conductor). The contacts act as electron sources and drains, and are characterised only by macroscopic quantities such as temperature, chemical potential, etc. The leads are waveguides [54] for electrons and connect the scattering region to the contacts. Each lead supports a finite number of current carrying electron modes or channels, depending on the transverse confinement of the electrons [16]. The electrons injected from the contact traverse the mesoscopic device without loosing phase coherence, if we consider the device dimensions within ballistic regime. The electronic states are therefore most appropriately described in terms of scattering states [55]. In the next section we will discuss more on electron transport within a mesoscopic conductor. By transport we mean the way electrons travel across a conductor, which is given by 'Ohm's law'. But Ohm's law is valid in macroscopic systems or in classical transport. Now the question arises is, whether ohm's law is valid in mesoscopic systems, if no, then how is it modified in mesoscopic

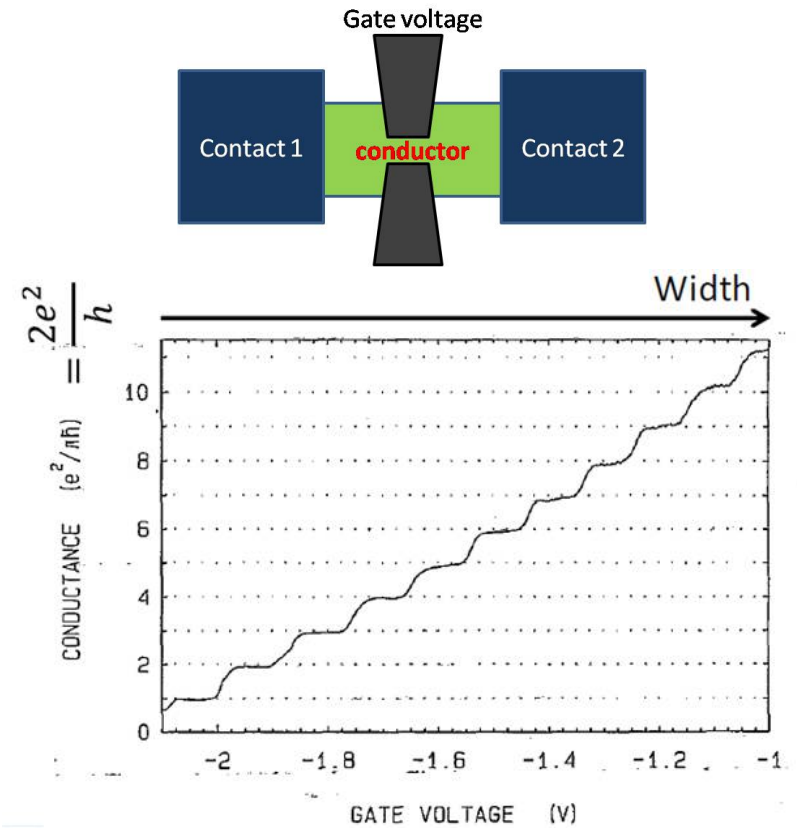

Figure 3.1 Point contact conductance as a function of gate voltage. The constriction becomes wider as the voltage is moved towards higher values. This figure is adapted from ref. [56].

systems, this is what is discussed in the next section.

3.1 Quantized resistance

Let us start with a one dimensional ballistic conductor of length L and width W ($L >> W$), sandwiched between two contacts. Then according to Ohm's law, the resistance is given by,

$$R_c = G_c^{-1} = \frac{V}{I} = \frac{L}{W}\rho$$

where, L and W are length and width of the conductor, ρ is the resistivity, V is the applied voltage and I is the current flowing through the conductor on application of the voltage. Resistance depends on the geometry (and the material) of the conductor, whereas the resistivity only depends on the material. This is the macroscopic case. If we reduce the geometry (length) of the conductor to zero, then we

expect the resistance to become zero,

$$\lim_{W,L\to 0} G_c^{-1} = 0$$

but this is not what is experimentally observed, i.e., ohm's law is not valid for small conductors belonging to mesoscopic scale. The first experiment was performed by B.J. van Wees in 1988 [56], where they reported the experimental study of the conductance (inverse of resistance) of ballistic point contacts in the 2-DEG of high-mobility $GaAs - GaA1As$ heterostructures (In Chapter 1, we have already discussed about the formation 2-DEG and fabrication of point contacts). The conductance approaches a limiting value G_c and is found to change in quantized steps of $\frac{2e^2}{h}$ at zero magnetic field, when gate voltage on top of the heterojunction is varied. The width of the conductor is controlled by the gate voltage. The experimentally observed conductance is shown in Fig. 3.1.

Now, the question arises is, where does this resistance (or, conductance) comes from? This resistance arises from the interface between the conductor and the contacts, which are different materials. Mode reflection at the interface of two dissimilar materials causes finite conductance even with a ballistic conductor. We refer to this limiting resistance G_c^{-1} as contact resistance, since it is occurring at the interface between the contacts and the conductor where the carriers have to be transmitted from the infinite number of modes in the contacts to the finite number of modes in the conductor. To calculate this resistance, a general way is to start with the calculation of current through the conductor, for an applied bias.

3.1.1 Contact resistance

Let us consider a ballistic conductor connected to two large contacts (shown in Fig. 3.2). The contacts are assumed to be much larger than the conductor such that they can be considered to be carrier reservoirs with local Fermi-levels μ_1 and μ_2. The current is carried by a large number of transverse modes (or, sub-bands) in the contacts, but within the narrow conductor, the current is carried by only a few number of modes. Each mode has a dispersion relation $E(k)$ with a cut off energy ε_n, below which it cannot propagate. The number of transverse modes at an energy E is obtained by counting

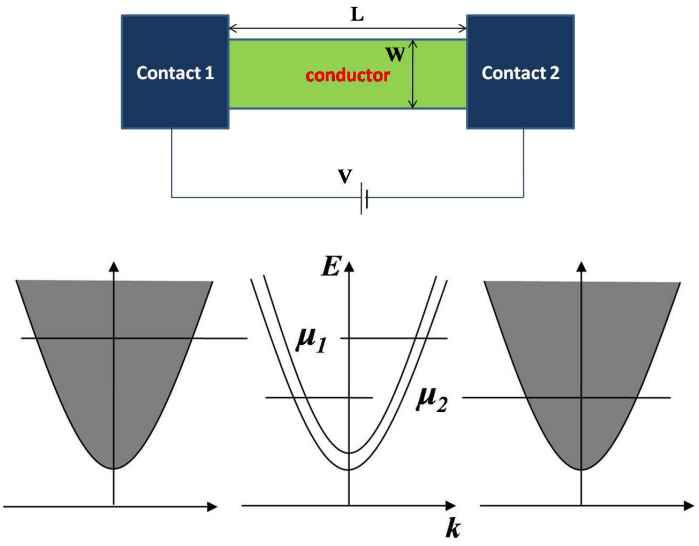

Figure 3.2 Upper: A ballistic conductor connected to two large contacts. Lower: The density of transverse modes in the contacts and the conductor is shown. The contacts have large number of transverse modes while the conductor has a very few transverse modes.

the number of modes having energies below E, i.e,

$$M(E) = \sum_n \vartheta(E - \varepsilon_n) \tag{3.1}$$

Consider a single transverse mode whose $+k$ states and $-k$ states[1] are occupied according to Fermi-Dirac distribution function, $f(E,\mu_1)$ and $f(E,\mu_2)$ respectively. The ballistic conductor has a mean free path length L_m much larger then device length L, such that electrons can pass without any energy or momentum relaxation due to scattering, leading to a transmission probability equal to one for each mode. In a ballistic conductor with two terminals the net current is a balance between the influx of electrons from the first contact minus that originating from the second contact. The current carried by single $+k$ state from left contact to right contact is,

$$dI^+ = evf(E,\mu_1)\frac{dn}{dE}dE \tag{3.2}$$

[1] In the case of zero bias and zero temperature electrons occupy both negative and positive k-states distributed symmetrically up to the Fermi level, giving rise to a zero net current. On introducing a finite bias, $+k$ states are not fully compensated by their negative mirror $-k$ states. $+k$ states are filled up to the μ_1 level whereas $-k$ states are occupied up to the μ_2 level. Consequently, the un-compensated states constitute a current flowing from the μ_1 side to the μ_2 side trying to re-establish equilibrium

where, v is the group velocity of electron at energy E, and $\frac{dn}{dE}$ is the number of states again at energy E. $v = \frac{1}{h}\frac{dE}{dk}$ and $\frac{dn}{dE} = \frac{dk}{dE}$, therefore $v\frac{dn}{dE}$ drops out from Eq. (3.2), leaving a factor of $\frac{1}{h}$, and we are left with,

$$dI^{+} = \frac{e}{h} f(E,\mu_1)dE \tag{3.3}$$

Similarly, current carried by single $-k$ state from right to left is,

$$dI^{-} = \frac{e}{h} f(E,\mu_2)dE \tag{3.4}$$

The net current carried by a single k state within the conductor is the difference between the right flowing and left flowing current.

$$dI = \frac{e}{h}[f(E,\mu_1) - f(E,\mu_2)] \tag{3.5}$$

The net current within the conductor is carried by all possible k states, i.e., integrating over entire energy range,

$$\begin{aligned} I(E) &= \frac{2e}{h}\int_{-\infty}^{\infty}[f(E,\mu_1) - f(E,\mu_2)]dE \\ \text{or,} \qquad I(E) &= \frac{2e}{h}(\mu_1 - \mu_2) \end{aligned} \tag{3.6}$$

The factor 2 in the above equation is added to include the spin degeneracy of the electron. The above expression is the current carried by a single mode within the conductor. If there are M transverse modes within the interval $(\mu_1 - \mu_2)$, then the net current carried is,

$$\begin{aligned} I(E) &= \frac{2e}{h}M(\mu_1 - \mu_2) = \frac{2e^2}{h}MV \\ \Rightarrow G_c^{-1} &= \frac{V}{I} = \frac{h}{2e^2M} \end{aligned} \tag{3.7}$$

Eq. (3.7) is the expression for contact resistance of a ballistic conductor. Since the number of propagating modes M in Eq. (3.1) depends strongly on the width W of the channel, the measured conductance, shown in Fig. 3.1 exhibits plateaus that correspond to a constant number of propagating modes. The conductance of each plateau corresponds exactly to the number of modes times the conduction quantum G_c which is the proof that ballistic quantum transport has been observed.

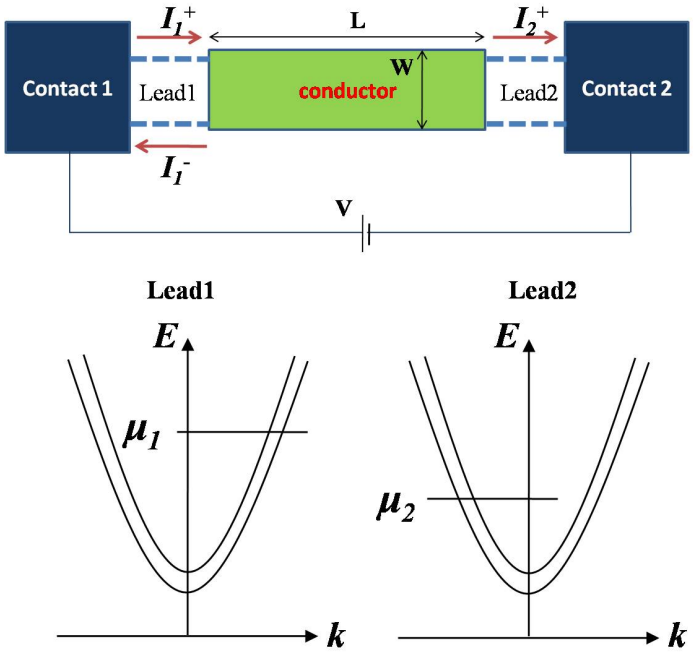

Figure 3.3 Upper: A ballistic conductor is connected to two large contacts through ideal (ballistic) leads shown by dotted lines. lower: The density of transverse modes in the leads is shown.

The contact resistance is independent of sample or conductor geometry (L and W), but only depends on the number of transverse modes carrying the current. But according to Ohm's law the resistance is a material property, than how to get Ohm's law from contact resistance. This connection can be obtained from Landauer formula [57–59] that was introduced by Landauer in 1988 [57]. To obtain the ballistic transport properties of more general devices that exhibit non-unitary transmission, Landauer extended this picture of the quantized conductance by introducing a weighting factor for the transmission probability, namely the transmission function $T(E)$, which we will discuss in the next subsection. Moreover, we will show that in Landauer formula, the resistance has two parts, one is the geometry independent interface or contact resistance and another is the scatterer resistance. The scatterer resistance inhibits the material property and hence obeys Ohm's law.

3.1.2 Landauer formula

Now we consider a conductor connected to two large contacts by two ideal leads (lead 1 and lead 2) each with M transverse modes, as shown in Fig. 3.3. The leads are considered ideal in the sense

that there is no scattering in the leads. The contacts allow the electrons that are absorbed to relax to the Fermi distribution of the contact, and thus serve as reservoirs of thermalized electrons. Due to the inelastic processes leading to relaxation in energy, the phase of the electron is destroyed in this process. When the electron is re-emitted it has no knowledge of its past. This means that there is no correlation between the electrons emitted from different contacts. The contacts are assumed to be reflectionless, so that all the right moving electrons in the left lead (lead 1) have originated in the left contact (contact 1), and all the left moving electrons in the right lead (lead 2) have originated in the right contact (contact 2). One can then assume that the distribution of electrons is the same in both the contacts. The contacts have different electrochemical potentials μ_1 and μ_2, the current is carried by states lying between μ_1 and μ_2. Again following the same formalism, the influx of electrons from lead 1 is [16],

$$I_1^+ = \frac{2e}{h} M(\mu_1 - \mu_2) \tag{3.8}$$

The outflux of electrons at lead 2, that is transmitted from lead 1 is,

$$I_2^+ = \frac{2e}{h} MT(\mu_1 - \mu_2) \tag{3.9}$$

where, $T = T(E)$ is the transmission function. The rest of the flux is reflected back to contact 1 and is given by,

$$I_1^- = \frac{2e}{h} M(1-T)(\mu_1 - \mu_2) \tag{3.10}$$

Then the net current flowing through the conductor is,

$$I = I_1^+ - I_1^- = I_2^+ = \frac{2e}{h} MT(\mu_1 - \mu_2) = \frac{2e^2}{h} MTV \tag{3.11}$$

hence the resistance is given by,

$$\begin{aligned} G^{-1} = \frac{h}{2e^2 MT} &= \frac{h}{2e^2 M} + \frac{h}{2e^2 M}\frac{(1-T)}{T} \\ &= G_c^{-1} + G_s^{-1} \end{aligned} \tag{3.12}$$

where, G_s^{-1} is the conductor or scatterer resistance. This is the formalism for two probe set up, for the multi-probe set up this formalism is extended and generalised by Büttiker and is known as Landauer-Büttiker formula, for details please see ref. [16].

Now, the transmission probability through a long conductor (a collection of many scatterers) of length L is given by (see Appendix B),

$$T = \frac{L_0}{L + L_0} \tag{3.13}$$

where, L_0 is a characteristic length of the order of mean free path. Then,

$$\frac{(1-T)}{T} = \frac{L}{L_0} \tag{3.14}$$

Now,

$$G_s^{-1} = \frac{h}{2e^2 M}\frac{L}{L_0} \propto \frac{L}{W} \tag{3.15}$$

Since the number of transverse modes depends on the width of the conductor W. Thus, Ohm's law for G_s^{-1} is obtained, considering the limiting case of a long conductor including many scatterers.

The transmission probability T is related to scattering matrix elements by the following relation,

$$T_{ij} = \mid S_{ij} \mid^2 \tag{3.16}$$

Therefore, by using scattering theory the relevant information needed to describe the ballistic transport of an open device can be obtained from the S-matrix. Also density of states, which is another very important feature of mesoscopic systems are related to scattering matrix elements more precisely, scattering phase shifts.

In mesoscopic systems, there is a hierarchy of density of states, which is unique for mesoscopic systems; and hence this is another difference between mesoscopic and macroscopic systems in addition to those discussed earlier in the introduction part of Chapter 1. In the next section a brief review of ref. [53, 60, 61] is given, where starting from Larmor clock, a set of density of states is introduced which are related to spin precession and spin rotation. Here also we start with an introduction to Larmor precession time. The Larmor time is one of the most widely discussed approach to determine the time-scales of tunnelling processes. The idea behind this time is that the motion of electrons in a narrow region of magnetic field can be used to explore the time spent by the electrons within this region.

3.2 Larmor precession time

When magnetic field is applied, the magnetic moments experience a torque because of which they precess about the magnetic field, this precession is called Larmor precession. If $\vec{\mu}$ is the magnetic moment for magnetic field $\vec{B}$, then the torque experienced is,

$$\tau = \vec{\mu} \times \vec{B} = \gamma(\vec{J} \times \vec{B}) \tag{3.17}$$

where γ is the gyromagnetic ratio. $\vec{J}$ is the angular momentum vector, which precesses with angular frequency ω_L called Larmor frequency. Let us consider a one dimensional scattering problem with electrons moving along y-axis in a potential $V(y)$. In the absence of magnetic field $\vec{B}$, the scattering matrix elements are $s_{\alpha\beta}(E, V(y))$ for spin up as well as spin down electrons. Here, α and β are the indices for outgoing and incoming leads, we adopt here the language from mesoscopic transport discussions and call the region of large negative y the incident lead β and the region of large positive y the outgoing lead α. E is the energy of the incident electrons. In the presence of magnetic field, $V(y)$ changes to $V(y) \mp dV(y)$, the perturbation in potential is $-dV(y)$ for spin up electrons and $+dV(y)$ for spin down electrons. Thus the scattering matrix in the presence of magnetic field, (using Taylor series expansion) is,

$$s^{\pm}_{\alpha\beta}(E, V(y) \mp dV(y)) = s_{\alpha\beta}(E, V(y)) \mp \int dy' \frac{\delta s_{\alpha\beta}}{\delta V(y')} \delta V(y') + ... \tag{3.18}$$

where, s^+ and s^- are the scattering matrix for spin up and spin down electrons. The spin system is shown in Fig. 3.4. We consider that the incident spin is in x-direction and is spin polarized, and the magnetic field is along z-direction. Because of the torque $\gamma(\vec{J} \times \vec{B})$, the spins precesses and develops a y-component. The basis spinor which determine this precession is given by,

$$|\psi_1\rangle = \begin{bmatrix} \psi_{1+} \\ \psi_{1-} \end{bmatrix} = \frac{1}{\sqrt{|s^+_{21}|^2 + |s^-_{21}|^2}} \begin{bmatrix} s^+_{21} \\ s^-_{21} \end{bmatrix}$$

Here the indices 21 means that we consider electrons transmitted from channel 1 to channel 2. For this $1 \to 2$ scattering, the y-component of spin is,

$$\langle s_y \rangle_{21} = \langle \psi_1 | \frac{\hbar}{2} \sigma_y | \psi_1 \rangle \tag{3.19}$$

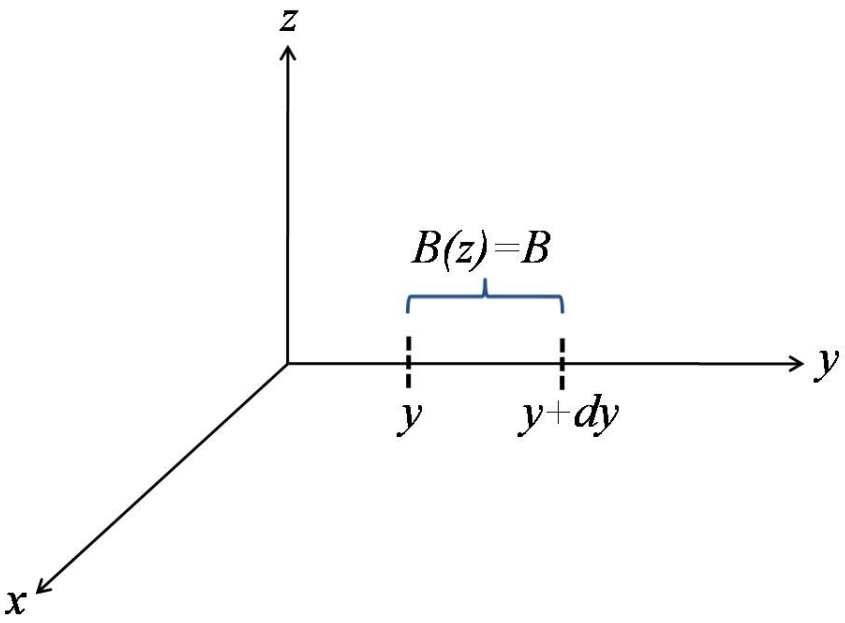

Figure 3.4 Schematic representation of the spin precession in the presence of magnetic field. The field is restricted within y to $y+dy$. The incident electrons are spin polarised, subject to the magnetic field, the transmitted electrons experience both spin precession and spin rotation [62].

where σ_y is y-component of Pauli matrices.

$$\langle s_y\rangle_{21} = \frac{\hbar}{2}\frac{1}{|s_{21}^+|^2+|s_{21}^-|^2}\begin{bmatrix} s_{21}^{+\,*} & s_{21}^{-\,*}\end{bmatrix}\begin{bmatrix}0 & -i\\ i & 0\end{bmatrix}\begin{bmatrix}s_{21}^+\\ s_{21}^-\end{bmatrix}$$

$$= \frac{\hbar}{2}\frac{1}{|s_{21}^+|^2+|s_{21}^-|^2}\left(-is_{21}^{+\,*}s_{21}^- + is_{21}^{-\,*}s_{21}^+\right) = \frac{-i\hbar}{2}\frac{1}{|s_{21}^+|^2+|s_{21}^-|^2}\left(s_{21}^{+\,*}s_{21}^- - s_{21}^{-\,*}s_{21}^+\right)$$

Using the expansion of $s_{21}^{\pm}$ from Eq. 3.18, we get

$$\begin{aligned}\langle s_y\rangle_{21} &= \frac{-i\hbar}{2\left(|s_{21}^+|^2+|s_{21}^-|^2\right)}\left[\left(s_{21}^* - \int dy'\frac{\delta s_{21}^*}{\delta V(y')}\delta V(y')\right)\left(s_{21}+\int dy'\frac{\delta s_{21}}{\delta V(y')}\delta V(y')\right)\right]\\ &+ \frac{i\hbar}{2\left(|s_{21}^+|^2+|s_{21}^-|^2\right)}\left[\left(s_{21}^* + \int dy'\frac{\delta s_{21}^*}{\delta V(y')}\delta V(y')\right)\left(s_{21}-\int dy'\frac{\delta s_{21}}{\delta V(y')}\delta V(y')\right)\right]\end{aligned}$$

Multiplying and retaining the terms upto first order in $\delta V(y')$, we get,

$$\begin{aligned}\langle s_y\rangle_{21} &= \frac{-i\hbar}{2T}\left[\int dy' s_{21}^*\frac{\delta s_{21}}{\delta V(y')}\delta V(y') - HC\right]\\ &= \frac{-i\hbar}{2T}\left[\int dy'\left(s_{21}^*\frac{\delta s_{21}}{\delta V(y')} - HC\right)\delta V(y')\right]\end{aligned}$$

where, $T = |s_{21}^{+}|^2 + |s_{21}^{-}|^2$ and HC stands for Hermitian conjugate. For simplicity it is considered that the magnetic field is constant in a small interval $[y, y+dy]$ and takes there the value B. $\delta V(y)$ is the perturbation in potential due to the presence of magnetic field, hence $\delta V(y)$ vanishes everywhere except in the interval $[y, y+dy]$, where it takes the value $\frac{\hbar\omega_L}{2}$ (due to Zeeman effect). The potential is reduced by $\frac{\hbar\omega_L}{2}$ for spin up electrons and increases by $\frac{\hbar\omega_L}{2}$ for spin down electrons. Therefore in this interval, we can drop the integral and then the y-component of spin is given by,

$$\langle s_y \rangle_{21} = \frac{-i\hbar}{2T}\left[dy'\left(s_{21}^{*}\frac{\delta s_{21}}{\delta V(y')} - HC\right)\frac{-\hbar\omega_L}{2}\right]$$

At point y, it is given by,

$$\langle s_y \rangle_{21} = \frac{-i\hbar}{2T}\left[\left(s_{21}^{*}\frac{\delta s_{21}}{\delta V(y)} - HC\right)\frac{-\hbar\omega_L}{2}\right]$$

For unit spin, the y-component developed is given by,

$$\langle s_y \rangle_{21} \equiv \frac{\langle s_y \rangle_{21}}{\frac{\hbar}{2}} = \frac{i\hbar}{2T}\left[\left(s_{21}^{*}\frac{\delta s_{21}}{\delta V(y)} - HC\right)\omega_L\right] \tag{3.20}$$

Component of unit spin is dimensionally equivalent to angle of precession of the electrons. Dividing this quantity by Larmor frequency ω_L, then a quantity having dimension of time can be defined, which is called Larmor precession time and is given by,

$$\begin{aligned}\tau_y(2,y,1) &= \frac{i\hbar}{2T}\left[\left(s_{21}^{*}\frac{\delta s_{21}}{\delta V(y)} - HC\right)\right] \\ &= \frac{-h}{4\pi i T}\left[\left(s_{21}^{*}\frac{\delta s_{21}}{\delta V(y)} - HC\right)\right]\end{aligned} \tag{3.21}$$

For a general scattering problem, the time spent by an electron within the scattering region at point $\mathbf{r}$ is given by,

$$\tau(\alpha,\mathbf{r},\beta) = \frac{-h}{4\pi i|s_{\alpha\beta}|^2} Tr\left(s_{\alpha\beta}^{\dagger}\frac{\delta s_{\alpha\beta}}{\delta V(\mathbf{r})} - s_{\alpha\beta}\frac{\delta s_{\alpha\beta}^{\dagger}}{\delta V(\mathbf{r})}\right) \tag{3.22}$$

where, $s_{\alpha\beta}$ is the scattering matrix element for electrons incoming from β and outgoing from α and Tr is trace which represents summation over incident and outgoing transverse mode (channel) indices. Both β and α can take values $1, 2, 3, ...$ From Larmor precession time, a hierarchy of partial density of states (DOS) is introduced in ref. [53]. In the next section, the hierarchy of DOS is introduced.

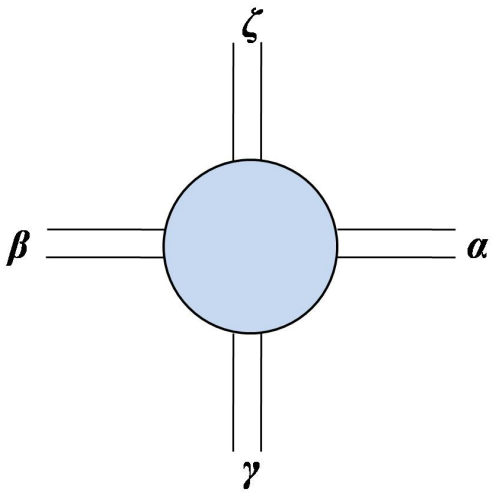

Figure 3.5 Schematic representation of the scattering system considered in section 3.2.1. The scattering region is shown by the blue region. The scattering region is connected to multiple leads $\alpha, \beta, \gamma, \delta$. The electrons enters and leaves the scattering region from all possible leads.

3.2.1 Density of states

Let us start by considering a scattering region or sample connected with multiple leads shown in Fig. 3.5. The scattering region or the sample is shown by shaded (blue) region. Here, α and β be the indices for outgoing and incoming leads. The electrons are incident from say lead β, then enters the scattering region having an arbitrary potential $V(\mathbf{r})$. Larmor precession time is connected to the local partial density of states (LPDOS) and the relationship is given by,

$$\tau(\alpha, \mathbf{r}, \beta) = \frac{h}{|s_{\alpha\beta}|^2} \rho'(\alpha, \mathbf{r}, \beta)$$

where,

$$\rho'(\alpha, \mathbf{r}, \beta) = -\frac{1}{4\pi i} Tr \left(s^{\dagger}_{\alpha\beta} \frac{\delta s_{\alpha\beta}}{\delta V(\mathbf{r})} - s_{\alpha\beta} \frac{\delta s^{\dagger}_{\alpha\beta}}{\delta V(\mathbf{r})} \right) \tag{3.23}$$

is the LPDOS and lies at the bottom of the hierarchy of DOS. $\rho'(\alpha, \mathbf{r}, \beta)$ gives the contribution to the density of states localised at point $\mathbf{r}$ of electrons incident from lead β and leaving the sample from lead α. In order to measure this we require to specify both the incident and the outgoing leads simultaneously, which is not quantum mechanically possible. But if we sum over any of the lead indices α or β, then the quantity to be measured require to specify either the incident or the outgoing lead. Summing over one of the indices, we get the next member of the hierarchy. If we sum over all

outgoing leads α, then we get injectivity of contact β,

$$\rho'(\mathbf{r},\beta) = -\frac{1}{4\pi i}\sum_{\alpha} Tr\left(s^{\dagger}_{\alpha\beta}\frac{\delta s_{\alpha\beta}}{\delta V(\mathbf{r})} - s_{\alpha\beta}\frac{\delta s^{\dagger}_{\alpha\beta}}{\delta V(\mathbf{r})}\right) \tag{3.24}$$

Injectivity of contact β gives the contribution to the density of states localised at point $\mathbf{r}$ of electrons incident to the sample through lead β, irrespective of the lead through which it leaves the sample. This member of density of states is widely studied in this thesis. The reason behind studying injectivity is that it is quantum mechanically feasible. While measuring $\rho'(\alpha,\mathbf{r},\beta)$, requires a pre-estimation of both the incoming and outgoing leads, the measurement of injectivity only requires the knowledge of incident lead. Injectivity is measured in many experiments, an example of which is, if an scanning tunnelling microscope (STM) tip is brought close to the mesoscopic sample or the scattering region (shown in Fig. 3.5), then the current delivered by the tip, gives the measure of injectivity.

If we sum over the incoming leads β, then we get another member in the same level of hierarchy as injectivity, called emissivity,

$$\rho'(\alpha,\mathbf{r}) = -\frac{1}{4\pi i}\sum_{\beta} Tr\left(s^{\dagger}_{\alpha\beta}\frac{\delta s_{\alpha\beta}}{\delta V(\mathbf{r})} - s_{\alpha\beta}\frac{\delta s^{\dagger}_{\alpha\beta}}{\delta V(\mathbf{r})}\right) \tag{3.25}$$

Emissivity gives the contribution to density of states localised at point $\mathbf{r}$ of those electrons which leave the sample through lead α irrespective of the lead through which it enters the sample.

Finally if we sum over all injectivities or emissivities, we get the highest member of the hierarchy, which is local density of states,

$$\begin{aligned}\rho'(\mathbf{r}) = \sum_{\beta}\rho'(\mathbf{r},\beta) &= \sum_{\alpha}\rho'(\alpha,\mathbf{r}) \\ &= -\frac{1}{4\pi i}\sum_{\alpha\beta} Tr\left(s^{\dagger}_{\alpha\beta}\frac{\delta s_{\alpha\beta}}{\delta V(\mathbf{r})} - s_{\alpha\beta}\frac{\delta s^{\dagger}_{\alpha\beta}}{\delta V(\mathbf{r})}\right)\end{aligned} \tag{3.26}$$

Till now, the density of states, we have discussed are all local in nature, that is at a point $\mathbf{r}$ within the scattering region. But mostly, people are interested to study the density of states not at a point but of the entire scattering region. This can be obtained, when we consider the total volume (say Ω) of the scattering region, and integrate the local density of states over $\mathbf{r}$ for this volume.

3.2.2 Global Density of states

Integrating LPDOS given by Eq. (3.23) over $\mathbf{r}$ for the volume Ω, we get,

$$\rho(\alpha,\beta) = -\frac{1}{4\pi i}\int_{\Omega} d\mathbf{r}^3 Tr\left(s^{\dagger}_{\alpha\beta}\frac{\delta s_{\alpha\beta}}{\delta V(\mathbf{r})} - s_{\alpha\beta}\frac{\delta s^{\dagger}_{\alpha\beta}}{\delta V(\mathbf{r})}\right) \tag{3.27}$$

$\rho(\alpha,\mathbf{r},\beta)$ is the partial density of states (PDOS). In semi-classical case, it is possible to replace the functional derivative with respect to the local potential $V(\mathbf{r})$ by an energy derivative, i.e.,

$$-\int_{\Omega}\frac{\delta}{\delta V(\mathbf{r})} \cong \frac{d}{dE} \tag{3.28}$$

Applying this approximation we get semi-classical PDOS,

$$\rho(\alpha,\beta) \approx \frac{1}{4\pi i} Tr\left(s^{\dagger}_{\alpha\beta}\frac{ds_{\alpha\beta}}{dE} - s_{\alpha\beta}\frac{ds^{\dagger}_{\alpha\beta}}{dE}\right) \tag{3.29}$$

Integrating injectivity given by Eq. (3.24) over space and applying the semi-classical approximation we get,

$$\rho(\beta) \approx \frac{1}{4\pi i}\sum_{\alpha} Tr\left(s^{\dagger}_{\alpha\beta}\frac{ds_{\alpha\beta}}{dE} - s_{\alpha\beta}\frac{ds^{\dagger}_{\alpha\beta}}{dE}\right) \tag{3.30}$$

$\rho(\beta)$ is semi-classical injectance. Similarly, semi-classical emittance is obtained from Eq. (3.25) and is given by,

$$\rho(\alpha) \approx \frac{1}{4\pi i}\sum_{\beta} Tr\left(s^{\dagger}_{\alpha\beta}\frac{ds_{\alpha\beta}}{dE} - s_{\alpha\beta}\frac{ds^{\dagger}_{\alpha\beta}}{dE}\right) \tag{3.31}$$

and, finally applying Eq. (3.28), after integrating Eq. (3.26) over volume Ω, we get density of states $\rho(E)$.

$$\rho(E) \approx \frac{1}{4\pi i}\sum_{\alpha\beta} Tr\left(s^{\dagger}_{\alpha\beta}\frac{ds_{\alpha\beta}}{dE} - s_{\alpha\beta}\frac{ds^{\dagger}_{\alpha\beta}}{dE}\right) \tag{3.32}$$

The scattering matrix elements are complex wave functions $s_{\alpha\beta} =\mid s_{\alpha\beta} \mid e^{i\theta_{s_{\alpha\beta}}}$, with scattering coefficient $\mid s_{\alpha\beta} \mid^2$ and scattering phase shift $\theta_{s_{\alpha\beta}}$, then we can expand the above equation and write,

$$\rho(E) \approx \frac{1}{2\pi}\sum_{\alpha\beta} Tr\left(\mid s_{\alpha\beta} \mid^2 \frac{d\theta_{s_{\alpha\beta}}}{dE}\right) \tag{3.33}$$

Hence we get a relation between density of states and energy derivative of scattering phase shift. This is Friedel sum rule. The Friedel sum rule (FSR) relates the density of states (DOS) of a system to the phase of the eigenvalues of the scattering matrix and is given by,

$$\pi\rho(E) \approx \frac{d}{dE}\theta_f \tag{3.34}$$

where, θ_f is the Friedel phase and is given by,

$$\theta_f = \frac{1}{2i}log(det[S]) = \frac{1}{2}\sum_j \xi_j$$

where, S is the unitary scattering matrix and $e^{i\xi_j}$ are the eigenvalues of S matrix[2]. The S matrix tells us the response at one lead due to excitation at the other lead, but a more powerful concept called 'Green's function' gives the response at any point (inside or outside the conductor) due to an excitation at any other point. Moreover, S matrix and density of sates are also related to Green's function. Let us start with an introduction to Green's function.

3.3 Green's function

Whenever the response R is related to the excitation S by a differential operator $\hat{D}$,

$$\hat{D}R = S$$

we can define a Green's function $\hat{G}$ and express the response in the form,

$$R = \hat{D}^{-1}S = \hat{G}S$$

Hence, Green's function can be defined as inverse of a differential operator. Obtaining the Green's function is usually simpler than solving the differential equation itself which makes the Green's function method very useful.

[2]Say for a matrix S, $e^{i\xi_j}$ are the eigenvalues, then as known from basic matrix calculus,

$$det[S] = \prod_j e^{i\xi_j} = e^{\sum_j i\xi_j}$$

Now,

$$log(det[S]) = log\left[e^{\sum_j i\xi_j}\right] = \sum i\xi_j$$

A scattering problem can be expressed in the form of inhomogeneous Schrödinger equation,

$$\left[E-\hat{H}\right]\Psi = S \tag{3.35}$$

where, Ψ is the wave function, H is the Hamiltonian operator with eigenenergy E and S is an equivalent excitation term due to a wave incident from one of the leads. The corresponding Green's function can be written as,

$$\hat{G} = \left[E-\hat{H}\right]^{-1} \tag{3.36}$$

The inverse of a differential operator is not uniquely specified till we specify the boundary conditions. Depending on the boundary conditions, two different Green's function can be defined, retarded and advanced.

3.3.1 Retarded and advanced Green's function

Let us consider a simple one dimensional wire with constant potential V_0, then the Green's function is given by,

$$\hat{G} = \left[E - V_0 + \frac{\hbar^2}{2m_e}\frac{d^2}{dx^2}\right]^{-1} \tag{3.37}$$

where, $-\frac{\hbar^2}{2m}\frac{d^2}{dx^2} + V_0$ is the Hamiltonian. The above equation be rewritten as,

$$\left(E - V_0 + \frac{\hbar^2}{2m_e}\frac{d^2}{dx^2}\right) G(x,x') = \delta(x-x') \tag{3.38}$$

Eq. (3.38) is similar to Schrödinger equation, expect the source term $\delta(x-x')$ in the R.H.S. $G(x,x')$ acts as the wave function at x due to unit excitation at x', and satisfy Eq. (3.38) at every point except point $x = x'$. Physically, such an excitation can result two different waves travelling along $+x$ and $-x$ from the point of excitation, with amplitudes A^+ and A^-. One result is two outgoing waves that originate at the point of excitation, which is referred to as retarded Green's function G^R in mesoscopic literature [16]. A pictorial representation is given in Fig. 3.6(a). We can write

$$G^R(x,x') = A^+ e^{ik(x-x')}, \text{for } x > x' \tag{3.39}$$

$$G^R(x,x') = A^- e^{-ik(x-x')}, \text{for } x < x' \tag{3.40}$$

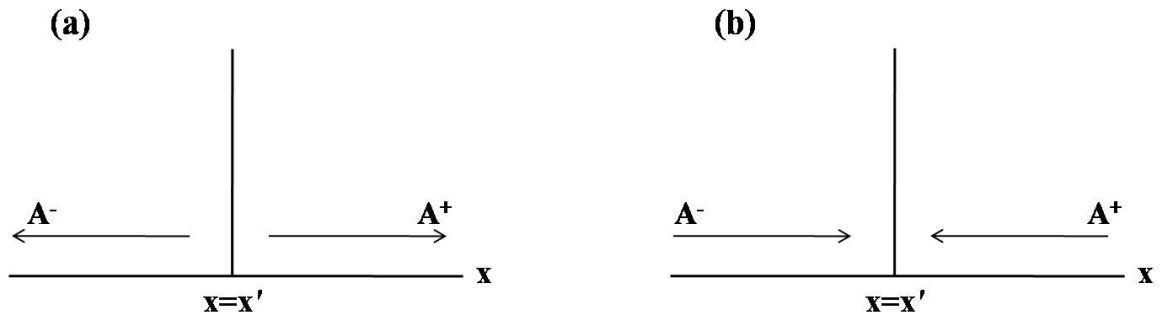

Figure 3.6 (a) Retarded Green's function and (b) Advanced Green's function, for an infinite one dimensional wire.

where, $k = \sqrt{\frac{2m_e(E-V_0)}{\hbar^2}}$ is the wave vector of the wire. At $x = x'$, Green's function must be continuous and its first derivative must be discontinuos by $\frac{2m_e}{\hbar^2}$. That is,

$$\left[G^R(x,x')\right]_{x=x'+} = \left[G^R(x,x')\right]_{x=x'-} \tag{3.41}$$

$$\text{and} \qquad \left[\frac{dG^R(x,x')}{dx}\right]_{x=x'+} - \left[\frac{dG^R(x,x')}{dx}\right]_{x=x'-} = \frac{2m_e}{\hbar^2} \tag{3.42}$$

[3] Substituting Eqs. (3.39) and (3.40) into Eqs. (3.41) and (3.43), we get

$$A^+ = A^- \qquad \text{and} \qquad ik\left(A^+ + A^-\right) = \frac{2m_e}{\hbar^2} \tag{3.43}$$

Hence,

$$A^+ = A^- = -\frac{i}{\hbar v} \tag{3.44}$$

where, $v = \frac{\hbar k}{m_e}$ is the velocity of the outgoing waves. Hence, the retarded Green's function is given by,

$$G^R(x,x') = -\frac{i}{\hbar v} e^{ik|x-x'|} \tag{3.45}$$

There is another solution to Eq. (3.38) which is given by,

$$G^A(x,x') = +\frac{i}{\hbar v} e^{-ik|x-x'|} \tag{3.46}$$

This solution refers to the situation, of incoming waves that disappear at the point of excitation at $x = x'$, and is referred to as advanced Green's function [16]. If an infinitesimal imaginary energy $i\eta$ is

[3] By, $x'+$, we mean evaluated from right of x' and by $x'-$ we mean evaluated from the left of x'.

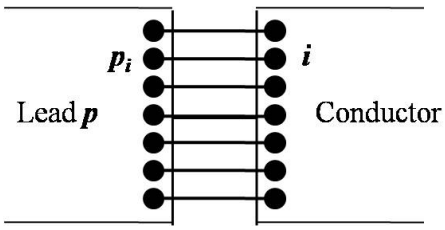

Figure 3.7 Coupling between a lead and the conductor.

added to Eq. (3.38), then the wave vector develops a positive imaginary component $i\delta$, then retarded and advanced Green's function takes the form,

$$G^R = \left[E + i\eta - \hat{H}\right]^{-1} = -\frac{i}{\hbar v} e^{ik(1+i\delta)|x-x'|} \tag{3.47}$$

$$\text{and} \qquad G^A = \left[E - i\eta - \hat{H}\right]^{-1} = +\frac{i}{\hbar v} e^{-ik(1-i\delta)|x-x'|} \tag{3.48}$$

The imaginary part $i\delta$ in the wave vector makes the advanced function grow indefinitely as we move away from the excitation. This makes the retarded function, the only feasible solution to Eq. (3.38), since a proper solution must be bounded. The example considered above is limited to single mode, let us now try to analyse the Green's function for multi mode infinite wire. In this case apart from the longitudinal part, a transverse part will add on the solution to Green's function, which can be written as,

$$G^R(x,y;x',y') = \sum_m -\frac{i}{\hbar v_m} \chi_m(y)\chi_m(y') e^{ik_m|x-x'|} \tag{3.49}$$

$G^R(x,y;x',y')$ represents the response at point (x,y), due to excitation at point (x',y'). where, m is the index for transverse modes, $\chi_m(y)$ are the transverse mode wave functions with quantized eigenenergies ε_m, $\frac{k_m = \sqrt{2m_e(E-\varepsilon_m)}}{\hbar}$ and $v_m = \frac{\hbar k_m}{m_e}$.

Again, scattering matrix S is related to Green's function by Fisher-Lee relation [63], (see Appendix C.1)

$$s_{nm} = -\delta_{nm} + i\hbar\sqrt{v_n v_m} \iint \chi_n(y_q) \left[G^R_{qp}(y_q;y_p)\right] \chi_m(y_p) dy_q dy_p \tag{3.50}$$

where, m,n are indices for transverse modes and p,q are indices for leads (left and right).

One can obtain a matrix representation for Hamiltonian operator H and thus calculate the inverse to get Green's function. A common approach for matrix representation of an operator is to discretize

the spatial coordinate. Then the Green's function becomes a matrix : $G^R(x,x') \rightarrow G^R(i,j)$, where, the indices i, j are points on a discrete lattice. In matrix form, Eq. (3.47) reduces to,

$$[(E-i\varepsilon)I-H]\,G^R = I$$

$$\text{or} \qquad G^R = [(E-i\varepsilon)I-H]^{-1} \tag{3.51}$$

where, $[I]$ is identity matrix and $[H]$ is the matrix representation of the Hamiltonian operator H. Now that we know $[H]$ matrix, we can find out the inverse and hence calculate the Green's function G^R. The only problem is that the matrix is infinite dimensional. This is because the system considered is an open system connected to leads that stretch to infinity. If we simply truncate the matrices at some point, then we would effectively be describing a closed system with fully reflecting boundaries. Let us consider a discrete lattice for both the conductor and the lead, the adjacent lattice points in the conductor and a lead p can be coupled as shown in Fig. 3.7. The overall Green's function for both conductor and lead can be partitioned into a Green's function for the conductor G_C, for the lead G_p and two coupling Green's functions conductor-lead G_{Cp} and lead-conductor G_{pC}

$$\begin{bmatrix} G_p & G_{pC} \\ G_{Cp} & G_C \end{bmatrix} = \begin{bmatrix} (E+i\varepsilon)I-H_p & \tau_p \\ \tau_p^\dagger & EI-H_C \end{bmatrix}^{-1} \tag{3.52}$$

where, $[(E-i\varepsilon)I-H_p]$ represents matrix for the isolated lead, while $[EI-H_C]$ represents the matrix for isolated conductor[4], $[\tau_p]$ is the coupling matrix between the leads and the conductor and $[\tau_p^\dagger]$ is the coupling matrix between the conductor and the leads. The coupling matrix is non-zero for adjacent points i (of the conductor) and p_i (of the leads) i.e.,

$$\tau_{p_i,i} = t$$

where, t is the hopping matrix element. Eq. (3.52) can be written as,

$$[(E-i\varepsilon)I-H_p]G_p + [\tau_p]G_{Cp} = I$$

$$[(E-i\varepsilon)I-H_p]G_{pC} + [\tau_p]G_C = 0$$

[4] H_C is the finite dimensional Hamiltonian matrix of the isolated conductor. The dimension of the matrix is given by number of lattice points within the conductor, if there are n number of points in the conductor then dimension of H_C is $n \times n$.

$$[\tau_p^\dagger]G_p + [EI - H_C]G_{Cp} = 0$$

$$[\tau_p^\dagger]G_{pC} + [EI - H_C]G_C = I$$

Our purpose is to get an expression for the sub-matrix G_C, hence retaining the equation containing G_C, we get,

$$G_C = \left[EI - H_C - \tau_p^\dagger g_p^R \tau_p\right]^{-1} \tag{3.53}$$

where,

$$g_p^R = [(E - i\varepsilon)I - H_p]^{-1} \tag{3.54}$$

g_p^R is the retarded Green's function for isolated semi-infinite lead p[5]. Using the fact that the coupling matrix τ_p is zero at all points except those adjacent to each other, then we can obtain,

$$\left[\tau_p^\dagger g_p^R \tau_p\right]_{ij} = t^2 g_p^R(p_i, p_j) = \Sigma_p^R(i,j) \tag{3.55}$$

where, Σ_p^R is the self energy. Its real part describes the energy shift of an electron entering the conductor, and the imaginary part determines the life time of a state in the sample. When multiple independent leads are attached to the same conductor, the effects of the self energies for each lead simply add up and we can define Σ^R,

$$\Sigma^R = \sum_p \Sigma_p^R(i,j) \tag{3.56}$$

self energy due to multiple leads. This term represents the effective Hamiltonian describing the interaction of leads with the conductor. Hence, the Green's function[6] can be written as,

$$G^R = \left[EI - H_C - \Sigma^R\right]^{-1} \tag{3.57}$$

[5]The infinite lead is taken into account exactly by the term $\tau_p^\dagger g_p^R \tau_p$. It might appear that to get g_p^R, we have to invert an infinite matrix again, so this formulation is not at all worthy. However, this is not the case, as g_p^R represents Green's function of an isolated lead, it can be determined analytically and is shown in Appendix C.2.

[6]We have replaced G_C by G_R, as this is the only component of the overall Green's function that takes into account the propagation of electrons between two points inside the conductor. The effect of leads is accounted by the self energy term Σ^R.

Further using the concept of Green's function, spectral function A, which is the matrix version of density of sates can be defined,

$$A = G^R \Gamma G^A = G^A \Gamma G^R = i\left[G^R - G^A\right] \tag{3.58}$$

where, Γ is the coupling matrix connecting the conductor to the leads, and is represented the anti-Hermitian part of self energy Σ^R,

$$\begin{aligned} \Gamma &= i(\Sigma^R - \Sigma^{R^\dagger}) \\ &= i(\Sigma^R - \Sigma^A) \qquad \text{Since, } \Sigma^{R^\dagger} = \Sigma^A \end{aligned} \tag{3.59}$$

Local density of states (LDOS) is given by the diagonal elements of the spectral function A, i.e.,

$$\rho(\mathbf{r}, E) = \frac{1}{2\pi} A(\mathbf{r}, \mathbf{r}, E) = -\frac{1}{\pi} Im[G^R(\mathbf{r}, \mathbf{r}, E)] \tag{3.60}$$

These are few definitions and notations most often used in mesoscopic physics while studying quantum transport of carriers or electrons.

Chapter 4

Injectance and a paradox

4.1 Introduction

A series of experiments has recently confirmed that scattering phase shifts in quantum mechanics can be measured [47–49, 64–66]. Non-locality in quantum mechanics does not allow us to determine a particular path in which the electron wave propagates. This is unlike classical waves. This problem was overcome by using additional probes and controlled decoherence [47,64]. Ref. [50] confirms that Hilbert transform of the measured conductance data gives the measured phase data which confirms that the scattering phase shift was correctly measured. Thus the scattering phase shift as well as the scattering cross section of an arbitrary quantum system (say, its impurity configuration and confinement potential is not known) can be measured. While measuring scattering cross section is an old story, measuring scattering phase shifts is novel and new. So one can ask the question that from the measured scattering phase shift what can we learn about the quantum system.

Friedel sum rule (FSR) relates scattering phase shift to density of states (DOS) in the system [67] and Wigner Smith delay time (WSDT) relates scattering phase shift to a time scale at the resonances [68]. The two are basically the same as both density of states and life time of a resonance are given by the imaginary part of the retarded Greens function [16]. Although, it is to be noted that different works have interpreted the WSDT in different ways which will be discussed later. Also for this reason we will generally refer to WSDT as a time scale. FSR and WSDT are semi-classical formulas that

are not a priori applicable to quantum systems in mesoscopic regime. The quantum versions of these formulas are not completely in terms of the experimental data. A number of works have studied FSR and WSDT in the single channel case [69–72]. Another physical quantity of interest is injectivity or injectance [61]. In this work we calculate injectivity and injectance in the single channel as well as two channel regime, as this also reveals the paradoxical nature of the scattering phase shift at Fano resonance.

4.2 Friedel Sum Rule and Wigner Smith Delay Time

Let us consider plane wave incident from left hand side on a three dimensional scatterer. The scattered or asymptotic wave function in spherical polar coordinates (r, θ, ϕ) is given by [41],

$$\frac{1}{r}sin(kr-\frac{l\pi}{2}+\theta_t)P_l cos(\phi)$$

Here θ_t is the scattering phase shift. Assume a large sphere of radius R and let us count the number of nodes inside the sphere. Number of states is one more than the number of nodes. To count the number of nodes inside the sphere we can set the wave function to zero on the boundary of the sphere, i.e., [67]

$$kR-\frac{l\pi}{2}+\theta_t=n\pi \quad or, \frac{d\theta_t}{dk}+R=\frac{dn}{dk}\pi \tag{4.1}$$

In absence of scatterer,

$$kR=n_0\pi \quad or, R=\frac{dn_0}{dk}\pi \tag{4.2}$$

As, $E=\frac{\hbar^2k^2}{2m_e}$, we get from Eqs. (4.1) and (4.2), $\frac{d\theta_t}{dE}=\pi[\rho(E)-\rho_0(E)]$ where, $\rho(E)=\frac{dn}{dE}$ is the density of states in the presence of scatterer and $\rho_0(E)=\frac{dn_0}{dE}$ is the density of states in the absence of scatterer. Instead one can put $\theta_t+kR\equiv\theta_t$ that is scattering phase shift is defined with respect to phase shift kR in absence of scatterer. In which case FSR becomes [67],

$$\frac{d\theta_t}{dE}=\pi\rho(E) \tag{4.3}$$

In the rest of the paper we will use this definition for scattering phase shift. This is a semi-classical result because it is valid only when, $dn \ll n$. This assumption is related to non-dispersive wave packets or stationary phase approximation as shown below. In this case we restrict to one dimension

as Eq. (4.3) can be shown in one dimension too where the large sphere of radius R become just two points at a large distance of $x = \pm R$.

Consider a wave packet incident from left on a one dimensional scatterer, i.e.,

$$\psi_{in}(x,t) = \int_{-\infty}^{+\infty} a_k e^{ikx - i\omega t} dk$$

After scattering the transmitted wave packet at $(x+\Delta x, t+\Delta t)$ is,

$$\psi_{sc}(x+\Delta x, t+\Delta t) = \int_{-\infty}^{+\infty} \mid t(k) \mid a_k e^{ik(x+\Delta x) - i\omega(t+\Delta t) + i\theta_t} dk \tag{4.4}$$

where, $t(k)$ is the transmission amplitude and θ_t is its phase. A classical particle is either transmitted completely or reflected completely without any distortion. Assuming there is no reflected part, along with the assumption of no dispersion of wave packet (known as stationary phase approximation), one can write [68],

$$kx + k\Delta x - \omega t - \omega\Delta t + \theta_t = K \tag{4.5}$$

where K is a constant. This implies that the phase of the amplitude component a_k remain stationary or that the wave packet remains undispersed. Therefore from Eq. (4.5),

$$\frac{d\theta_t}{d\omega} = \Delta t - \frac{\Delta x}{v_g} \qquad or, \quad \hbar\frac{d\theta_t}{dE} = \Delta t - \Delta t_0 \tag{4.6}$$

where $v_g = \frac{d\omega}{dk}$ is the group velocity. Semi-classical behaviour is pictorially depicted in Figs. 4.1(a) and 4.1(b). When $E \gg V$ then a wave packet can get completely transmitted with Eq. (4.5) approximately satisfied (it is never exactly satisfied as electron dispersion is quadratic). It can also happen when $E \ll V$ then a wave packet can get completely reflected with very little dispersion. In this case, θ_t is to be replaced by θ_r, the reflected phase shift. Thus we find that when a wave packet remains undispersed, then the time spent by the particle in the scattered region $(\Delta t - \Delta t_0)$, is given by energy derivative of scattering phase shift. This life time (WSDT) is also related to DOS as both are given by the imaginary part of retarded Green's function (ref. [16], page 155-156). Hence, as we have seen in Eq. (4.3), the DOS can also be found from the energy derivative of scattering phase shift, which is FSR. These formulas are obviously not valid in the quantum regime i.e., $E \sim V$, where there will be transmission as well as reflection. Also in this regime the scattering phase shifts will be so strongly energy dependent that stationary phase approximation cannot remain valid and a wave packet will

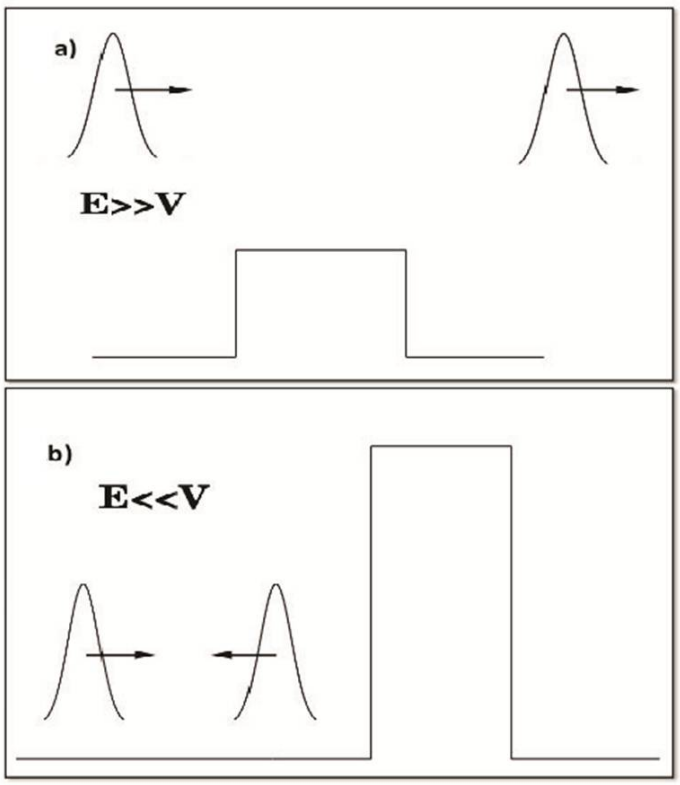

Figure 4.1 The figure shows a wave packet is incident on a barrier of height V in one dimension. a) The energy of incidence E of the centroid of the wave packet is much larger than the barrier potential V, i.e $E \gg V$, and, b) The energy of incidence E is much smaller than the barrier potential V, i.e $E \ll V$. These limits correspond to semi-classical regimes.

always undergo dispersion. Refs. [73, 74] have looked into the one dimensional problem when both transmission and reflection is present. They have computed the correction term and explained the significance of it. They have shown that the correction term arises because of quantum interference effect. Note that both dispersion and quantum interference arises due to the superposition principle in quantum mechanics. Their result will be discussed latter.

4.3 Larmor Precession Time and Injectance

The quantum regime can be treated exactly and also yields the following formula for time, already discussed in Chapter 3 as Larmor precession time (LPT) [53, 60, 61] is given by,

$$\tau(\alpha,\mathbf{r},\beta) = \frac{-h}{4\pi i} Tr\left(s^{\dagger}_{\alpha\beta} \frac{\delta s_{\alpha\beta}}{\delta V(\mathbf{r})} - s_{\alpha\beta} \frac{\delta s^{\dagger}_{\alpha\beta}}{\delta V(\mathbf{r})} \right) \tag{4.7}$$

Connection between LPT and WSDT or FSR is explained below. $\tau(\alpha,\mathbf{r},\beta)$ is the time spent by one particle incident along channel β and scattered to channel α at r. LPT is exact in the sense that when summed over α and β and divided by $\hbar$, it gives the exact DOS as calculated from the internal wave function. δ stands for functional derivative. Note that the functional derivative is with respect to the local potential implying that exact DOS cannot be expressed by Eq. (4.7) using asymptotic wave function alone. Dividing Eq. (4.7) by $\hbar$ we get a local partial density of states (LPDOS) for such a process (a particle incident along β and scattered to α). That is $\frac{\tau(\alpha,\mathbf{r},\beta)}{\hbar} = \rho'(\alpha,\mathbf{r},\beta)$, where $\rho'(\alpha,\mathbf{r},\beta)$ is LPDOS. Such a process requires to specify both the incoming and outgoing channel which is impossible in quantum mechanics because a single particle in quantum mechanics behave probabilistically when it encounters a potential and gets scattered. Only when an ensemble of particles is considered, the probability of transmission and that of reflection are given by Schrödinger equation. One can indirectly measure the consequences of such a LPDOS [53, 60, 61], but an experimental set up that can directly probe this LPDOS requires us to take a sum over at least one of the channels (i.e., α or β). So, we can specify the incoming channel and scattering can take the particle to any arbitrary output channel. That is, $\sum_\alpha \rho'(\alpha,\mathbf{r},\beta) = \rho'(\mathbf{r},\beta)$ is a physical quantity called injectivity.

$$\begin{aligned}\rho'(\mathbf{r},\beta) &= -\frac{1}{4\pi i}\sum_\alpha Tr\left(s^\dagger_{\alpha\beta}\frac{\delta s_{\alpha\beta}}{\delta V(\mathbf{r})} - s_{\alpha\beta}\frac{\delta s^\dagger_{\alpha\beta}}{\delta V(\mathbf{r})}\right)\\ &= \sum_\alpha -\frac{1}{2\pi}\mid s_{\alpha\beta}\mid^2 \frac{\delta\theta_{s_{\alpha\beta}}}{\delta V(\mathbf{r})}\end{aligned} \tag{4.8}$$

where, $\theta_{s_{\alpha\beta}} = \arctan\frac{Im(s_{\alpha\beta})}{Re(s_{\alpha\beta})}$. This quantity can be experimentally observed and is the topic of study in this work. A special situation where this quantity can be observed is when we bring a scanning tunnelling microscope (STM) tip close to a mesoscopic sample at *r* connected to one or more leads. Injectivity gives current delivered by the tip.

Not summing over β reveals the true nature of the paradox. This is because then the incident wave packet comes along a single channel β and after scattering it will either disperse or will not disperse. If we sum over β then the incidence is along all possible channels. So wave packets are incident along β channels and their scattering and dispersion can compensate each other. Also refs. [73, 74] have calculated the correction term for this injectivity in the single channel case and the paradox can be quantitatively explained in terms of this correction term.

The semi-classical limit can be obtained from the following substitution,

$$-\int_{\Omega} \frac{\delta}{\delta V(\mathbf{r})} \cong \frac{d}{dE} \tag{4.9}$$

Hence, from Eq. (4.8)

$$\rho(\beta) \approx \sum_{\alpha} \frac{1}{2\pi} \mid s_{\alpha\beta} \mid^2 \frac{d}{dE} \theta_{s_{\alpha\beta}} \tag{4.10}$$

This quantity is called injectance. $\mid s_{\alpha\beta} \mid^2$ appears because when we allow scattering (Eq. (4.6) correspond to a case when everything is transmitted without scattering) then $\mid s_{\alpha\beta} \mid^2$ number of particles are scattered from channel β to channel α and each ones contribution to time is related to $\frac{d\theta_{s_{\alpha\beta}}}{dE}$. In the single channel case, say for $\beta = 1$, it can be explicitly written as

$$\rho(1) \approx \frac{1}{2\pi} \left[\mid r \mid^2 \frac{d\theta_r}{dE} + \mid t \mid^2 \frac{d\theta_t}{dE} \right] \tag{4.11}$$

The approximate equality can be replaced by an equality if we add a correction term on the right hand side [73, 74].

$$\rho(1) = \frac{1}{2\pi} \left[\mid r \mid^2 \frac{d\theta_r}{dE} + \mid t \mid^2 \frac{d\theta_t}{dE} + \frac{m_e \mid r \mid}{\hbar k^2} \sin(\theta_r) \right] \tag{4.12}$$

where k is the wave vector of the incident channel. Note that the correction term contains material and sample specific parameters like m_e (the effective mass of electron) and k which depend on width and confinement of a quantum wire. Refs. [73, 74] have stressed that the correction term can be zero if $\mid r \mid = 0$ (corresponding to Fig. 4.1(a)), but $\sin(\theta_r)$ cannot be zero as it comes from quantum interference which is always there in a quantum system. $\sin(\theta_r)$ can be zero only when the potential is infinitely high because then there is obviously no interference effect [73, 74] (corresponding to Fig. 4.1(b)). Or it sometimes become zero far away from resonances that are almost classical regimes [73, 74]. Therefore, just as dispersion of a wave packet cannot disappear, interference effects cannot disappear. Both originate from the linear superposition principle in quantum mechanics. Only when dispersion or interference can be ignored we get the semi-classical limit, i.e, Eq. (4.10).

4.4 The Paradox: Single Propagating Channel

We will first show that there is a situation where $\sin(\theta_r)$ can become zero at a resonance where $\mid r \mid \neq 0$, making Eq. (4.10) exact in a quantum regime. This is in complete contradiction to what is

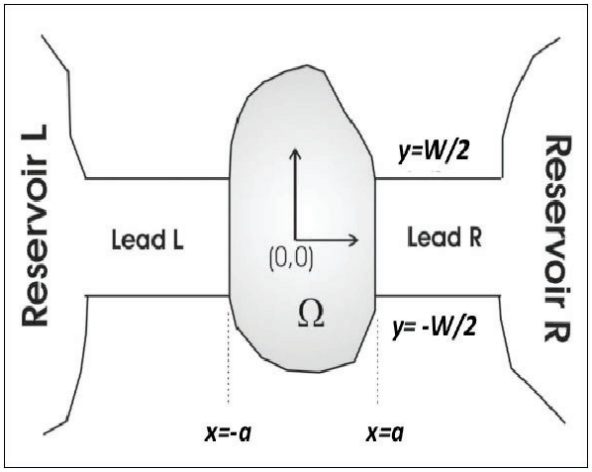

Figure 4.2 A general scattering problem in quasi one dimension. The reservoir L inject electrons to the left lead L and hence to the scattering region with arbitrary potential $V_g(x,y)$, shown by the shaded region. Reservoir R absorb electrons transmitted through the shaded region, through right lead R. The electrons reflected from the shaded region are collected in reservoir L. Here we have considered one propagating channel in the leads and electrons are incident from the left.

known so far [73, 74]. A general proof for a single channel scattering is given below. This can have useful implications to experimentalists in the sense that although injectance depends on the potential inside the scatterer, it can be determined from asymptotic wave function that can be experimentally measured. Consider a quasi one dimensional (Q1D) system with scattering potential $V_g(x,y)$ shown in Fig. 4.2 by the shaded region. Lead L and lead R connect the system to electron reservoirs L and R, respectively. They act as source and sink for electrons, respectively. The confinement potential in the leads, in the y-direction (or, transverse direction) is taken to be hard wall, given by,

$$V(y) = \infty \text{ for } |\, y \,| \geq \frac{W}{2}$$

$$= 0 \text{ for } |\, y \,| < \frac{W}{2}$$

The Schrödinger equation in the two dimensional system (the third direction is eliminated by quantization [16]) is,

$$\left[-\frac{\hbar^2}{2m_e}\left(\frac{\partial^2}{\partial x^2}+\frac{\partial^2}{\partial y^2}\right)+V(y)+V_g(x,y)\right]\Psi(x,y) = E\Psi(x,y) \tag{4.13}$$

where m_e is the effective mass of the electron, and W is the width of leads L and R. In the leads where there is no scatterer ($V_g(x,y) = 0$), the Schrödinger equation can be decoupled. The y-component is,

$$\left[-\frac{\hbar^2}{2m_e}\frac{d^2}{dy^2} + V(y)\right]\chi_m(y) = \varepsilon_m\chi_m(y) \tag{4.14}$$

and the x-component is,

$$-\frac{\hbar^2}{2m_e}\frac{d^2}{dx^2}c_m(x) = (E-\varepsilon_m)c_m(x) \tag{4.15}$$

with $\chi_m(y) = \sqrt{\frac{2}{W}}\sin\frac{m\pi}{W}(y+\frac{W}{2})$ and $\varepsilon_m = \frac{m^2\pi^2\hbar^2}{2m_eW^2}$. E is the energy of incidence from reservoir L, given by,

$$E = E_{m,k_m} = \frac{m^2\pi^2\hbar^2}{2m_eW^2} + \frac{\hbar^2k_m^2}{2m_e} \tag{4.16}$$

It is known that for potentials that have symmetry in x-direction, i.e.,$V(x,y) = V(-x,y)$, we can write solutions to (4.15) given below [75].

$$c_m^e(x) = \sum_{m=1}^{\infty}(\delta_{mn}e^{-ik_mx} - S_{mn}^e e^{ik_mx})\frac{1}{\sqrt{k_m}} \tag{4.17}$$

$$c_m^o(x) = \sum_{m=1}^{\infty}(\delta_{mn}e^{-ik_mx} - S_{mn}^o e^{ik_mx})\frac{1}{\sqrt{k_m}} \tag{4.18}$$

where, $c_m^e(x) = c_m^e(-x)$ and $c_m^o(x) = -c_m^o(-x)$. Then both transmitted wave function (at $x > a$) and reflected wave function (at $x < -a$) are given by [69, 75]

$$c_m(x) = \frac{c_m^e(x) - c_m^o(x)}{2} \tag{4.19}$$

E can be so adjusted by adjusting the Fermi energy of reservoir L, that $\frac{\pi^2\hbar^2}{2m_eW^2} < E < \frac{4\pi^2\hbar^2}{2m_eW^2}$. Then k_1 is real and from Eqs. (4.17), (4.18) and (4.19)

$$c_1(x) = e^{ik_1x} + \tilde{r}_{11}e^{-ik_1x} \text{ for } x < -a$$

$$= \tilde{t}_{11}e^{ik_1x} \text{ for } x > a$$

where

$$\tilde{r}_{11} = -\frac{(S_{11}^o + S_{11}^e)}{2} \tag{4.20}$$

$$\tilde{t}_{11} = \frac{(S_{11}^o - S_{11}^e)}{2} \tag{4.21}$$

For $m > 1$, energy conservation in Eq. (4.16) is not violated as k_m^2 can become negative. That yields evanescent solutions with $k_m \to i\kappa_m$. Inclusion of the evanescent modes is very important to get the correct solutions [76]. Due to the same principle, i.e., any function can be written as a sum of an even function and odd function and any square matrix can be written as a sum of a symmetric matrix and an anti-symmetric matrix, the wave function in the scattering region ($-a < x < a$) can be written as a sum of an even function and an odd function. We denote them as $\eta_m^e(x,y)$ and $\eta_m^o(x,y)$, i.e., $\Psi(x,y) = \frac{\eta_m^e(x,y)+\eta_m^o(x,y)}{2}$ for $-a < x < a$.

$$\eta_m^e(x,y) = \sum_{n=1}^{\infty} d_n \zeta_n^e(x,y) \tag{4.22}$$

$$\eta_m^o(x,y) = \sum_{n=1}^{\infty} d_n \zeta_n^o(x,y) \tag{4.23}$$

ζ_n^e and ζ_n^o are the basis states that satisfy the condition that they go to zero at the upper edge and lower edge of the shaded region in Fig. 4.2.

One can define the matrix elements,

$$F_{m,n}^{eo} = \frac{2}{W(k_m k_n)^{\frac{1}{2}}} \int_{-b}^{b} \chi_m(y) \left(\frac{\partial \zeta_n^{eo}}{\partial x}\right)_{x=a} dy \tag{4.24}$$

Here eo stands for even or odd, i.e., e/o. One can match the wave function and conserve the current at $x = \pm a$ for all y to obtain a matrix equation given by,

$$\sum_{n=1}^{\infty} \left[F_{rn}^{eo} - i\delta_{rn}\right] e^{ik_n a} S_{nm}^{eo} = \left[F_{rm}^{eo} + i\delta_{rm}\right] e^{-ik_m a} \tag{4.25}$$

Solving for S_{mn}^{eo}, we can find the scattering matrix elements. Bound states can be determined from the singularities of the matrix equation (4.25), on setting right hand side to zero. That is

$$det\left[F_{cc}^{eo} - i1\right] = 0 \tag{4.26}$$

Here 'cc' means evanescent channel (or closed channel) for which both k_m and k_n in Eqs. (4.24, 4.25), are imaginary. Solving Eq. (4.25), one can get,

$$S_{11}^{eo} = e^{-2ik_1 a} \frac{G^{eo} + i}{G^{eo} - i} = e^{2iarccot[G^{eo}]} = e^{2i\theta^{eo}} \tag{4.27}$$

where,

$$G^{eo} = F_{11}^{eo} - \sum_{m=2,n=2} F_{1n}^{eo} \left[\left(F_{cc}^{eo} - i1\right)^{-1}\right]_{nm} F_{m1}^{eo} \tag{4.28}$$

and

$$\theta^{eo} = arccot[G^{eo}] \tag{4.29}$$

Here scattering phase shift θ^{eo} is defined with respect to phase shift in the absence of scatterer. Using Eqs. (4.20), (4.21), (4.27) and defining new variables,

$$\phi = \theta^e - \theta^o \text{ and } \quad \theta_r = \theta^e + \theta^o \tag{4.30}$$

we get transmission amplitude and reflection amplitude

$$\tilde{t}_{11} = i\sin(\phi)e^{i\theta_r} \text{ and } \quad \tilde{r}_{11} = \cos(\phi)e^{i\theta_r} \tag{4.31}$$

The correction term of Eq. (4.12) in case of the system in Fig. 4.2 is $\frac{m_e|\tilde{r}_{11}|}{\hbar k_1^2}\sin(\theta_r)$.

Threshold energy E for the second channel is given by $E = \frac{4\pi^2\hbar^2}{2m_eW^2}$, i.e., above this energy k_2 becomes real. Below this energy the second channel can have bound states. Such bound states will occur at energies given by the solution to Eq. (4.26). At these energies the first channel can be propagating as its threshold is given by $E = \frac{\pi^2\hbar^2}{2m_eW^2}$ and S_{11} is given by Eq. (4.27). But at bound state energy, G^{eo} will diverge as it includes matrix elements of $[F_{cc}^{eo} - i1]^{-1}$ as can be seen from equations (4.26) and (4.28). That in turn implies that at resonance (as can be seen from Eq. (4.29))

$$\theta^e = p\pi \text{ and } \quad \theta^o = q\pi \tag{4.32}$$

where p and q are integers. Therefore, from Eq. (4.32),

$$\sin(\theta_r) = \sin(\theta^e + \theta^o) = 0 \tag{4.33}$$

Thus we have shown that the correction term in Eq. (4.12) is zero precisely because $\sin(\theta_r) = 0$. At this point $\mid r \mid \neq 0$ as can be seen from Eqs. (4.30, 4.31). Note that if we ignore the correction term, then all terms on right hand side can be determined experimentally by measuring asymptotic solutions [64]. So injectance can be known from the asymptotic solutions. So the correction term being zero at a resonance can have useful implication to experimentalists.

4.5 The Paradox: Multiple Propagating Channels

We cannot study the multichannel case generally. We will study the two channel case for a particular potential, i.e., $V_g(x,y) = \gamma\delta(x)\delta(y-y_j)$, to show the paradox there along with other puzzling facts.

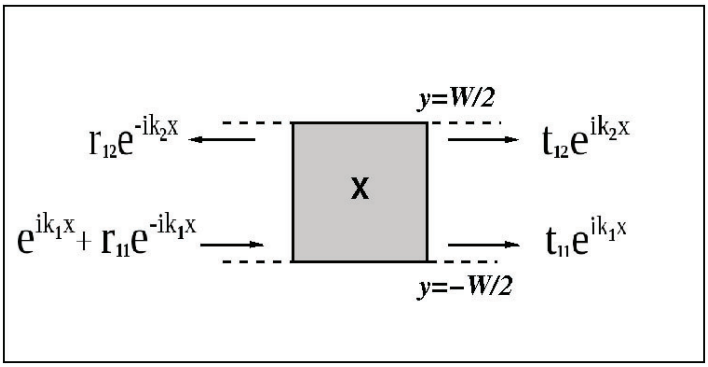

Figure 4.3 A similar scattering set up as in Fig. 4.2, with general potential $V_g(x,y)$ replaced by a delta function potential $\gamma\delta(x)\delta(y-y_j)$. Here we are considering two propagating channels. Incidence is along only one channel which is the fundamental channel ($m=1$) from the left.

In Fig. 4.3, the shaded region is a two dimensional quantum wire with a delta function potential at position (0, y_j) marked X. The dotted lines represent the fact that the quantum wire is connected to electron reservoirs.

Injectance can be obtained from the scattering (S) matrix as described earlier, for the system described in Fig. 4.3. The two channel injectance with incidence along $m=1$ channel from left as shown in Fig. 4.3, in the semi-classical limit is given by,

$$\rho(1) \approx \frac{1}{2\pi}\left[\mid r_{11}\mid^2 \frac{d\theta_{r_{11}}}{dE} + \mid r_{12}\mid^2 \frac{d\theta_{r_{12}}}{dE} + \mid t_{11}\mid^2 \frac{d\theta_{t_{11}}}{dE} + \mid t_{12}\mid^2 \frac{d\theta_{t_{12}}}{dE}\right] \tag{4.34}$$

Here, 1 signifies the incident channel transverse quantum number, i.e., $m=1$. We can break this up as $\rho(1) \approx \rho(1)^L + \rho(1)^R$, where,

$$\rho(1)^L = \frac{1}{2\pi}\left\{\mid r_{11}\mid^2 \frac{d\theta_{r_{11}}}{dE} + \mid r_{12}\mid^2 \frac{d\theta_{r_{12}}}{dE}\right\} \tag{4.35}$$

and

$$\rho(1)^R = \frac{1}{2\pi}\left\{\mid t_{11}\mid^2 \frac{d\theta_{t_{11}}}{dE} + \mid t_{12}\mid^2 \frac{d\theta_{t_{12}}}{dE}\right\} \tag{4.36}$$

That is, $\rho(1)^L$ consist of reflection channels and $\rho(1)^R$ consist of transmission channels. The correction term depends on parameters of the incident channel only and gives the following identity.

$$\rho(1) = \rho(1)^L + \rho(1)^R + \frac{1}{2\pi}\frac{m_e \mid r_{11}\mid}{\hbar k_1^2}\sin(\theta_{r_{11}}) \tag{4.37}$$

Similarly, injectance of channel 2 is,

$$\begin{aligned}\rho(2) &= \frac{1}{2\pi}\left[\mid r_{22}\mid^2 \frac{d\theta_{r_{22}}}{dE} + \mid r_{21}\mid^2 \frac{d\theta_{r_{21}}}{dE} + \mid t_{22}\mid^2 \frac{d\theta_{t_{22}}}{dE}\right. \\ &+ \left. \mid t_{21}\mid^2 \frac{d\theta_{t_{21}}}{dE} + \frac{m_e \mid r_{22}\mid}{\hbar k_2^2}\sin(\theta_{r_{22}})\right] \end{aligned} \tag{4.38}$$

and in the semi-classical limit, it is given by,

$$\rho(2) \approx \frac{1}{2\pi}\left[\mid r_{22}\mid^2 \frac{d\theta_{r_{22}}}{dE} + \mid r_{21}\mid^2 \frac{d\theta_{r_{21}}}{dE} + \mid t_{22}\mid^2 \frac{d\theta_{t_{22}}}{dE} + \mid t_{21}\mid^2 \frac{d\theta_{t_{21}}}{dE}\right] \tag{4.39}$$

The R.H.S can be determined from the S-matrix. This S-matrix approach is easily accessible to experimentalists. We will now calculate this injectance from internal wave function which allows numerical verification.

$$\rho(1) = \int_{-\infty}^{\infty} dx \int_{-\frac{W}{2}}^{\frac{W}{2}} dy \sum_{k_1} |\Psi(x,y,1)|^2 \, \delta(E - E_{1,k_1}) \tag{4.40}$$

where $\Psi(x,y,1)$ is the wave function in the scattering region for incidence along channel $m = 1$, and is of the form [77],

$$\Psi(x,y,1) = \sum_m f_m(x,1)\chi_m(y) \tag{4.41}$$

Here $\chi_m(y)s$ are solutions in the leads in the transverse direction which is a square well potential in y-direction. $\chi_m(y)s$ form a complete set and Eq. (4.41) is derived from the fact that at a given point x, the wave function in the scattering region can be expanded in terms of $\chi_m(y)s$. f_ms are generally of the form given below [77],

$$f_1(x,1) = e^{ik_1x} + r_{11}e^{-ik_1x} \text{ for } x < 0$$

$$= t_{11}e^{ik_1x} \text{ for } x > 0$$

$$f_2(x,1) = r_{12}e^{-ik_2x} \text{ for } x < 0$$

$$= t_{12}e^{ik_2x} \text{ for } x > 0$$

and for $m > 2$,

$$f_m(x,1) = r_{1m}e^{\kappa_m x} \text{ for } x < 0$$

$$= t_{1m}e^{-\kappa_m x} \text{ for } x > 0$$

Here r_{mn} and t_{mn} are unknowns to be determined. The scattering problem described above can be solved using mode matching technique. The reflection amplitudes are given by,

$$r_{mn}(E) = -\frac{i\frac{\Gamma_{mn}}{2\sqrt{k_m k_n}}}{1+\sum_e \frac{\Gamma_{ee}}{2\kappa_e} + i\sum_m \frac{\Gamma_{mm}}{2k_m}} \tag{4.42}$$

Γ_{mn} is the coupling strength between m^{th} and n^{th} modes, given by $\Gamma_{mn} = \gamma \sin\frac{m\pi}{W}(y_j + \frac{W}{2})\sin\frac{n\pi}{W}(y_j + \frac{W}{2})$. The transmission amplitudes are given by, $t_{mn}(E) = r_{mn}(E)$ for $m \neq n$ and, $t_{mm}(E) = 1 + r_{mm}(E)$. $\sum_e$ denotes sum over evanescent modes and runs from 3 to ∞, while $\sum_m$ denotes the same for propagating modes (i.e. m=1 and m=2). We will present our results for the case of two propagating channels but the analysis and results are same for any number of channels.

If the delta function potential is negative ($\gamma < 0$) then there can be bound states. In general, the quasi bound state for channel m=s is given by,

$$1 + \sum_{e=s}^{\infty} \frac{\Gamma_{ee}}{2\kappa_e} = 0 \tag{4.43}$$

Only the bound state for m=1 channel is a true bound state and it is given by the solution to the following equation, $1 + \sum_{e=1}^{\infty} \frac{\Gamma_{ee}}{2\kappa_e} = 0$. The bound state for m=2 is given by, $1 + \sum_{e=2}^{\infty} \frac{\Gamma_{ee}}{2\kappa_e} = 0$. At this energy we get a bound state for m=2, but at that energy m=1 channel is a propagating channel. Hence the bound state given by this equation is a quasi bound state or a resonance.

The delta function in Eq. (4.40) summed over k_1 can be shown to yield a factor $\frac{1}{hv_1}$, where $v_1 = \frac{\hbar k_1}{m}$. Using the orthonormality of $\chi_m(y)s$, we get,

$$\begin{aligned}
\rho(1) &= \frac{1}{hv_1}\left[\int_{-\infty}^{\infty} dx \sum_m |f_m(x,1)|^2\right] \\
&= \frac{1}{hv_1}\left[\int_{-\infty}^{\infty} dx \mid f_1(x,1)\mid^2 + \int_{-\infty}^{\infty} dx \mid f_2(x,1)\mid^2\right. \\
&+ \left.\int_{-\infty}^{\infty} dx \mid f_3(x,1)\mid^2 + \int_{-\infty}^{\infty} dx \mid f_4(x,1)\mid^2 + \cdots\right]
\end{aligned}$$

Substituting the values of $f_m(x,1)s$, we get,

$$\begin{aligned}
\rho(1) &= \frac{1}{hv_1}\left[\int_{-\infty}^{0} dx \left[1 + \mid r_{11}\mid^2 + 2\mid r_{11}\mid \cos(2k_1 x + \phi_1)\right]\right. \\
&+ \int_0^{\infty} dx \mid t_{11}\mid^2 + \int_{-\infty}^{0} dx \mid r_{12}\mid^2 + \int_0^{\infty} dx \mid t_{12}\mid^2 \\
&+ \left.\frac{\mid t_{13}\mid^2}{\kappa_3} + \frac{\mid t_{14}\mid^2}{\kappa_4} + \cdots\right]
\end{aligned}$$

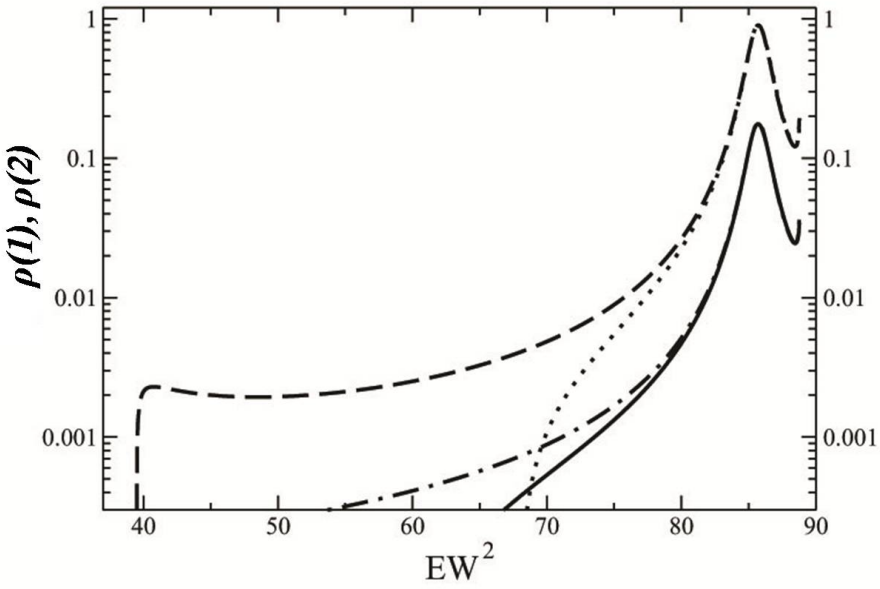

Figure 4.4 The plot is of injectance versus EW^2 for $\gamma = -13$, and $y_j = .45W$. The solid curve shows semi-classical injectance of channel 1 (i.e., incidence is along $m = 1$ transverse channel from left) calculated using S-matrix (Eq. (4.34)), the dot-dashed curve is the exact injectance, for the same channel calculated using internal wave function (Eq. (4.45)). The dotted curve is semi-classical injectance for channel 2 (i.e., incidence is along $m = 2$ transverse mode from the left) from S-matrix (Eq. (4.39)), the dashed curve is the exact injectance, for for the same channel calculated using internal wave function (Eq. (4.46)). We use $\hbar = 1$, $2m = 1$. The figure shows that semi-classical formula becomes exact at resonance where there is a peak in injectance.

Here, $r_{11} = \mid r_{11} \mid e^{-i\phi_1}$. Note that for $m > 2$,

$$\begin{aligned}\int_{-\infty}^{\infty} dx \sum_m |f_m(x,1)|^2 &= |\, t_{1m}\,|^2 \left[\int_{-\infty}^{0} e^{2\kappa_m x} dx + \int_0^{\infty} e^{-2\kappa_m x} dx\right] \\ &= \frac{|\, t_{1m}\,|^2}{\kappa_m}\end{aligned}$$

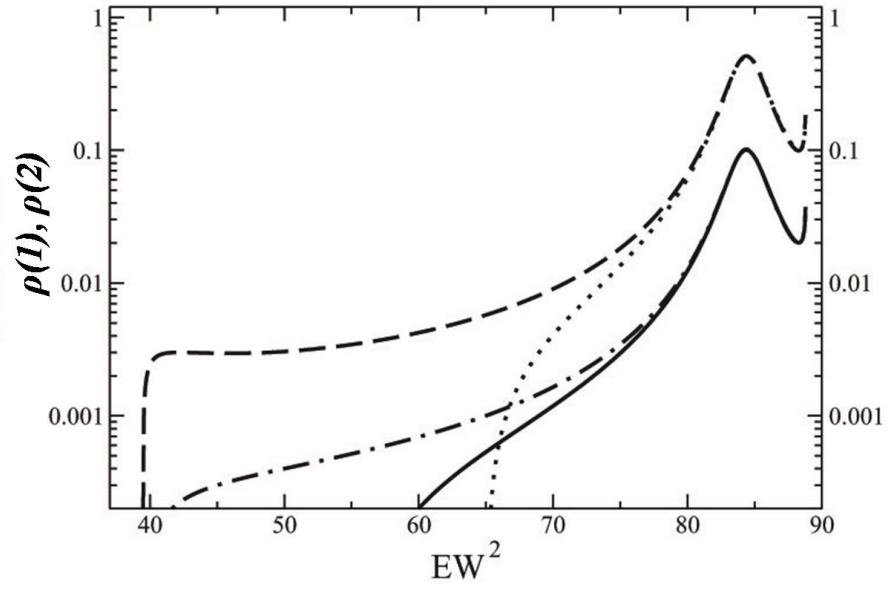

Figure 4.5 The plot is of injectance versus EW^2 for $\gamma = -15$, and $y_j = .45W$. The solid curve shows semi-classical injectance of channel 1 (i.e., incidence is along $m = 1$ transverse channel from left) calculated using S-matrix (Eq. (4.34)), the dot-dashed curve is the exact injectance, for the same channel calculated using internal wave function (Eq. (4.45)). The dotted curve is semi-classical injectance for channel 2 (i.e., incidence is along $m = 2$ transverse channel from the left) from S-matrix (Eq. (4.39)), the dashed curve is the exact injectance, for the same channel calculated using internal wave function (Eq. (4.46)). We use $\hbar = 1, 2m = 1$. The figure shows that semi-classical formula becomes exact at resonance where there is a peak in injectance.

Using time reversal symmetry, i.e, $r_{12} = r_{21}$ and $t_{12} = t_{21}$, we get,

$$\begin{aligned}
\rho(1) &= \frac{1+|\,r_{11}\,|^2+|\,r_{21}\,|^2}{hv_1}\int_{-\infty}^{0} dx \\
&+ \frac{|\,t_{11}\,|^2+|\,t_{21}\,|^2}{hv_1}\int_{0}^{\infty} dx \\
&+ \frac{2\,|\,r_{11}\,|}{hv_1}\int_{-\infty}^{0} dx\cos(2k_1x+\phi_1) \\
&+ \frac{1}{hv_1}\left(\frac{|\,t_{13}\,|^2}{\kappa_3}+\frac{|\,t_{14}\,|^2}{\kappa_4}+\cdots\right)
\end{aligned}$$

Adding and subtracting the following terms,

$$\frac{|t_{11}|^2}{hv_1}\int_{-\infty}^{0} dx,\ \frac{|t_{21}|^2}{hv_1}\int_{-\infty}^{0} dx,$$

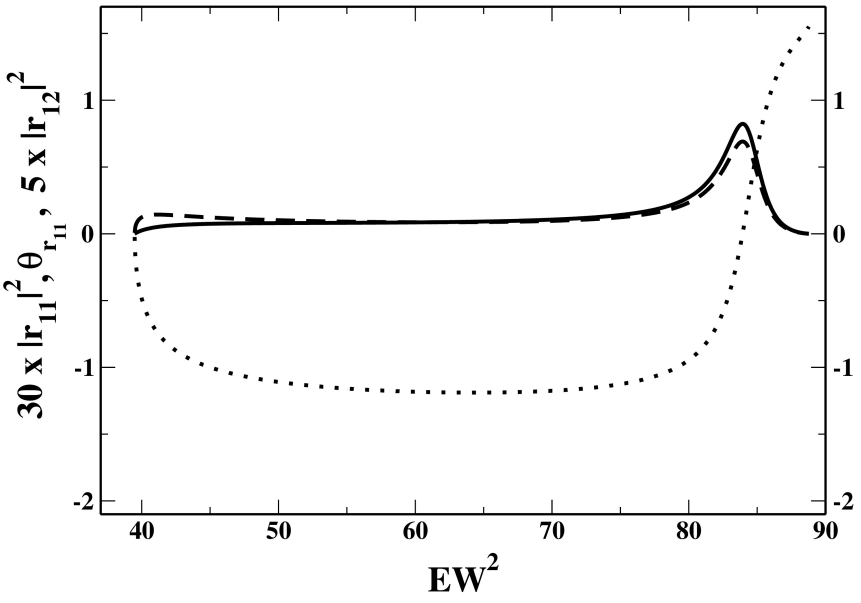

Figure 4.6 Here we are using the same parameters as that of Fig. 4.5. The solid curve shows 30x$|\ r_{11}\ |^2$, the dotted curve is for $\theta_{r_{11}}$. The dashed curve is for 5x$|\ r_{12}\ |^2$. The figure shows that at resonance, there is large fluctuation in $|\ r_{11}\ |^2$, $\theta_{r_{11}}$ and $|\ r_{12}\ |^2$. Also it shows that $|\ r_{11}\ | \neq 0$ but $\sin(\theta_{r_{11}}) = 0$ at the resonant energy EW^2=84.29.

and using the fact that,

$$\frac{|t_{11}|^2}{hv_1}\int_{-\infty}^{0} dx = \frac{|t_{11}|^2}{hv_1}\int_{0}^{\infty} dx$$

and, $|\ r_{11}\ |^2 + |\ r_{21}\ |^2 + |\ t_{11}\ |^2 + |\ t_{21}\ |^2 = 1$, we get,

$$\begin{aligned}\rho(1) &= \frac{1}{hv_1}\int_{-\infty}^{\infty} dx + \frac{|\ r_{11}\ |}{hv_1}\int_{-\infty}^{\infty} dx\cos(2k_1x+\phi_1) \\ &+ \frac{1}{hv_1}\left(\frac{|\ t_{13}\ |^2}{\kappa_3} + \frac{|\ t_{14}\ |^2}{\kappa_4} + \cdot\cdot\right) \end{aligned} \tag{4.44}$$

$\frac{1}{hv_1}\int_{-\infty}^{\infty} dx = \rho_0$ is the injectance in the absence of scatterer. Again if the scattering phase shift is defined with respect to the phase shift in absence of scatterer then this term can be dropped.

Now,

$$\int_{-\infty}^{\infty} dx\cos(2k_1x+\phi_1) = \delta(2k_1)\cos(\phi_1)$$

As $k_1 = 0$ is not a propagating state contributing to transport, hence this term of Eq. (4.44) reduces to

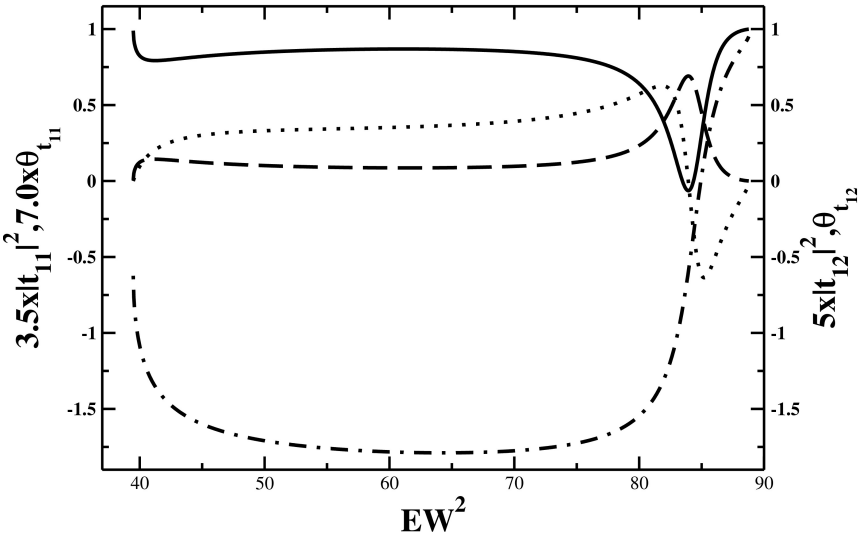

Figure 4.7 Here we are using the same parameters as that of Fig. 4.5. The solid curve shows $(3.5\text{x}|\,t_{11}\,|^2 - 2.5)$, the dotted curve is for $7.0\text{x}\theta_{t_{11}}$. The dashed curve is for $5\text{x}|\,t_{12}\,|^2$, and the dot-dashed curve is for $\theta_{t_{12}} - 0.6$. The figure shows that at resonance (EW^2=84.29), there is large fluctuation in $|\,t_{11}\,|^2$, $\theta_{t_{11}}$, $\theta_{t_{12}}$ and $|\,t_{12}\,|^2$. Also note that there is a negative slope in $\theta_{t_{11}}$

zero, and we are left with,

$$\rho(1) = \frac{1}{hv_1}\left(\frac{|\,t_{13}\,|^2}{\kappa_3} + \frac{|\,t_{14}\,|^2}{\kappa_4} + \cdots\right) \tag{4.45}$$

Similarly, for incidence along channel 2, one can obtain the injectance,

$$\rho(2) = \frac{1}{hv_2}\left(\frac{|\,t_{23}\,|^2}{\kappa_3} + \frac{|\,t_{24}\,|^2}{\kappa_4} + \cdots\right) \tag{4.46}$$

Note that contribution to injectance come from evanescent channels only. This is a tunnelling problem because the lateral confinement makes the effective potential very large and extended in the propagating direction [78]. In Figs. 4.4 and 4.5 we consider two propagating channels and show that semi-classical formula for injectance becomes exact at a resonance. Injectance for both the channels is shown. $\rho(1)$ is the injectance for incidence along channel $m = 1$ and $\rho(2)$ is the same for incidence along channel $m = 2$. The resonance condition is given by Eq. (4.43) and this occur at $EW^2 = 85.62$ in Fig. 4.4 and at $EW^2 = 84.29$ in Fig. 4.5. At the resonant energy we can see a peak in the injectance in both channels which is a consequence of the resonance. At the peak, solid curve (semi-classical $\rho(1)$

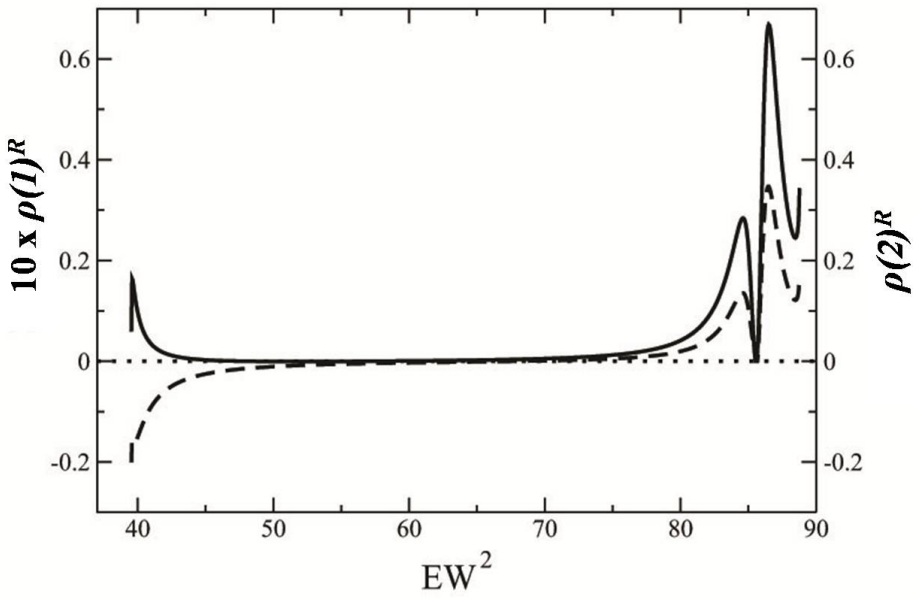

Figure 4.8 Here we are using the same parameters as in Fig. 4.4. The solid curve shows $10\text{x}\rho(1)^R$, the dashed line is for $\rho(2)^R$. Both of them get exactly zero at the resonance i.e., at $EW^2 = 85.62$.

obtained from Eq. (4.34)) coincides with dot-dashed curve (exact $\rho(1)$ obtained from Eq. (4.45)), and, dotted curve (semi-classical $\rho(2)$ obtained from Eq. (4.39)) coincides with dashed curve (exact $\rho(2)$ obtained from Eq. (4.46)). Exactness of the semi-classical formula is counter-intuitive because at this point scattering probability and scattering phase shift show strong energy dependence, so the stationary phase approximation needed to get Eqs. (4.34) and (4.39) cannot be valid. Also at this energy, $\mid r_{11} \mid \neq 0$ and $\mid r_{22} \mid \neq 0$, rather, $\sin(\theta_{r_{11}}) = 0$ and $\sin(\theta_{r_{22}}) = 0$ implying interference effects disappear and so correction term in Eqs. (4.34, 4.38) disappear making semi-classical formula exact. All this along with the energy dependence of the scattering matrix elements can be seen in Fig. 4.6 and Fig. 4.7 for the parameters used in Fig. 4.5. The negative slope in the scattering phase shift $\theta_{t_{11}}$ (see dotted curve in Fig. 4.6) is due to Fano resonance and is another puzzling feature, explained below.

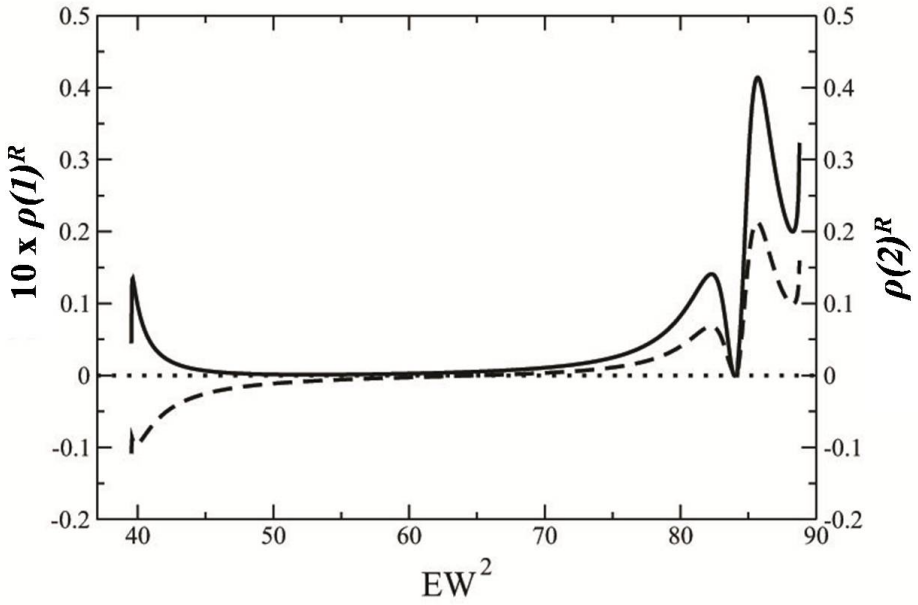

Figure 4.9 Here we are using the same parameters as in Fig. 4.5. The solid curve shows $10\text{x}\rho(1)^R$, the dashed line is for $\rho(2)^R$. Both of them get exactly zero at the resonance i.e., at $EW^2 = 84.29$.

4.6 Negative Time Scales

It can be proved that $\rho(1,2)^R = 0$ at the resonance, from Eqs. (4.36) and (4.42). It is shown in Figs. 4.8 and 4.9 for the parameters used in Figs. 4.4 and 4.5, respectively. As explained before that $\rho(1,2)^R(E)$ (within a factor of $\hbar$) is a time scale associated with particles that escape to the right lead. There has been a great amount of controversy regarding, what negative or zero times mean. $\rho(2)$ as defined in Eq. (4.46) (within a factor of $\hbar$) is known as dwell time and it is definitely positive. Dwell time is exact because it is defined from the internal wave-function that can be calculated exactly and also defined in terms of probability regarding which there is no controversy in quantum mechanics. This time scale is associated with particles that traverse the potential region independent of to which channel it is scattered to. Each of the four times on the R.H.S of Eq. (4.39) are Wigner Smith delay time (again within a factor of $\hbar$). These time scales can be negative as the scattering phase shift can have negative slopes with respect to energy. These time scales are for particular scattering

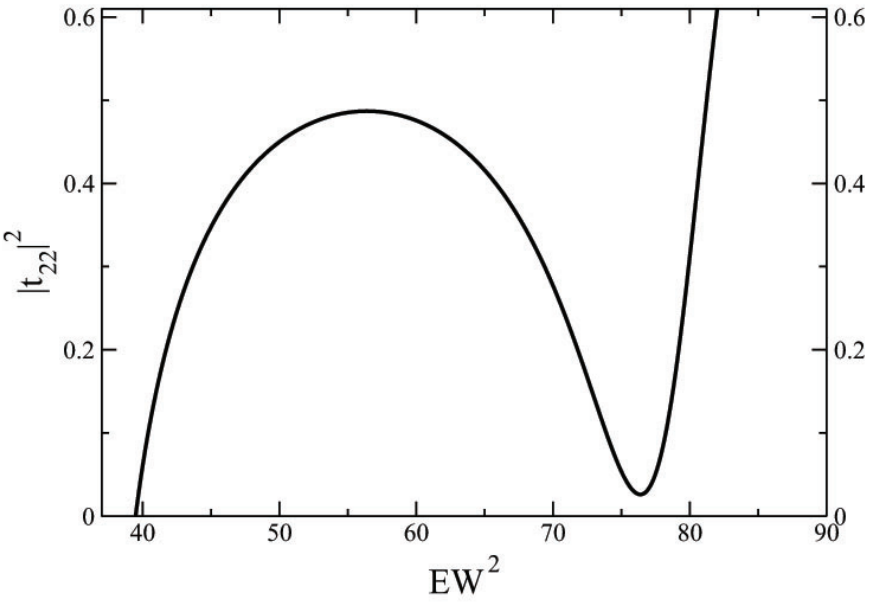

Figure 4.10 Here the energy dependence of $|\, t_{22}\,|^2$ is shown, using the same variables as in Fig. 4.5.

processes and there are four possible processes. For example $|r_{22}|^2 \frac{d\theta_{r_{22}}}{dE}$ is the time scale associated with particles that are incident along $m = 2$ channel from the left and scattered to $m = 2$ channel on the right. Hence the four WSDT should have added up to give the dwell time but they do not as they are semi-classical. So it remains a question as to what WSDT actually mean in a quantum regime where they can become negative. Note that $\rho(2)^R$ (dashed curve in Fig. 4.8 and Fig. 4.9) becomes negative for $40 < EW^2 < 50$. So far researchers have mainly studied this low energy quantum regime [53, 68, 79–82] for observing and understanding negative time scales. In this regime the correction term (or quantum interference term) is non-zero. The controversies arise due to the lack of equality (between dashed and dotted curves in Figs. 4.4 and 4.5 between Eqs. (4.39) and (4.46), which leaves room for different interpretations of the different times. So since negative times are seen in quantum regime only, negative times are also subject to interpretations. Many of these times, positive or negative, are experimentally accessible [83]. Only at $EW^2 = 39.51$ when $k_2 \to 0$, the correction term disappear because $\frac{V}{k_2} \to \infty$ (see Fig. 4.1(b)). Hence if someone can do an experiment at this energy

then the negative times may be observed and experimental results are free of controversy. But at this point quite ironically, $|t_{22}| \to 0$ and so one has to wait infinitely long to see a negative time delay that is free from controversies. On the other hand at the Fano resonance ($EW^2 = 85.62$ in Fig. 4.8 and at $EW^2 = 84.29$ in Fig. 4.9), both the solid curve and the dashed curve become zero, implying there are time scales that go to zero at this energy. So the same puzzling question can be asked again, as to how can time scales be negative or zero? Unlike the low energy regime, at this energy, the correction term is zero implying Wigner Smith delay times add up to give dwell time, and also transmission is finite. We show the finiteness of $|\, t_{22}\,|^2$, for same parameters as in Fig. 4.5, in Fig. 4.10 at the resonant energy where $\rho(2) = 0$. So there is no room for different interpretations and also one does not have to wait infinitely to observe a negative or zero time delay. In fact $|t_{22}|^2 \frac{d\theta_{t_{22}}}{dE}$ is strongly negative here and so if one observes the transmission from the $m = 2$ channel on the left to $m = 2$ channel on the right, then one can see strongly negative delays. It should not be difficult to separate such transmission processes from t_{21} transmission processes, as in the former case the transmitted wave packet move much slowly (being constructed from k_2 instead of k_1). Experimentalists may try to do similar experiments in this regime. Specially as one can see, the transmissions at this energy is finite.

4.7 Conclusion

Study of injectance of a quantum system coupled to finite thickness leads has established many novel facts. First of all the correction term to injectance, obtained in refs. [73, 74], become zero very paradoxically in a quantum regime of a Fano resonance. For single channel leads this has been proved generally and for multichannel leads this has been shown for a delta function potential. Thus, semi-classical formulas for injectance become exact at Fano resonance. All the terms that appear in semi-classical formulas can be determined experimentally from asymptotic wave functions. Hence, although injectance strongly depend on the scattering potential, can be determined without knowing the scattering potential. Besides, the quantum interference term going to zero can unambiguously establish the possibility of negative time scales in quantum mechanics.

Chapter 5

Negative partial density of states in mesoscopic systems

Since the experimental observation of quantum mechanical scattering phase shift in mesoscopic systems, several aspects of it has not yet been understood. The experimental observations has also accentuated many theoretical problems related to Friedel sum rule and negativity of partial density of states. We address these problems using the concepts of Argand diagram and Burgers circuit. We can prove the possibility of negative partial density of states in mesoscopic systems. Such a conclusive and general evidence cannot be given in one, two or three dimensions. We can show a general connection between phase drops and exactness of semi classical Friedel sum rule. We also show Argand diagram for a scattering matrix element can be of few classes and all observations can be classified accordingly.

5.1 Introduction

A number of experimental [47–49, 65, 66, 84, 85] and theoretical works [50, 70–72, 86–92] have recently studied the scattering phase shift in low dimensional mesoscopic systems where the electron dynamics is determined by quantum mechanics. Essentially, the asymptotic states are that of free particles in a quantum wire and the scatterer is embedded in the path of this quantum wire [88, 93]. Model specific approach so far has led to contradictory and confusing results [61, 70–72, 85, 92].

Heiblum et al [85] quote that '*There is by now vast theoretical evidence that the transmission phase depends on the specific properties of the QD's levels that participate in the transport*'. However, in all these studies there is no reference to well established theorems and results on phase changes and lapses known for a long time in the community that studies classical wave trains [94, 95]. Such phase changes are still very important in mesoscopic physics as they are related to breakdown of parity effect [86], interpretation of Friedel sum rule (FSR) [70–72, 89, 96], relation to partial density of states (PDOS) [53, 61, 79, 97, 98], etc. that determine the thermodynamic properties of a mesoscopic system which is absent in case of classical waves. So in this work we analyse theoretical and experimental observations in mesoscopic systems, in terms of some known facts ('*Argand diagram*' and '*Burgers circuit*') to resolve the puzzles. Argand diagram is a plot of real versus imaginary parts of an analytic complex function and Burgers circuit is about phase changes and lapses being determined by phase singularities.

We shall show that the scattering phase shift behaviour of different experimentally [47–49, 65, 66, 84, 85] and theoretically [50, 70–72, 86–92] studied systems can be understood from the Argand diagrams and analyticity. Argand diagram for the scattering matrix element of any system can be classified as, a) Argand diagram is closed, b) Argand diagram is open, c) Argand diagram encloses the phase singularity, d) Argand diagram does not enclose the phase singularity, e) Argand diagram is simply connected and f) Argand diagram is multiply connected due to the presence of sub-loops. Specific properties of the scatterer only matter to the extent that the Argand diagram changes from one of these to another. Among them some changes are topologically possible and others are not. Understanding how an Argand diagram changes from one to the other explains most of the puzzles not understood so far. In section 5.3 we will analyse slips in the scattering phase shift [47, 86]. We will first explain the features not understood so far. And then we will show how Argand diagram and Burgers circuit can explain the features. In section 5.4 we will show that FSR too can be understood from Argand diagrams although its manifestation seems to be completely different for different potentials [89, 90]. We will also show why FSR can become exact whenever there is a phase lapse. This is a physically counter-intuitive result that has been proven for particular potentials so far [89, 99]. We will show that this result depends on the properties of Argand diagram and hence very general and

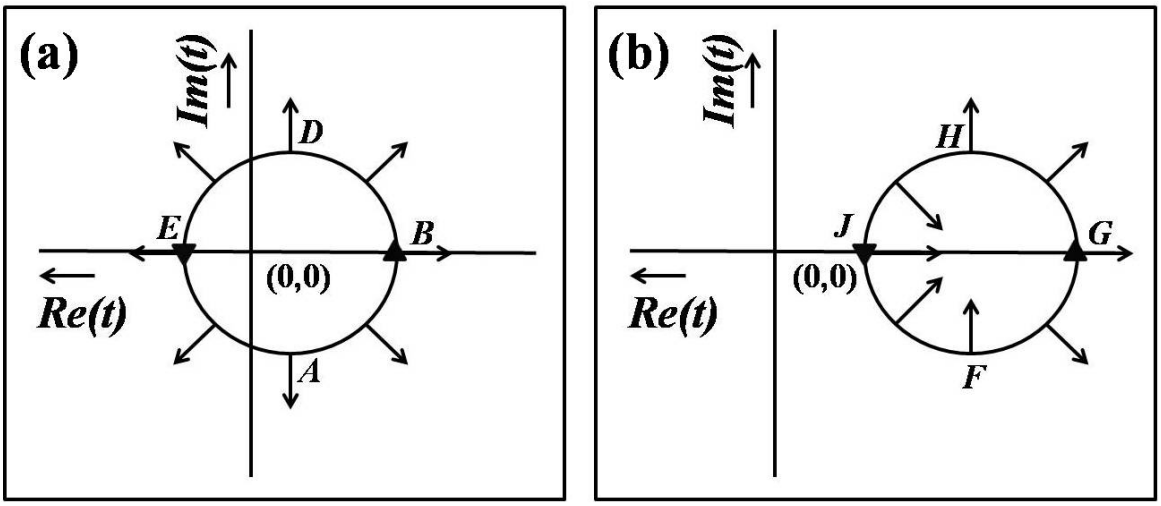

Figure 5.1 Schematic Argand diagrams that exemplify Eq. (5.2). (a) When the Argand diagram contour encloses the singular point at $(0,0)$ and (b) when the contour does not enclose the singular point.

independent of the scattering potential. In section 5.4 we will also prove the possibility of negative partial density of states in real mesoscopic systems.

5.2 Burgers Circuit: An introduction

Given a complex function t, if there is a phase singularity [95] in its complex plane, then one can specify the strength of the singularity as follows [95],

$$I = sgnIm\left(\nabla t^* \times \nabla t\right).\widehat{n} \tag{5.1}$$

I is a topological quantum number which is always conserved in an interaction. For a generalised 'Burgers circuit' (BC) [94],

$$\oint_C d\phi = 2\pi I \tag{5.2}$$

where, $\phi = Arctan\frac{Im(t)}{Re(t)}$. If the contour C does not enclose the phase singularity then I is 0. When the contour C enclosing a phase singularity is clockwise then I is -1 and when the contour C enclosing a phase singularity is counter-clockwise then I is +1. A scattering matrix element is a complex function for which Argand diagram can be drawn and concept of BC can be applied. Argand diagram for a scattering matrix element is generally counter-clockwise, as incident energy of the scattering particle

increases. At the phase singularity, $Re(t) = 0$ and $Im(t) = 0$, implying the phase singularity is at the origin. Figs. 5.1(a) and 5.1(b), shows schematic Argand diagrams for a complex function t. Fig. 5.1(a), shows a typical counter-clockwise contour (ABDEA) of an Argand diagram enclosing the phase singularity at the origin. Hence for this case, $I = +1$. The contour trajectory (ABDEA) is concave throughout with respect to the singular point at the origin. Following Eq. (5.2), the net change in phase in tracing ABDEA, in Fig. 5.1(a), is 2π. Thus the phase monotonously increases for a concave trajectory. Fig. 5.1(b) shows a typical contour (FGHJF) of an Argand diagram not enclosing the phase singularity at the origin. Hence for this case, $I = 0$. The contour has both concave (FGH) and convex (HJF) trajectories with respect to the singular point at the origin. Following Eq. (5.2), the total change in phase in Fig. 5.1(b) is zero. It is possible if the phase increases for the concave trajectory and decreases for the convex trajectory, the net phase change being zero. This can be easily verified by calculating ϕ at any point $(Re(t), Im(t))$ of the trajectory and will be further demonstrated below. Thus for both Figs. 5.1(a) and 5.1(b), the phase change is determined by the singular point and the two follow the same principle. As a special case of the two, one can have a situation where the contour touches the singular point. In which case too the phase change can be understood from the same principle and will be explained later. Also if it is a closed contour as in Figs. 5.1(a) and 5.1(b), then Eq. (5.2) is exact. In the real systems we will discuss in this work, the contours may not be closed. However, we will extend Eq. (5.2) to understand such cases too.

Whatever be the shape of a closed contour C, the phase change is given by Eq. (5.2). As a consequence, the real and imaginary parts of t are not independent of each other but are related. Let us say the complex transmission amplitude be $t(U) = |t(U)|e^{i\theta_t(U)}$ where U can be any parameter like incident energy or gate voltage. Then

$$Re\,(t(U)) = \frac{1}{\pi} P \int_{-\infty}^{\infty} \frac{Im(t(U^{'}))}{U^{'} - U} dU^{'} \tag{5.3}$$

$$Im\,(t(U)) = -\frac{1}{\pi} P \int_{-\infty}^{\infty} \frac{Re(t(U^{'}))}{U^{'} - U} dU^{'} \tag{5.4}$$

These are the well known Kramers-Kronig relations [51]. Another way in which the relation can be stated is in terms of Hilbert Transform [50],

$$ln|t(U)| = \frac{1}{\pi} P \int_{-\infty}^{\infty} \frac{\theta_t(U^{'})}{U^{'} - U} dU^{'} \tag{5.5}$$

$$\theta_t(U) = -\frac{1}{\pi} P \int_{-\infty}^{\infty} \frac{ln|t(U')|}{U' - U} dU' \tag{5.6}$$

Since I is a conserved quantity, by adding terms to a Hamiltonian (or details to the states in the scatterer) we cannot remove the phase singularities of the wave function in the complex plane. Phase changes are typically determined by the phase singularities. Depending on the interaction the Argand diagram can however change and so a theoretical understanding of the experimental data may not crucially depend on the details of the sample or model. Sample details can change the shape of the contour C, but as these theorems state, to understand the phase changes, we do not need all these details. Englman and Yahalom [50] had shown that the experimental data for scattering phase shift and scattering cross section of a quantum dot, are consistent with Hilbert transforms. We will show that the principles of analyticity and Eq. (5.2) can be used to explain most of the puzzles not understood so far.

5.3 Model Potentials

In this section we analyse scattering phase shifts for different potentials that has been theoretically studied [72] so far, for analysing the experimental observations [47–49]. Again as explained with Eq. (5.2), we do not need very complicated realistic potentials to understand the phase shifts but we need representative potentials that can be exactly solved and help us understand different aspects of Eq. (5.2).

5.3.1 Double delta function potential in one dimension

Let us first consider scattering by a double delta function potential in one dimension (1D) schematically shown in Fig. 5.2(a), that was recently studied in ref. [72]. Although a simple potential, it exhibits pronounced Breit Wigner (BW) resonances. We will use Eq. (5.2) to understand the scattering phase shift for this system and hence for BW resonances. The scattering potential for this system can be written as,

$$V_1(x) = \gamma_1 \delta(x)$$

$$V_2(x) = \gamma_2 \delta(x-a)$$

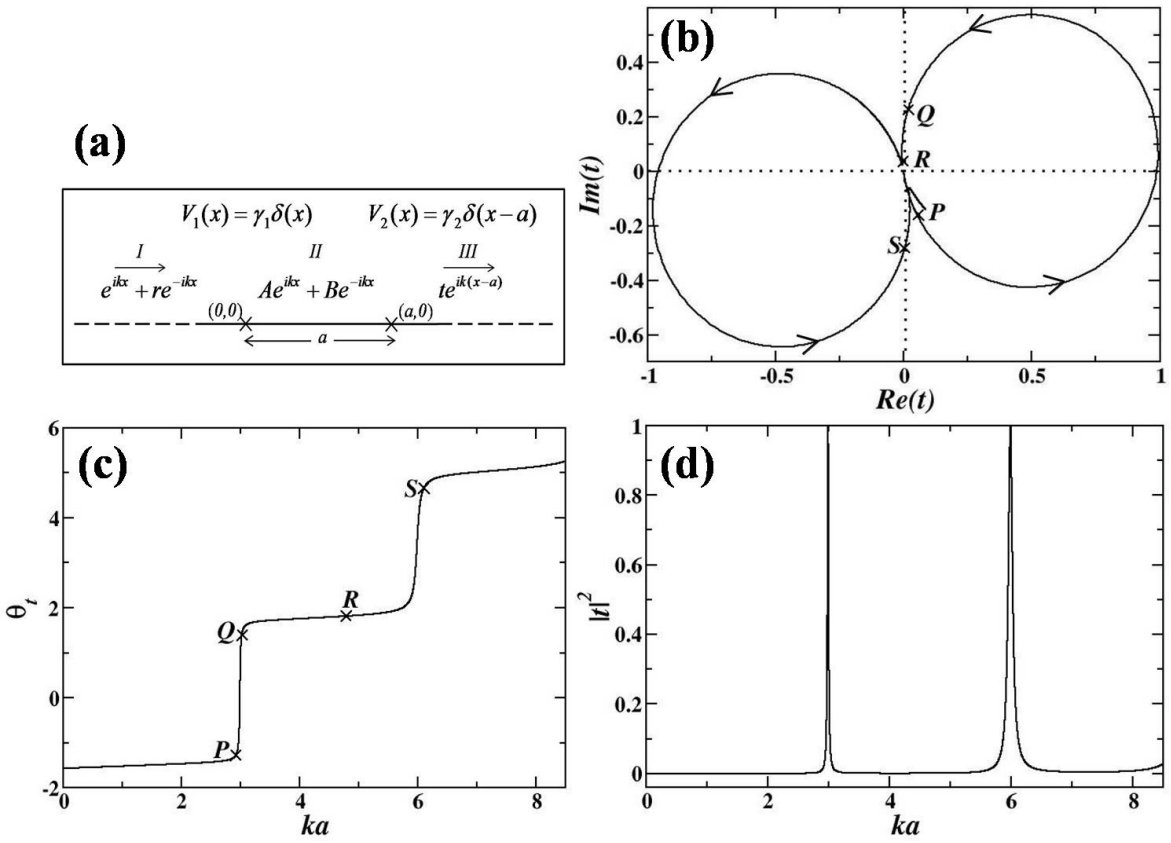

Figure 5.2 (a) Schematic representation for scattering of electrons by a double delta function potential in one dimension. The direction of incident and scattered electrons are represented by arrows. The solid line represents a quantum wire with double delta function potentials at positions $x = 0$ and $x = a$ respectively shown by cross (X) marks. γ_1 and γ_2 are the strengths of the potentials. The dashed lines represent the fact that the quantum wire is connected to electron reservoirs via leads. (b) Argand diagram for transmission amplitude for the double delta function potential. (c) Plot of transmission phase shift θ_t versus ka and (d) plot of transmission coefficient $|t|^2$ versus ka, for the double delta function potential using parameters $e\gamma_1 a = e\gamma_2 a = 40$, $a = 1$, $e = 1, 2m_e = 1$ and $\hbar = 1$.

where γ_1 and γ_2 are the strengths of potential V_1 and V_2, respectively. The wave function in different regions marked I, II and III are (see Fig. 5.2(a)),

$$\psi(x) = \begin{cases} e^{ikx} + re^{-ikx}, for\ x < 0, \\ Ae^{ikx} + Be^{-ikx}, for\ 0 < x \leq a, \\ te^{ik(x-a)}, for\ x > a. \end{cases}$$

Here r and t are the reflection and transmission amplitudes, $k = \sqrt{\frac{2m_e}{\hbar^2}E}$ is the wave vector and E is incident Fermi energy. $t = \mid t \mid e^{i\theta_t}$, where, $\theta_t = Arctan\frac{Im(t)}{Re(t)}$ is transmission phase shift and $|t| = \sqrt{Im(t)^2 + Re(t)^2}$ is transmission modulus. The Argand diagram for t is shown in Fig. 5.2(b), where energy is varied to remain within the first Riemann surface. There is a phase singularity at the origin where $t = 0$. The Argand diagram encloses the singularity but is not closed in the first Riemann surface. Figs. 5.2(c) and 5.2(d) shows the transmission phase shift θ_t and the transmission coefficient $|t|^2$, respectively, as a function of ka, using the same parameters as in Fig. 5.2(b).

In Fig. 5.2(b), the contour starts from the origin where $E = 0$, goes first through point P and then through Q, R and S. *The trajectory facing the singular point at the origin is concave throughout, and thus as discussed with Fig. 5.1, the phase increases continuously.* This is evident in Fig. 5.2(c) where the points P, Q, R and S are also shown at their respective values of ka. As the trajectory comes closer to the point of phase singularity, phase changes are very small and energy cost is very high. In Fig. 5.2(b), the energy at the points marked P, Q, R and S are $8.614a^2$, $9.12a^2$, $23.61a^2$ and $37.58a^2$. Thus the energy change in going from P to Q (a large arc in the trajectory in Fig. 5.2(b)) is very small, whereas the energy change in going from Q to R (a small arc in the trajectory in Fig. 5.2(b)) is very high. The point R is very close to the singular point. Thus it costs a lot of energy as the Argand diagram trajectory tries to approach the point of phase singularity.

5.3.2 Stub potential

Another scattering potential often studied [72, 100] to understand the experiments [47–49] is known as the stub, which is an infinite one-dimensional quantum wire with a finite side branch. A schematic representation of this system is shown in Fig. 5.3(a). This system is topologically not the same as a one dimensional system, as in this case the origin $(0,0)$ (see Fig. 5.3(a)) is connected to three other directions. This potential shows discontinuous phase drops by π [72, 100] similar to that observed in experiments [47, 49]. Prior to that this discontinuos scattering phase shift was shown to cause breakdown of parity effect of single particle states [86]. However, if there is an energy scale associated with such a sharp phase change has remained a puzzle [47]. Heiblum et al [47] quote that '*The appearance of a second energy scale in the phase jump between resonances also cannot be understood...*'. It sug-

gests existence of an infinitely large energy scale. We will use Eq. (5.2) to understand why scattering phase shift can change discontinuously as some parameter is varied. Electrons are incident from left (see Fig. 5.3(a)) with energy E. The thin lines represent one dimensional quantum wires with zero potential, while the bold line represents quantum wire with a finite potential $V(y)$ given by,

$$V(y) = \begin{cases} 0, for\ 0 < y \leq l_1, \\ iV_0, for\ l_1 < y \leq l, \\ \infty, for\ y > l. \end{cases}$$

The potential $V(y)$ is taken to be imaginary, as it allows us to make the Argand diagram trajectory approach and cross the point of phase singularity. This cannot be done with real potentials as I in Eq. (5.2) is a conserved quantity. Imaginary potentials are known as optical potentials [101–104]. They are often used to simulate the effect of decoherence and open systems. If the system itself changes (for example from a closed one to an open one) then I may be different for the two cases. When V_0 is 0 then $V(y)$ is 0 and the system is a closed conserved system. And when V_0 is non-zero then $V(y) = iV_0$ and it is an open system. The wave function in the different regions are given by,

$$\psi(x,y) = \begin{cases} e^{ikx} + re^{-ikx}, for\ x < 0, \\ te^{ikx}, for\ x > 0, \\ Ae^{iky} + Be^{-iky}, for\ 0 < y \leq l_1, \\ Ce^{iq(y-l_1)} + De^{-iq(y-l_1)}, for\ l_1 < y < l, \\ 0, for\ y = l. \end{cases}$$

Here r and t are the reflection and transmission amplitudes, $k = \sqrt{\frac{2m_e}{\hbar^2}E}$ is the wave vector along thin lines, $q = \sqrt{\frac{2m_e}{\hbar^2}(E - iV_0)}$ is the wave vector along the bold line, and E is the Fermi energy. Solving the scattering problem using Griffiths boundary conditions [101–104], that the wave function is continuous and the currents are conserved at the junction at $(0,0)$ in Fig. 5.3(a), we get r and t as a function of energy, E.

$$r = \frac{1 - \frac{ik-q_1}{ik+q_1}e^{-2ikl_1}}{1 + 3\frac{ik-q_1}{ik+q_1}e^{-2ikl_1}} \tag{5.7}$$

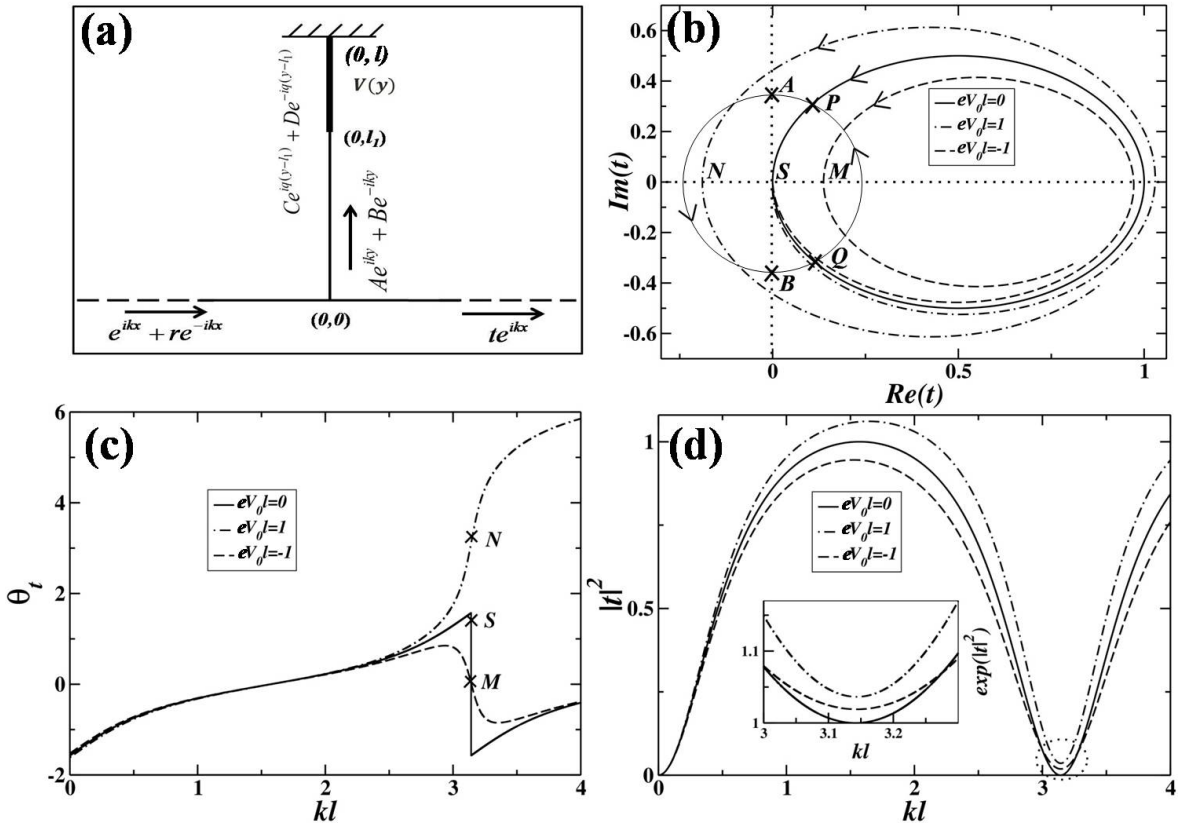

Figure 5.3 (a) Schematic representation for scattering of electrons by a stub potential. The direction of incident and scattered electrons are shown by arrows. The potential, represented by the bold line along y-axis, is $V(y) = iV_0$. (b) Argand diagram for transmission amplitude for different values of eV_0l, where, e is electronic charge and l is the length shown in (a). The thick solid line is Argand diagram for the case when $eV_0l = 0$, the dot-dashed line is that for $eV_0l = 0.5$ and the dashed line is for $eV_0l = -0.5$. Here $l_1 = .5l$, $l = 1$, $e = 1, 2m_e = 1$ and $\hbar = 1$. (c) Plot of transmission phase shift θ_t and (d) plot of transmission coefficient $|t|^2$, as a function of dimensionless wave vector kl, taking the same notations and parameters as in Fig. 5.3(b).

$$t = \frac{2(1+\frac{ik-q_1}{ik+q_1}e^{-2ikl_1})}{1+3\frac{ik-q_1}{ik+q_1}e^{-2ikl_1}} \tag{5.8}$$

where, $q_1 = q\,[cot\,(q(l-l_1))]$. Transmission phase shift is given by $\theta_t = Arctan\frac{Im(t)}{Re(t)}$. Fig. 5.3(b) show the Argand diagrams for the transmission amplitudes, given by Eq. (5.8), for different values of eV_0l, where energy is varied to remain within the first Riemann surface. The thick solid line is for $eV_0l = 0$, the dot-dashed line is for $eV_0l = 0.5$ and the dashed line is for $eV_0l = -0.5$. There is a phase singularity at $t = 0$ marked as S in Fig. 5.3(b). Figs. 5.3(c) and 5.3(d) shows the transmission phase

shift θ_t and transmission coefficient $|t|^2$, respectively, as a function of kl for different values of eV_0l, using the same parameters and same notations as in Fig. 5.3(b).

In Fig. 5.3(b), if we draw a circle (thin solid line through *PABQP*) around the phase singularity, then Eq. (5.2) implies the total phase change along the contour is 2π. If the shape and size of the contour is altered, the net phase change along the contour remains the same provided the contour encircles the phase singularity. The phase change while going from Q to P along the arrow in the contour is less than π as the phase change in going from B to A is π. In the limit when the radius of the circle P,A,B,Q is tending to zero, P approaches A, Q approaches B and P,A,B,Q all coincide with the singular point S. In this limit going from Q to P would imply a discontinuous phase change of π. Therefore a trajectory that tangentially touches the singular point S like the thick solid line for $eV_0l = 0$ in Fig. 5.3(b), will exhibit a discontinuous phase change of π at S. This phase change can be seen in the solid line for $eV_0l = 0$ in Fig. 5.3(c) (at point S marked at the same value of kl as in Fig. 5.3(b)), where we have plotted the transmission phase shift θ_t vs kl. We have already discussed in the previous section that as the Argand diagram trajectory approaches the point of phase singularity, the energy cost is very high. So, it is surprising that in a mesoscopic system, one can have such a high energy scale and one can realize discontinuos phase drops that are generally not seen for classical wave transport. In fact, it is not a real energy scale but an effective energy scale. Scattering by a stub can be mapped into a problem of a delta function potential in one dimension where the strength of the delta function potential is $kcot(kl)$. That is, $V^{eff}(x) = kcot(kl)\delta(x)$ has same reflection amplitude r and transmission amplitude t as in Eqs. (5.7) and (5.8). This is an effective potential that the electrons encounter while the real potential is $V_0 = 0$. At $kl = \pi$, a small change in k or l means a very large change in the effective potential $V^{eff}(x)$. Such large effective energy scales are known in other areas of condensed matter physics, for example, the effective electron mass becomes ∞ at the band edge.

For $eV_0l = 0.5$, the Argand diagram trajectory shown by the dot-dashed line in Fig. 5.3(b), intersects the $Re(t)$ axis at point N at $kl = \pi$. The Argand diagram trajectory facing the phase singularity at S is concave throughout. So, Eq. (5.2) implies a monotonously increasing phase. This phase behaviour can be seen in the dot-dashed line in Fig. 5.3(c) where we have plotted the transmission phase shift θ_t vs kl and marked N at $kl = \pi$. For $eV_0l = -0.5$, the Argand diagram trajectory shown

by the dashed line in Fig. 5.3(b), intersects the $Re(t)$ axis at point M at $kl = \pi$. The Argand diagram trajectory facing the phase singularity is partially convex and partially concave. As discussed with respect to Eq. (5.2), the phase increases for the concave part and decreases for the convex part of the trajectory. This phase behaviour can be seen in the dashed curve in Fig. 5.3(c) where we have plotted the transmission phase shift θ_t vs kl and marked the point M similarly. Therefore, if eV_0l is continuously changed from 0.5 to -0.5, then the point N moves to M crossing the point of phase singularity. This implies that with an imaginary potential, just by changing sign of the potential it is possible to cross the singular point. I for dot-dashed line is 1 and that for the dashed line is 0. In other words by changing an imaginary potential we can make I change from 1 to 0. This is difficult with a real potential. If we tried to cross the singular point with real potentials it would cost an infinite amount of energy. We have discussed an effective real potential that can make an Argand diagram trajectory tangentially touch the point of phase singularity. Any effective potential that can make Argand diagram trajectory cross the point of phase singularity is not known.

In Fig. 5.3(c), we observe two different types of phase drops. For $eV_0l = 0$, we get a discontinuous phase drop (shown by the solid curve in Fig. 5.3(c)) and for $eV_0l = -0.5$, we get a gradual phase drop (shown by the dashed curve in Fig. 5.3(c)). If we make $eV_0l < -0.5$, the point M in Fig. 5.3(b) will shift more to the right and the phase drop will be less in magnitude and also less sharp. In Fig. 5.3(d), using the same parameters and same notations as in Figs. 5.3(b) and 5.3(c), transmission coefficient $|t|^2$ is plotted as a function of kl for different values of eV_0l. The inset in Fig. 5.3(d) shows the transmission coefficient $|t|^2$ in exponential scale in the region around $kl = \pi$ (shown by dotted circle). At $kl = \pi$, the thick solid curve for $eV_0l = 0$ goes to zero, while the dot-dashed and dashed curves for $eV_0l = 0.5$ and $eV_0l = -0.5$ respectively, go through a non-zero minima. The phase behaviours for dot-dashed and dashed curves are completely different as can be seen from Fig. 5.3(c).

Thus in this section, we have explained using Argand diagram and Burgers circuit, why phase (scattering phase shift) drops can occur discontinuously? Why such a phase drop can disappear or change from discontinuous to gradual? The gradual phase drop in the dashed curve of Fig. 5.3(c) at M is related to the analytic property of complex transmission amplitude and how the trajectory encloses the singularity. Whether the gradual drop is sharp or slow, depends on the distance SM (Fig.

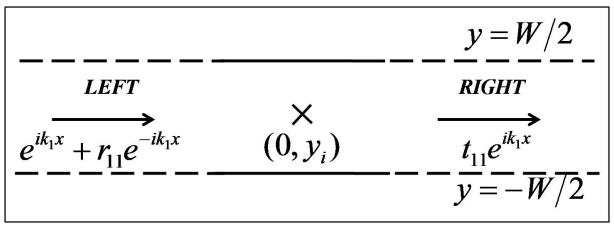

Figure 5.4 Schematic representation for scattering of electrons by a one dimensional delta function potential. The position of a delta function potential is shown by cross (X) mark.

5.3(b)) at which the convex trajectory intercepts the $Re(t)$ axis.

5.3.3 Single channel quantum wire

The next scattering potential we consider, is a delta function potential in a single channel quantum wire [89]. This essentially means, there is a single propagating channel while all other channels are evanescent. These evanescent channels are characteristic of quasi one dimension (Q1D), and make this scattering potential completely different from that of a delta function potential in one dimension [105–107]. This system gained relevance with respect to the experiments of Schuster et al. [47], Yang Ji et al. [48, 49], etc., because it too shows phase drops [87] like those observed in case of the stub. The delta function potential can create a bound state in the continuum and it is this bound state that non-trivially affects the scattering. Any other potential in quasi one dimension that can sustain a bound state will produce similar effects. Essentially, such a bound state cause a Fano resonance which is at the heart of the features observed for this potential. In this section we will explain the scattering phase shift for this potential from Argand diagram. The system is shown in Fig. 5.4. The quantum wire is shown by solid line with a delta function potential at position $(0, y_i)$ shown by a cross mark. W is width of the quantum wire. The dashed lines represent the fact that the quantum wire is connected to electron reservoirs via leads. Electrons are injected from the left reservoir into the left lead. The electrons are allowed to propagate along x direction, but confined along y direction. The confinement potential in the leads is taken to be hard wall potential and is given by,

$$V_c(y) = \begin{cases} \infty, for\ |y| \geq \frac{W}{2}, \\ 0, for\ |y| < \frac{W}{2}. \end{cases}$$

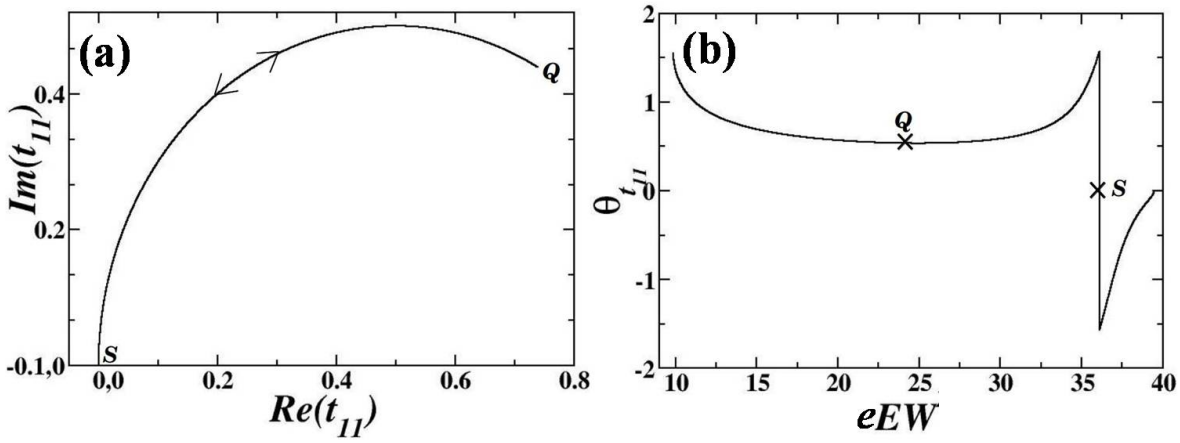

Figure 5.5 (a) Argand diagram for transmission amplitude and (b) plot of transmission phase shift $\theta_{t_{11}}$ versus EW, for scattering by a delta function potential in a single channel quantum wire. Here $e\gamma W = -1.5$, $y_i = 0.21W, e = 1, W = 1$ and we have considered 500 evanescent modes.

The direction of propagation is shown by arrows. The scattering potential shown by cross mark is given by,

$$V(x,y) = \gamma\delta(x)\delta(y-y_i)$$

Here γ is the strength of the delta function potential. The asymptotic wave function in different regions are shown in Fig. 5.4. One can solve the scattering problem [77] to find,

$$r_{11} = -\frac{i\frac{\Gamma_{11}}{2k_1}}{1+\sum_{n\geq 2}\frac{\Gamma_{nn}}{2\kappa_n}+i\frac{\Gamma_{11}}{2k_1}} \tag{5.9}$$

$$t_{11} = \frac{1+\sum_{n\geq 2}\frac{\Gamma_{nn}}{2\kappa_n}}{1+\sum_{n\geq 2}\frac{\Gamma_{nn}}{2\kappa_e}+i\frac{\Gamma_{11}}{2k_1}} \tag{5.10}$$

Here r_{11} and t_{11} are the reflection and transmission amplitudes and Γ_{nm} is given by,

$$\Gamma_{nm} = \gamma sin\left[\frac{n\pi}{W}\left(y_i+\frac{W}{2}\right)\right] sin\left[\frac{m\pi}{W}\left(y_i+\frac{W}{2}\right)\right] \tag{5.11}$$

where, m and n are integers. $k_1 = \sqrt{\frac{2m_e}{\hbar^2}E - \frac{\pi^2}{W^2}}$ is the wave vector for the propagating channel, $\sum_n$ denotes sum over evanescent modes, $\kappa_n = \sqrt{\frac{n^2\pi^2}{W^2} - \frac{2m_e}{\hbar^2}E}$ where n takes values $2,3,...\infty$ and E is the incident Fermi energy. Transmission phase shift is given by, $\theta_{t_{11}} = Arctan\frac{Im(t_{11})}{Re(t_{11})}$.

The Argand diagram for transmission amplitude t_{11} is shown in Fig. 5.5(a). There is a phase singularity at the origin where, $t_{11} = 0$ (shown by the point S). Fig. 5.5(b) shows transmission phase

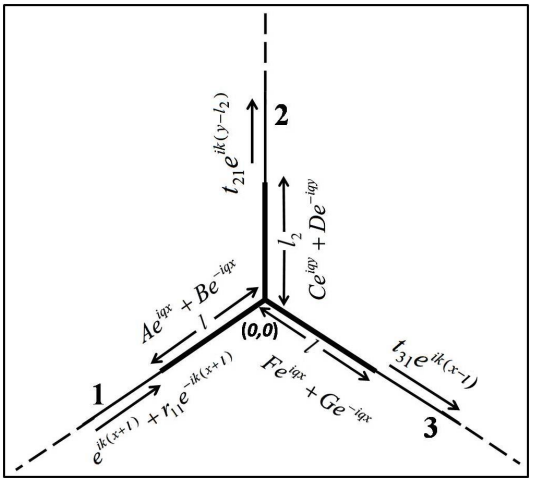

Figure 5.6 Schematic representation of scattering of electrons by a three prong potential. The direction of incident and scattered electrons are shown by arrow heads. The potential is non-zero along the bold lines of lengths l, l_2 and l along $-x, +y$ and $+x$ axes, respectively.

shift $\theta_{t_{11}}$ as a function of energy, for the same parameters as in Fig. 5.5(a). In Fig. 5.5(a), the trajectory (shown by thick solid line) starts from the origin (point marked S) goes upto point Q, and traces back the same path to pass the origin making SQS a closed contour. The direction of the trajectory is therefore shown by a double headed arrow. At the energy, where the trajectory goes from Q to S and touches the point of phase singularity at origin, i.e. point S, we expect a discontinuous phase drop of π, following the same argument as in the case of the stub. This phase drop can be seen in Fig. 5.5(b), where the points Q and S are also marked at their respective energies. Thus the discontinuous phase drop is a natural consequence of Eq. (5.2).

5.3.4 Three prong potential

We now consider another potential called the three prong potential [90]. This potential will help us to demonstrate other non-trivial aspects that follow from Eq. (5.2). A schematic representation of the three prong potential is shown in Fig. 5.6. The thin lines represent one dimensional quantum wires with potential $V = 0$, and the bold lines represent quantum wires with non zero potential, i.e., $V \neq 0$. The arms of the prong are labelled as 1, 2 and 3 as shown in Fig. 5.6. The electrons are considered to be incident from left, the direction of incidence being shown by arrows. The wave function in the different regions are given by,

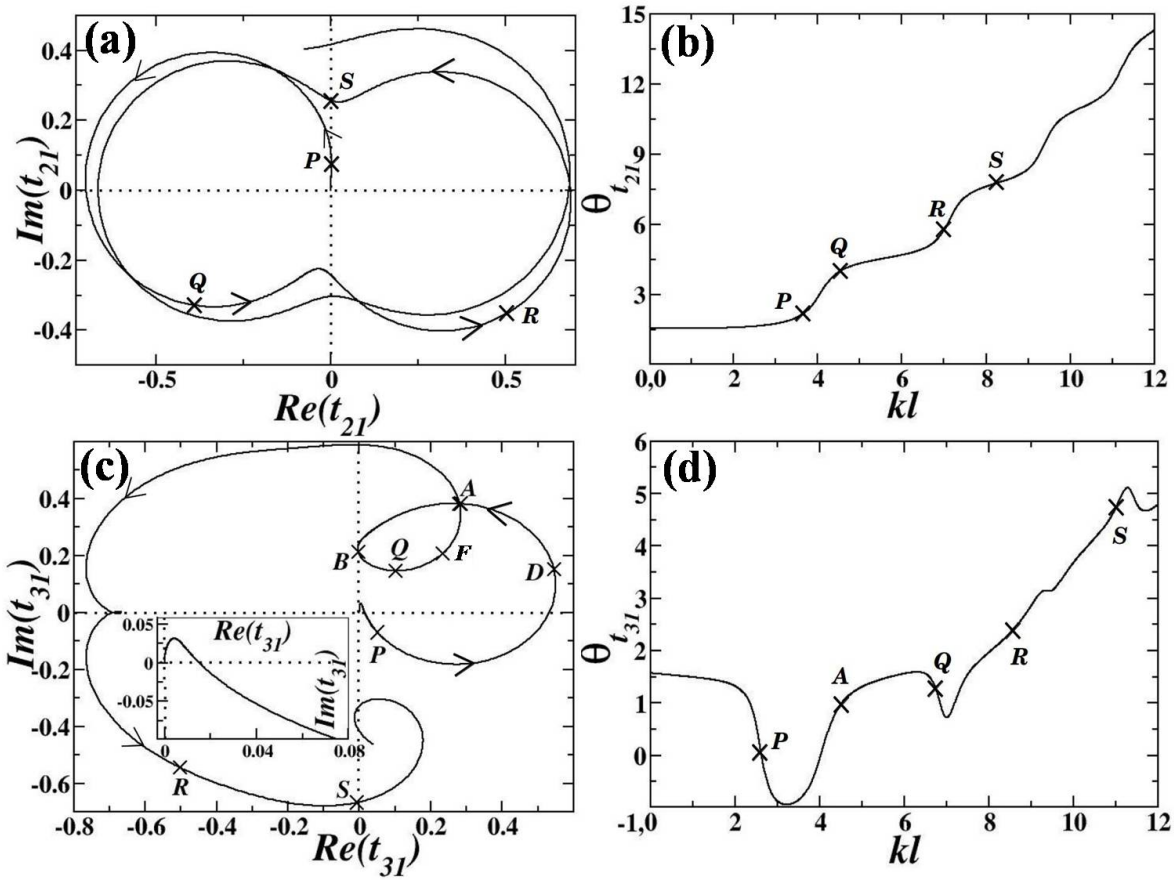

Figure 5.7 (a) Argand diagram for transmission amplitude t_{21} and (b) plot of scattering phase shift $\theta_{t_{21}}$ as a function of kl varying the wave vector from 0 to 12. (c) Argand diagram for transmission amplitude t_{31} and (d) plot of scattering phase shift $\theta_{t_{31}}$ as a function of kl varying the wave vector from 0 to 12. For all the figures, $l = 1$, $l_2 = 5l$, $e = 1$ and $eVl = -1000$.

$$\psi(x,y,z) = \begin{cases} e^{ik(x+l)} + r_{11}e^{-ik(x+l)}, for\ x < -l, \\ Ae^{iqx} + Be^{-iqx}, for\ -l < x < 0, \\ Ce^{iqy} + De^{-iqy}, for\ 0 < y < l_2, \\ Fe^{iqx} + Ge^{-iqx}, for\ 0 < x < l, \\ t_{21}e^{ik(y-l_2)}, for\ y > l_2, \\ t_{31}e^{ik(x-l)}, for\ x > l. \end{cases}$$

where $k = \sqrt{\frac{2m_e}{\hbar^2}E}$ is the wave vector along the thin lines, $q = \sqrt{\frac{2m_e}{\hbar^2}(E-V)}$ is the wave vector along the bold lines and E is the Fermi energy. Here r_{11} is the reflection amplitude for electrons incident from 1 and reflected back to 1, t_{21} is the transmission amplitude for electrons incident from 1 and transmitted to 2 and t_{31} is the transmission amplitude for electrons incident from 1 and transmitted to 3. These scattering matrix elements can be solved using Griffiths boundary conditions [101–104]. The respective transmission phase shifts are given by, $\theta_{r_{11}} = Arctan\frac{Im(r_{11})}{Re(r_{11})}$, $\theta_{t_{21}} = Arctan\frac{Im(t_{21})}{Re(t_{21})}$ and $\theta_{t_{31}} = Arctan\frac{Im(t_{31})}{Re(t_{31})}$.

Fig. 5.7(a) shows the Argand diagram for transmission amplitude t_{21}. There is a phase singularity at the origin, where $t_{21} = 0$. In Fig. 5.7(a) the trajectory of Argand diagram for t_{21} starts from the origin, goes through P and then through Q, R and S following counter-clockwise direction shown by arrows. The trajectory is concave throughout and Eq. (5.2) implies monotonously increasing phase. This monotonously increasing phase can be seen in Fig. 5.7(b), where scattering phase shift $\theta_{t_{21}}$ is plotted as a function of kl and here also the points P, Q, R and S are marked at the corresponding values of kl.

The Argand diagram for t_{31} shows something interesting. This Argand diagram is shown in Fig. 5.7(c). There is a phase singularity at the origin, where $t_{31} = 0$. In Fig. 5.7(c), the trajectory of Argand diagram for t_{31} starts from origin, goes through P and then through D, A, B, Q, F, R and S, following counter-clockwise direction shown by arrows. Here interestingly, the trajectory develops a sub-loop $ABQFA$. This sub-loop results in a convex arc BQF in the trajectory that does not go through the origin. There will be a gradual phase drop whenever such a convex arc is observed, following Eq. (5.2). This can be seen in Fig. 5.7(d), where scattering phase shift $\theta_{t_{31}}$ is plotted as a function of kl and here also the points P, A, Q, R and S are marked. Presence or absence of such a sub-loop has no consequence on the line integral of phase along $PDABQFRS$. This is because the contribution to the line integral coming from the sub-loop $ABQFA$ is 0 and its presence or absence has no bearing on the value of I. So, such a sub-loop as $ABQFA$ in Fig. 5.7(c) can appear or disappear as some parameter is varied as will be demonstrated in the next section.

5.4 Injectance and Friedel sum rule

Local partial density of states (LPDOS) is defined as [53, 61, 97, 98]

$$\rho'(\alpha,\mathbf{r},\beta) = -\frac{1}{4\pi i}\left(s^{\dagger}_{\alpha\beta}\frac{\delta s_{\alpha\beta}}{\delta V(\mathbf{r})} - s_{\alpha\beta}\frac{\delta s^{\dagger}_{\alpha\beta}}{\delta V(\mathbf{r})}\right) \tag{5.12}$$

Here, $s_{\alpha\beta} =\mid s_{\alpha\beta} \mid e^{i\theta_{s_{\alpha\beta}}}$ is the scattering matrix element for electrons incident from channel β and transmitted to channel α and $\frac{\delta}{\delta V(\mathbf{r})}$ stands for a functional derivative with respect to the local potential $V(\mathbf{r})$. Time spent at $\mathbf{r}$ by an electron going from channel β to α is given by [53]

$$\tau'(\alpha,\mathbf{r},\beta) = \frac{h}{|s_{\alpha\beta}|^2}\rho'(\alpha,\mathbf{r},\beta)$$

Therefore, time spent by an electron going from channel β to α, within the scattering region is given by [53]

$$\tau(\alpha,\beta) = \frac{h}{|s_{\alpha\beta}|^2}\int_{Screg} d\mathbf{r}^3\rho'(\alpha,\mathbf{r},\beta) \tag{5.13}$$

where, 'Screg' stands for scattering region. For a mesoscopic sample coupled to leads, this scattering region is by definition the sample [53]. So, partial density of states (PDOS) of a mesoscopic sample is defined as [53]

$$\rho(\alpha,\beta) = -\frac{1}{4\pi i}\int_{sample} d\mathbf{r}^3\left(s^{\dagger}_{\alpha\beta}\frac{\delta s_{\alpha\beta}}{\delta V(\mathbf{r})} - s_{\alpha\beta}\frac{\delta s^{\dagger}_{\alpha\beta}}{\delta V(\mathbf{r})}\right) \tag{5.14}$$

$$= -\frac{1}{2\pi}\int_{sample} d\mathbf{r}^3\left(|s_{\alpha\beta}|^2\frac{\delta\theta_{s_{\alpha\beta}}}{\delta V(\mathbf{r})}\right) \tag{5.15}$$

PDOS are quite physical and manifests in a variety of experimental situations in mesoscopic systems [53, 97, 98]. For example, decoherence in the scattering region is proportional to the time electrons spend in the scattering region. As another example, consider a sinusoidal voltage of frequency ω, $V_\beta(\omega)$ applied at incident lead β. The current measured at lead α will be [53],

$$I_\alpha(\omega) = G_{\alpha\beta}(\omega)V_\beta(\omega) \tag{5.16}$$

where, $G_{\alpha\beta}(\omega)$ is the dynamical conductance matrix and is given by [53],

$$G_{\alpha\beta}(\omega) = G^0_{\alpha\beta} - i\omega E_{\alpha\beta} + K_{\alpha\beta}\omega^2 + O(\omega^3) \tag{5.17}$$

$G^0_{\alpha\beta}$ is the dc-conductance matrix. $E_{\alpha\beta}$ is proportional to ω and governs the displacement currents and is given by [53],

$$E_{\alpha\beta} = e^2\rho(\alpha,\beta) - e^2\int d\mathbf{r}'\rho(\alpha,\mathbf{r}')\int d\mathbf{r}g(\mathbf{r},\mathbf{r}')\rho(\mathbf{r},\beta) \tag{5.18}$$

where, $g(\mathbf{r},\mathbf{r}')$ is the effective interaction potential.

The integration over $\mathbf{r}$ in Eq. (5.14) can easily be done for a global change (for all $\mathbf{r}$ in the sample as well as in the leads) in $V(\mathbf{r})$ by a constant amount ε, i.e. $\delta V(\mathbf{r}) = \varepsilon$ for all $\mathbf{r}$. Such a constant global increase in potential is equivalent to decrease in incident energy E, i.e.,

$$\int_{global} d\mathbf{r}^3 \frac{\delta}{\delta V(\mathbf{r})} \equiv -\frac{d}{dE} \tag{5.19}$$

and, therefore,

$$\int_{sample} d\mathbf{r}^3 \frac{\delta}{\delta V(\mathbf{r})} \cong -\frac{d}{dE} \tag{5.20}$$

is expected to work in the semi-classical limit [61]. So, from Eq. (5.14)

$$\begin{aligned}
\rho(\alpha,\beta) &= -\frac{1}{4\pi i}\int_{sample} d\mathbf{r}^3 \left(s^\dagger_{\alpha\beta}\frac{\delta s_{\alpha\beta}}{\delta V(\mathbf{r})} - s_{\alpha\beta}\frac{\delta s^\dagger_{\alpha\beta}}{\delta V(\mathbf{r})}\right) \\
&\approx -\frac{1}{4\pi i}\int_{global} d\mathbf{r}^3 \left(s^\dagger_{\alpha\beta}\frac{\delta s_{\alpha\beta}}{\delta V(\mathbf{r})} - s_{\alpha\beta}\frac{\delta s^\dagger_{\alpha\beta}}{\delta V(\mathbf{r})}\right) \\
\text{or, } \rho(\alpha,\beta) &\approx \frac{1}{4\pi i}\left(s^\dagger_{\alpha\beta}\frac{ds_{\alpha\beta}}{dE} - s_{\alpha\beta}\frac{ds^\dagger_{\alpha\beta}}{dE}\right) \qquad \text{(Using Eq. (5.19))}
\end{aligned}$$

On simplifying we get,

$$\rho(\alpha,\beta) \approx \frac{1}{2\pi}\left(|s_{\alpha\beta}|^2\frac{d\theta_{s_{\alpha\beta}}}{dE}\right) \tag{5.21}$$

It is known that $\frac{d\theta_{s_{\alpha\beta}}}{dE}$ can be negative. Eq. (5.21) is an approximate equality, which implies if R.H.S is negative, the L.H.S is not necessarily negative. In spite of the approximate equality in Eq. (5.21), PDOS $\rho(\alpha,\beta)$ too can be in principle negative as can be demonstrated from Eq. (5.14) for some strictly 1D simple potentials in very low energy regime. 1D potentials are an idealization and not physical and neither one can go to the necessary low energy regime in an experiment. The problem was theoretically studied in two different ways strictly in 1D. One is negative PDOS and the other

is negative time scales. Measured time scales did not lead to any unique physical understanding and a review on the topic can be seen in ref. [108]. Ref. [108] did conclude that $\rho(\alpha,\beta)$ or $\tau(\alpha,\beta)$ are physical and later on found to be so [53]. But regimes where they become negative has not received any attention beyond 1D. In other words negative $\rho(\alpha,\beta)$ has not yet been shown for any physical system. Negative slopes in scattering phase shift in mesoscopic systems has recently gained prominence. First they were observed to lead to breakdown of parity effect [86] and then they were also measured [47–49]. Experiments [47–49] inspired many theoretical papers that study negative slopes in scattering phase shift in mesoscopic systems [50, 70–72, 87, 88]. In section 5.3, we have explained these negative slopes in scattering phase shift of mesoscopic systems (sometimes discontinuous and sometimes gradual) using Argand diagram. It has been emphasised that these negative slopes are a consequence of the topology of the Argand diagram contour. Hence, these negative slopes do not depend on the details of the scattering potential but are manifestation of the fact that the Argand diagram has a few limited options. Any realistic potential in Q1D can show negative slopes. The scattering potentials considered in refs. [89, 99] are realistic multichannel scattering problems.

PDOS as defined in Eq. (5.14) can be negative without violating any physical principle, because they add up to give the correct DOS [53]. One can sum the PDOS (given by Eq. 5.14) over α to get injectance [53, 61, 99] of lead β,

$$\rho(\beta) = -\frac{1}{4\pi i}\sum_{\alpha}\int_{sample} d\mathbf{r}^3 \left(s^{\dagger}_{\alpha\beta}\frac{\delta s_{\alpha\beta}}{\delta V(\mathbf{r})} - s_{\alpha\beta}\frac{\delta s^{\dagger}_{\alpha\beta}}{\delta V(\mathbf{r})} \right) \tag{5.22}$$

This is a measure of current delivered by the electrons incident along lead β and outgoing through all possible leads. Similarly injectance can be defined for all possible leads and they are completely independent of each other. For example, the scattering problem depicted in Fig. 5.6 can define $\rho(1)$. To get $\rho(2)$ one has to solve a completely different scattering problem where the incident particle is from lead 2. Using Eq. (5.20) we get for the semi-classical limit of Eq. (5.22),

$$\rho(\beta) \approx \frac{1}{4\pi i}\sum_{\alpha}\left(s^{\dagger}_{\alpha\beta}\frac{ds_{\alpha\beta}}{dE} - s_{\alpha\beta}\frac{ds^{\dagger}_{\alpha\beta}}{dE} \right) \tag{5.23}$$

Summing $\rho(\beta)$ over the β independent channels, we can obtain density of states (DOS) $\rho(E)$, i.e., from Eq. (5.22),

$$\rho(E) = -\frac{1}{4\pi i}\sum_{\alpha\beta}\int_{sample} d\mathbf{r}^3 \left(s^{\dagger}_{\alpha\beta}\frac{\delta s_{\alpha\beta}}{\delta V(\mathbf{r})} - s_{\alpha\beta}\frac{\delta s^{\dagger}_{\alpha\beta}}{\delta V(\mathbf{r})} \right) \tag{5.24}$$

and in the semi-classical limit given by Eq. (5.20), we get,

$$\rho(E) \approx \frac{1}{4\pi i} \sum_{\alpha\beta} \left(s^{\dagger}_{\alpha\beta} \frac{ds_{\alpha\beta}}{dE} - s_{\alpha\beta} \frac{ds^{\dagger}_{\alpha\beta}}{dE} \right) \tag{5.25}$$

Further simplification of Eq. (5.25) gives

$$\pi\rho(E) \approx \frac{d}{dE}\theta_f(E) \tag{5.26}$$

This is Friedel sum rule (FSR), where $\theta_f(E) = \frac{1}{2i}\frac{d}{dE} log(det[S])$ is the Friedel phase, S is the scattering matrix and $\rho(E) = \frac{dN(E)}{dE}$ is density of states. Since injectance of all leads are independent while they add up to give FSR, it is important to understand injectance in order to understand FSR.

The potentials in sections 5.3.2, 5.3.3 and 5.3.4 are typical examples of mesoscopic systems, and as reported in ref. [72,89,90], FSR (or injectance) manifests in these systems, in different ways. Semi-classical regime being expressed by Eq. (5.20) is not sufficient. Sometimes, FSR (or injectance) is exact at all energies (for example the stub [72]) and sometimes it is exact at an energy where quantum fluctuations dominate [89]. There is a huge amount of system to system variation. It has been proved very generally that when the phase drops of π are discontinuous like the solid curve in Fig. 5.3(c), then at the energy corresponding to this drop injectance will become exact [89]. But when the phase drops are gradual like the dashed curve in Fig. 5.3(c), this has not been proved in general but shown for particular cases [89, 99]. The potentials considered in refs. [89, 99] are also realistic multichannel scattering problem.

In this section we will prove that negative $\frac{d\theta_{s_{\alpha\beta}}}{dE}$ in mesoscopic systems definitely signify negative PDOS. Also we will show that when there are such negative slopes in scattering phase shift of mesoscopic systems then semi-classical FSR can become exact in a quantum regime. Once again our proof will depend on Argand diagram and Eq. (5.2) and as our proof will be general and not depend on the specific properties of the scattering potential.

Let us first make the connection between Eq. (5.2) and injectance. When S matrix is 2×2 (for example, the cases of double delta function potential (Fig. 5.2(a)), stub (Fig. 5.3(a)), single channel quantum wire (Fig. 5.4)), Eq. (5.26) simplifies to,

$$\frac{d}{dE}\theta_t(E) \approx \pi\rho(E) \tag{5.27}$$

Here t is the transmission amplitude and $\theta_t = Arctan\frac{Im(t)}{Re(t)}$. Suppose when the energy is varied from 0 to E_1, then the Argand diagram for a typical scattering matrix element t traces a closed contour C. For such a case,

$$\oint_C d\theta_t = 2\pi N(E_1) \tag{5.28}$$

where, $N(E_1)$ is number of states (obtained by integrating DOS $\rho(E)$ from 0 to E_1) below energy E_1. Thus in a scattering problem, Eq. (5.28) is equivalent to Eq. (5.2). Comparing with Eq. (5.2) we see $\phi \equiv \theta_t$ and $S \equiv N(E_1)$. If C happens to be a completely closed contour, Eq. (5.28) is exact as it is equivalent to Eq. (5.2). Any complex function or its phase has to satisfy Eq. (5.2) and a scattering matrix element is no exception provided it is analytic. However, in most cases of scattering problems, C is not completely closed. In Fig. 5.2(b), there is a phase singularity at the origin and the contour enclosing the singularity is not closed in the first Riemann surface. One can restrict the discussion to the first Riemann surface to understand the injectance. When the contour continue to the second Riemann surface, then the contour integral starts including contribution from the second phase singularity in the second Riemann surface. And then one has to extend the discussions here to include the effect of the second singularity. This does not change the arguments given here except that sometimes the error from the first Riemann surface can cancel the error from the second Riemann surface which need not be a systematic behaviour. The contour C in Fig. 5.2(b) starts from origin with zero energy and ends in the first Riemann surface at point marked as S, where the energy is E_1 (say). It is now known that (see Eq. (6) in ref. [70, 71]),

$$\int_{C'} d\theta_t \;=\; \int_0^{E_1} \left[\pi\frac{dN(E)}{dE} - ImTr\left(G^a\frac{\partial F^a}{\partial E}\right)\right] dE \tag{5.29}$$

We will replace C by C', when the contour is not completely closed. G^a is the advanced Greens function and F^a is self energy due to coupling the system with the leads. One can then assume that $\int_0^{E_1} ImTr\left(G^a\frac{\partial F^a}{\partial E}\right) dE$ is the correction term to Eq. (5.28) arising because contour C' is not closed. This assumption can be justified because, when the self energy is energy independent, then the contour C is closed as well as the correction term is zero implying Eq. (5.29) becomes Eq. (5.28). For a double delta function potential in one dimension the correction term is very important to consider. There, energy dependence of self energy can be seen very easily in the broadening of consecutive resonance peaks (shown in Fig. 5.2(d)).

In case of the solid line in Fig. 5.3(b), the potential everywhere is real and is 0. It traces a closed contour in the first Riemann surface. Thus for this system Eq. (5.28) will become exact. Explicit calculations of density of states [72] for the stub show this and so everything is consistent with Eq. (5.2). However, for scattering by a delta function potential (Fig. 5.4) in a single channel quantum wire we get a counter intuitive result. In this case, the contour of the Argand diagram (shown in Fig. 5.5(a)) is closed in a special way and so we expect Eq. (5.28) to be exact. But explicit calculations of density of states [89] show, that is not the case. It has been shown earlier that for this system the fundamental theorem of Büttiker-Thomas-Pretre (BTP) also breaks down [109] due to the non-analyticity of scattering matrix elements. This is a consequence of the fact that delta function potential in Q1D incorporates a log divergence in scattering matrix elements. Hence this is a situation where Eq. (5.2) cannot be applied.

For the three prong potential, shown in Fig. 5.6, the scattering matrix is 3×3 and the correct form of FSR is given by Eq. (5.26). Whenever the scattering matrix has a rank greater than 2, the connection between FSR in Eq. (5.26) and Eq. (5.2) is not straight forward. However, we can make this connection for each partial density of states (PDOS) and is shown below. Let us consider the Argand diagrams for the three prong potential shown in Figs. 5.7(a) and 5.7(c). None of the Argand diagrams (e.g. Figs. 5.7(a), 5.7(c)) are closed in the first Riemann surface. Let us, for example, consider the Argand diagram for t_{31} tracing a contour C' (*PDABQFARS* shown in Fig. 5.7(c)) as energy is varied from 0 to E_1. We can show that (see Appendix D.1),

$$\int_{C'} d\theta_{t_{31}} \approx 2\pi \int_0^{E_1} \frac{\rho(3,1)(E)}{|t_{31}|^2} dE \tag{5.30}$$

Now we can safely assume that for any closed curve like *ABQFA* in Fig. 5.7(c), Eq. (5.30) is exact. That is,

$$\oint_{ABQFA} d\theta_{t_{31}} = 2\pi \oint_{ABQFA} \frac{\rho(3,1)(E)}{|t_{31}|^2} dE \tag{5.31}$$

This assumption can be justified as follows. For a closed contour, L.H.S of Eq. (5.31) is zero. Also for a closed contour R.H.S of Eq. (5.31) will be zero as justified in Appendix D.2. Hence from Eq. (5.14) it follows that R.H.S of Eq. (5.31) is also zero. Now,

$$\oint_{ABQFA} d\theta_{t_{31}} = \oint_{ABQFA} \frac{d\theta_{t_{31}}}{dE} dE = 0 \tag{5.32}$$

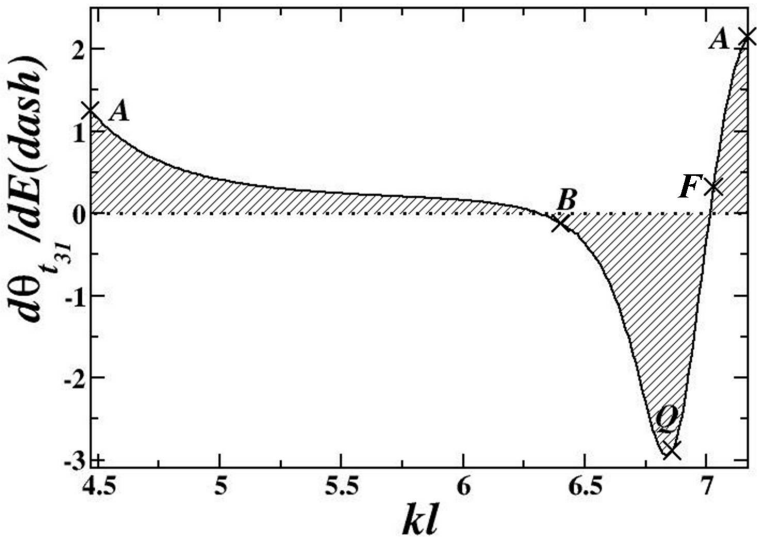

Figure 5.8 $\frac{d\theta_{t_{31}}}{dE}$ as a function of kl for the three prong potential. Here $l = 1$, $l_2 = 5l$, $e = 1$ and $eVl = -1000$.

In Fig. 5.8, $\frac{d\theta_{t_{31}}}{dE}$ is shown in the energy range covering the sub-loop *ABQFA* of Fig. 5.7(c). As is implied by Eq. (5.32), $\frac{d\theta_{t_{31}}}{dE}$ is somewhere positive and somewhere negative to ensure the area under the curve (shaded region in Fig. 5.8) is zero. Similarly the R.H.S of Eq. (5.31) is zero implies that $\frac{\rho(3,1)(E)}{|t_{31}|^2}$, will also be positive as well as negative in certain energy values (or kl values). Thus $\rho(3,1)$ is conclusively negative in some energy values.

We will now show how negative slopes in mesoscopic systems are fundamentally different from that studied earlier [108] in 1D. Note the negative slope at point P in Fig. 5.7(d). This kind of negative slope at very low energies can arise for scattering in 1D and one can easily check this for a square well potential. In terms of our analysis we understand the negative slope at point P in Fig. 5.7(d) due to a convex trajectory at P in Fig. 5.7(c) which is originating due to the fact that the Argand diagram starts from the origin and behaves anomalously as the trajectory starting from the origin is neither clockwise nor anti-clockwise with respect to the singular point (i.e. origin). See the expanded Argand diagram trajectory shown in the inset of Fig. 5.7(c). The trajectory moves up, turns around and moves down to become convex in a small energy window and then winds around the origin anti-clockwise. Although $\frac{d\theta_{t_{31}}}{dE}$ is negative at P in Fig. 5.7(d), there is no conclusive evidence that PDOS $\rho(3,1)$ is negative at energy corresponding to point P. Such a negative slope is fundamentally different from the negative slope at Q in Fig. 5.7(d) that originate from a closed sub-loop *ABQFA* in

Fig. 5.7(c), that we encounter only in Q1D and mesoscopic scattering. We have shown that the sub-loop seen in Fig. 5.7(c) implies the presence of this negative slope in scattering phase shift $\theta_{t_{31}}$ and also implies PDOS $\rho(3,1)$ is negative. We have shown that an Argand diagram for such a scattering matrix element curls around and forms a sub-loop without violating the topological constraints of Eq. (5.2). The line integration along the sub-loop *ABQFA* in Fig. 5.7(c) does not contribute to the line integration over the trajectory *PDABQFARS* of Fig. 5.7(c) or I in Eq. (5.2) is unaffected by the presence or absence of a sub-loop in the closed contour C. Negative slopes of this second type (i.e. observed at Q in Fig. 5.7(d)) that we have discussed here in-fact can appear or disappear very easily and can be found at much higher energies. In Fig. 5.9, we have shown the Argand diagram for t_{31} upto very high value of energy (or, kl). We can see many sub-loops which again implies the presence of negative slopes in scattering phase shift and negative PDOS. Sometimes there is a cusp in the Argand diagram and such a cusp means a sub-loop has disappeared [94]. Thus the phase drop will also disappear as we go to such energies. Disappearance of a sub-loop can be demonstrated by varying any other parameter like V, l, l_2 of the three prong geometry.

$\rho(3,1)$ being negative is a counter intuitive feature of quantum mechanics and can have interesting physical significance. Obviously, ac-response of a mesoscopic system will change drastically if $\rho(\alpha,\beta)$ in Eq. (5.18) changes sign. Also, it means an electron that is incident along lead 1 and transmitted to lead 3, dwells in some negative number of states (PDOS is negative) inside the scatterer. Total charge being electronic charge times number of states will be positive for these negatively charged electrons. So other electrons that are incident along lead 1 and transmitted to lead 2 or reflected back to lead 1 will be attracted by this positively behaving charge of electrons going from 1 to 3. This could be the explanation for the electron-electron attraction observed in the numerical experiment of ref. [110], where no explanation could be given. In the next section we will argue that this could have been also observed in an experiment.

Now let us try to understand if there is a connection between negative slope and injectance becoming exact as observed in some earlier works [99]. Eq. (5.31) holds for the integrals and does not imply equality of the integrands. However, using Eq. (5.21) we can write

$$\rho(3,1) \approx \frac{1}{2\pi}|t_{31}|^2\frac{d\theta_{t_{31}}}{dE} \tag{5.33}$$

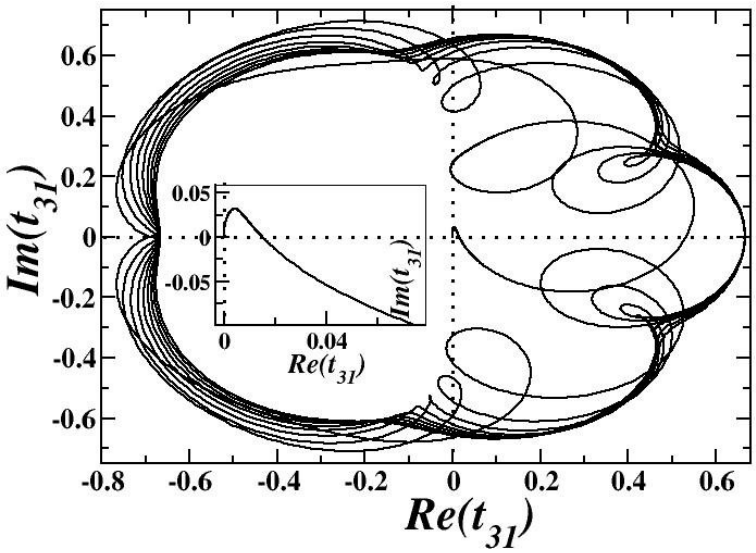

Figure 5.9 Argand diagram for transmission amplitude t_{31}, varying kl from 0 to 50, for the three prong potential. Here $l = 1$, $l_2 = 5l$, $e = 1$ and $eVl = -1000$.

$$\rho(2,1) \approx \frac{1}{2\pi}|t_{21}|^2\frac{d\theta_{t_{21}}}{dE} \tag{5.34}$$

$$\rho(1,1) \approx \frac{1}{2\pi}|r_{11}|^2\frac{d\theta_{r_{11}}}{dE} \tag{5.35}$$

Finally using Eqs. (5.33), (5.34) and (5.35), we can write

$$\rho(1,1)+\rho(2,1)+\rho(3,1) \approx \frac{1}{2\pi}|r_{11}|^2\frac{d\theta_{r_{11}}}{dE}+\frac{1}{2\pi}|t_{21}|^2\frac{d\theta_{t_{21}}}{dE}+\frac{1}{2\pi}|t_{31}|^2\frac{d\theta_{t_{31}}}{dE} \tag{5.36}$$

L.H.S of Eq. (5.36), i.e., $\sum_\alpha \rho(\alpha,\beta)$ is well known as injectance as defined in Eq. (5.22). The R.H.S of Eq. (5.36) is the semi-classical limit of injectance. The topological interpretation of Eqs. (5.33), (5.34), (5.35) in terms of Argand diagrams leading to Eq. (5.36) is very useful. The correction term to Eq. (5.36) is known [99] i.e.,

$$\rho(1,1)+\rho(2,1)+\rho(3,1) = \frac{1}{2\pi}\left[|r_{11}|^2\frac{d\theta_{r_{11}}}{dE}+|t_{21}|^2\frac{d\theta_{t_{21}}}{dE}+|t_{31}|^2\frac{d\theta_{t_{31}}}{dE}+\frac{m^*|r_{11}|}{\hbar k^2}sin(\theta_{r_{11}})\right] \tag{5.37}$$

Let us say that,

$$\rho(1)^e = \rho(1,1)+\rho(2,1)+\rho(3,1) \tag{5.38}$$

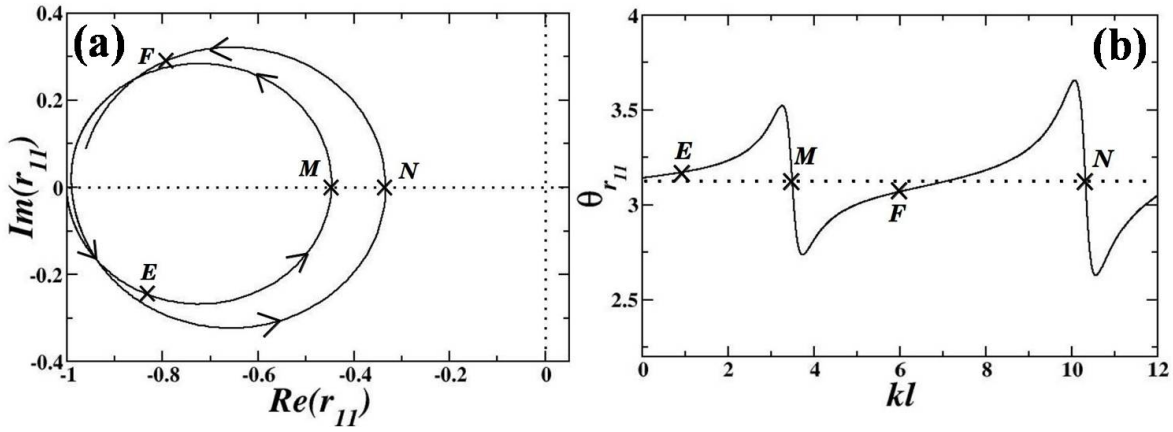

Figure 5.10 (a) Argand diagram for reflection amplitude r_{11} and (b) plot of reflection phase shift $\theta_{r_{11}}$, versus kl for the three prong potential. Here $l = 1$, $l_2 = 5l$, $e = 1$ and $eVl = -10000$.

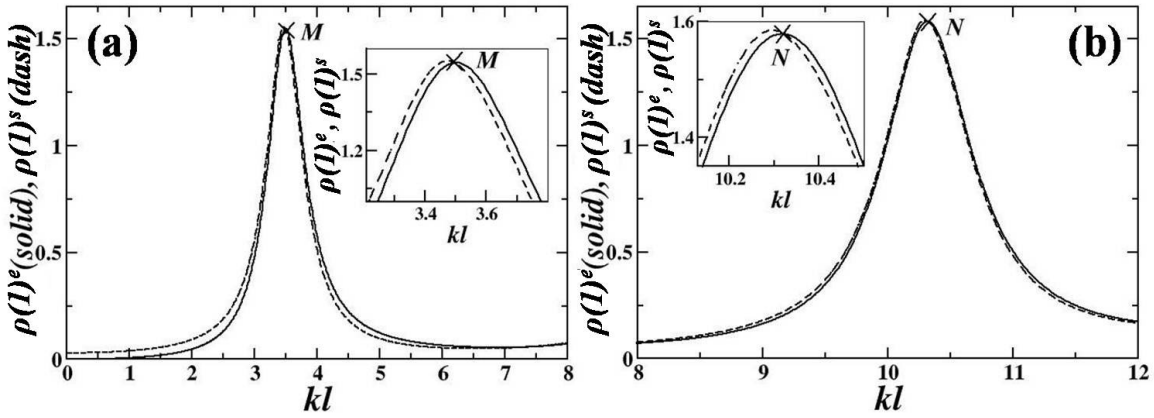

Figure 5.11 Plot of exact injectance $\rho(1)^e$ (solid line) and semi-classical injectance $\rho(1)^s$ (dashed line) as a function of kl for the three prong potential. The peaks in the injectance are shown separately, (a) shows the first peak, (b) shows the second peak, for the same parameters as in Fig. 5.10. The insets show the magnified curves at points M and N.

is exact injectance, defined in Eq. (5.22). And,

$$\rho(1)^s = \frac{1}{2\pi}\left[|r_{11}|^2\frac{d\theta_{r_{11}}}{dE} + |t_{21}|^2\frac{d\theta_{t_{21}}}{dE} + |t_{31}|^2\frac{d\theta_{t_{31}}}{dE}\right] \tag{5.39}$$

is generally referred to as semi-classical injectance. Eq. (5.37) implies that $\rho(1)^e$ and $\rho(1)^s$ will be equal at energies, where the correction term is zero or $|r_{11}|sin(\theta_{r_{11}}) = 0$. According to the arguments of Leavens and Aers [74], in the semi-classical limit $|r_{11}| \longrightarrow 0$ and $\rho(1)^s = \rho(1)^e$. But in all the cases of studies on injectance or FSR in mesoscopic systems [89, 99], $|r_{11}| \neq 0$ at the energy where $\rho(1)^s = \rho(1)^e$, but not very consistently as already discussed in the paragraph after Eq. (5.26). We

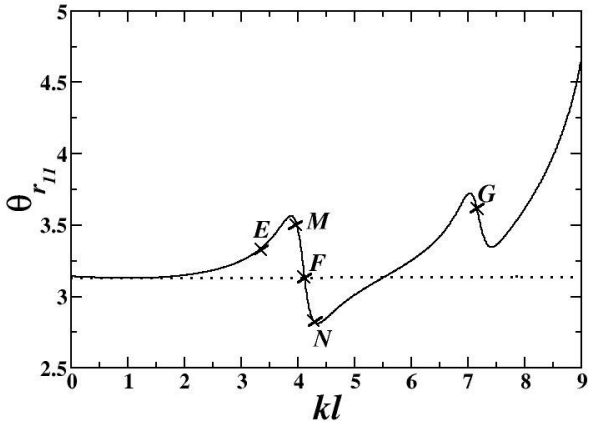

Figure 5.12 Plot of reflection phase shift $\theta_{r_{11}}$ versus kl for the three prong potential. Here $l = 1$, $l_2 = 5l$, $e = 1$ and $eVl = -1000$.

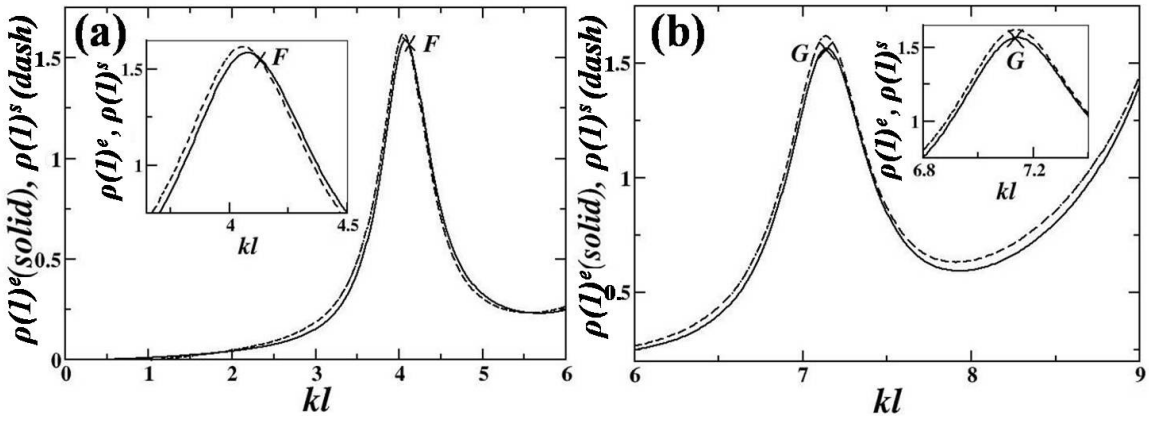

Figure 5.13 Plot of exact injectance $\rho(1)^e$ (solid line) and semi-classical injectance $\rho(1)^s$ (dashed line) as a function of kl for the three prong potential. The peaks in the injectance are shown separately, (a) shows the first peak, (b) shows the second peak, for the same parameters as in Fig. 5.12. The insets show the magnified curves at points F and G.

will show how the Argand diagram is responsible for this behaviour and therefore provides a general understanding. In Figs. 5.10(a) and 5.10(b), we have shown the Argand diagram and phase shift for scattering matrix element r_{11}, respectively. kl is varied from 0 to 12 in both the plots. The Argand diagram in Fig. 5.10(a) is restricted to one side of the phase singularity (i.e. origin) and in the first Riemann surface resulting in sub-loops. This will naturally mean that, the contour has both concave and convex parts in the trajectory. Scattering phase shift in Fig. 5.10(b) increases with kl, reaches a peak value and then drops to become π at M. The pattern repeats as kl increases and the scattering phase shift becomes π again at N. Therefore the correction term $|r_{11}|sin(\theta_{r_{11}})$ to semi-

classical injectance (Eq. (5.37)) is zero at M and N. Thus at M and N, the semi classical injectance (Eq. (5.39)) is exact. The exactness of semi-classical injectance is shown in Fig. 5.11 (for clarity see the inset) at points M and N corresponding to same kl values as in Fig. 5.10. For monotonously increasing phase, Argand diagram extends to higher Riemann surfaces and line integrals include the effect of other singularities in higher Riemann surface. Of course phase can be integral multiples of π (i.e., $2\pi, 3\pi, ..$), but for open Argand diagram trajectories as argued before, this is not a consistent behaviour, except in some simple one dimensional scattering problems. This inconsistent behaviour can be for example, checked for an one dimensional Aharanov-Bohm ring with different arm lengths. Drops in $\theta_{r_{11}}$ resulting in $\theta_{r_{11}}$ being π and $sin(\theta_{r_{11}}) = 0$, leading to semi classical injectance being exact can be understood from the Argand diagram in a single Riemann surface, involving a single phase singularity in the line integral and hence is not an accident. Drops in $\theta_{r_{11}}$ is a pure quantum mechanical behaviour and hence exactness of semi classical injectance at the energies corresponding to the phase drops, is counter-intuitive. As argued before, these drops coming from sub-loops in Argand diagram are tunable and can be removed by varying some parameter. In Fig. 5.12, we plot the phase behaviour for the same system, after decreasing the potential V of the same system as in Figs. 5.10 and 5.11. The phase drop at point F as usual decreases to π, and hence semi classical injectance is exact at this point which can be seen in Fig. 5.13(a). Point F is marked at the same value of kl as in Fig. 5.12. But, in Fig. 5.12, the phase drop at G is now not sharp enough to decrease to π. It is due to tuning the potential, that the sub-loop has now reduced in area, and consequently the drop has also reduced and will eventually disappear. At such point $\rho(1)^e$ is not equal to $\rho(1)^s$, i.e. semi classical injectance is not exact in spite of a phase drop. This can be seen in Fig. 5.13(b)) where point G is marked at the same value of kl, as in Fig. 5.12. One would have expected that when we decrease the potential and make it weaker, semi-classical behaviour will be favoured. But on the contrary, for stronger potential the semi-classical injectance is exact at point N in Fig. 5.10(b), while for a weaker potential in the same system the semi-classical injectance is not exact at point G in Fig. 5.12(b). Therefore, the drops in scattering phase shift of mesoscopic system, originating from sub-loops in Argand diagram involves completely new physics. One has to discard the usual concept of semi-classical regimes wherein the de-Broglie wavelength of the electron is much smaller than the

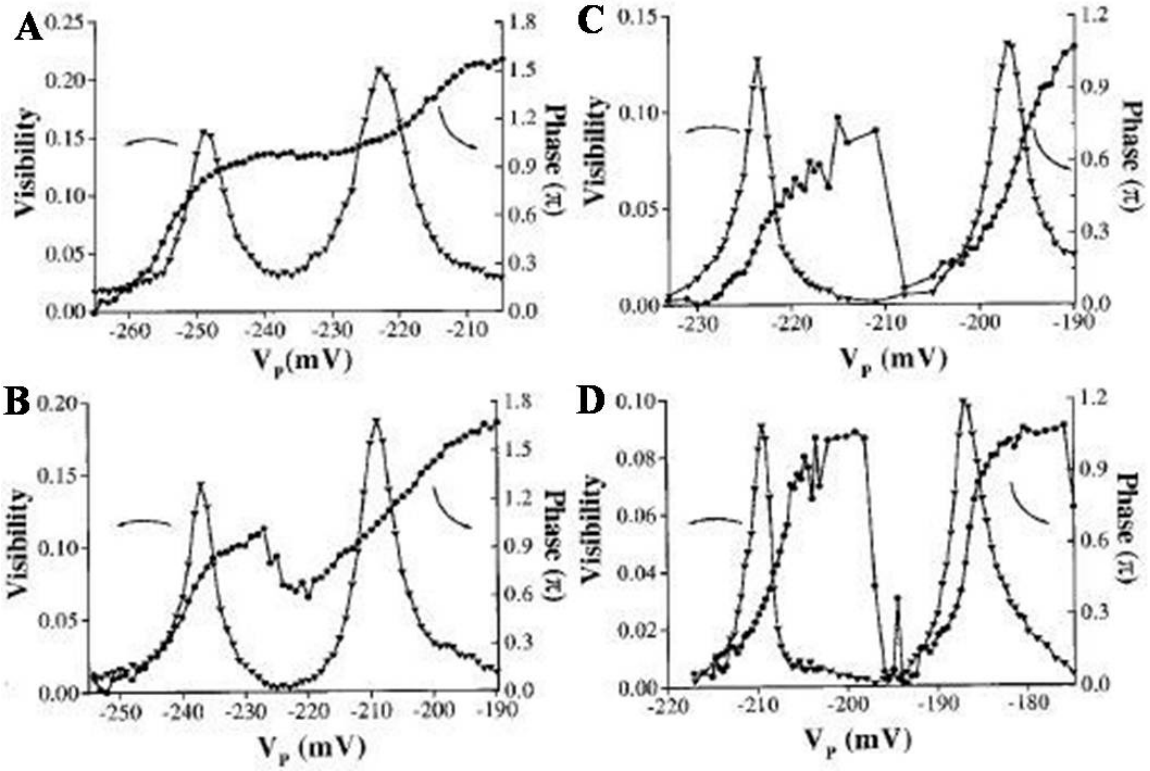

Figure 5.14 Transmission coefficient and scattering phase shift evolution in a QD as the coupling between the dot and leads is changed. This figure is taken with permission, from ref. [48].

scale of the potential, mathematically expressed by Eq. (5.20) [61].

5.5 Comment on Experimental Observations

We will try to construct the Argand diagram from the experimental data given in refs. [48, 85], to see if something can be understood. Yang Ji et al. [48] measured the transmission coefficient and transmission phase shift of a quantum dot (QD). The experimentally observed transmission coefficient and transmission phase shift as a function of gate voltage, for different coupling strengths between QD and the leads, are shown in Fig. 5.14. A phase drop is observed in Fig. 5.14D when the coupling strength is small. As coupling gradually increases, the dot enters the strongly interacting regime and the phase drop decreases and finally vanishes. This gradual phase disappearance follows the sequence D to A in Fig. 5.14. We have seen in our theoretical calculations that such phase drops

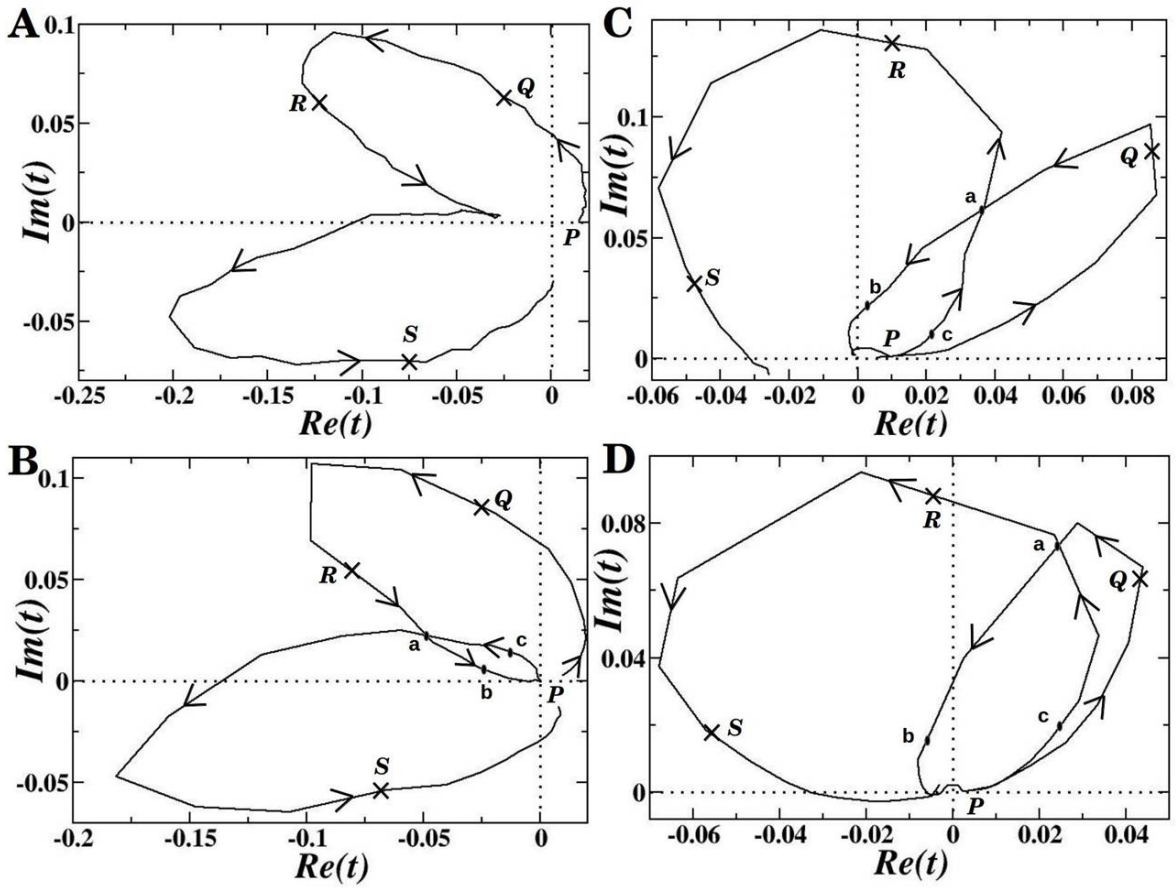

Figure 5.15 Argand diagram for the transmission amplitude, obtained from Fig. 5.14. In this figure the labelling A,B,C,D follows that in Fig. 5.14.

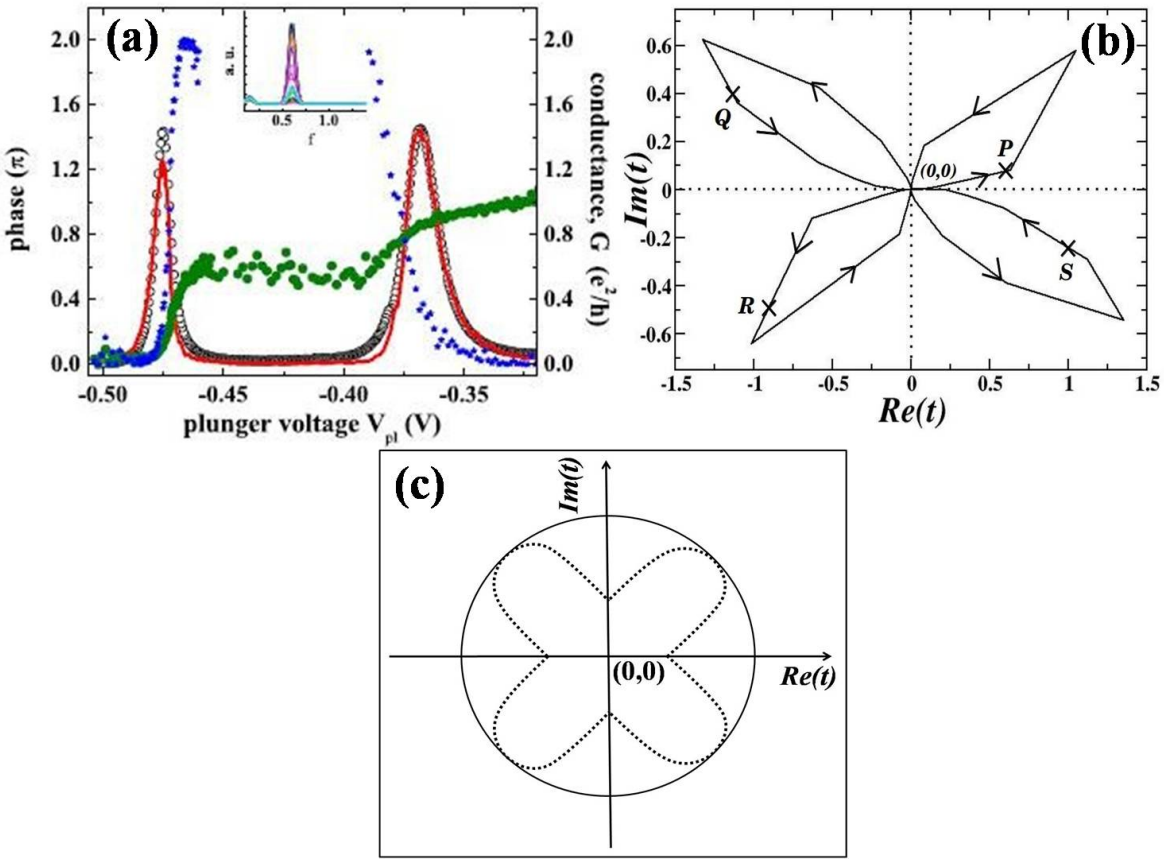

Figure 5.16 (a) Typical transmission coefficient and scattering phase shift of a QD in the Kondo regime. This figure is taken with permission from ref. [85]. (b) Argand diagram for transmission amplitude constructed from the experimental data. (c) We hope future experiments will give such Argand diagrams in greater resolution and how they evolve. For example an Argand diagram that encircles the phase singularity (solid line) can develop lobes (dotted line) and finally reduce to the Argand diagram in (b) as Kondo effect sets in.

can disappear and there are two possible reasons. One possibility is that when the coupling to leads is changed then it introduces some de-coherence for which the Argand diagram trajectory crosses the singularity and I changes from 0 to 1. The second possibility is that I remains conserved and the Argand diagram trajectory develops a sub-loop. Argand diagrams can be constructed from the experimental data given in Fig. 5.14 and is shown in Fig. 5.15. There is a lot of fluctuations in the data probably due to experimental error. However, one can roughly see that there is a sub-loop *abca* in Fig. 5.15, that gradually decreases in area as we go from D to A and clearly disappears in A with the formation of a cusp. The experimentalists had thought that as coupling increases, Kondo effect sets in and the disappearance of phase drop could be due to that. However, the phase behaviour seen in Fig. 5.14A is not typical of Kondo resonance. Typical phase behaviour of Kondo resonance is that, it increases by $\frac{\pi}{2}$ and forms a plateau. Such a behaviour was observed by the same experimental group [85] subsequently, in which they restricted the dot occupancy to one electron, and is shown in Fig. 5.16(a). One may conclude that the disappearing phase behaviour in Fig. 5.14A has nothing to do with Kondo effect. We have already discussed in section 5.4, that when Argand diagram of transmission amplitude shows a sub-loop, PDOS associated with the transmitting electrons is negative. The transmitted particles and reflected particles can attract each other and that can result in a bound state. This bound state is expected to be effective only in the strongly interacting regime, i.e. for the case of Fig. 5.14A. In the weakly interacting regime, we may not see any effect of this interaction induced bound state and the phase drops occur very generally in scattering by a mesoscopic system. We hope future experiments will focus on how Argand diagram evolves as one observes changes in scattering phase shift.

5.6 Conclusions

Argand diagram of scattering matrix elements are drawn for different model potentials and for a few experimental data. Several conclusions can be drawn from the properties of the Argand diagram without referring to the Hamiltonian or to the scattering potential. Usually the Argand diagram trajectory encircles the phase singularity. But in mesoscopic systems we find that the Argand diagram develops sub-loops. The sub-loop does not enclose the phase singularity at the origin and hence topologically

allowed. The sub-loop can therefore appear or disappear on varying some parameter. It does not matter what parameter (say E) is varied to obtain the Argand diagram or what parameter (say V) is varied to make the sub-loop disappear. Many unexplained features so far can be explained by the appearance and disappearance of such a sub-loop. When the sub-loop appears there will be a drop in the scattering phase shift and when the sub-loop disappear the drop will also disappear. Hence appearance and disappearance of phase drop is also very natural and poses no conceptual problem. Just as the sub-loop appears on varying some parameter, it can also grow in size as the parameter is varied. As the sub-loop becomes large and comes closer to the origin the phase drops also become large and sharp making the scattering phase shift decrease to π and then injectance or Friedel sum rule becomes exact. This is very counter intuitive as the strong phase drop signifies onset of pure quantum mechanical behaviour while Friedel sum rule is expected to become exact in semi-classical regimes. Also we prove that whenever there is a sub-loop (big or small) there will be negative partial density of states. For example if there is a sub-loop in the range ΔE then there is also negative partial density of states in the range ΔE. Conclusive evidence of negative partial density of sates in a real system has never been reported before. Since all these results are drawn from the properties of the Argand diagram, the results are general and independent of the Hamiltonian or the scattering potential. The physics originating from sub-loops is completely new and upsets our way of understanding semi-classical behaviour.

Chapter 6

Localization of electrons in quasi one dimension

6.1 Introduction

Spontaneous symmetry breaking by definition refers to a situation when the Hamiltonian has a certain symmetry but the solution does not have that symmetry. The definition does not refer to any phase transition. As a special case, when the effect is considered in the thermodynamic limit then symmetry breaking transition can become very sharp and then it is called a phase transition. Thus while phase transition is an example of spontaneous symmetry breaking the converse is not true. Linear superposition principle tells us that spontaneous symmetry breaking is not possible in quantum mechanics as the infinite number of degenerate states that are associated with spontaneous symmetry breaking can superpose to give a general state that has the same symmetry as the Hamiltonian. In spite of it, certain heavy nuclei exhibit rotational excitations, that can not be explained by the shell structure alone of a spherical nucleus. Initial understanding of this was provided by Bohr and Mottelson [111] in terms of collective modes of oscillation of a deformed nucleus. Such nuclear deformation may well be due to spontaneous symmetry breaking and commonly referred to as internal symmetry breaking in nuclear physics [111]. However as nuclear forces and nuclear Hamiltonian are still not precisely known, a first principle quantum mechanical analytic understanding is not yet possible. Similar ideas

of spontaneous symmetry breaking can also explain the details of the mass spectra of alkali metal clusters and indicate the existence of a spin density wave in quantum dots [112–115]. The electronic properties of metal clusters is of immense technological importance [116].

For a few electrons in a two dimensional quantum dot, the exact Hamiltonian is rotationally invariant (commutes with L_z) and can also be solved. In these systems, since earlier days, researchers have approached the problem from two practical points of view although it becomes difficult to obtain a clear, reconciled understanding. In the first approach, one either makes a numerical solution of Hartree-Fock equations or the Kohn-Sham equations for a few electrons and obtain the electron density. The density profile shows a typical crystal like structure consisting of hills and valleys (charge density wave (CDW)) [112–114]. It is known that this is an artefact of the non linearity of the equations in use while the exact theory is linear [117]. In the other approach, one makes an exact diagonalization for even fewer electrons. Whereby, the density is uniform (density has the same symmetry as Hamiltonian) and do not show any signature of broken symmetry because of the linear superposition principle. However if one calculates the pair correlation function, then that show oscillations [114, 118, 119]. Generally speaking, these oscillations survive over a finite length and decay rapidly which is expected in finite size systems. The correlation function is not defined in Hartree-Fock Theory or Density Functional Theory. The density oscillations obtained therein do not decay beyond a length scale. Still one makes the ad hoc assumption that the non linearity of Hartree-Fock Theory or Density Functional Theory show density oscillations by projecting the pair correlation function and consequently, the discrepancy of the decay disappears for infinite systems.

With exact diagonalization, one also looks at the degeneracy of eigen energies after subtracting the center of mass energy and checks if the degeneracy can be explained by the representative point group corresponding to the broken symmetry crystalline state [115]. Although in name exact diagonalization, it uses a Configuration-interaction (CI) calculation resulting in truncating the Fock space [115], besides incorporating substantial numerical errors. For example, substantial lack of degeneracy can be seen in Fig. 4 of Ref. [115] where a comparison with Hiesenberg model is given. One cannot go to very large energy limits or more than seven or eight electrons due to numerical problems. Nevertheless, this paper [115] introduces the idea of looking at yrast spectrum to see degeneracies and

to identify the representative point group, a technique that was instrumental in understanding nuclear deformations [111]. A recent work [118] has shown that eight non interacting spinless electrons in a one dimensional ring, has an yrast spectrum that can be interpreted in terms of localization of the electrons in the internal frame (centre of mass frame). The yrast spectrum can be "... understood as rotational vibrational spectrum of classical particles..." (see the conclusion of section 4 on page number 6 of Ref. [118]). Thus quite some work has been done on this problem so far [111–115, 117–119] and the localized electrons in internal frame are also referred to as density waves in the internal frame or as formation of a crystal in the internal frame, or a rigid rotor in the internal frame or just spontaneous symmetry breaking. The purpose of our work is to show that this result can be analytically extended to quasi one dimension whose thickness can be increased arbitrarily in a particular way. We also address the actual problem by-passing the cumbersome numerical technical issues associated with the problem. Once the exact periodicity can be shown in the non-interacting limit we give an analytical proof for another way of looking into this transition through fractional flux periodicity of Aharonov-Bohm effect. We show that inclusion of Coulomb interaction will not change the periodicity of Aharanov-Bohm effect. It will be ϕ_0/N in the broken symmetry state and there will be deviation from ϕ_0/N periodicity in the symmetric state. We can prove this for arbitrarily wide rings that can be considered to be a two dimensional (2D) system. Following the convention of nuclear physics wherein the yrast spectrum is used to identify the representative point group in internal frame, we will refer to this localization phenomenon as spontaneous symmetry breaking or internal symmetry breaking. Thus our work is a non-trivial extension of Ref. [118].

Mesoscopic systems give a unique opportunity to study the few electron system both experimentally as well as with theoretical models and hence provide an opportunity to study how few electron properties evolve into macroscopic collective properties as we increase the number of electrons. Wigner crystallization [120–122] of electrons, one such bulk phenomenon of spontaneous symmetry breaking proposed long ago, is still a debatable issue. We exclude here the situation when quantum mechanical kinetic energy or the uncertainty of an electron can be quenched by a strong magnetic field [123–126] or the situation when explicit symmetry breaking leads to an electron crystal state [127–131]. Localization of electrons in the internal frame (centre of mass frame) resulting in

CDW is different from a typical notion of a phase transition in condensed matter physics like localization of electrons in the laboratory frame. As mentioned in the earlier paragraph, in all the systems we study in this work, the density in the laboratory frame is always homogeneous due to linear superposition principle. And hence it is also not necessary to refer to Mermin Wagner theorem. It is to be noted that an unpinned CDW or a sliding CDW in condensed matter physics correspond to a Goldstone mode where the CDW moves in time and is different from the internal symmetry breaking discussed here, wherein the density obtained from time independent Schrödinger equation is uniform in the laboratory frame. However, there can be connection between internal symmetry breaking discussed here and spontaneous symmetry breaking in condensed matter physics which we will not explore in this paper. We will just point out the similarity between yrast spectrum to be discussed here (see Figs. 6.1(a) and 6.2(a)) and the spectrum shown in Fig. 1 of Ref. [132].

In this paragraph we briefly review section 3 and section 4 of Ref. [118]. For a finite number of electrons in a 1D ring [118], eigen energies are shown in Fig. 6.1. The electrons localize and form a crystal in the center of mass frame while the center of mass rotates like a free particle and hence the solid and dashed curve in Fig. 6.1 increases parabolically. The points B and C correspond to excitations that are therefore decoupled from the center of mass motion and corresponds to vibrations of localized electrons in center of mass frame. If the parabolic contribution is subtracted then the yrast spectra show periodic oscillation (Fig. 6.1b). Fig. 6.1b imply that eight spin up electrons, crystallized in the centre of mass frame in a 1D ring has eight-fold discrete symmetry while four up and four down has a four-fold discrete symmetry [118]. Hence the yrast spectrum repeats modulo eight and four respectively in Fig. 6.1b. Eight-fold symmetry for spinless electrons (which is same as eight spin up electrons) is again CDW and four-fold symmetry for four spin up and four spin down is spin density wave (SDW). Thus spontaneous symmetry breaking in 1D with eight spin up and four spin up-four spin down non interacting electrons is now well established [118]. This procedure of analysing degeneracies in the yrast spectrum after subtracting a parabolic part assigned to rotational energy is also well established in nuclear physics for a much longer time [111]. The features seen in Fig. 6.1, if encountered in quasi one dimension (Q1D) can be interpreted in the same way as spontaneous symmetry breaking leading to CDW and SDW.

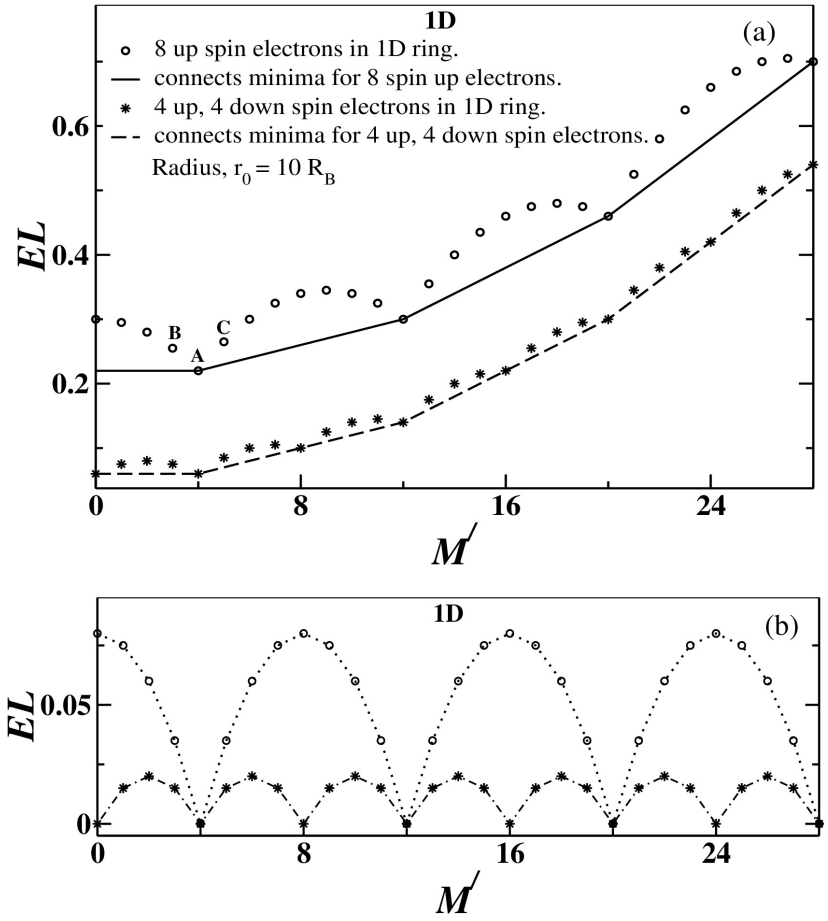

Figure 6.1 (a) Yrast spectra for eight electrons in an one dimensional ring. The electrons are interacting only through statistics whence Coulomb interaction is ignored. The solid and dashed line fall on a parabola given by $M'^2/2I$ where M' is the total angular momentum and I is the moment of inertia for 8 classical electrons in an one dimensional ring. (b) The energy values are plotted after subtracting solid and dashed lines from the data points in Fig. 6.1*a*. This figure is taken from Ref. [118].

6.2 Quasi one dimensional ring

Let us consider N number of electrons in a quasi one dimensional (Q1D) ring. The Schrödinger equation in presence of a magnetic field perpendicular to the plane of the ring is given by

$$\left\{\sum_{j=1}^{N}\left[\frac{1}{2m^*}\left(-i\hbar\overrightarrow{\nabla}_j-\frac{e}{c}\overrightarrow{A}(\overrightarrow{r_j})\right)^2+V(\overrightarrow{r_j})\right]+\frac{1}{2}\frac{1}{4\pi\varepsilon_0}\sum_{i\neq j}\frac{e^2}{|\overrightarrow{r_i}-\overrightarrow{r_j}|}\right\}$$
$$\psi(\overrightarrow{r_1},\overrightarrow{r_2},..,\overrightarrow{r_i},..,\overrightarrow{r_N})=E\,\psi(\overrightarrow{r_1},\overrightarrow{r_2},..,\overrightarrow{r_i},..,\overrightarrow{r_N}) \tag{6.1}$$

where $V(r_j)=0$ for $r_{in}\leq r_j\leq r_{out}$ and ∞ elsewhere, is the confinement potential for jth electron. Here r_{in} is the inner radius and r_{out} is the outer radius of the ring. We use a unit system where $\hbar$=1, e=1, $4\pi\varepsilon_0$=1 and m^*=0.5 and we choose the Bohr radius ($R_B=\frac{4\pi\varepsilon_0\hbar^2}{m^*e^2}$) to be the unit of length. Such a Q1D ring can be experimentally realized [16]. The Schrödinger equation in the absence of Coulomb interaction is given by

$$\sum_{j=1}^{N}\left[\frac{1}{2m^*}\left(-i\hbar\overrightarrow{\nabla}_j-\frac{e}{c}\overrightarrow{A}(\overrightarrow{r_j})\right)^2+V(\overrightarrow{r_j})\right]$$
$$\psi(\overrightarrow{r_1},\overrightarrow{r_2},...,\overrightarrow{r_i},...,\overrightarrow{r_N})=E\,\psi(\overrightarrow{r_1},\overrightarrow{r_2},...,\overrightarrow{r_i},...,\overrightarrow{r_N}) \tag{6.2}$$

$\psi(\overrightarrow{r_1},\overrightarrow{r_2},...,\overrightarrow{r_i},...,\overrightarrow{r_N})$ is the many body wave function in the absence of Coulomb interaction where electrons are interacting due to statistics. For fermions $\psi(\overrightarrow{r_1},\overrightarrow{r_2},...,\overrightarrow{r_i},...,\overrightarrow{r_N})$ of Eq. (6.2) is given by a Slater determinant. In Fig. 6.2a we consider a ring of inner radius $8R_B$ and outer radius $12R_B$ and plot the yrast spectra for (i) 8 up spin electrons and (ii) 4 up, 4 down spin electrons. It can be seen clearly that, we obtain an identical behaviour in Q1D (Fig. 6.2) as compared to in 1D depicted in Fig. 6.1. This demonstratively signifies the breakdown of symmetry (CDW and SDW) in the internal frame (centre of mass frame) as has already been explained along with Fig. 6.1. We can see in Fig. 6.1b that for the open circles every eighth level is degenerate and for the stars, every fourth level is degenerate. Degeneracy always comes from a symmetry. M' is the generator for rotation and like in 1D or in nuclear physics, we can interpret the degeneracy for every eighth value of M' is due to localization of electrons in the internal frame, resulting in an eight fold discrete symmetry. 4 up and 4 down electrons in the ring is expected to appear in the broken symmetry state with spin up and spin down electrons occurring alternately which will make the discrete symmetry 4 fold and hence for the stars (Fig. 6.2b) the degenerate levels come after every four values of M'. We fit the local minima to

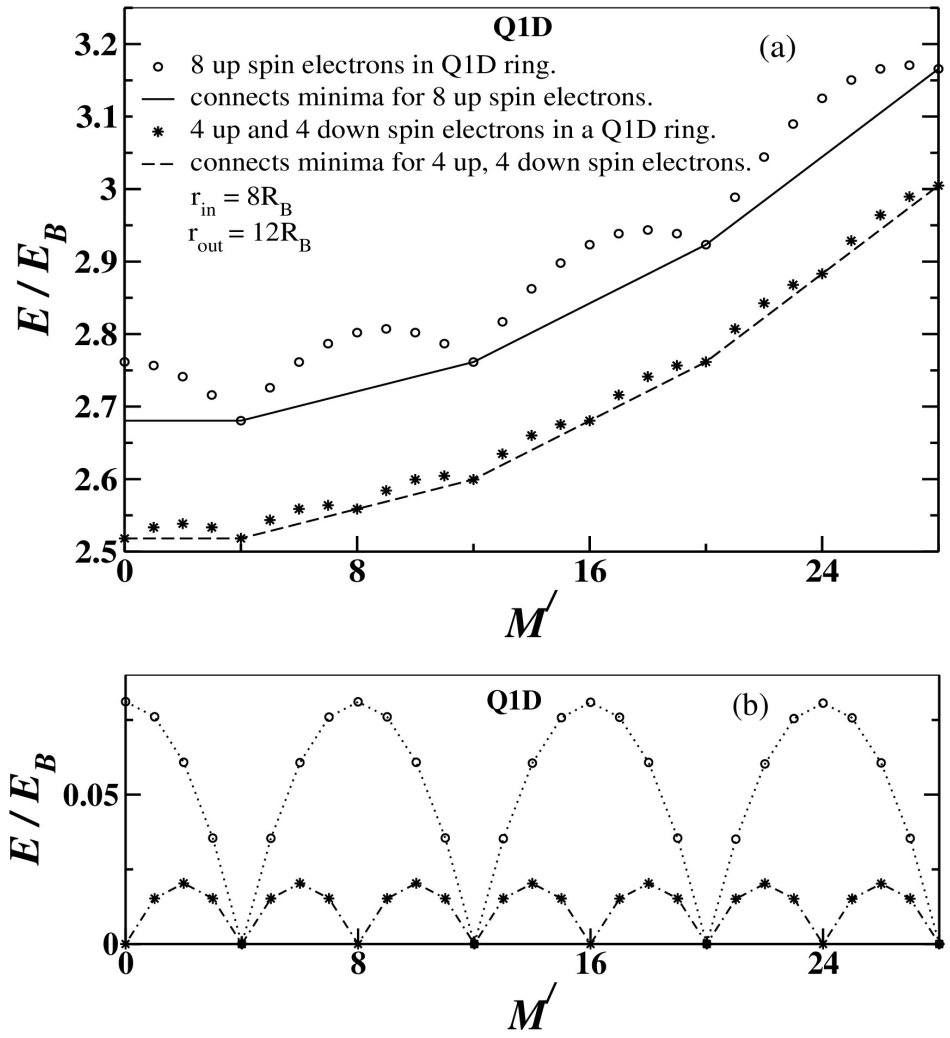

Figure 6.2 Here also the electrons are interacting only through statistics in a Q1D ring and Coulomb interaction is ignored. Note the similarities with Fig. 6.1 and we have represented the different curves just like in Fig. 6.1. Here $E_B = \frac{\hbar^2}{m^* R_B^2}$ and $R_B = \frac{4\pi\varepsilon_0\hbar^2}{m^* e^2}$.

$M'^2/2I$, where M' is the total angular momentum which has been calculated quantum mechanically. We have used I as a fitting parameter and have obtained the value of I to be 791.4 $m_e R_B^2$ for a ring of inner radius $8R_B$ and outer radius $12R_B$. The moment of inertia for 8 classical electrons placed at equal distances in a ring like arrangement and rotating on a ring of radius $10R_B$ is 800 $m_e R_B^2$. This further confirms a semi rigid classical structure and hence symmetry breaking.

We will now show that in Q1D unlike in 1D there can be a transition that can be effected by increasing the thickness of the ring. Hence we plot the yrast spectra (Fig. 6.3a) for a ring of inner radius $4R_B$ and outer radius $12R_B$. Fig. 6.3b is not exactly periodic. We again fit the local minima

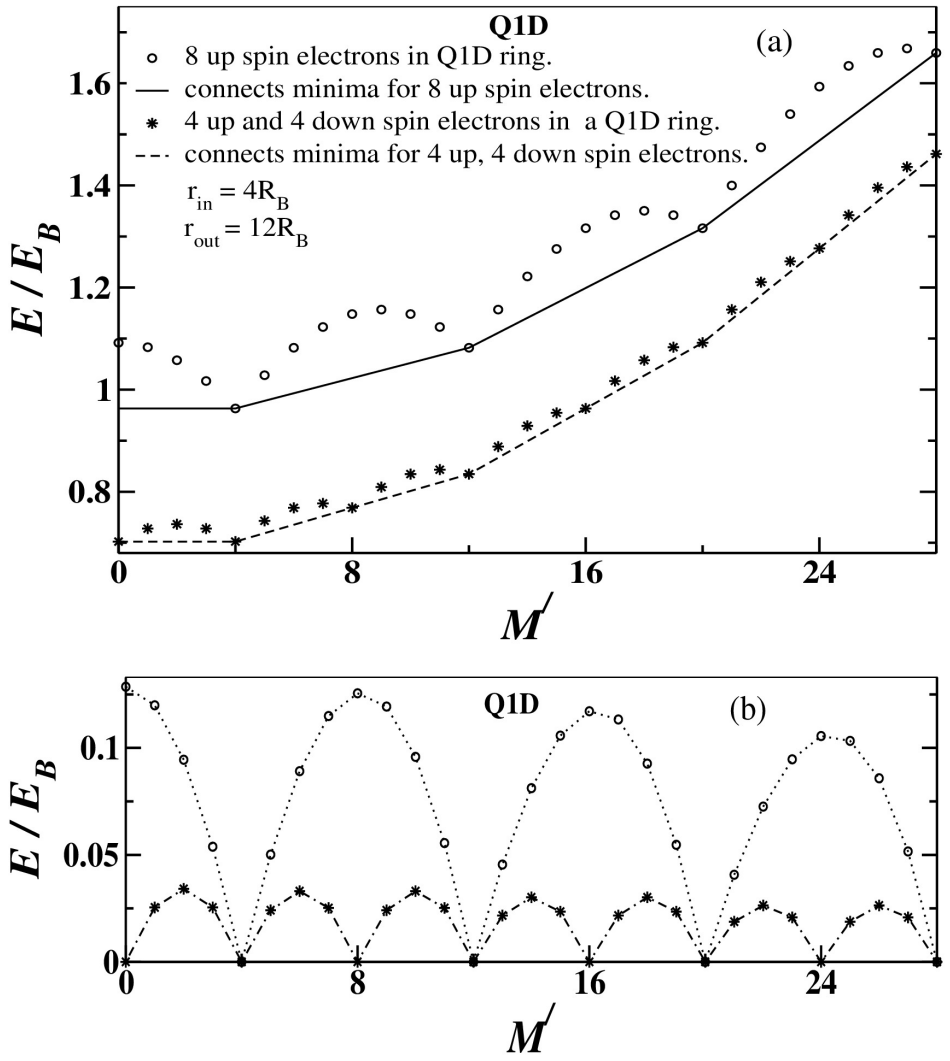

Figure 6.3 Same as in Fig. 6.2, but for a wider ring. On subtracting the parabolic data, we find the peak values in (b) are gradually decreasing and hence periodicity is absent.

to $M'^2/2I$. The value of I we obtain from the fitting is nowhere close to the moment of inertia for 8 classical electrons sitting at equal distance in a ring like arrangement. Hence no signature of broken symmetry is seen here.

6.3 Single particle states

To prove symmetry breaking for an arbitrarily wide ring including Coulomb interaction, it makes sense to make a one to one correspondence with that in 1D and for this, we study the single particle

levels of the Q1D ring. Single particle Schrödinger equation corresponding to Eq. (6.2) is

$$\left[\frac{1}{2m^*}\left(-i\hbar\overrightarrow{\nabla}-\frac{e}{c}\overrightarrow{A}\right)^2+V(\overrightarrow{r})\right]\psi(\overrightarrow{r})=\varepsilon\psi(\overrightarrow{r}) \tag{6.3}$$

We use two dimensional polar coordinates (r,θ). The vector potential in Coulomb gauge ($\overrightarrow{\nabla}\cdot\overrightarrow{A}=0$) is given by

$$\overrightarrow{A}(\overrightarrow{r})=\frac{Br_f^2}{2r}\hat{\theta}=\frac{\omega_c m^* c r_f^2}{2er}\hat{\theta} \tag{6.4}$$

where B is the magnetic field passing through a finite circle of radius $r_f < r_{in}$ and $\omega_c=(eB/m^*c)$ is the cyclotron frequency. The above equation can be solved [133, 134]. One uses

$$\psi(r,\theta)=R(r)\Theta(\theta), \quad x'=\sqrt{\frac{2m^*\varepsilon}{\hbar^2}}r=kr \tag{6.5}$$

to get,

$$x'^2\frac{d^2R}{dx'^2}+x'\frac{dR}{dx'}+\left(x'^2-m'^2\right)R=0 \tag{6.6}$$

$$\frac{d^2\Theta}{d\theta^2}-i2\alpha\frac{d\Theta}{d\theta}+\lambda\Theta=0 \tag{6.7}$$

where λ is a constant, $\alpha=\frac{m^*\omega_c r_f^2}{2\hbar}=\frac{\Phi}{\Phi_0}$ and $m'=\sqrt{\alpha^2+\lambda}$. Φ is the flux passing through the ring and Φ_0 is the flux quantum given by $\frac{ch}{e}$. The complete solution can be written as,

$$\psi(r,\theta)=\frac{1}{\sqrt{2\pi}}\left[A_{m'}J_{m'}(k_n r)+B_{m'}N_{m'}(k_n r)\right]e^{i(m'+\frac{\Phi}{\Phi_0})\theta} \tag{6.8}$$

where $J_{m'}$ and $N_{m'}$ are the Bessel and Neumann functions of order m'. Here k_n is defined as $\varepsilon_n=\frac{\hbar^2k_n^2}{2m^*}$. The azimuthal wave function $\Theta(\theta)$ satisfy twisted periodic boundary condition, i.e., $\Theta(\theta)=\Theta(\theta+2\pi)e^{-i2\pi\frac{\phi}{\phi_0}}$ that gives

$$m'=0,\pm1,\pm2,\ldots \tag{6.9}$$

For the radial function, $R(r_{in})=R(r_{out})=0$ gives

$$N_{m'}(kr_{in})J_{m'}(kr_{out})=N_{m'}(kr_{out})J_{m'}(kr_{in}) \tag{6.10}$$

Eq. (6.10) determines the allowed values of energy for a particular m'. This is shown for $n=1$, and $n=2$ in Fig. 6.4. m' values corresponding to a particular n value form a distinct band signifying

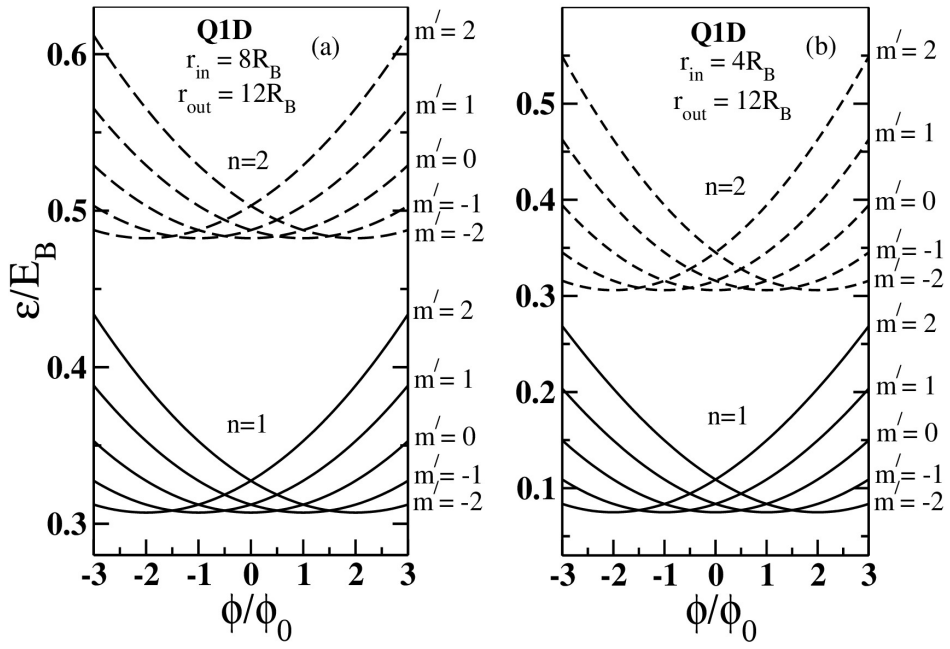

Figure 6.4 Single particle eigen energies vs magnetic flux for an electron in a Q1D ring, where the energy is expressed in units of $E_B = \frac{\hbar^2}{m^* R_B^2}$. In (a), we have subtracted 0.75 from the energy value for $n = 2$. All the curves are parabolic and minima of all the curves for a particular n value is the same.

decoupling of radial energy and azimuthal energy. Each curve is a parabola for both $n = 1$ and $n = 2$ just like what we get in a one dimensional ring. We can get further insight when we move into higher dimensions by noting the similarities between Q1D and 1D. Multiplying both sides of Eq. (6.6) and Eq. (6.7) by $\frac{\hbar^2}{2m^* r^2}$ and adding $\frac{m^* \omega_c^2 r_f^2}{8r^2}$ to both sides of Eq. (6.7) and then using Eq. (6.5) one can obtain the following equations

$$-\frac{\hbar^2}{2m^*}\left[\frac{1}{r}\frac{d}{dr}\left(r\frac{d}{dr}\right)\right]R(r) = \varepsilon_1(r)R(r) \tag{6.11}$$

$$\frac{1}{2m^*}\left(-i\hbar\frac{1}{r}\frac{\partial}{\partial\theta} - \frac{e}{c}A(\vec{r})\right)^2 \Theta(\theta) = [\varepsilon - \varepsilon_1(r)]\,\Theta(\theta) \tag{6.12}$$

where,

$$\varepsilon_1(r) = \frac{\hbar^2}{2m^* r^2}\left(x'^2 - m'^2\right) = \frac{\hbar^2}{2m^*}\left(k^2 - \frac{m'^2}{r^2}\right) \tag{6.13}$$

Since $rd\theta = dx$, Eq. (6.12) becomes

$$-\frac{\hbar^2}{2m^*}\left(\frac{d}{dx} - \frac{ieA(r)}{c\hbar}\right)^2 \Theta(x) = [\varepsilon - \varepsilon_1(r)]\Theta(x) \tag{6.14}$$

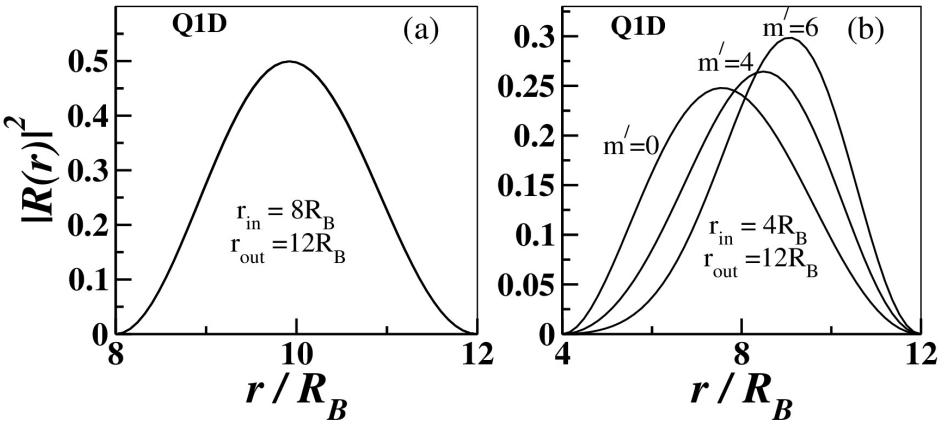

Figure 6.5 Probability distribution of radial wave function of an electron in a ring for different m' values, for zero flux and $n = 1$. In (a) all the curves corresponding to different m' values overlap on each other but in (b) they are distinct. Situation in (a) leads to a broken symmetry state and for (b) symmetry is restored.

Θ which is a function of m' and θ in Eq. (6.12) now becomes a function of k and x in Eq. (6.14). The r dependence of A is of no consequence as $A(r)$ in Eq. (6.14) can be gauged away in a manner just as one does in the 1D case to give

$$-\frac{\hbar^2}{2m^*}\frac{d^2}{dx^2}\Theta'(x) = [\varepsilon - \varepsilon_1(r)]\Theta'(x) \tag{6.15}$$

where Θ', the gauge transformed version of Θ and it results in a change of boundary condition in the presence of magnetic field.

$$\Theta'(x) = \Theta(x)e^{-i\frac{e}{\hbar c}\int A(r)rd\theta} \tag{6.16}$$

Note that (see Eq. (6.13)) m' is angular momentum quantum number and $\frac{m'}{r}$ behaves like k which is linear momentum quantum number. Hence although $\varepsilon_1(r)$ in Eq. (6.15) seems to be a function of r it behaves like the square of decoupled linear momentum or energy. The azimuthal energy being $[\varepsilon - \varepsilon_1(r)]$. Ref. [135] writes for a 1D ring

$$-\frac{\hbar^2}{2m^*}\frac{d^2}{dx^2}\Theta'(x) = \varepsilon_{1D}\Theta'(x) \tag{6.17}$$

Note that Eq. (6.15) and Eq. (6.17) give similar energy spectrum as has already been clearly explained in Fig. 6.4. $[\varepsilon - \varepsilon_1(r)]$ in Eq. (6.15) corresponds to ε_{1D} in Eq. (6.17). Only difference is that $[\varepsilon - \varepsilon_1(r)]$ in Eq. (6.15) has to be determined from Eq. (6.11) and the radial wave function compensates in such a way that the eigen energies of the system turn out to be similar in Q1D as well

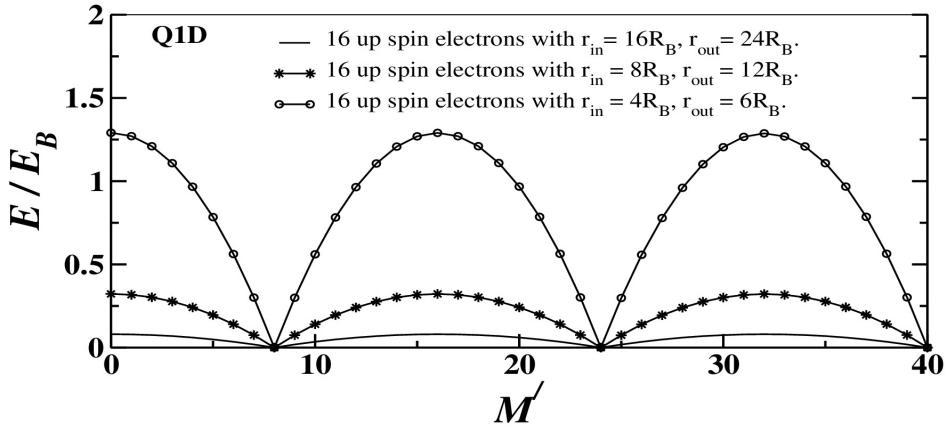

Figure 6.6 Periodicity is seen when the radius and thickness are increased simultaneously.

as in 1D. This is true for a narrow ring as well as a wide ring. A gradual crossover to an extremely wide ring that can be considered as a two dimensional system does not change this feature. The only change of feature will be in the nature of the radial wave functions. This is well demonstrated in Fig. 6.5 for a narrow ring that exhibits broken symmetry (parameters corresponding to Fig. 6.2) and a wide ring that does not exhibit broken symmetry (parameters corresponding to Fig. 6.3). For narrow rings, the wave functions corresponding to possible different m' values look identical. However, for wider rings this is not true. In 1D, statistics plays a major role as the electrons can not cross each other. In a Q1D ring with inner radius $8R_B$ and outer radius $12R_B$, we see that the radial probability distribution for all m' values coincide with each other (Fig. 6.5a). In this case, it looks like the effect is similar to the case of 1D and that the electrons can not cross each other due to Fermi statistics. Hence, this system shows spontaneous symmetry breaking just like in 1D. For a ring of inner radius $4R_B$ and outer radius $12R_B$ the position of peaks of the radial probability distribution changes with m' (Fig. 6.5b). In this case it appears that unlike in 1D the electrons can cross each other inside the ring and symmetry breaking is not seen.

6.4 Effect of ring thickness and two dimensions

From Fig. 6.3 and associated narrations, it seems that symmetry breaking is not possible in two dimensions that can be obtained by gradually increasing the thickness of a Q1D ring. But if we increase the radius and the thickness simultaneously, it results in symmetry breaking as we will explain now.

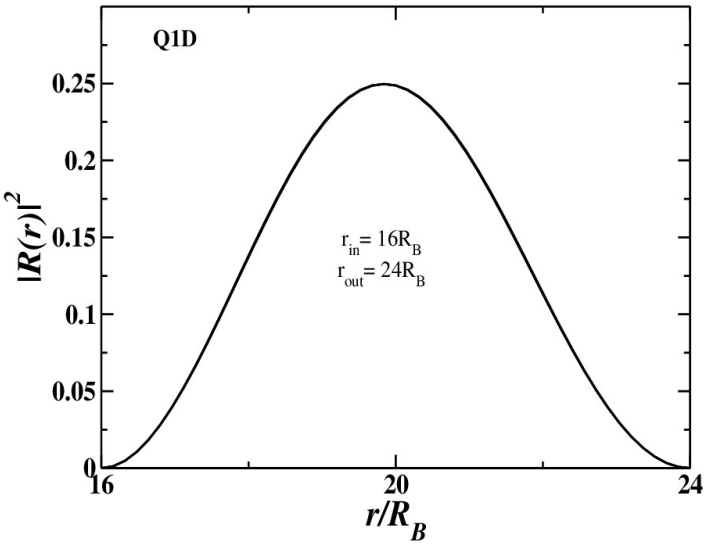

Figure 6.7 Probability distribution of radial wave function of an electron in a ring with inner radius $r_{in} = 16R_B$, outer radius $r_{out} = 24R_B$, for different m' values and $n = 1$.

We take 16 electrons interacting only due to Fermi statistics and compare the energy spectra for three rings. One with inner radius $4R_B$ and outer radius $6R_B$, other with inner radius $8R_B$ and outer radius $12R_B$ and another with inner radius $16R_B$ and outer radius $24R_B$. Here we have plotted the energy values after subtracting the parabolic data we obtain by connecting the minima (Fig. 6.6). We see that all the curves show the same periodicity, signifying broken symmetry. The amplitude of oscillation for the ring with inner radius $16R_B$ and outer radius $24R_B$ is 1/4-th of the amplitude for the ring with inner radius $8R_B$ and outer radius $12R_B$, and is 1/16-th of the amplitude for the ring with inner radius $4R_B$ and outer radius $6R_B$. This is also similar to the case of a 1D ring, where if one makes the radius double, the energy becomes 1/4-th. Note that although $\frac{r_{in}}{r_{out}}$ ratio is same in the three rings, their thickness is increasing. And as seen in Fig. 6.3, we do not expect symmetry breaking leading to CDW as the thickness increases. Note that the curve represented by solid line in Fig. 6.6 is for a ring of thickness $8R_B$ like that in Fig. 6.3 but unlike Fig. 6.3, it shows a broken symmetry. For this ring too the radial probability distribution is independent of m' and shown in Fig. 6.7. Hence if this trend continues then by increasing the radius and the thickness simultaneously one can observe symmetry breaking for a very thick ring, and as one assumes when applying Born-von Karman boundary condition one may say properties deep inside the sample is independent of boundary conditions. The act

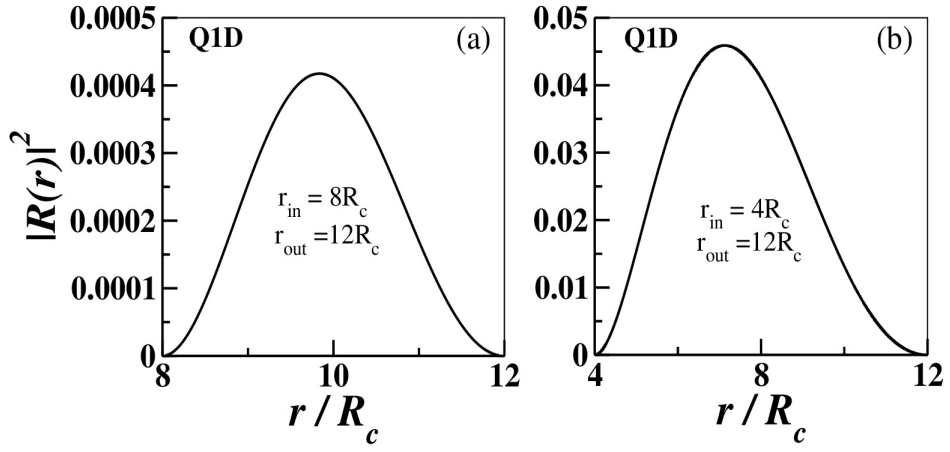

Figure 6.8 Probability distribution of radial wave function of an electron in a ring for different m' values and $n = 1$. Here the radius is taken in units of $R_c = \frac{(4\pi\varepsilon_0)^2\hbar^3 c}{(m^*)^2 e^4}\sqrt{\frac{\hbar c}{G}} \simeq 10^{14} meters$, where $G = 6.67 \times 10^{-11} Nm^2 kg^{-2}$, is the Gravitational constant. Therefore in (a) we are considering a ring of width $4 \times 10^{14} meters$ and in (b) that of width $8 \times 10^{14} meters$.

of increasing the radius consequently lowers the azimuthal component of the momentum and the act of increasing the thickness lowers the radial component of the momentum. When r_{in} becomes very large, one can use the asymptotic forms of Bessel function and Neumann function. In that case one can prove analytically that radial probability distribution is independent of m'. This is demonstrated in Fig. 6.8. Note that Fig. 6.8a is for a ring of thickness $4 \times 10^{14} meters$ and Fig. 6.8b is for a ring of thickness $8 \times 10^{14} meters$. In the next section we will prove that even if we include Coulomb interaction, we will get a broken symmetry state when radial probability distribution is independent of m'.

6.5 A proof including Coulomb Interaction

From Eq. (6.8), the wave function for the many body Scrödinger equation in Eq. (6.1) can be written as

$$\Psi_N(\{r_j, \theta_j\}) = \sum_{\{m'_j\}} a_{\{m'_j\}} \mathscr{A} \prod_{j=1}^{N} \left[\left(A_{m'_j} J_{m'_j}(k_{n_j} r_j) + B_{m'_j} N_{m'_j}(k_{n_j} r_j) \right) \left(\frac{1}{\sqrt{2\pi}} e^{i(m'_j + \frac{\Phi}{\Phi_0})\theta_j} \right) \right] \tag{6.18}$$

where $a_{\{m'_j\}}$s are unknown coefficients, $\mathscr{A}$ stands for anti-symmetrizing operator. $\left\{m'_j\right\}$ corresponds to the set of all allowed m'_j values appearing in the product of Eq. (6.18). We now introduce the center of mass (ξ) and relative (ζ_i) coordinates defined as

$$\xi = \frac{1}{N}\sum_{j=1}^{N}\theta_j, \quad \zeta_j = \theta_j - \xi \tag{6.19}$$

If we look at the many body Hamiltonian of Eq. (6.1) in terms of these coordinates then the first term and the Coulomb interaction term are interesting to note.

$$\mathbf{H} = \sum_{j=1}^{N}\frac{-\hbar^2}{2m^* r_j^2}\frac{1}{N^2}\frac{\partial^2}{\partial\xi^2} + ... + \frac{1}{2}\sum_{i\neq j}\frac{1}{4\pi\varepsilon_0}\frac{e^2}{\sqrt{r_i^2+r_j^2-2r_i r_j\cos(\zeta_i-\zeta_j)}} \tag{6.20}$$

Our calculations shown in Fig. 6.2 suggests that in some regime (e.g. for parameters chosen for Fig. 6.2) r_j = constant = r_{1D} (say). Then the first term in Eq. (6.20) is $\hat{M'}^2/2I$ where $\hat{M'} = -i\hbar\frac{\partial}{\partial\xi}$ and $I = m^* N r_{1D}^2$. $\frac{\partial^2}{\partial\xi^2}$ commutes with $\mathbf{H}$ in Eq. (6.20). This essentially implies that Coulomb interaction (the last term) will not change the center of mass angular momentum and hence $\sum m'_j = M'$ (where M' is the eigenvalue corresponding to $\hat{M'}$) will be a conserved quantity for each of the sets $\left\{m'_j\right\}$ in Eq. (6.18). Therefore, from Eq. (6.18) and Eq. (6.19) on using the fact, that in the broken symmetry state the radial probability distribution is independent of m'_j (see Appendix E)

$$\Psi_N(\{r_j,\theta_j\}) = e^{i\left(M'+N\frac{\Phi}{\Phi_0}\right)\xi}\sum_{\{m'_j\}}a_{\{m'_j\}}\mathscr{A}$$
$$\prod_{j=1}^{N}\left[\left(A_{m'_j}J_{m'_j}\left(k_{n_j}r_j\right)+B_{m'_j}N_{m'_j}\left(k_{n_j}r_j\right)\right)\left(\frac{1}{\sqrt{2\pi}}e^{im'_j\zeta_j}\right)\right] \tag{6.21}$$

If we switch off the Coulomb interaction then the sum will not appear and the exact wave function is

$$\Psi_N(\left\{r_j,\theta_j\right\}) = e^{i\left(M'+N\frac{\Phi}{\Phi_0}\right)\xi}\mathscr{A}\prod_{j=1}^{N}\left[\left(A_{m'_j}J_{m'_j}\left(k_{n_j}r_j\right)+B_{m'_j}N_{m'_j}\left(k_{n_j}r_j\right)\right)\right.$$
$$\left.\left(\frac{1}{\sqrt{2\pi}}e^{im'_j\zeta_j}\right)\right] \tag{6.22}$$

Eq. (6.21) implies an Aharanov-Bohm effect of periodicity Φ_0/N. This is because the term inside the summation in Eq. (6.21) does not contain flux and the periodicity will be Φ_0/N as can be seen from the exponential factor in Eq. (6.21). Therefore when there is no Coulomb interaction, we first prove that in the broken symmetry state, $r_j \longrightarrow r_{1D}$ and radial probability distribution is independent of m'_j.

This can happen for arbitrarily wide rings when r_{in} is very large. Then in this section, we prove that if these two conditions are satisfied then the many body wave function (including Coulomb interaction) will show Φ_0/N periodicity with flux Φ. For the symmetric case (parameters corresponding to Fig. 6.3), the same argument for r_j and m'_j cannot be given. Such Φ_0/N periodicity again implies a Nparticle rigid rotor structure (CDW) due to spontaneous symmetry breaking. Aharonov-Bohm effect in a ring can be observed [136] by observing the persistent currents [137]. So changes in periodicity can also be observed and can give us the demonstration of symmetry breaking transition. Also note that if we fix the flux, let us say $\phi/\phi_0 = 1$, then from Eq. (6.21) we can see that $\Psi_N^{M'+\nu N} = e^{i\nu N\xi}\Psi_N^{M'}$, where ν is an integer. Thus we get identically the same structure for the many body wave function as that of Maksym [138] and it corresponds to a rigid rotation of the N particle state like a single particle with mass Nm^*.

6.6 Three dimensions

The system we study in this section is shown by the shaded region in Fig. 6.9. The shaded region can be expressed in terms of (r, θ, ϕ) coordinates, where r varies from r_{in} to r_{out}, ϕ varies from 0 to 2π and θ is infinitesimally small. This is a special form of torus. If the sharp edges are rounded then we get a torus. If $r_{in} \longrightarrow 0$, $r_{out} \longrightarrow R$ and θ is allowed to vary from 0 to $\pi/2$, then we get the sphere of radius R shown by dotted line in Fig. 6.9. Thus we can express $\Psi = R(r)P(\theta,\phi)$ and single particle Schrödinger equation reduces to,

$$\begin{aligned} &-\frac{1}{R}\left[\frac{\partial}{\partial r}\left(r^2\frac{\partial}{\partial r}\right) - \frac{2m^*r^2}{\hbar^2}V(r) + \frac{2m^*r^2E}{\hbar^2}\right]R(r) \\ &= \frac{1}{P}\left[\frac{1}{sin\theta}\frac{\partial}{\partial\theta}\left(sin\theta\frac{\partial}{\partial\theta}\right) + \frac{1}{sin^2\theta}\frac{\partial^2}{\partial\phi^2}\right]P(\theta,\phi) = \lambda \end{aligned} \tag{6.23}$$

We can take $V(r) = 0$ inside the shaded region and $V(r) = \infty$ outside. We want to ask the question that is it possible to analyse the wave functions in the same footing as done so far and show symmetry breaking inside the shaded region. If θ is very small then $sin\theta = \theta$ and Eq. (6.23) becomes

$$\begin{aligned} &-\frac{1}{R}\left[\frac{\partial}{\partial r}\left(r^2\frac{\partial}{\partial r}\right) - \frac{2m^*r^2}{\hbar^2}V(r) + \frac{2m^*r^2E}{\hbar^2}\right]R(r) \\ &= \frac{1}{P}\left[\frac{1}{\theta}\frac{\partial}{\partial\theta}\left(\theta\frac{\partial}{\partial\theta}\right) + \frac{1}{\theta^2}\frac{\partial^2}{\partial\phi^2}\right]P(\theta,\phi) = \lambda \end{aligned} \tag{6.24}$$

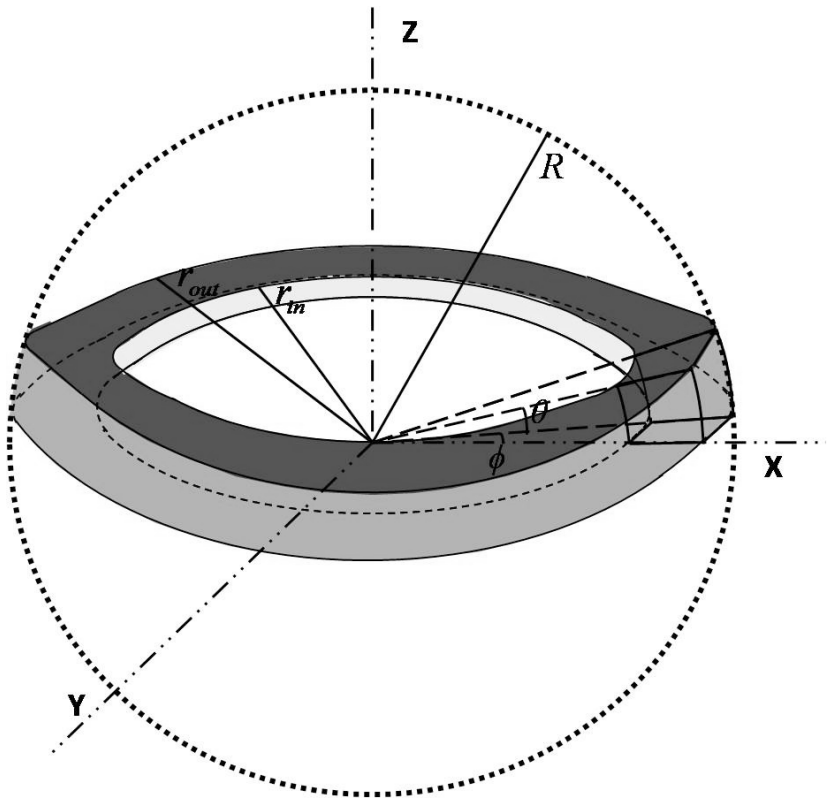

Figure 6.9 The three dimensional system, that we consider, is shown by the shaded region. The potential is zero inside the shaded region and ∞ outside the shaded region.

Once again the radial part effectively decouples and one can have

$$\left[\frac{1}{\theta}\frac{\partial}{\partial\theta}\left(\theta\frac{\partial}{\partial\theta}\right)+\frac{1}{\theta^2}\frac{\partial^2}{\partial\phi^2}\right]P(\theta,\phi)=\lambda P(\theta,\phi) \tag{6.25}$$

In the differential equation given in Eq. 6.25, if we replace θ by r and ϕ by θ, then Eq. (6.25) will look identical to Eqs. (6.11) and (6.12) in the absence of magnetic field. Magnetic field and Coulomb interaction can then be treated in the same way as we have done for Eq. (6.11). In such a system, therefore the equation of motion is just like in Q1D and hence we can again expect symmetry breaking. However, if $sin\theta$ can not be approximated by θ then we should not expect symmetry breaking in three dimensions. Therefore in a 3D sphere of radius R (there is an infinitesimal cavity at the centre) where the potential inside the sphere is zero and ∞ outside (hard walls), we do not expect symmetry breaking. If the hard wall is replaced by a central potential then also it is natural to expect that there will be no symmetry breaking. Therefore, we cannot get symmetry breaking in atoms.

6.7 Conclusion

Spontaneous symmetry breaking in quantum mechanics has been an important problem for a long time. It is thought to manifest in several phenomenon like Wigner crystal, deformation of nuclear shells, charge density wave and spin density wave in quantum dot, etc. Theoretical study of each of these phenomenon has its own drawback. Wigner crystal occur in the thermodynamic limit and the system has so many degrees of freedom that one can only approach the problem phenomenologically and explicit symmetry breaking can never be ruled out in an experiment. Although, Wigner proposed it as a spontaneous symmetry breaking. Nuclear Hamiltonian is not exactly known and so one is more interested in explaining some experimental data rather than probing the reality of spontaneous symmetry breaking, although text books [111] refer it as spontaneous symmetry breaking or internal symmetry breaking. Quantum dot has so far been only studied numerically and there are too many disconnected notions about what happens in quantum dot as explained in the introduction. At the heart of the problem is the issue that linear superposition principle in quantum mechanics makes it very counter-intuitive to accept the existence of rotational and vibrational modes in a system whose Hamiltonian is rotationally invariant. Such rotational and vibrational modes suggest the existence of localized electrons after referred to as charge and spin density waves. By taking electrons in a quasi one dimensional ring and putting a magnetic field we neither break the symmetry explicitly, nor tamper with the linear superposition principle. But the system is physical and has a total angular momentum, and we can show that linear superposition principle is not a deterrent to observe rotational and vibrational modes. Charge and spin density waves in the internal frame is well established in 1D for fermions because of restricted spatial degrees of freedom, i.e., electrons cannot cross each other in 1D. There is no transition in 1D. Unlike 1D which is ideal, Q1D rings can be fabricated in the laboratory. The ring geometry in Q1D can be treated analytically. Thickness can be varied and scaling can be studied. We can show charge and spin density waves in the internal frame and also restoration of symmetry with variation of thickness. The charge and spin density waves in broken symmetry state show identical behaviour as in 1D. Further comparison with 1D show that in the broken symmetry state, the electrons are situated at the mean radius of the ring and in-spite of the radial spread of their wave functions, do not avail this degree of freedom and behave like or scale like

a 1D system. In the symmetric state, they do not behave that way. Increasing the width and mean radius simultaneously, one can retain the broken symmetry state for thicker rings. The behaviour in Figs. 6.5a, 6.7 and 6.8 (the single particle radial probability distribution being independent of m'_j) allows us to prove analytically that the many body state including electron-electron interaction will show fractional Aharanov-Bohm effect i.e., a N body system will show ϕ_0/N periodicity. The N body state forms a rigid rotor in the internal frame of reference and the fundamental periodicity of Aharanov-Bohm effect for such a rigid rotor is ϕ_0/N. This result is true for arbitrarily thick rings when r_{in} is very large. Then we show that in a thin 3D ring (shown in Fig. 6.9) the equation of motion is the same and so the same analysis and analytical treatment can be done to obtain the same results as in Q1D. However, the geometry of Fig. 6.9 can be continuously modified to give a sphere (with a hole in the centre) but the equation of motion change with this modification and same results as in Q1D cannot be expected. Replacing the hard wall by a soft wall (say a central potential like in atoms which too has an unavailable region of space at the centre) is not expected to be different as the issue of internal symmetry breaking is related to dimensions and not the details of the potential.

Chapter 7

Future scope

7.1 Spontaneous symmetry breaking

The phenomenon is well known in physics in different names and manifests across a variety of faculties. In nuclear physics an interesting phenomenon is that certain heavy nuclei are deformed. Since they are deformed they exhibit rotational and vibrational excitations. A spherical or rotationally invariant nucleus cannot show such excitations. Since the nuclear Hamiltonian is not exactly known till date the main motivation there is to build a phenomenological approach to explain experimental data. However, to every bodies discomfort, atomic orbitals (heavy or light) have never shown any signature of rotational and vibrational excitations, or any other signature of deformation. In fact one can simply use the superposition principle to claim that atoms will never get deformed. Because there are infinitely many directions of deformations and the atomic orbital will always get into a linear superposed state of all these deformed states which is a rotationally invariant state. So why the nucleus is so?

Condensed matter systems are not so clean and defect free as atoms or nucleus. Presence of defects do not rule out explicit symmetry breaking. In condensed matter also the drive for industry applications make physicists again focus on phenomenological approaches and guess work to explain experiments. However, condensed matter physics is not limited by the same constraints as in nuclear physics where the Hamiltonian is unknown. And as we have seen many times in the past it is difficult

to guess two steps than to guess one. So first principle approaches are always very important, but nothing has been done so far. It is known that in one dimension electrons can undergo spontaneous symmetry breaking that leads to a crystal like structure. Such a crystal can exhibit vibrational excitations. These excitations can be bosonized. Charge and spin decoupling takes place. One dimension is however an ideal case. In one dimension differentiation cannot be made between hard core bosons and fermions as neither can cross each other. Two dimensions is however not an ideal case because one can find many realistic systems that are two dimensional. Bosonization in two dimensions is a very important and unsolved problem in spite of a lot of effort. In this respect, approaching the problem from a different point of view, that is the mesoscopic point of view may yield some non-trivial insight.

In this mesoscopic approach one starts from a few electrons in a confinement, say a quantum dot or a quantum ring. So far people have only approached the problem numerically and tried to apply the same kind of reasoning as done in nuclear physics. A careful reading will show that we do not learn anything more than what we already know in nuclear physics. The actual problem is never addressed due to the assumptions used and cumbersome numerical procedure. We have recently taken an analytical approach to the problem. We take a number of electrons in a quasi one dimensional ring of width W. That is the ring has an inner radius of r_{in} and an outer radius of r_{out}, with $(r_{in} - r_{out}) = W$. We note that the problem has a lot of similarities with one dimension and shows the same kind of symmetry breaking. Unlike in one dimension, where the symmetry is always broken, electronic states in the quasi one dimensional ring can exhibit a transition from a broken symmetry to a symmetric state. We can prove that for an infinitely thick ring $W \to \infty$ the broken symmetry state can exist provided r_{in} also tends to infinity. r_{in} tending to infinity is required to lower the azimuthal energy and this fits with our notion that such broken symmetry state will exist only for very low energy states. We can exhibit this for a ring whose r_{in} is of the order of 10^{14} meters and width is also of the same order, for arbitrarily large number of electrons. The broken symmetric state is identified by fractional Aharanov-Bohm effect. An N electronic state that crystallizes in a ring and moves as a rigid rotor will show ϕ_0/N periodicity where ϕ_0 is a single flux quantum.

In the future we would like to put these results in the language of condensed matter physics. A

ring of thickness 10^{14} meters is a two dimensional system in all sense as states will be very little affected by the boundary. Several questions remain. a) Can this system be bosonized where the bosonic excitations are just the vibrations of electrons frozen in a rigid rotor like structure. Given the similarity of the problem with the one dimensional case in terms of the equations of motion a very similar approach as that in one dimension can be used. b) Can one prove the decoupling of charge and spin degrees of freedom for this system. For example, we know that in a one dimensional Luttinger liquid fractional Aharanov-Bohm effect can arise due to decoupling of charge and spin degrees of freedom. The charge and spin move with different velocities. The charge can go round the ring once but that has no manifestations on Aharanov-Bohm effect. Only when the charge and spin have gone round N times they meet again because of their commensurate velocities and then we see Aharanov-Bohm effect [139]. Is this a different way of saying the electrons in a ring form a rigid rotor of N particles and show fractional periodicity?

We can also state that unlike the quasi one dimensional ring a three dimensional sphere has no similarity with the one dimensions in terms of the guiding equations of motion. So we do not expect vibrational excitations in atoms. And that reopens the problem in nuclear physics.

7.2 Statistical mechanics of small systems

While text book statistical mechanics tells us that equal a priori probability and ergodicity holds very well for large systems the microscopic equations of motion tell us a different story. Microscopic equations of motion tell us that initial and final conditions play a major role and all states are not equally probable. In fact the state of a system of particles depend very sensitively on its initial and final conditions. So when system size becomes smaller and smaller at some point we have to properly account for this sensitivity to initial and final conditions and so we need to develop a new branch of statistical mechanics namely known as mesoscopic grand canonical systems.

A mesoscopic grand canonical system is coupled to electron reservoirs with leads through which they exchange electrons (or phonons) with the reservoir. Electrons enter or leave the system through these reservoirs and the leads determine these initial and final conditions. A proper theory of mesoscopic systems has to include the electron dynamics in the leads and the coupling of the leads to the

system. Landauer-Büttiker formalism is very good at including the effect of the leads by formulating the problem in terms of the scattering matrix elements. The Landauer two probe and four probe conductance formulas show the importance of the leads in determining the linear response conductance of small quantum systems. Electrons entering the system through lead A and leaving through lead B are characterized by the scattering matrix element S_{AB}. Such electrons do not access all the states inside the system but only a part of it leading to the notion of partial density of states. The partial density of states depend very crucially on the nature of the leads, position where they attach to the system, and strength of its coupling to the system. Current from A to B, resistance between points A and B, current injected by an STM tip to a particular point in a mesoscopic system all depend crucially on this partial density of states rather than the density of states.

S_{AB} is a complex quantity with an amplitude and a phase. While measuring the amplitude is an old story recently it has been possible to measure the phase very reliably. A lot of information can be obtained from the scattering phase shift if we can interpret it correctly. We have shown that the most accurate knowledge of partial density of states can be obtained from the scattering phase shift. We have also noticed that in some parameter regime the partial density of states can become negative. Such negative partial density of states is possible in quantum mechanics and is not a surprise. However, the broad range of physical situations where we have shown the possibility of negative partial density of states is very interesting. In the future I will focus on the physical consequence of such negative partial density of states. For example, consider a mesoscopic system coupled to multiple leads say A, B, C, D. If the scattering phase shift from A to B show negative partial density of states, it means electrons entering the system through A and leaving through B pass through a negative number of states inside the system. Negatively charged electrons in a negative number of states will behave as positive charge (total charge being number of states times occupation probability given by fermi factor times the negative charge of the electron). Such electrons in the A to B channel will non-trivially affect the electrons in the C to D channel. There can be electron electron attraction and electron electron bound states. We intend to study this in details.

Appendix A

Different dimensional mesoscopic systems and there density of states

In this appendix different dimensional mesoscopic systems are discussed along with their density of states is derived.

A.1 Different dimensional mesoscopic systems

A major feature that distinguishes different mesoscopic systems is their dimensionality. Let us consider a system with dimension L_x, L_y and L_z in x, y and z directions, and confine electrons in this system. If the length scale is less than a characteristic length scale L_0 (say), then the electron propagation along that direction is restricted, and the system is quantum confined. The dimension of a system in general can be written as, $(3-n)$D, if $L_i < L_0$, where, $i = 1, n$. The categories are,

- Three dimensional (3D): $L_x, L_y, L_z > L_0$, i.e, $n = 0$.

  Three dimensional systems are so named because in these systems, electron motion is not restricted along any directions. For example bulk, which is a well known no confinement system. In bulk (macro), the dimensions of the semiconductor crystal are much larger than theoretical exciton Bohr radius R_B, allowing the exciton to extend to its natural limit.

- Two dimensional (2D): $L_z < L_0$, i.e, $n = 1$.

Two dimensional systems are so named because in these systems, electron motion is restricted along one direction but free to move along rest of the two directions. For example 'quantum well', a well known singly confined system. The one dimension is reduced to nanometer range, so that the size is comparable to the de-Broglie wavelength of the exciton, while other two dimensions remain large, one obtains a structure known as quantum well.

- One dimensional (1D): $L_y, L_z < L_0$, i.e, $n = 2$.

  One dimensional system are so called because in these system, electron motion is restricted along two direction, but can freely propagate in one direction. For example 'quantum wire', a well known two directional confinement system. In one dimensional, if two dimensions are reduced and one remains large; the resulting structure is referred to a nanowire. But if two dimensions of nanowire become comparable to Bohr exciton radius, then this structure is known as quantum wire.

- Zero dimensional (0D):$L_x, L_y, L_z < L_0$, i.e, $n = 3$.

  Zero dimensional systems are so named because in these systems, electron motion is restricted along all three directions, i.e. full confinement system. The resulting structure is called quantum dot. All systems of the dimensions of 0D are in the nanometric size range. Consequently, such materials have electronic properties intermediate between those of bulk semiconductors and those of discrete molecules.

Different dimensional mesoscopic systems are shown in Fig. A.1.

A.2 Density of states

The density of states describes the number of sates per unit energy per unit volume, that are available to the system, and is important to calculate the carrier concentration and energy distribution.

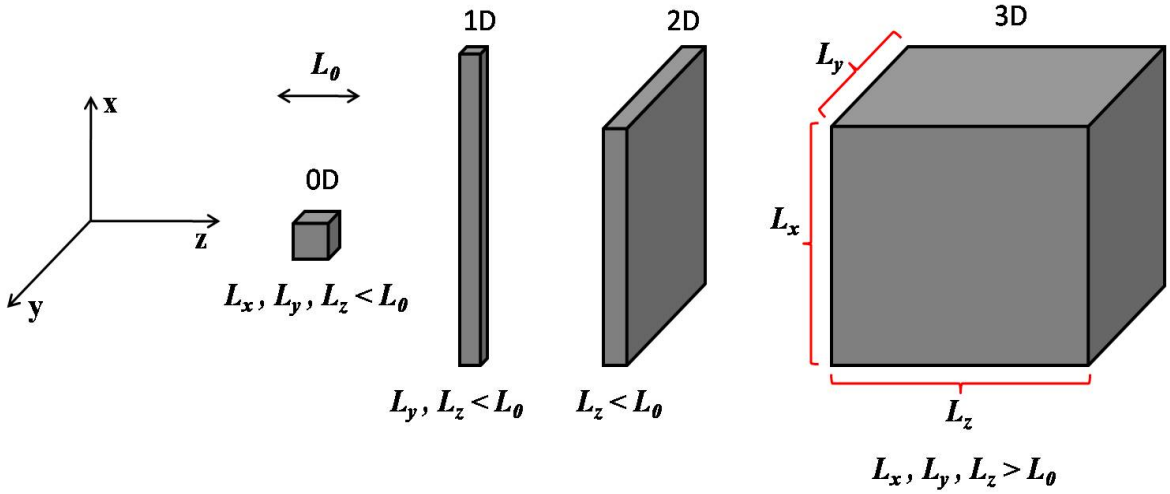

Figure A.1 Different dimensional mesoscopic systems.

A.2.1 Three dimensional density of states

From introductory solid state physics [19, 20], it is known that for a three dimensional sample (say cube of dimension L), the allowed values of wave vector $\vec{k}$ or rather its components are,

$$k_x = \frac{2\pi}{L} n_x, \qquad k_y = \frac{2\pi}{L} n_y, \qquad k_z = \frac{2\pi}{L} n_z$$

where, n_x, n_y, n_z are integers and are continuous quantum numbers. The available k-space volume per state is,

$$V_{single-state} = \left(\frac{2\pi}{L}\right)\left(\frac{2\pi}{L}\right)\left(\frac{2\pi}{L}\right) = \frac{8\pi^3}{L^3} \tag{A.1}$$

Now we wish to consider a system of N non-interacting electrons, all we have to do is to take account of the Pauli exclusion principle for electrons with spin $s = \pm\frac{1}{2}$, each value of $\vec{k}$ can accommodate at most two electrons. Obviously when constructing the ground-state we must consider filling these $\vec{k}$-states from $\vec{k} = 0$ and successively filing states of higher energy (energy $\propto k^2$). This leads us directly to the concept of the Fermi surface. In 3D, The Fermi space is a sphere of radius k_F, volume of the Fermi space is,

$$V_{space} = \frac{4}{3}\pi k_F^3 = \frac{4}{3}\pi \left(\frac{2m_e}{\hbar^2} E_F\right)^{\frac{3}{2}} \tag{A.2}$$

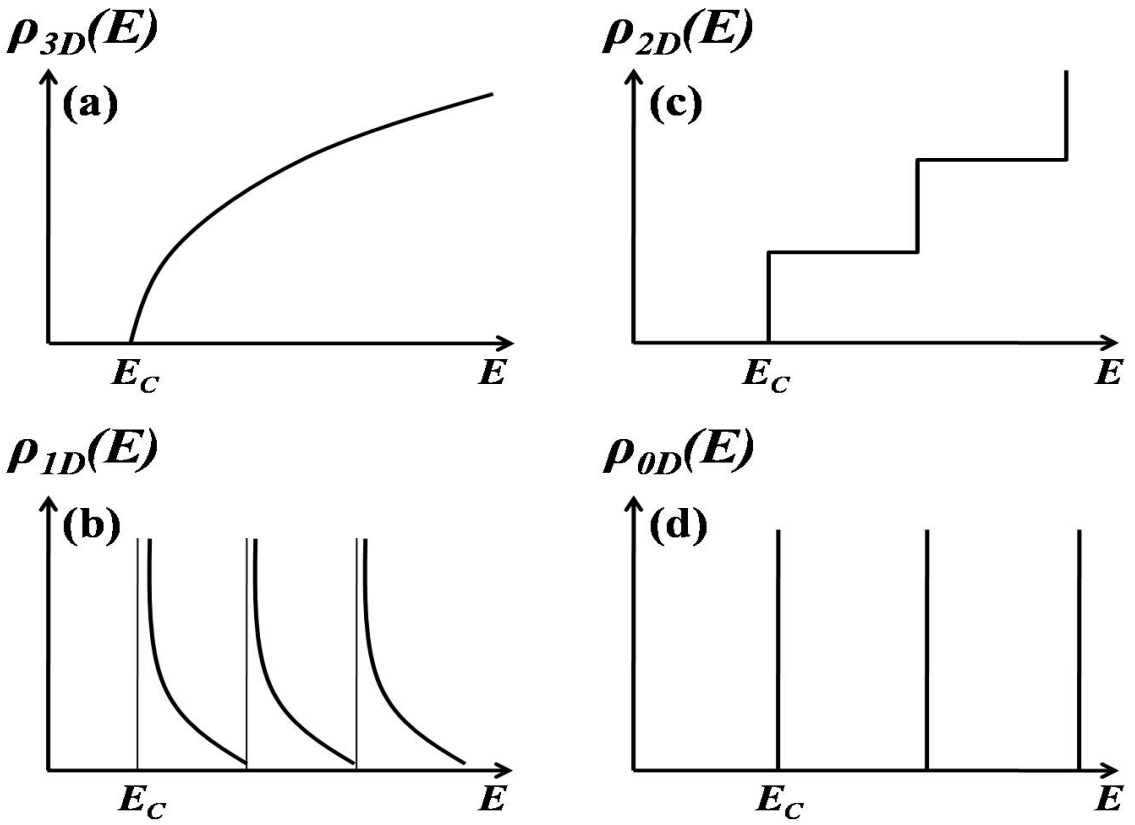

Figure A.2 Density of states for different dimensional mesoscopic systems.

At T = 0 all states within the sphere are occupied while outside, all states are empty. The number N_{3D} of states occupied below the Fermi energy is given by,

$$N_{3D} = \frac{2 \times V_{space}}{V_{single-state}} = \frac{1}{3}\left(\frac{2m_e}{\hbar^2}E_F\right)^{\frac{3}{2}}\frac{L^3}{\pi^2} \tag{A.3}$$

Then density of states for three dimensional system is given by,

$$\begin{aligned} & \rho_{3D} = \frac{\frac{dN}{dE}}{L^3} = \frac{m_e}{\pi^2\hbar^3}\left(2m_eE_F\right)^{\frac{1}{2}} \\ \text{or,} \quad & \rho_{3D} \propto E_F^{\frac{1}{2}} \end{aligned} \tag{A.4}$$

The three dimensional density of states ρ_{3D} as a function of energy is shown in Fig. A.2(a).

A.2.2 Two dimensional density of states

In a similar way as shown in the 3D case, the allowed values of components of $\vec{k}$ are,

$$k_x = \frac{2\pi}{L}n_x, \qquad k_y = \frac{2\pi}{L}n_y, \qquad k_z = k_0, k_1, ..$$

that is the components of $\vec{k}$ along x and y direction are continuous, but that along z is quantized. Hence the energy along z direction is also quantized. The available k-space volume per state is,

$$V_{single-state} = \left(\frac{2\pi}{L}\right)\left(\frac{2\pi}{L}\right) = \frac{4\pi^2}{L^2} \tag{A.5}$$

In 2D, the Fermi space is a circle of radius k_F, thus "volume" (area) of the Fermi space is,

$$V_{space} = \pi k_F^2 = \pi\left(\frac{2m_e}{\hbar^2}E_F\right) \tag{A.6}$$

The number N_{2D} of states occupied below the Fermi energy is given by,

$$N_{2D} = \frac{2 \times V_{space}}{V_{single-state}} = \left(\frac{m_e}{\hbar^2}E\right)\frac{L^2}{\pi} \tag{A.7}$$

Then density of states for two dimensional system is given by,

$$\begin{aligned} \rho_{2D} &= \frac{\frac{dN}{dE}}{L^2} = \frac{m_e}{\pi\hbar^2} \\ or, \rho_{2D} &\propto E^0 \end{aligned} \tag{A.8}$$

The two dimensional density of states ρ_{2D} as a function of energy is shown in Fig. A.2(b). It is clear that the two dimensional density of states does not depend on energy. Immediately, as the top of the energy-gap is reached, a significant number of states are available. The discrete energy level along the confined direction gives rise to a staircase-like density of states as a function of energy.

A.2.3 One dimensional density of states

The allowed values of components of $\vec{k}$ are,

$$k_x = \frac{2\pi}{L}n_x, \qquad k_y = k_{y0}, k_{y1}.., \qquad k_z = k_{z0}, k_{z1}..$$

that is the components of $\vec{k}$ along x direction is continuous, but that along y and z directions are quantized. Hence the energy along y and z directions are also quantized. The available k-space volume per state is,

$$V_{single-state} = \left(\frac{2\pi}{L}\right) \tag{A.9}$$

In 1D, the Fermi space is a line of magnitude k_F, thus “volume" of the Fermi space is,

$$V_{space} = k_F \tag{A.10}$$

The number N_{2D} of states occupied below the Fermi energy is given by,

$$N_{1D} = \frac{2 \times V_{space}}{V_{single-state}} = \frac{2k}{\frac{2\pi}{L}} = \frac{L}{\pi}\left(\frac{2m_e}{\hbar^2}E\right)^{\frac{1}{2}} \tag{A.11}$$

Then density of states for two dimensional system is given by,

$$\begin{aligned} \rho_{1D} &= \frac{\frac{dN}{dE}}{L} = \frac{1}{\pi\hbar}\left(\frac{2m_e}{E}\right)^{\frac{1}{2}} \\ or, \rho_{1D} &\propto E^{\frac{-1}{2}} \end{aligned} \tag{A.12}$$

The one dimensional density of states ρ_{1D} as a function of energy is shown in Fig. A.2(c).

A.2.4 Zero dimensional density of states

The size of the system becomes so small due to the confinement, that the energy states allowed are no longer continuous but discrete. In 0D, the energy states can be represented by Dirac delta function and is given by,

$$\rho_{0D}(E) = \delta(E - E_C) \tag{A.13}$$

The one dimensional density of states ρ_{1D} as a function of energy is shown in Fig. A.2(d).

Appendix B

Transmission for a series of ballistic conductors

In this appendix we will show the transmission for a long conductor of length L, which is actually a series of small conductors. Let us for simplicity consider two serial ballistic conductors with transmission probabilities T_1 and T_2 respectively. A schematic representation of the system is shown in Fig. B.1. This scattering system can have multiple processes, for instance, transmission without reflection, transmission with two reflections, transmission with four reflections and so on. Then the total probability of transmission T_{12} is obtained by summing all possible reflection as well as transmission paths. Since, we have considered ballistic conductors, there is no phase randomisation. The net transmission probability of the scattering system is,

$$\begin{aligned} T_{12} &= T_1T_2 + T_1R_2R_1T_2 + T_1R_2^2R_1^2T_2 + \cdots\cdots \\ &= T_1T_2\left(1 + R_2R_1 + R_2^2R_1^2 + \cdots\cdots\right) \end{aligned}$$

This is a geometric series with common ratio

$$T_{12} = T_1T_2\left(\frac{1}{1-R_1R_2}\right)$$

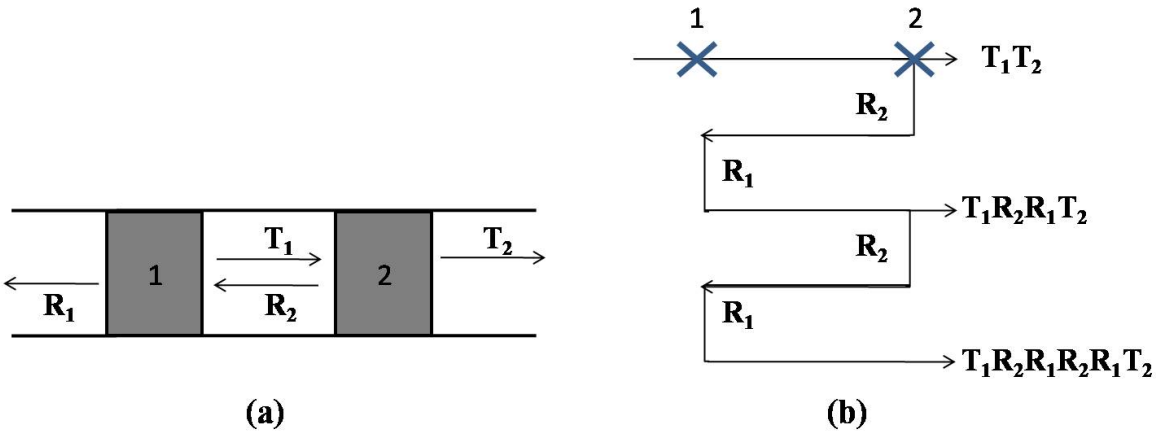

Figure B.1 (a)Two scatterers 1 and 2 in series having transmission probabilities T_1 and T_2, and reflection probabilities R_1 and R_2, respectively. (b) Feynmann diagram to represent all possible paths taken by the electron. Summing all the terms, we get the total transmission probability T_{12}.

Again using the relations, $R_1 = 1 - T_1$ and $R_2 = 1 - T_2$, we can write,

$$\begin{aligned} T_{12} &= \frac{T_1 T_2}{(1-T_1)(1-T_2)} \\ \Rightarrow \frac{1}{T_{12}} &= \frac{(1-T_1-T_2+T_1T_2)}{T_1T_2} \end{aligned}$$

Subtracting both sides by 1, we can write,

$$\begin{aligned} \frac{1-T_{12}}{T_{12}} &= \frac{(1-T_1-T_2)}{T_1T_2} \\ \text{or,} \quad \frac{1-T_{12}}{T_{12}} &= \frac{1-T_1}{T_1} + \frac{1-T_2}{T_2} \end{aligned} \tag{B.1}$$

Thus the quantity $\frac{1-T_{12}}{T_{12}}$ has an additive property. Generalising Eq. (B.1) for N number of scatterers, then we can write the transmission probability as,

$$\frac{1-T_{1N}}{T_{1N}} = \sum_j \frac{1-T_j}{T_j} \tag{B.2}$$

If the transmission probability for all the N scatterers is same T (say), then Eq. (B.2) reduces to,

$$\frac{1-T_{1N}}{T_{1N}} = N\frac{1-T}{T} \tag{B.3}$$

Let ν be the linear density of the scatterers, then we can replace N by νL in Eq. (B.3) and obtain

$$\begin{aligned} \frac{1-T_{1N}}{T_{1N}} &= \frac{\nu L(1-T)}{T} \\ \Rightarrow T_{1N} &= \frac{T}{\nu L(1-T)+T} \end{aligned} \tag{B.4}$$

Let us consider $L_0 = \frac{T}{\nu(1-T)}$, then

$$\frac{L+L_0}{L_0} = \frac{\nu L(1-T)+T}{T} \tag{B.5}$$

Substituting Eq. (B.5) in Eq. (B.4), we get the transmission probability as a function of L,

$$T_{1N} = \frac{L_0}{L+L_0} \tag{B.6}$$

Appendix C

Fisher Lee relation and Green's function for isolated lead

In this appendix we will show two results the Fisher Lee relation, a relation between scattering matrix elements and Green's function, and the analytical expression of g_p^R, Green's function for semi-infinite lead, described in chapter 3.

C.1 Fisher Lee relation

Let us consider a conductor connected to a pair of leads (p and q). The interface between the leads and the conductor are defined by $x_p = 0$ and $x_q = 0$. We define,

$$G_{qp}^R(y_q;y_p) \equiv G_{qp}^R(x_q = 0, y_q; x_p = 0, y_p) \tag{C.1}$$

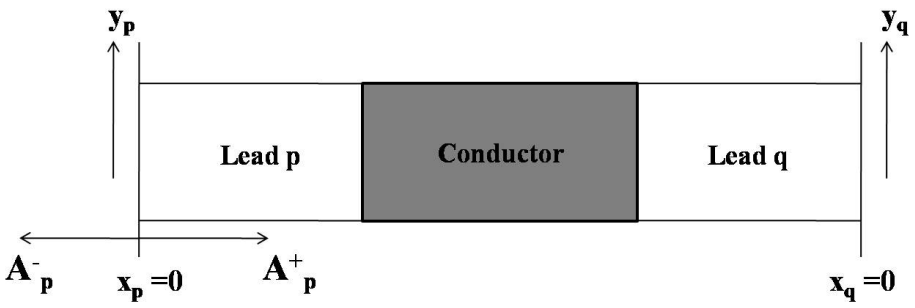

Figure C.1 A conductor connected to leads p and q.

which connects two points lying in the two planes $x_p = 0$ and $x_q = 0$, with transverse coordinates y_p and y_q. Our purpose is to write G^R_{qp} in terms of scattering S-matrix elements. For this, let us neglect the transverse direction and consider the one dimensional case with unit excitation at $x_p = 0$. As discussed in chapter 3, this excitation gives rise to two types of waves, one travelling towards the conductor with amplitude A^+_p and another travelling away from the conductor with amplitude A^-_p.

$$G^R_{qp} = A^+_p e^{ikx_p}, \text{for } x_p > 0 \tag{C.2}$$

$$G^R_{qp} = A^-_p e^{-ikx_p}, \text{for } x_p < 0 \tag{C.3}$$

Applying boundary conditions on G^R_{qp} at x_p,

$$\left[G^R_{qp}\right]_{x_p=0+} = \left[G^R_{qp}\right]_{x_p=0-}$$

$$\text{and} \qquad \left[\frac{dG^R_{qp}}{dx}\right]_{x_p=0+} - \left[\frac{dG^R_{qp}}{dx}\right]_{x_p=0-} = \frac{2m_e}{\hbar^2}$$

we get the amplitudes $A^\pm_p$,

$$A^+_p = A^+_p = -\frac{i}{\hbar v_p} \tag{C.4}$$

where, v_p is the velocity of the outgoing waves from lead p.

The wave travelling towards the conductor is scattered to the leads with amplitude $s'_{qp}A^+_p$, hence single mode G^R_{qp} is given by,

$$G^R_{qp} = \delta_{qp}A^-_p + s'_{qp}A^+_p \tag{C.5}$$

But the matrix elements s'_{qp} are generally not unitary, to incorporate unitary it is customary to divide the matrix elements by square root of velocity, i. e.,

$$s_{qp} = \frac{s'_{qp}}{\sqrt{v_p/v_q}} \tag{C.6}$$

Using Eqs. (C.4) and (C.6), Eq. (C.5) can be written as,

$$G^R_{qp} = -\frac{i}{\hbar v_p}\delta_{qp} - \frac{i}{\hbar v_p}\frac{s_{qp}}{\sqrt{v_q/v_p}}$$

$$\text{or,} \qquad s_{qp} = -\delta_{qp} + i\hbar\sqrt{v_q v_p} \tag{C.7}$$

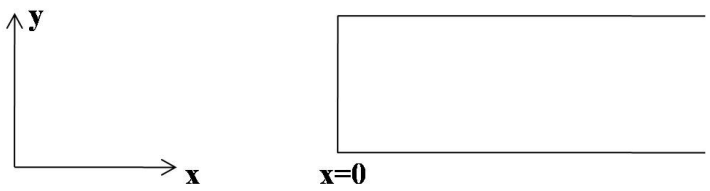

Figure C.2 A semi-infinite wire with hard walls at $x = 0$. In the y-direction, there is a confining potential $V(y)$ leading to transverse modes $\chi_m(y)$.

This is the desired Fisher-Lee relation in the case of single mode conductor. If we take multiple modes in consideration, then the relation modifies to

$$s_{nm} = -\delta_{nm} + i\hbar\sqrt{v_n v_m}\iint \chi_n(y_q)\left[G^R_{qp}(y_q;y_p)\right]\chi_m(y_p)dy_q dy_p \tag{C.8}$$

C.2 Analytical form of g_p^R

To derive the Green's function for isolated semi-infinite leads, we start with the retarded Green's function in terms of eigenfunction Ψ_m and eigenenergies ε_m,

$$G^R = \sum_m \frac{\Psi_m^* \Psi_m}{E - \varepsilon_m + i\eta} \tag{C.9}$$

The Schrödinger equation of a semi-infinite wire (shown in Fig. C.2) with a transverse confinement potential $V(y)$ can be written as,

$$\left[-\frac{\hbar^2}{2m_e}\left(\frac{\partial^2}{\partial x^2} + \frac{\partial^2}{\partial y^2}\right) + V(y)\right]\Psi(x,y) = \varepsilon_m \Psi(x,y)$$

then solving the Schrödinger equation using separation of variables one can write,

$$\left[-\frac{\hbar^2}{2m_e}\frac{d^2}{dx^2}\right]\psi(x) = (\varepsilon_m - \varepsilon_{m0})\psi$$
$$\left[-\frac{\hbar^2}{2m_e}\frac{d^2}{dx^2} + V(y)\right]\chi(y) = \varepsilon_{m0}\chi(y)$$

where, ε_{m0} is a constant. Then the solution is given by,

$$\Psi_m(x,y) = \frac{2}{\sqrt{L}}\chi_m(y)sin(\kappa x) \tag{C.10}$$

where,

$$(\varepsilon_m - \varepsilon_{m0}) = \frac{\hbar^2\kappa^2}{2m_e} \tag{C.11}$$

Substituting Eq. (C.10) in Eq. (C.9), one can write,

$$G(x,y;x,y') = \frac{2}{L}\sum_m\sum_\kappa \frac{\chi_m(y)\chi_m(y')sin^2(\kappa x)}{E-\varepsilon_{m0}-\frac{\hbar^2\kappa^2}{2m_e}+i\eta} \tag{C.12}$$

where, we have set $x' = x$, since we are now interested in the sites with same x-coordinate. Because the lead is infinite in the x-direction, κ is continuous and the sum over κ can be replaced by an integral using the common rule,

$$\sum_\kappa \to \frac{L}{\pi}\int d\kappa$$

then the above Green's function can be rewritten as,

$$G(x,y;x,y') = \frac{2}{\pi}\sum_m \chi_m(y)\chi_m(y')\int_0^\infty \frac{sin^2(\kappa x)}{E-\varepsilon_{m0}-\frac{\hbar^2\kappa^2}{2m_e}+i\eta}d\kappa$$

One can easily write,

$$\begin{aligned} sin^2(\kappa x) &= \frac{1-cos(2\kappa x)}{2} \\ &= \frac{1}{2}-\frac{e^{2i\kappa x}+e^{-2i\kappa x}}{4} \\ &= \frac{1-e^{2i\kappa x}}{4}+\frac{1-e^{-2i\kappa x}}{4} \end{aligned}$$

Therefore,

$$\begin{aligned} G(x,y;x,y') &= \frac{1}{2\pi}\sum_m \chi_m(y)\chi_m(y')\int_{-\infty}^\infty \frac{1-e^{2i\kappa x}}{E-\varepsilon_{m0}-\frac{\hbar^2\kappa^2}{2m_e}+i\eta}d\kappa \\ &= -\frac{m_e}{\pi\hbar^2}\sum_m \chi_m(y)\chi_m(y')\int_{-\infty}^\infty \frac{1-e^{2i\kappa x}}{\kappa^2-k_m^2(1+i\delta)}d\kappa \end{aligned} \tag{C.13}$$

where,

$$k_m^2 = \frac{2m_e}{\hbar^2}(E-\varepsilon_m) \qquad \text{and} \qquad \delta = \frac{\eta}{E-V_0} \tag{C.14}$$

Using Cauchy's integral theorem [140] the integral in Eq. (C.13) can be solved. The integrand has two poles at,

$$\kappa = \pm k_m\sqrt{1+i\delta} = \pm k_m, \qquad \text{Since,} \qquad \delta \to 0.$$

The pole $+k_m$ lies in the contour $x > 0$ and other pole $-k_m$ in the contour $x < 0$. Since the region we are interested in is positive x-direction, the pole $-k_m$ does not contribute to the integral. The value of

the integral (for $\delta \to 0$) is then given by residue at pole $+k_m$, i.e,

$$\begin{aligned}\int_{-\infty}^{\infty} \frac{1-e^{2i\kappa x}}{\kappa^2-k_m^2} d\kappa &= 2\pi i \lim_{\kappa \to +k_m} \frac{1-e^{2i\kappa x}}{\kappa + k_m} \\ &= 2\pi i \frac{1-e^{2ik_m x}}{2k_m} \\ &= 2\pi e^{ik_m} sin(k_m x) \end{aligned} \tag{C.15}$$

Substituting, Eq. (C.15) in Eq. (C.13) we get,

$$G(x,y;x,y') = -\frac{m_e}{\pi\hbar^2} \sum_m \chi_m(y)\chi_m(y') 2\pi e^{ik_m} sin(k_m x) \tag{C.16}$$

$$= -\sum_m \frac{2sin(k_m x)}{\hbar v_m} \chi_m(y) e^{ik_m} \chi_m(y') \tag{C.17}$$

$$\text{Using,} \qquad v_m = \frac{\hbar k_m}{m_e}$$

To obtain the corresponding Green's function in matrix form, we can simply replace y, y' by p_i, p_j and x by lattice spacing a, then we get,

$$\begin{aligned} g_p^R &= G^R(x,y;x,y') \mid_{(x=a, y=p_i, y'=p_j)} \\ &= -\sum_m \frac{2sin(k_m a)}{\hbar v_m} \chi_m(p_i) e^{ik_m} \chi_m(p_j) \end{aligned} \tag{C.18}$$

Appendix D

Appendix for Chapter 5

In this appendix we will explicitly justify Eqs. (5.30) and (5.31).

D.1 Justification of Eq. (5.30)

From Eq. (5.15), we can write

$$\rho(3,1) = -\frac{1}{2\pi}\int d\mathbf{r}^3 |t_{31}|^2 \frac{\delta\theta_{t_{31}}}{\delta V(\mathbf{r})} \tag{D.1}$$

In Eq. (D.1) using the well known semi classical approximation $\int d\mathbf{r}^3 \frac{\delta t_{31}}{\delta V(\mathbf{r})} \cong -\frac{dt_{31}}{dE}$ [61], we get, (see Eq. (5.21))

$$\rho(3,1) \approx \frac{1}{2\pi}|t_{31}|^2 \frac{d\theta_{t_{31}}}{dE} \tag{D.2}$$

Now, for a contour C' traced when energy is varied from 0 to E_1,

$$\begin{aligned} \int_{C'} d\theta_{t_{31}} &= \int_0^{E_1} \frac{d\theta_{t_{31}}}{dE} dE \\ &= \int_0^{E_1} \frac{\frac{1}{2\pi}|t_{31}|^2 \frac{d\theta_{t_{31}}}{dE}}{\frac{1}{2\pi}|t_{31}|^2} dE \\ \text{Using Eq. (D.2)} \qquad \int_{C'} d\theta_{t_{31}} &\approx 2\pi \int_0^{E_1} \frac{\rho(3,1)}{|t_{31}|^2} dE \end{aligned} \tag{D.3}$$

D.2 Justification of Eq. (5.31)

We know that in a scattering problem increasing incident energy by dE is equivalent to decreasing the potential globally by a constant amount $\Delta\varepsilon$, such that $dE = -e\Delta\varepsilon$, where e is electronic charge that we will set to 1 to simplify our arguments. That is, the new potential is $V'(\mathbf{r}) = V(\mathbf{r}) - \Delta\varepsilon$. Hence if we can generate a closed sub-loop in the Argand diagram by varying E, then we can also do so by globally changing the potential and for such a closed contour like *ABQFA* in Fig. 5.7(c),

$$\oint_{ABQFA} \delta\theta_{s_{\alpha\beta}} = 0$$

$$\text{i.e.} \qquad -\oint_C \int_{global} \frac{\delta\theta_{s_{\alpha\beta}}}{\delta V(\mathbf{r})} \Delta\varepsilon d\mathbf{r}^3 = 0 \tag{D.4}$$

Now we replace the global integration over $\mathbf{r}$ by an integration over the sample or the scattering region only, since we have seen that it can be done in case of closed contours or inside an integration of the type $\oint_C$ in Eq. (D.4). This has already been discussed with respect to Eqs. (5.28) and (5.29).

$$\begin{aligned}
\text{Therefore} \qquad -\oint_C \int_{sample} \frac{|s_{\alpha\beta}|^2}{|s_{\alpha\beta}|^2} \frac{\delta\theta_{s_{\alpha\beta}}}{\delta V(\mathbf{r})} \Delta\varepsilon d\mathbf{r}^3 &= 0 \\
\text{or,} \qquad -\oint_C \frac{1}{|s_{\alpha\beta}|^2} \Delta\varepsilon \int_{sample} |s_{\alpha\beta}|^2 \frac{\delta\theta_{s_{\alpha\beta}}}{\delta V(\mathbf{r})} d\mathbf{r}^3 &= 0 \\
\text{or,} \qquad 2\pi \oint_C \frac{\rho(\alpha,\beta)}{|s_{\alpha\beta}|^2} \Delta\varepsilon &= 0 \qquad \text{Using Eq. (5.15)}
\end{aligned}$$

Therefore, the R.H.S of Eq. (5.31) is justified if an electronic charge is multiplied to the numerator.

Appendix E

Appendix for Chapter 6

From Eq. (6.18),

$$\Psi_N(\{r_j,\theta_j\}) \quad = \quad \sum_{\{m'_j\}} a_{\{m'_j\}} \mathscr{A}\tau \tag{E.1}$$

where,

$$\tau = \prod_{j=1}^{N}\left[\left(A_{m'_j}J_{m'_j}\left(k_{n_j}r_j\right)+B_{m'_j}N_{m'_j}\left(k_{n_j}r_j\right)\right)\left(\frac{1}{\sqrt{2\pi}}e^{i(m'_j+\frac{\Phi}{\Phi_0})\theta_j}\right)\right]$$

Introducing centre of mass and relative coordinates, ξ and ζ_j respectively,

$$\xi = \frac{1}{N}\sum_{j=1}^{N}\theta_j, \qquad \zeta_j = \theta_j - \xi.$$

and substituting in the above equation, we get,

$$\tau = \prod_{j=1}^{N}\left[\left(A_{m'_j}J_{m'_j}\left(k_{n_j}r_j\right)+B_{m'_j}N_{m'_j}\left(k_{n_j}r_j\right)\right)\left(\frac{1}{\sqrt{2\pi}}e^{i(m'_j(\zeta_j+\xi)+\frac{\Phi}{\Phi_0}(\zeta_j+\xi))}\right)\right]$$

In some regime, for example, for parameters corresponding to Figs. 6.5a, 6.7 and 6.8, radial wave functions are independent of m'_j. So for $n_j = 1$,

$$\tau = \left(A_{m'_j}J_{m'_j}\left(k_{n_j}r_j\right)+B_{m'_j}N_{m'_j}\left(k_{n_j}r_j\right)\right)^N \frac{1}{\sqrt{2\pi}}e^{(i\sum_{j=1}^{N}m'_j\zeta_j+i\xi\sum_{j=1}^{N}m'_j+i\frac{\Phi}{\Phi_0}\sum_{j=1}^{N}\zeta_j+i\frac{\Phi}{\Phi_0}\sum_{j=1}^{N}\xi)}$$

Noting that $\sum_{j=1}^{N}m'_j = M'$ and $\sum_{j=1}^{N}\zeta_j = 0$, one gets,

$$\begin{aligned}\tau &= \left(A_{m'_j}J_{m'_j}\left(k_{n_j}r_j\right)+B_{m'_j}N_{m'_j}\left(k_{n_j}r_j\right)\right)^N\left(\frac{e^{i(M'+N\frac{\Phi}{\Phi_0})\xi}}{\sqrt{2\pi}}\prod_{j=1}^{N}e^{im'_j\zeta_j}\right)\\ &= e^{i(M'+N\frac{\Phi}{\Phi_0})\xi}\prod_{j=1}^{N}\left[\left(A_{m'_j}J_{m'_j}\left(k_{n_j}r_j\right)+B_{m'_j}N_{m'_j}\left(k_{n_j}r_j\right)\right)\left(\frac{e^{im'_j\zeta_j}}{\sqrt{2\pi}}\right)\right]\end{aligned}$$

Therefore from Eq. (E.1), we get,

$$\Psi_N(\{r_j,\theta_j\}) = \sum_{\{m'_j\}} a_{\{m'_j\}} \mathscr{A} e^{i(M'+N\frac{\Phi}{\Phi_0})\xi} \prod_{j=1}^{N}\left[\left(A_{m'_j}J_{m'_j}\left(k_{n_j}r_j\right)+B_{m'_j}N_{m'_j}\left(k_{n_j}r_j\right)\right)\left(\frac{e^{im'_j\zeta_j}}{\sqrt{2\pi}}\right)\right]$$

Using the fact that when symmetry is broken, $\hat{M}'$ commutes with Hamiltonian **H** (given by Eq. (6.20)), M' the eigenvalue corresponding to $\hat{M}'$ is a conserved quantity for each sets of $\left\{m'_j\right\}$, we get

$$\Psi_N(\{r_j,\theta_j\}) = e^{i(M'+N\frac{\Phi}{\Phi_0})\xi} \sum_{\{m'_j\}} a_{\{m'_j\}} \mathscr{A}$$
$$\prod_{j=1}^{N}\left[\left(A_{m'_j}J_{m'_j}\left(k_{n_j}r_j\right)+B_{m'_j}N_{m'_j}\left(k_{n_j}r_j\right)\right)\left(\frac{e^{im'_j\zeta_j}}{\sqrt{2\pi}}\right)\right] \tag{E.2}$$

Bibliography

[1] G. C. Ghirardi, A. Rimini and T. Weber, Phys. Rev. D **34**, 470 (1986).

[2] E. Schrödinger, Phys. Rev. **28**, 1049 (1926).

[3] L. de Broglie, Nature **112**, 540 (1923).

[4] Y. Omar, Contemp. Phys. **46**, 437 (2005).

[5] D. J. Griffiths, *Introduction to Quantum Mechanics* (Pearson Education, 2005) .

[6] W. Heisenberg, Zeitschrift für Physik **43**, 172 (1927).

[7] K. J. Laidler, *The World of Physical Chemistry* (Oxford University Press, 2001).

[8] *Correlated Electron Transport in One dimensional Mesoscopic Conductors*, Ph.D Thesis by Na Young Kim, (Stanford University, 2006).

[9] Y. Murayama, *Mesoscopic Systems: Fundamentals and Applications* (Wiley- VCH, 2001).

[10] *Directions in Condensed Matter Physics*, edited by G. Grinstein and G. Mazenko (World Scientific, Philadelphia, 1986).

[11] *Mesoscopic Phenomena in Solids*, edited by B. L. Altshuler, P. A. Lee and R. A. Webb (Elsevier Science, Amsterdam, 1991).

[12] *Quantum Coherence in Mesoscopic Systems*, edited by B. Kramer (Plenum Press, New York, 1991).

[13] *Granular Nanoelectronics*, edited by D. K. Ferry, J.R. Barker and C. Jacoboni (Plenum Press, New York, 1991).

[14] *Nanostructures and Mesoscopic Systems*, edited by W. P. Kirk and M. A. Reed (Academic Press, New York, 1992).

[15] *Single-Electron Tunnelling and Mesoscopic Devices*, edited by H. Koch and H. Lubbig (Springer-Verlag, New York, 1992).

[16] S. Datta, *Electronic transport in mesoscopic systems*, (Cambridge University Press, Cambridge, UK, 1995).

[17] *New Directions in Mesoscopic Physics*, edited by R. Fazio, V. F. Gantmakher and Y. Imry (Kluwer Academic Publishers, Netherlands, 2003).

[18] *Opto-electronic and quantum transport properties of semiconductor nanostructures*, Ph.D Thesis by Matthias Sabathil, (Technische Universität München, 2004).

[19] C. Kittel, *Introduction to Solid state physics*, (Wiley, 1996).

[20] N. W. Ashcroft and N. D. Mermin, *Solid State physics*, (Saunders, 1976).

[21] K. von Klitzing, Rev. Mod. Phys. **58**, 519 (1986).

[22] Y. Alhassid, Rev. Mod. Phys. **72**, 895 (2000).

[23] B. J. van Wees, H. van Houten, C. W. J. Beenakker, J. G. Williamson, L. P. Kouwenhoven, D. van der Marel, and C. T. Foxon, Phys. Rev. Lett. **60**, 848 (1988).

[24] D. A. Wharam, T. J. Thornton, R. Newbury, M. Repper, H. Ahmed, J. E. F. Frost, D. G. Hasko, D. C. Peacock, D. A. Ritchie, and G. A. C. Jones, J. Phys. C, **21**, 209 (1988).

[25] C. Davisson and L. H. Germer, Phys. Rev. **30**, 705 (1927).

[26] N. Bohr, Phil. Mag. S. **26**, 1 (1913).

[27] C. Harmans, *Mesoscopic Physics: An introduction*, (2nd version, 2003).

[28] Paul A. M. Dirac, Proc. of Roy. Soc. Series A **112** 661 (1926).

[29] J. T. Edwards and D. J. Thouless, J. Phys. C: Solid State Phys. **5**, 807 (1972).

[30] Yu. V. Sharvin, Sov. Phys. JETP **21**, 655 (1965).

[31] V. S. Tsoi, JETP Lett **19**, 114 (1974).

[32] I. K. Yanson, Sov. Phys. JETP **66**, 1035 (1974).

[33] A. G. M. Jansen, A. P. van Gelder, and P Wyder, J. Phys. C **13**, 6073 (1980).

[34] C. G. Eugster and J. A. del Alamo, Phys. Rev. Lett. **67**, 3586 (1991).

[35] H. van Houten and C. W. J. Beenakker, Phys. Today **49**, 22 (1996).

[36] K. Berggren and M. Pepper, Physics World **37**, 15 (2002).

[37] Harry J. Levinson, *Principles of Lithography*,(2*nd*. Ed., SPIE, 2005).

[38] K. G. Majumdar and B. Ghosh, *A Textbook on light* (5*th*. Ed., 2009).

[39] Francis A. Jenkins and Harvey E. White, *Fundamentals of optics* (Tata McGraw-Hill Education, 2001).

[40] Y. Aharonov, *On the aharonov-bohm effect and why heisenberg captures nonlocality better than Schrödinger*. arXiv preprint, arXiv:1303.2137 (2013).

[41] E. Merzbacher, *Quantum Mechanics*, (Wiley, New York, 1997).

[42] Y. Aharanov and D. Bohm, Phys. Rev. **115**, 485 (1959); Y. Aharanov and D. Bohm, Phys. Rev. **123**, 1511 (1961).

[43] R. A. Webb, S. Washburn, C. P. Umbach and R. B. Laibowitz, Phys. Rev. Lett. **52**, 2696 (1985).

[44] S. Washburn and R. A. Webb, Adv. in Phys. **35**, 375 (1986).

[45] A. M. Jayannavar and P. S. Deo, Mod. Phys. Lett. B **8** 301 (1994).

[46] Jian-Bai Xia, Phys. Rev. B **45**, 3593 (1992).

[47] R. Schuster, E. Buks, M. Heiblum, D. Mahalu, V. Umansky and Hadas Shtrikman, Nature (London) **385**, 417 (1997).

[48] Y. Ji, M. Heiblum, D. Sprinzak, D. Mahalu and H. Shtrikman, Science **290**, 779 (2000).

[49] Y. Ji, M. Heiblum and H. Shtrikman, Phys. Rev. Lett. **88**, 076601 (2002).

[50] R. Englman and A. Yahalom, Phys. Rev. B **61**, 2716 (2000).

[51] J. D. Jackson, *Classical Electrodynamics*, (3*rd* Ed., 1999).

[52] A. E. Miroshnichenko, S. Flach and Y. S. Kivshar, Rev. Mod. Phys. **82**, 2257 (2010).

[53] *Time in Quantum Mechanics*, edited by J. G. Muga, R. Sala Mayato, and I. L. Egusquiza (Springer, 2002).

[54] M. Büttiker, Phys. Rev. B **46**, 12485 (1992).

[55] M. Büttiker, Phys. Rev. Lett. **65**, 2901 (1990).

[56] B.J. van Wees, Phys. Rev. Lett, 60, 29 (1988).

[57] R. Landauer, Physica Scripta, T42, 110 (1992).

[58] J. Frenkel, Phys. Rev. B 36, 1604 (1930).

[59] W. Ehrenberg, and H. Honl, Z. Phys. 68, 289 (1931).

[60] M. Büttiker, H. Thomas and A. Pretre, Z. Phys. B **94**, 133 (1994).

[61] M. Büttiker, Pramana Journal of Physics **58**, 241 (2002).

[62] M. Büttiker, Phys. Rev. B **27**, 6178 (1993).

[63] Daniel S. Fisher and Patrick A. Lee, Phys. Rev. B, **23**, 6851 (1981).

[64] E. Buks, R. Schuster, M. Heiblum, D. Mahalu, V. Umansky, and H. Shtrikman, Phys. Rev. Lett. **77**, 4664 (1996).

[65] K. Kobayashi, H. Aikawa, S. Katsumoto and Y. Iye, Phys. Rev. B **68**, 235304 (2003).

[66] K. Kobayashi, H. Aikawa, A. Sano, S. Katsumoto and Y. Iye, Phys. Rev. B **70**, 035319 (2004).

[67] J. M. Ziman, *Principles of the Theory of Solids*, (Cambridge University Press, Cambridge, UK, 1979).

[68] F.T. Smith, Phys. Rev. **118**, 349 (1960.

[69] P. Singha Deo, Phys. Rev. B **75**, 235330 (2007).

[70] H. W. Lee, Phys. Rev. Lett **82**, 2358 (1999).

[71] A. L. Yeyati and M. Büttiker, Phys. Rev. B **62**, 7307 (2000).

[72] T. Taniguchi and M. Büttiker, Phys. Rev. B **60**, 13814 (1999).

[73] E. H. Hauge, J. P. Falck, and T. A. Fjeldly, Phys. Rev. B **36**, 4203 (1987).

[74] C. R. Leavens and G. C. Aers, Phys. Rev. B **39**, 1202 (1989).

[75] B. F. Bayman and C. J. Mehoke, Am. J. Phys. **51**, 875 (1983).

[76] D.F. Urban and H. Grabert, Phys. Rev. Lett. **91**, 256803-1 (2003).

[77] P. F. Bagwell, Phys. Rev. B **41**, 10354 (1990).

[78] H. Wu, D. W. L. Sprung and J. Martorell, Phys. Rev. B **45**, 11960 (1992).

[79] V. Gasparian, T. Christen, and M. Büttiker, Phys. Rev. A **54**, 4022 (1996).

[80] H. M. Nussenzvig, Phys. Rev. A **62**, 042107 (2000).

[81] C. Texier and M. Büttiker, Phys. Rev. B **67**, 245410 (2003).

[82] H. G. Winful, Phys. Rev. Lett. **91**, 260401 (2003).

[83] M. D. Stenner, D. J. Gauthier and M. A. Neifeld Nature **425**, 695 (2003).

[84] M. Avinun-Kalish, M. Heiblum, O. Zarchin, D. Mahalu and V. Umansky, Nature (London) **436**, 529 (2005).

[85] M. Zafflon, Aveek Bid, M. Heiblum, D. Mahalu, and V. Umansky, Phys. Rev. Lett. **100**, 226601 (2008).

[86] P. S. Deo, Phys. Rev. B **53**, 15447 (1996).

[87] P. Singha Deo, Solid State Commun. **107**, 69 (1998).

[88] G. Hackenbroich, Phys. Reports **343**, 463 (2001).

[89] S. Bandopadhyay and P. S. Deo, Phys. Rev. B **68**, 113301 (2003).

[90] P. S. Deo and M. Manninen, J. Phys.: Condens. Matter **18**, 5313 (2006).

[91] B. Solís, M. L. Ladrón de Guevara, P. A. Orellana, Phys. Lett. A **372**, 4736 (2008).

[92] V. Vargiamidis and V. Fessatidis, Phys. Lett. A **374**, 4438 (2010).

[93] U. Gerland, J. von Delft, T. A. Costi and Y. Oreg, Phys. Rev. Lett. **84**, 3710 (2000).

[94] J. F. Nye and M. V. Berry, Proc. Roy. Soc. Lond. A **336**, 165 (1974).

[95] M. V. Berry, J. Mod. Opt. **45**, 1845 (1998).

[96] P. S. Deo, J. Phys.: Condens. Matter **21**, 285303 (2009).

[97] T. Gramespacher and M. Büttiker, Phys. Rev. B **56**, 13026 (1997).

[98] T. Gramespacher and M. Büttiker, Phys. Rev. B **60**, 2375 (1999).

[99] U. Satpathi and P. Singha Deo, Int. J. Mod. Phys. B **26**, 1250028 (2012).

[100] P. S. Deo and A. M. Jayannavar, Mod. Phys. Lett. B **10**, 787 (1996).

[101] A. M. Jayannavar, Phys. Rev. B **49**, 14718 (1994).

[102] A. K. Gupta and A. M. Jayannavar, Phys. Rev. B **52**, 4156 (1995).

[103] T. P. Pareek, S. K. Joshi and A. M. Jayannavar, Phys. Rev. B **57**, 8809 (1998).

[104] S. K. Joshi, D. Sahoo and A. M. Jayannavar, Phys. Rev. B **62**, 880 (2000).

[105] V. Gasparian and A. Suzuki, J. Phys.: Condens. Matter **21**, 405302 (2009).

[106] V. Gasparian, M. Cahay and E. Jódar, J. Phys.: Condens. Matter **23**, 045301 (2011).

[107] V. Gasparian and E. Cuevas, Solid State Commun. **164**, 11 (2013).

[108] R. Landauer and Th. Martin, Rev. Mod. Phys. **66**, 217 (1994).

[109] P. Singha Deo, Int. J. Mod. Phys. B **19**, 899 (2005).

[110] P. S. Deo, Pramana J. Phys. **58**, 195 (2002).

[111] A. Bohr and B. R. Mottelson, *Nuclear Structure*, Vol. 2 (Benjamin, New York, 1975).

[112] S. M. Reimann, M. Koskinen, and M. Manninen, Phys. Rev. B **59**, 1613 (1999).

[113] M. Koskinen, M. Manninen, and S. M. Reimann, Phys. Rev. Lett. **79**, 1389 (1997).

[114] S. M. Riemann and M. Manninen, Rev. Mod. Phys. **74**, 1283 (2002).

[115] M. Koskinen, M. Manninen, B. Mottelson, and S. M. Reimann, Phys. Rev. B **63**, 205323 (2001).

[116] S. Datta, M. Kabir, T. Saha- Dasgupta, and A. Mookerjee, Phys. Rev. B **80**, 085418 (2009), and references therein.

[117] S. Viefers, P. S. Deo, S. M. Reimann, M. Manninen, and M. Koskinen, Phys. Rev. B **62**, 10668 (2000).

[118] S. Viefers, P. Koskinen, P. Singha Deo P. and M. Manninen, Physica E, **21**, 1 (2004).

[119] A. V. Filinov, M. Bonitz and Yu. E. Lozovik, Phys. Rev. Lett. **86**, 3851 (2001).

[120] F. M. Peeters, Phys. Rev. B **30**, 159 (1984).

[121] F. M. Peeters and Xiaoguang Wu, Phys. Rev. A **35**, 3109 (1987).

[122] G. Goldoni and F. M. Peeters, Phys. Rev. B **53**, 4591 (1996).

[123] V. M. Bedanov and F. M. Peeters, Phys. Rev. B **49**, 2667 (1994).

[124] V. A. Schweigert and F. M. Peeters, Phys. Rev. B **51**, 7700 (1995).

[125] Ashoori R. C., Nature **379**, 413 (1996).

[126] M. Manninen, M. Koskinen, S. M. Riemann and B. Mottelson, Eur. Phys. J. D **16**, 381 (2001).

[127] B. Reusch and R. Egger, Europhys. Lett. **64**, 84 (2003.;

[128] A. D. Guclu, J.-S. Wang, and H. Guo, Phys. Rev. B **68**, 035304 (2003).

[129] B. Szafran and F. M. Peeters, Europhys. Lett. **66**, 701 (2004).

[130] B. Szafran, F. M. Peeters, S. Bednarek, and J. Adamowski, Phys. Rev. B **69**, 125344 (2004).

[131] B. Szafran, F. M. Peeters, S. Bednarek, and J. Adamowski, Phys. Rev. B **70**, 235335 (2004).

[132] F. D. M. Haldane, J. Phys. C: Solid State Phys. **14**, 2585 (1981).

[133] D. Sheka, B. Ivanov and F. G. Mertens, Phys. Rev. A **68**, 012707 (2003).

[134] D. D. Sheka and F. G. Mertens, Phys. Rev. A **74**, 052703 (2006).

[135] Ho-Fai Cheung, Y. Gefen, E. K. Riedel, and Wei-Heng Shih, Phys. Rev. B **37**, 6050 (1988).

[136] T. Chakraborty and P. Pietiläinen, Phys. Rev. B **50**, 8460 (1994).

[137] V. Chandrasekhar, R. A. Webb, M. J. Brady, M. B. Ketchen, W. J. Gallagher and A. Kleinsasser , Phys. Rev. Lett. **67**, 3578 (1991).

[138] P. A. Maksym, Phys. Rev. B **53**, 10871 (1996).

[139] E. A. Jagla and C. A. Balseiro, Phys. Rev. Lett. **70**, 639 (1993).

[140] G. Arfken, *Mathematical Methods for Physicists*, (3*rd*. Ed. Academic Press, 1985).